Development of polymeric nanoparticles for gene delivery applications

Randa Ahmad Zoqlam

Thesis submitted in fulfilment of the requirements for the degree of Doctor of Philosophy, University of East Anglia. Norwich, United Kingdom

November 2021

Acknowledgements

I would like to express my gratitude to my supervisors Professor Sheng Qi and Dr Chris Morris, for all their help, advice, and invaluable encouragement throughout my PhD. I would also like to thank Professor Peter Belton and Professor Alaaldin M. Alkilany for their input and consistent support. Thanks, are also to Professor Ian Clark and Paige Paddy for their invaluable help in designing and conducting the qPCR experiments. Also, I wish to extend my special thanks to Dr Paul Thomas and Mr Bertrand Leze for their continuous help and technical support during the running of this project. I also would like to extend thanks to Dr Lorina Bisharat for her advice and kind words of support and encouragement.

I would like to express my thanks to all my fellow PhD students in the drug delivery group for being very helpful and supportive when I needed it most. Also, gracious thanks to my friends in Norwich: Zuzana, Carla, Enana, Hannah, Veronica and Afrah, for being always there through thick and thin. To my friends back home: Dana, Heba and Farah, thank you for your endless love, support, and encouragement throughout my PhD study. Your friendship and support have always lifted me up and kept me going.

To the person who taught me dedication and hard work, my wonderful father, whom without, this work would not have been possible, thanks for always believing in me!

To the most beautiful mother in the world, who lovingly listened to my daily lab experiments and research details for hours and encouraged me during the most challenging times, you inspire me to be the best version of myself, thank you for your endless love and support!

To my sister, Razan, I am beyond lucky to have been gifted a sister like you; thank you for all your love, care and support during my PhD study. Finally, I would like to extend thanks to all my precious family members for their love and support.

Abstract

Recent years have witnessed growing attention toward synthesising polymeric nanoparticles for pharmaceutical and biomedical applications. Therefore, microfluidics was introduced in an effort to advance nanoparticles synthesis and scaling up. However, a profound understanding of the synthesis processing parameters impact on the nanoparticle's properties is of utmost importance to ensure their successful application. Although various research efforts have demonstrated the capacity of microfluidics to fabricate polymeric nanoparticles, there remains a need for a consistent study to examine the difference between microfluidics and the conventional synthesis methods in terms of nanoparticles properties, limitations, and ease of synthesis.

Polymeric nanoparticles have been exploited for gene delivery applications due to their advantages. Therefore, several studies examined the use of polymeric nanoparticles for pDNA/miRNAs delivery to target the molecular mechanisms underlying disease development. Osteoarthritis is among these diseases with no effective treatments. Therefore, several studies have focused on explaining the molecular mechanisms underlying osteoarthritis development and the role of miRNAs to address the potential gene targets that could be targeted by miRNAs delivery. However, to the best of our knowledge, no prior studies have examined the use of polymeric NPs for targeting potential gene targets of osteoarthritis by miRNA delivery.

The work presented herein offers a comprehensive description and comparison of the different synthesis methods of polymeric nanoparticles, emphasising the advantages and limitations of each synthesis method. In addition, the synthesised nanoparticles were tested for their efficacy in gene delivery applications, including pDNA delivery, to examine the impact of the nanoparticle's properties on their transfection efficiency and miRNA-140 for targeting the molecular mechanisms underpinning osteoarthritis. The work conducted herein resulted in fabricating novel polymeric NPs that can efficiently deliver miRNA-140 to the chondrocytes to restore homeostasis by regulating the expression of *FZD6*, *ADAMTS5*, and *MMP 13*, three of the well-identified potential gene targets in osteoarthritis.

Table of Contents

List of Publications

1. Hamdallah, S. I., **Zoqlam, R.**, Erfle, P., Blyth, M., Alkilany, A. M., Dietzel, A., & Qi, S. (2020). Microfluidics for pharmaceutical nanoparticle fabrication: The truth and the myth. International journal of pharmaceutics, 584, 119408.

2. **Zoqlam, R**., Morris, C. J., Akbar, M., Alkilany, A. M., Hamdallah, S. I., Belton, P., & Qi, S. (2021). Evaluation of the Benefits of Microfluidic-Assisted Preparation of Polymeric Nanoparticles for DNA Delivery. Materials Science and Engineering: C, 112243.

List of Abbreviations

NPs	Nanoparticles
PNPs	Polymeric nanoparticles
PLGA	Polylactic-co-glycolic acid
PLA	Polylactide
PEG-co-PLA	Polyethylene glycol co-lactide
PEI	Polyethyleneimine
LA	Lactic acid
GA	Glycolic acid
PVA	Poly vinyl alcohol
PDMS	Polydimethylsiloxane
PET	Polyethene terephthalate
PS	Polystyrene
PC	Polycarbonate
PMMA	Polymethyl methacrylate
PCL	Polycaprolactone
CA	Cellulose acetate
PVP	Polyvinylpyrrolidone
Vitamin E TPGS	D-α-tocopheryl polyethylene glycol succinate
PTA	Phosphotungstic acid
DMSO	Dimethyl sulfoxide
DCM	Dichloromethane
DMF	Dimethylformamide
THF	Tetrahydrofuran
GPC	Gas-Phase chromatography

HPLC	High-performance liquid chromatography
CE	Capillary electrophoresis
MF	Microfluidics
MIVM	Multi-inlet vortex mixer
CIJM	Confined impinging jets mixer
CLM	Coaxial lamination mixer
DSC	Differential scanning calorimetry
T_g	Glass transition temperature
ATR-FTIR	Attenuated total reflectance Fourier transform infrared spectroscopy
SEM	Scanning electron microscope
TEM	Transmission electron microscope
DLS	Dynamic light scattering
FSC	Forward scatter channel
SSC	Side scattering channel
BCA	Bicinchoninic acid
AAV	Adeno-associated virus
FDA	Food and Drug Administration
ECM	Extracellular matrix
CME	Clathrin-mediated endocytosis
ER	Endoplasmic reticulum
MVB	Multi-vesicular bodies
CM	Cellular membrane
DOS	Degree of supersaturation
VR	Volume ratio
S/AS	Solvent/Antisolvent

S/AS VR	Solvent/anti-solvent volume ratio
CFC	Critical flocculation concentration
t_{mix}	Time of mixing
t precipitation	Precipitation time
Da	Damkohler number
RE	Reynolds number
Pe	Peclet number
τ_{agg}	Aggregation time
FR	Flow rate
FRR	Flow rate ratio
TFR	Total flow rate
FFS	Flow focused stream
O/W	Oil/Water
$W_1/O/W_2$	Water/Oil/Water
API	Active pharmaceutical ingredients
CB-method	Conventional bulk nanoprecipitation method
MF-method	Microfluidics assisted nanoprecipitation method
PI	Propidium iodide
PBS	Phosphate buffer saline
FBS	Fetal bovine serum
BSA	Bovine serum albumin
PFA	Paraformaldehyde
DAPI	4',6-diamidino-2-phenylindole
MTT	Methylthiazolyldiphenyl-tetrazolium bromide

ITS-G	Insulin-Transferrin-Selenium medium
CY5	Cyanine 5
2D	Two dimensional
3D	Three dimensional
min	Minute
ms	Milliseconds
h	Hour
PDI	Polydispersity index
M. wt	Molecular weight
pDNA	Plasmid DNA
RNAi	RNA interference
miRNA	MicroRNA
siRNA	Short interference RNA
RISC	RNA- induced silencing complex
IL-10	Interleukin 10
IL-4	Interleukin 4
IL-1ß	Interleukin 1ß
GFP	Green fluorescent protein
OA	Osteoarthritis
NSAIDs	Non-steroidal anti-inflammatory
MMPs	Metalloproteinases
FZD6	Frizzled 6
TGF-β1	Transforming growth factor
XPO5	Exportin5
NPC	Nuclear pore complex

List of Figures

List of Tables

Chapter 1

Introduction

1.1 Nanotechnology: A solution for drug and gene delivery limitations

Nanomedicine forms an emerging field that has expanded rapidly into a wide range of clinical applications. The development of nanoparticles has witnessed growing attention recently as a solution for conventional drug and gene delivery limitations. Nanomedicine implicates the utilisation of nanoparticles that can circumvent biological barriers and overcome the limitations of delivering free therapeutics [1].

Conventional drug delivery using large-sized materials suffers a group of constraints, including poor solubility, poor bioavailability, lack of target-specific delivery and systemic adverse effects [1,2]. Therefore, nanoparticles were implicated in overcoming these challenges using their potential to improve the solubility and stability of the encapsulated cargos besides targeting specific parts or organelles [1,2]. Hence, using nanoparticle-based delivery systems offers a solution for these critical challenges and maximises the overall therapeutic efficacy.

As is the case for drug delivery, gene delivery suffers critical challenges. For example, unmodified nucleic acids have a rapid clearance rate due to their susceptibility to degradation by nucleases, limiting the serum half-life of small interfering RNA to 5-60 minutes and 10 minutes for naked pDNA [3]. Additionally, naked nucleic acids induce undesired off-target and on-target effects and suffer hindered cellular uptake due to the negatively charged groups of nucleic acids [4]. Therefore, the success of gene therapy depends on ascertaining an efficient delivery system that can circumvent a group of biological barriers, delivering intact nucleic acids to the targeted cells [5]. Hence, several NPs systems have been suggested as efficient gene vectors, including polymeric NPs, liposomes, micelles and nanoemulsions [6]. However, polymeric NPs (i.e., Polylactic-co-glycolic acid (PLGA) NPs) have drawn significant attention due to their biodegradability, biocompatibility and ease of preparation and tuneability. PLGA is one of the few polymers that have been approved by the Food and Drug Administration (FDA) for biomedical applications owing to its biodegradability, biocompatibility, stability, tuneable degradation rates and versatility in surface functionalisation. Therefore, polymeric NPs can be simply prepared and tuned by controlling the processing conditions to prepare different sizes or surface functional groups. Generally, these modifications offer better control of the pharmacokinetics and biodistribution of these NPs.

Although NPs can offer efficient delivery of gene therapeutics, the NPs properties should be controlled by choosing the appropriate processing conditions to ensure the highest transfection efficiency. Accordingly, this emphasises the need for examining the impact of the NPs synthesis methods on the NPs properties since NPs properties determine their intracellular fate and subsequent gene transfection efficiency.

1.2 Synthesis of polymeric PLGA nanoparticles (NPs) using the nanoprecipitation method

Poly (lactic-co-glycolic acid) (PLGA) is a synthetic aliphatic linear copolymer that can be synthesised at different proportions between its constituent monomers, lactic acid (LA) and glycolic acid (GA) [7,8]. PLGA nanoparticles have shown considerable potential in the pharmaceutical drug delivery field attributed to a group of appealing properties. These properties can be summarised in the ability of PLGA NPs to provide sustained drug release profile, optimal drug bioavailability by preventing premature degradation in biological conditions and targeted delivery by surface functionalisation [9–11]. Therefore, several studies have demonstrated different fabrication techniques, and the nanoprecipitation technique is among the most well-established fundamental techniques for PLGA NPs fabrication [12,13].

Nanoprecipitation, also known as interfacial deposition or solvent displacement, is one of the first developed techniques for NPs fabrication by Fessi et al. [12]. Several studies adopted this technique for its myriad advantages. These advantages include simplicity, good reproducibility, ease of scalability, low volumes of toxic organic solvents, avoidance of high energy input and feasibility of producing small nanoparticles of submicron size and narrow size distribution profile [12]. However, it is noteworthy that the fabrication parameters should be carefully chosen to control the properties of the resulting NPs and fulfil the intended application requirements with the highest efficiency [13]. Thus, this requires a deep understanding of the nanoprecipitation theory and the impact of the fabrication parameters on the resulting NPs.

1.2.1 Nanoprecipitation theory: Nucleation and growth of NPs

Fundamentally, there are two approaches for NPs fabrication: bottom-up and top-down, which result in different NPs properties [14]. The top-down approach relies on reducing the size of larger particles using high pressure or energy equipment suitable for grinding the particles down to the nanosize [14]. This approach is generally used for fabricating inorganic metal

nanoparticles and is not commonly used in the pharmaceutical field. On the other hand, the bottom-up approach is widely used in the pharmaceutical field to synthesise organic nanoparticles [14]. The bottom-up approach consists of building nanostructured materials gradually from molecules or atoms into larger structures within the nanometre size [14–16]. This process occurs in an appropriate medium, which can be a liquid, gas or vapour phase [14].

Several methods lie under the bottom-up approach, where different fabrication parameters control the properties of the resulting NPs [14]. However, precipitation or phase separation of the required component (polymer/drug) from the solvent system is considered the common fundamental process for nanoparticles fabrication using this approach [15–17]. Therefore, the main difference between the methods that follow this approach is the mechanism used to induce the required component's phase separation (precipitation). Theoretically, phase separation can be induced by any physical change in the solvent system, such as temperature, pH or any change in the solubility of the components [14,15,17]. Therefore, the properties of the resulting NPs fabricated using this approach depend on the parameters that induce and control the precipitation. Therefore, it is crucial to understand the phase separation mechanism and identify the controlling parameters to select the appropriate method for preparing the desired nanoparticles.

The Nanoprecipitation technique is one of the bottom-up methods for fabricating polymeric NPs in which the polymer is dissolved in a water miscible organic solvent then thoroughly mixed with aqueous antisolvent to induce polymer precipitation [12–15,17]. Explaining the theory behind this process will offer a better understanding of the fabrication parameters influence on the NPs properties.

1.2.2 Thermodynamics of homogenous nanoprecipitation

Nucleation is the process that describes the separation of a single component from an initially homogeneous system driven by a change in the free energy and the equilibrium of the system. The nucleation process can be classified into homogenous and heterogeneous nucleation based on its inducing factors [18–20]. Therefore, nucleation is considered heterogeneous when impurities or dust particles act as nucleating surfaces [19–21]. However, homogeneous nucleation is the dominant mechanism that underlies NPs formation by the nanoprecipitation method. Homogeneous nucleation is driven by the significant increase in the Gibbs free energy of a supersaturated system induced by a change in the solute concentration to exceed its

equilibrium solubility or a drop in the temperature of the system below the phase transformation point (supercooling) [18–20]. The increase in the Gibbs free energy precedes the phase separation and the formation of atomic or molecular clusters known as nuclei. The growth and stability of the formed nucleus depend on its size since only the nuclei that reach a particular size known as the critical size (r^*) proceed to grow while smaller nuclei dissociate in the parent phase [20]. Hence, four stages are involved in forming a stable nucleus, as shown in **Figure 1.1**:

1. A change in the system's equilibrium induced by supersaturation.
2. Nucleus formation.
3. Nucleus growth to the critical size.
4. Stabilization or aggregation of NPs based on the NPs surface charge and the presence of stabilisers.

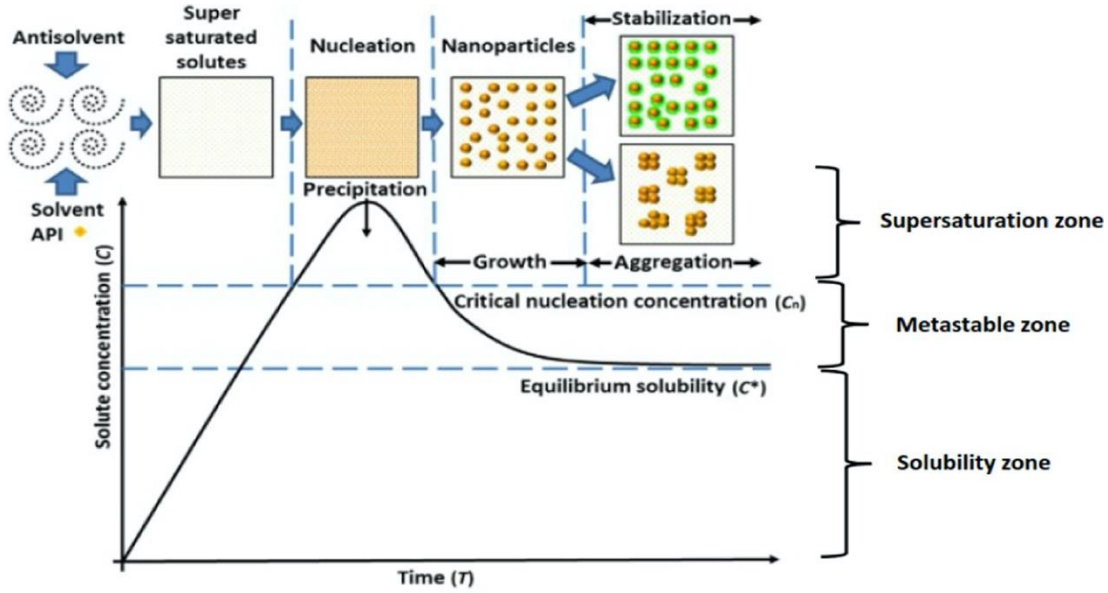

Figure 1.1: Stages of NPs formation by homogenous nucleation using the nanoprecipitation method (reprinted with permission from reference [22]).

The total change of the system free energy associated with the nucleus formation is given by Eq. (1.1-1.4) where ($\Delta\mu s$) is the surface free energy, ($\Delta\mu v$) is the volume free energy, γ is the surface energy per unit area and (ΔGv) is the change of Gibbs free energy per unit volume of the solid phase [20,21].

$$\Delta G = \Delta\mu v + \Delta\mu s \qquad \text{Eq. (1.1)}$$

$$\Delta\mu s = 4\pi r^2 \gamma \qquad \text{Eq. (1.2)}$$

$$\Delta\mu v = (4/3)\pi r^3 \Delta Gv \qquad \text{Eq. (1.3)}$$

$$\Delta G = \left(\frac{4}{3}\right) \pi r^3 \Delta Gv + 4\pi r^2 \gamma \qquad \text{Eq. (1.4)}$$

In a supersaturated system, ΔGv is a negative value, as explained by Eq. (1.5) [19]. Where ΔGv is the free energy of the bulk crystal/volume free energy, T is the absolute temperature (in Kelvin), k is Boltzmann's constant, C is the solute concentration, Co is the solubility, Ω is the atomic volume, and σ is the degree of supersaturation that equals (C-Co)/Co. This equation shows that in an undersaturated system, σ=0 and therefore ΔGv=0, thus nucleation cannot be induced. However, in a supersaturated system (i.e., C > Co), ΔGv is negative and spontaneous nucleation is induced and associated with a reduction in the total Gibbs free energy of the system due to the reduction in the volume energy (ΔGv). However, this reduction is compensated by the introduced surface energy by a value that equals the interfacial tension per unit area of the forming interface (Δμs). This explains the interpretation of the total change of the system free energy as the sum of the surface term and the volume term as shown in Eq. (1.1) and **Figure 1.2**.

$$\Delta Gv = -\frac{kT}{\Omega} \ln\left(\frac{C}{Co}\right) = -\frac{kT}{\Omega} \ln(1 + \sigma) \qquad \text{Eq. (1.5)}$$

As shown in **Figure 1.2**, the critical size (r^*) is the minimum size needed for the particle to proceed to the growth phase. The critical size can be interpreted as illustrated in Eq. (1.6) [20,21]. This interpretation is further illustrated in **Figure 1.2**, which shows the increase in the total free energy of the system with the nucleus size increase up to the critical size where the total free energy starts falling gradually.

$$r^* = -2\gamma / \Delta Gv \qquad \text{Eq. (1.6)}$$

Critical ΔG (ΔG*) is another important term, as shown in **Figure 1.2**. It can be defined as the energy barrier that must be overcome for a stable nucleus to be formed Eq. (1.7) [20,21]. Therefore, by considering Eq. (1.6) and Eq. (1.7), it can be concluded that the critical energy barrier and the nucleus critical size can be reduced in two ways. These include increasing the ΔGv, which can be achieved by increasing the degree of supersaturation or reducing the surface free energy (γ).

$$\Delta G^{*} = \frac{16\pi\gamma}{(3\,\Delta Gv)^{2}} \qquad \text{Eq. (1.7)}$$

The nucleation process is followed by the growth stage that impacts the NPs size distribution [20,23]. In the case of homogenous nucleation and as the nucleation is homogeneously spread throughout the solution and so is the monomer, the probability of any monomer growing on a nucleus is the same everywhere, so on average, all particles will grow at the same rate and will be of the same size.

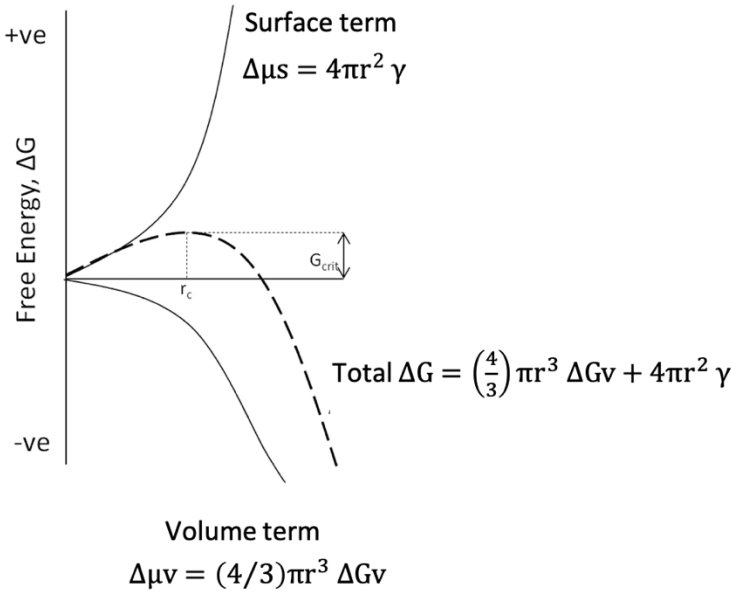

Figure 1.2: The total free energy change associated with nucleus formation by homogenous nucleation (reprinted with permission from reference [18]).

1.3 The controlling parameters of the nanoprecipitation process.

The properties of the polymeric NPs (PNPs), including size, surface charge and morphology, can be designed to meet the intended application. This can be achieved experimentally by controlling a group of inter-dependent processing parameters that significantly impact the properties of the resulting NPs **(Figure 1.3)**. Therefore, it is crucial to probe the impact of these parameters on the nanoprecipitation method and the resulting NPs.

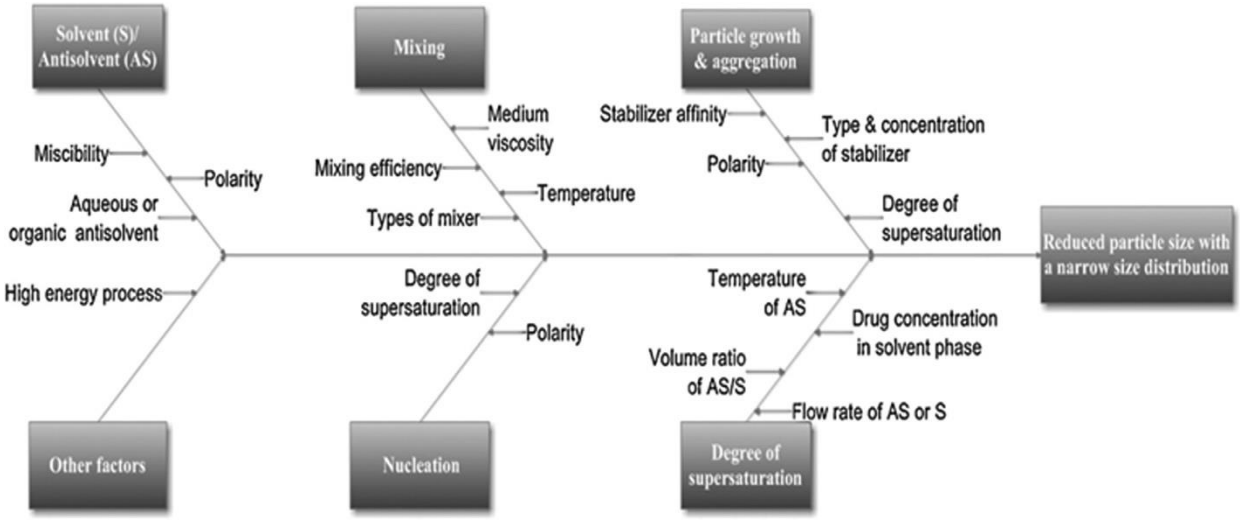

Figure 1.3*:* Fish-bone diagram illustrating a group of inter-dependent processing parameters that significantly impact the NPs properties (reprinted with permission from reference [23]).

1.3.1 The solute degree of supersaturation (DOS)

The rate of nucleation describes the number of nuclei that form in the system per unit of time and significantly affects the properties of the resulting NPs [19,21,23]. Smaller NPs with a narrow size distribution result from fast and uniform nucleation due to the formation of many nuclei that causes a significant drop in the solute concentration below the (C_{min}), where the nucleation ends and the NPs procced to grow up to the same size [15,24]. However, NPs with a broad size distribution profile result from slow nucleation, where a slow drop in the supersaturation level allows for a longer nucleation process. Therefore, it is essential to identify the processing parameters with the most significant effect on the nucleation and consequently the properties of the NPs.

A study conducted by Kwon and Hyeon has demonstrated that supersaturation has the most significant effect on the nucleation rate compared to the surface free energy and the temperature [25]. The degree of supersaturation (DOS) can be defined as the ratio between the solute concentration in the solvent/antisolvent binary mixture and its equilibrium solubility in that mixture as expressed by Eq. (1.8) [17,23]. Increasing the DOS increases the nucleation rate due to the spontaneous nucleation, resulting in smaller NPs and narrow size distribution. However, a low degree of supersaturation produces larger poly-dispersed NPs than those prepared at higher DOS since the system spends a longer time in the metastable zone where growth predominates nucleation [15].

$$\text{Degree of supersaturation} = \frac{C}{C_{Eq}} \qquad \text{Eq. (1.8)}$$

Factors that affect the equilibrium solubility of the solute concentration in the solvent/antisolvent binary mixture change the DOS. Therefore, any condition that reduces the solute solubility (i.e., reducing the temperature) in the binary mixture or increases the solute concentration in the binary mixture (increasing the solute concentration) increases the DOS [15]. However, it is noteworthy to mention that the DOS does not have a linear or direct effect on the properties of the NPs prepared by nanoprecipitation since the final properties could be affected by a group of other inter-dependent factors. For instance, if the conditions responsible for increasing the DOS affect the mixing efficiency, the particle size could increase due to incomplete mixing, which emphasises the complexity of the nanoprecipitation process.

1.3.2 Solvent and anti-solvent miscibility

The choice of the organic solvent in simple nanoprecipitation is made according to three requirements: (1) miscibility with water, (2) low boiling point to facilitate evaporation and (3) polymer dissolving capacity [12]. In addition, the diffusion coefficient of the solvent into the anti-solvent phase was found to affect the properties of the NPs. For instance, a study conducted by Guhagarkar et al. demonstrated a reduction in the NPs size when a mixture of THF and acetone was used compared to THF only [26]. Additionally, another study conducted by Cheng et al. has investigated the effect of solvent water miscibility on the properties of the NPs [27]. The study has demonstrated that solvents with higher water miscibility (i.e., dimethylformamide (DMF)) produced smaller NPs than solvents with lower miscibility (i.e., Tetrahydrofuran (THF)). Therefore, screening different solvent systems might be essential to obtain the desired NPs properties.

1.3.3 Solvent/anti-solvent volume ratio

The solvent/anti-solvent volume ratio (S/AS VR) affects the DOS of the system; consequently, it has a significant effect on the nucleation rate and the properties of the NPs. As expressed by Eq. (1.8), considering using a fixed solute content, increasing the solvent/anti-solvent ratio increases the solute equilibrium solubility in the binary mixture, reducing the DOS and nucleation rate [23]. Additionally, increasing the solvent content in the system promotes particle growth by the Ostwald ripening effect, which is an important factor that induces bigger

particles' growth at the expense of smaller ones [15,28]. Therefore, this explains the need for choosing solvents with high solute capacity so lower volumes of solvents could be used.

1.3.4 Solute (drug/polymer) concentration in the solvent organic phase

The solute concentration in the organic solvent phase affects the DOS, as explained in **section 1.3.1**. Therefore, increasing the solute concentration in the solvent phase increases the solute concentration in the binary mixture, increasing the DOS and the nucleation rate [15,17,29]. However, it is noteworthy to mention that there is an optimal solute concentration above which the NPs size starts increasing due to nuclei collision, promoting growth and aggregation. Therefore, the relation between the NPs size and the solute concentration is concentration-dependent, as shown in **Figure 1.4** [30].

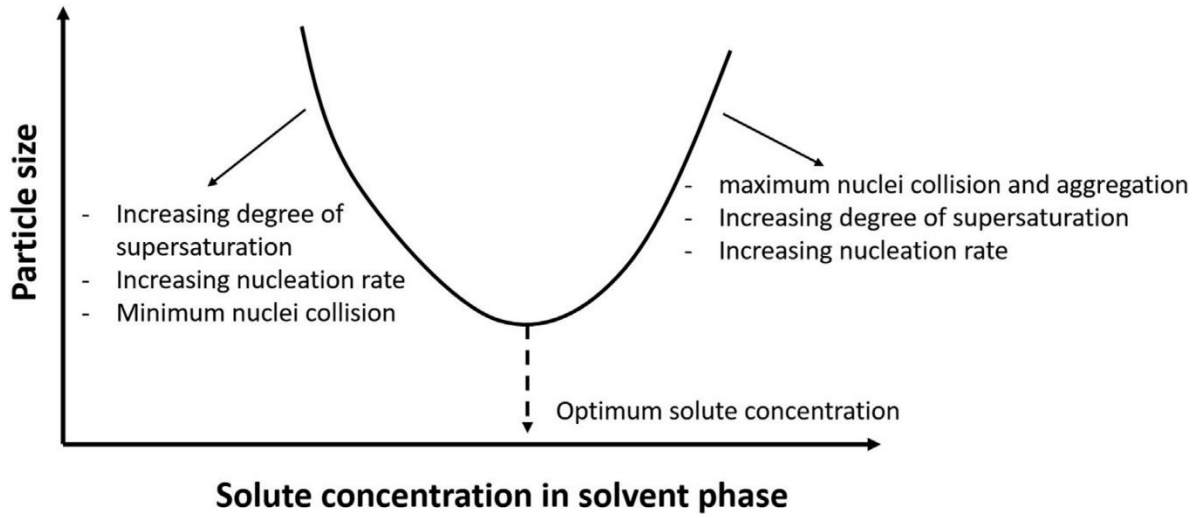

Figure 1.4: Solute concentration-dependent effect on NPs size (reprinted with permission from reference [17]).

1.3.5 Type and concentration of the stabilizer

Stabilisers can be classified into polymeric stabilisers (non-ionic, hydrophobic, amphiphilic, linear) and surfactants (ionic, non-ionic) [17]. Therefore, the surfactant type and its concentration should be decided based on the NPs type and the preparation method. The general rule for selecting an effective stabiliser is to choose the stabiliser with the highest affinity to the NPs surface. Therefore, the higher the stabiliser-NPs affinity, the faster it can occupy the surface of the NPs and reduce the aggregation-induced growth. Generally, stabilisers function by stabilising the NPs sterically in virtue of the long polymeric chains or statically by modifying the NPs surface charge [17]. Therefore, a blend of static and steric stabilisers could improve the NPs stability [31].

The stabiliser concentration is another important factor affecting the nucleation, growth, and NPs size distribution profile. Surfactants tend to lower the surface free energy when adsorbed on the NPs surface, reducing aggregation-induced growth. However, increasing the polymeric stabiliser concentration above the critical flocculation concentration (CFC) promotes growth and size enlargement due to the entanglement and flocculation of the long polymeric chains [17,32].

Due to the significant impact of the stabilisers on the NPs properties, several studies have screened the effect of the surfactants on the NPs size distribution profile. For example, a study conducted by Dong and Feng demonstrated no significant change in MPEG-PLA nanoparticle size when increasing the Pluronic F68 concentration [33]. Additionally, a study conducted by Zweers et al. showed that the polymeric NPs size (poly DL-lactide (PDLLA) and PLGA) decreases with increasing the Poly (vinyl alcohol) (PVA) concentration from (0-2 wt%) and remains constant after a further increase in the concentration (2-5 wt%); however, increases after a further increase in PVA concentration up to (5-10 wt%), whereas Allemann et al. reported a steady decrease in Eudragit S NPs with increasing the PVA concentration[34,35]. Other research groups explained these discrepancies by suggesting the presence of two competing effects determining the final size of the NPs. These are the improved colloidal stability achieved by PVA deposition on the NPs surface, promoting size reduction, and the increased aqueous antisolvent phase viscosity, which affects the mixing efficiency and results in larger NPs [17]. These findings emphasise that the effect of the processing parameters on the NPs properties cannot be generalised since their effect is highly system-dependent (processing conditions/ materials).

1.3.6 Solvent and anti-solvent mixing efficiency

The mixing efficiency of the organic solvent phase containing the solute and the aqueous anti-solvent phase significantly impacts nucleation's uniformity and rate [17,23]. Therefore, an efficient complete mixing provides a constant degree of supersaturation throughout the binary mixture, inducing uniform nucleation and producing smaller monodispersed NPs [23].

Two-time scales are used to describe the complete precipitation process; time of mixing (t_{mix}) and precipitation time ($t_{precipitation}$) [36]. In conventional nanoprecipitation, which uses magnetic

stirrers as the mixing device, the total mixing time is divided into micromixing and mesomixing [17,23]. Mass transfer is driven by molecular diffusion with micromixing, whereas with mesomixing, mass transfer is driven by advection due to turbulence caused by chaotic mixing. Therefore, the final particles size distribution depends on the balance between these two types of mixing, which can be controlled by adjusting the mixing conditions.

Consequently, a dimensionless number known as the Damkohler number was used to predict the mixing efficiency. The Damkohler number is expressed as the ratio of t_{mix} to $t_{precipitation}$. Thus, a lower value of the Damkohler number ($Da<1$) is favourable to achieve smaller monodispersed NPs [37]. Practically, this could be achieved by widening the difference between the t_{mix} and $t_{precipitation}$ [15].

Due to the importance of the mixing step, several tools were examined for their mixing efficiencies. These include the conventional static mixers and magnetic stirrers used with conventional nanoprecipitation and the advanced microfluidic chips with different junction geometries allowing controlled mixing. Microfluidics assisted nanoprecipitation is discussed in the following section **(section 1.4)**.

1.4 Microfluidics-assisted nanoprecipitation for polymeric NPs fabrication

1.4.1 Microfluidics: origin and applications

Microfluidics is a miniaturized technique employing micro-sized channels to manipulate fluids under controlled mixing conditions [38–40]. Microfluidics platforms have been exploited in several fields due to a group of advantages: the small size of the system, control over fluid dynamics and laminar flow behaviour of the fluids in microchannels, and enhanced mass and heat transfer due to the offered large surface area and short mixing time [38,41–43]. These advantages can be related to the structure of the microfluidics micro-sized chips that imposes a controlled laminar flow of the fluids, unlike the turbulent fluid flow in macroscopic systems where fluids mix convectively due to the dominance of inertial forces over viscosity forces [38]. The fluid behaviour at microscale differs from that at macro scale in different properties, such as energy dissipation, surface tension and fluid resistance due to viscosity dominance. Therefore, scaling laws were used to predict the changes in physical phenomenon balance due to miniaturizing a given system [42]. These laws showed that the surface-related forces dominate over the volume-related forces due to the increased surface area-to-volume ratio in

microfluidic systems. The flow behaviour can be predicted by the Reynolds number, a dimensionless number defined as the ratio between the inertia and viscous shear force Eq. (1.9) where ρ is the fluid density, μ is the fluid viscosity, ν is the fluid velocity, and L is the characteristic length of the system (channel diameter) [17,44]. Reynolds number below 2300 suggests a laminar flow, while a higher Reynolds indicates a chaotic and turbulent flow [42]. In microfluidics, the Reynolds number is smaller than 0.1 since the viscous force dominates over the inertia due to the small size of the microchannel; hence the flow is laminar [42].

$$\mathrm{Re} = \frac{Inertial\ forces}{Viscous\ forces} = \frac{\rho.v.L}{\mu} \qquad \text{Eq. (1.9)}$$

In biological and biomedical fields, microfluidics platforms were used for droplet cells encapsulation to assist fast and sensitive analysis of biomolecules secreted from cells within microdroplets [43]. Moreover, microdroplets were used to study the susceptibility of bacterial cells to antibiotics rapidly and sensitively. Thus, effective cell density increases when cells are encapsulated in small volumes (cell/droplet), which can be used to provide effective and rapid patient-specific treatment for bacterial infections. In the drug delivery field, microfluidics was used to produce monodispersed small NPs, Janus particles, multi-shells, chamber particles and microfibers [45]. In this thesis, the application of microfluidics in fabricating NPs by nanoprecipitation was investigated.

1.4.2 Microfluidics chip material

The earliest microfluidic devices were fabricated in glass and silicon, but later these materials were substituted with plastics. This is due to the limitations of glass and silicon as glass is inappropriate for the analyses of biological samples in water, and silicon is expensive and opaque to UV and visible light, making it difficult to be used with conventional optical methods of detection [38,42,46,47]. Therefore, most microfluidic devices are now made from polymers such as polydimethylsiloxane (PDMS), polyethene terephthalate (PET), polystyrene (PS), polycarbonate (PC) and polymethyl methacrylate (PMMA). These chips are cheaper and easier to be manufactured relative to glass chips. However, the disadvantage of using polymeric microfluidic chips is their deformability (swelling/shrinkage) caused by organic liquids, unlike glass chips that are resistant to these liquids [17,46]. Therefore, this emphasises the limitations of polymeric chips compared to glass chips.

1.4.3 The impact of the microfluidics chip design on the mixing process

Efficient mixing is generally driven by mass transfer, which can be achieved by molecular diffusion, whereby molecules move across an interface separating the phases to be mixed or by advection where the mass is carried by the fluid due to turbulence caused by chaotic mixing. Generally, the Peclet number (Pe) can be used to predict the mechanism of mass transfer in a given system Eq. (1.10), where ν is the flow velocity, L is the characteristic length, and D is the diffusion coefficient [17,44]. In microfluidics chips and given the small channel diameters, the (Pe) number is small, suggesting that molecular diffusion is the principal mass transfer mechanism. However, it is noteworthy that the MF chip design affects the mixing mechanism within the micron-sized channels.

$$\mathrm{Pe} = \frac{\text{advective transfer rate}}{\text{diffusive transfer rate}} = \frac{\nu\, \mathrm{L}}{\mathrm{D}} \qquad \text{Eq. (1.10)}$$

1.4.3.1 Laminar flow chips

Laminar flow chips are among the most used chips for drugs nanocrystals and polymeric NPs fabrication. Generally, these chips are made from glass or PDMS with a channel diameter ranging between 100 to 500 microns **(Figure 1.5 A and B)**. These chips can tolerate a moderate flow rate not exceeding 3 (mL/min) since a higher flow rate can generate higher pressure that disrupts the PDMS chips. In addition, in these chips, the Peclet and Reynolds numbers are below 1, suggesting a laminar flow where mass is transferred by molecular diffusion only [17,48]. However, the mixing efficiency is limited by the limited contact area between the solvent and the anti-solvent phase within the short distance of the mixing zone in these laminar chips. Therefore, advanced laminar microchips were developed to accelerate mixing by enlarging the contact area between the solutions. This concept can be achieved by several approaches, including stretching, folding, or splitting the fluid into several sub-streams using specific microstructures within the chip design. Therefore, different mixers were employed to accelerate the mixing by several approaches: lamination (parallel or sequential), segmentation (parallel or sequential) and chaotic advection [17,44].

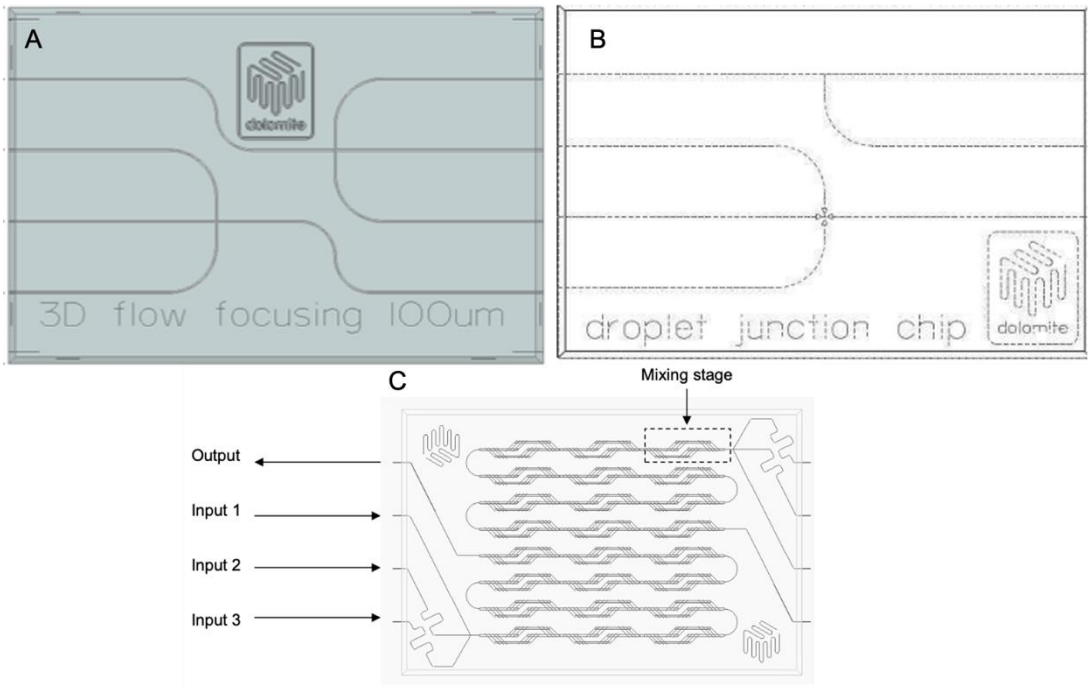

Figure 1.5: Laminar glass microfluidics flow focused chips: (A) single channel 100 μm, (B) single channel 190 μm and (C) 100 μm micromixer chip (reprinted with permission from reference [49]).

Parallel lamination mixers act by splitting the solutions to be mixed into a certain number of sub-streams (n) to be then merged together **(Figure 1.6 a)**. Thus, this shortens the diffusion distance, shortening the mixing time by a factor of n^2 compared to the laminar single-channel microchips. Sequential lamination employs a sequential design of repeating transformations structures that split the solutions into two sub-streams before being merged together **(Figure 1.6 b)**. Therefore, each sequence (split and recombine) doubles the sub-streams number (n). As a result, the diffusion distance is reduced significantly, and the mixing time is reduced by a factor of $4^{(n-1)}$[17,44].

In parallel segmentation, the solvent phase is injected through multiple nozzles into the main mixing channel that contains the anti-solvent phase. Therefore, the size of the nozzle and the velocity at which the solvent phase is injected (flux) determine the final contact area between the solutions. However, in sequential segmentation, the solvent and anti-solvent are injected into the main mixing channel in an alternating periodic sequence. Thus, the solutions are mixed by axial dispersion, which significantly accelerates the mixing [17,50].

Chaotic advection is another approach that utilises structural elements in the mixing channel. Thus, these elements redirect the laminar flow into transversal paths, resulting in continuous

folding, stretching and twisting of the fluid stream over the length of the channel [50]. However, these micromixers function correctly at a specific Reynolds number range since a low Reynolds number results in insufficient shear forces and high Reynolds number results in a second unwanted flow [17,50].

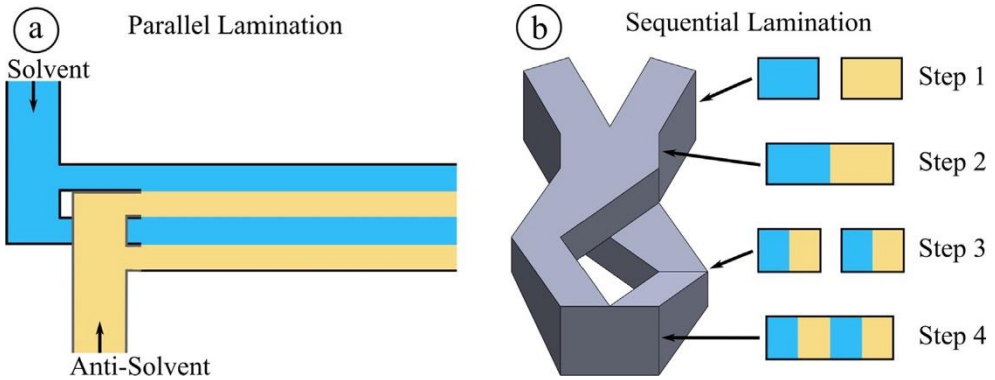

Figure 1.6: Schematic illustration of: (a) parallel lamination of two fluids and (b) sequential lamination of two fluids through split then re-join of solvent and antisolvent through the microchannel (reprinted with permission from reference [17]).

1.4.3.2 High pressure devices

High-pressure devices can tolerate high flow rates ranging between 40 to 120 ml/min [17]. These devices are generally made of aluminium or steel to withstand high pressure, such as a multi-inlet vortex mixer (MIVM) and confined impinging jets mixer (CIJM) **(Figure 1.7)**. Generally, these devices apply the concept of flash nanoprecipitation, where the solvent and the anti-solvent phases are injected at a very high speed to contact each other at certain angles, inducing turbulent mixing [37,51]. Therefore, mass transfer is driven mainly by advective processes in these systems.

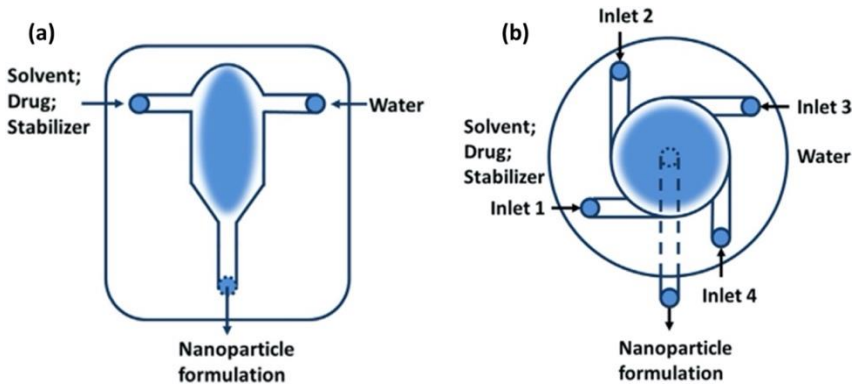

Figure 1.7: Schematic illustrations of: (a) confined imping jet mixer (CIJM) and (b) multi-inlet vortex mixer (MIVM) (reprinted with permission from reference [22]).

1.4.4 Factors affecting the MF assisted nanoprecipitation process

Microfluidics-assisted nanoprecipitation has been extensively used in the drug delivery field for NPs fabrication. This can be mainly related to the tuneable mixing offered by the microfluidics platforms, allowing for controlled mixing [52–55]. It is suggested that the NPs formation in straight hydrodynamic flow focusing chips occurs in three stages: (1) nucleation of NPS, (2) growth of NPs through aggregation and (3) kinetically locked NPs achieved after a particular aggregation time scale [56,57] **(Figure 1.8)**.

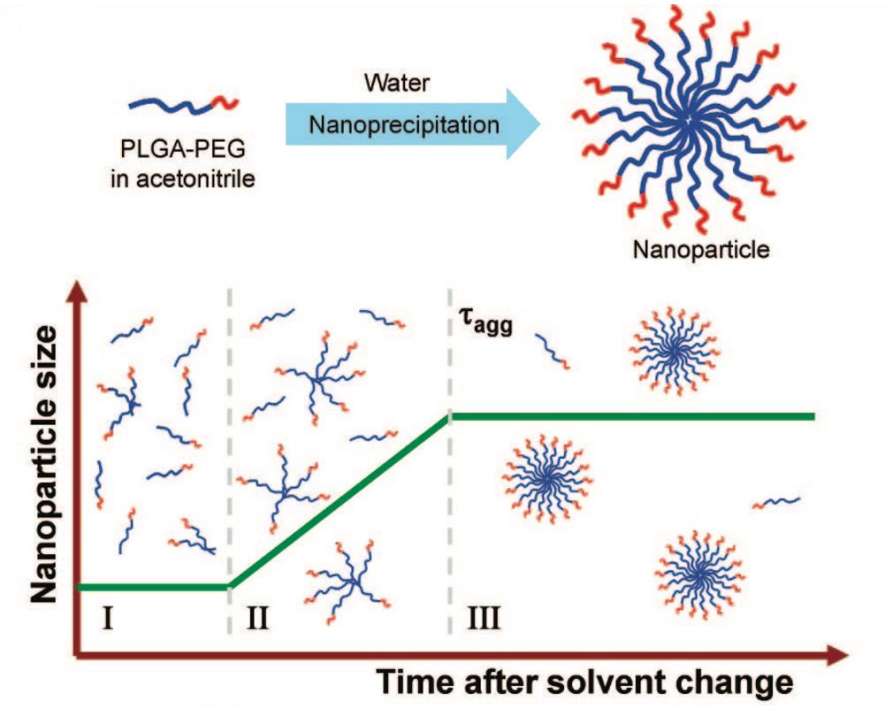

Figure 1.8: Stages of polymeric NPs formation in flow focused microfluidics chips (reprinted with permission from reference from reference [57]).

Tunning the size of NPs using MF is controlled by two-time scales: mixing time (τ_{mix}) and aggregation time (τ_{agg}) [56,57]. The mixing time scale represents the time scale of solvent diffusion into the antisolvent phase, and the aggregation time scale represents the time scale of NPs growth. Accordingly, several studies proposed that when mixing occurs faster than the NPs aggregation time scale (i.e., $\tau_{mix} < \tau_{agg}$), the NPs size is independent of the polymer concentration or mixing time, resulting in smaller monodispersed NPs compared to NPs prepared under slow mixing conditions [53,56,57]. Therefore, according to this hypothesis, processing conditions that affect these time scales (τ_{mix} and τ_{agg}) could alter the properties of the resulting NPs. The mixing time is expressed by Eq. (1.11) [57]. Where D is the diffusivity

of the solvent, w is the width of the chip, and R is the S/AS flow rate ratio (FRR). Therefore, several studies investigated the effect of the S/AS FRR, solvent and anti-solvent total flow rate (TFR) besides other factors, including the composition of the organic phase and the addition of stabilisers [52,53,55,57,58].

$$\tau_{mix} = \frac{w^2}{9D(1+\frac{1}{R})^2} \quad \text{Eq. (1.11)}$$

The FRR represents the ratio between the flow rate of the organic solvent containing the polymer or the drug and the flow rate of the aqueous phase. Therefore, increasing the S/AS FRR changes many factors such as the degree of supersaturation, the available drug or polymer concentration in the S/AS binary mixture, and NPs stability due to the Ostwald repining effect as explained in **section 1.3.3**. In addition to these effects, in MF systems where the mixing occurs across a flow-focused stream, increasing the S/AS FRR increases the flow-focused stream's width. Consequently, this increases the molecules diffusion distance from the solvent to the anti-solvent, which increases the mixing time as demonstrated by Eq. (1.11), resulting in larger NPs. Several studies in the literature demonstrated these findings [52,53,55,57–60].

The TFR representing the flow rate of the solvent and the anti-solvent is another critical factor affecting the NPs properties. Increasing the TFR reduces the fouling and blockages issues within the MF chips during the NPs fabrication by reducing the residence time of the phases within the chip [61]. Additionally, increasing the TFR increases the Peclet number, suggesting that mass transfer can be driven by advection and diffusion processes [22,51]. Accordingly, several studies reported a significant decrease in the NPs size with increasing the TFR [62–64].

Several studies have investigated other factors, such as the concentration of the polymer in the organic phase [53,55,57]. Collectively, these studies demonstrated a significant increase in the NPs size with increasing the polymer concentration. These findings were attributed to the increase in the organic phase viscosity, which could impede the diffusivity of the organic phase to the anti-solvent phase besides the formation of a large number of nuclei that can induce particle growth [55]. Additionally, several studies have screened different stabilisers' impact on the NPs size. For example, a study conducted by Lari et al. reported a significant increase in the size of the polycaprolactone (PCL) and cellulose acetate (CA) NPs in the presence of Tween 80 and PVA [58]. Additionally, a study conducted by Othman et al. demonstrated a

significant increase in the PCL NPs size when adding polyvinylpyrrolidone (PVP), polyvinyl alcohol (PVA), Tween 20, and Tween 80 [65]. These findings were related to two reasons: the deposition of these stabilisers on the NPs size, which could increase their size and the increase in the anti-solvent phase viscosity [55].

This discussion shows that it is vital to screen the effect of these parameters on the NPs properties since controlling the NPs properties by MF depends on a group of interdependent factors; hence, the results can be system-dependent (FRR, TFR, polymer type and concentration)

1.4.5 Limitations of MF in polymeric NPs fabrication

The material deposition into the microfluidics chips' walls with a particle-containing flow is known as fouling [66]. Fouling is considered the most significant challenge for NPs synthesis using MF since it results in irregular flow and eventually clogging of the chip [66–68]. Therefore, continuous fouling in MF chips limits reproducibility and scalability, explaining the low throughput compared to conventional methods [66]. A group of strategies can be applied to overcome the fouling issues, such as filtering the inlet solutions, modifying the formulation components and concentrations, coating the surface of the channels and using higher total flow rates [47,69–71]. However, these strategies suggest that the use of the MF system will be limited to specific formulation components and concentrations that cannot be changed or exceeded. For example, a study conducted by Lababidi et al. demonstrated fouling and clogging of the chip when using PLGA concentrations higher than 10 (mg/mL) [55]. Accordingly, several studies have been focused on modifying the chip's design to reduce the contact of the solutions with the microchannel walls. For example, developing 3d flow focused chips has been proposed as a practical design that could reduce the contact of the flow with channel walls to reduce the building up in the chip [66,72–75] **(Figure 1.9)**.

Additionally, several studies have tested the use of different channel/microcapillary designs to mitigate the fouling issues. For example, a recent study conducted by Erfle et al. showed the development of a unique coaxial lamination mixer (CLM) by implementing 3D features into a microfluidic device to avoid direct contact of the lipid solutions with the microchannel walls[66]. The study revealed the successful synthesis of stable size NPs for up to two hours. However, the study observed fouling onto the third stretch-and-fold element at total flow rates

of 400 (μL/min) and above or at higher flow rate ratios that can be overcome only by using lower total flow rates or flow rate ratios [66]. Moreover, fouling was observed at the first contact between the phases (at the nozzle), which can be only avoided by choosing appropriate processing parameters [66]. Therefore, despite the study proposing a unique MF system that improves the mixing efficiency and extends the production time to two hours, fouling cannot be entirely avoided unless the processing parameters are modified.

Confined impinging jets mixers (CIJMs) and multi-inlet vortex mixers (MIVMs) offer significantly higher throughput than conventional MF chips, which could reach 864 (g/day). This can be related to the high flow rates (around 100 mL/min) and pressure these systems operate at [37,51]. Therefore, the MF chips of these systems are made of steel to withstand these processing conditions. Therefore, these systems can be considered one approach to scaling up the yield of the MF systems. In addition, parallelization is another approach that can be used for scaling up, as demonstrated by Kang et al. study where the polymeric solvent and anti-solvent were mixed using parallel mixing lines in a 100-outlet chip using a TFR of 6 (mL/min) [76]. This approach was also applied by Lim et al. study that showed an enhanced throughput of polymeric NPs to reach 25 mg in 20 minutes compared to 5 hours in single layer microchips [73]. Thus, although MF scaling up is still considered challenging, several studies are focused on developing promising microchips to increase the NPs production rate.

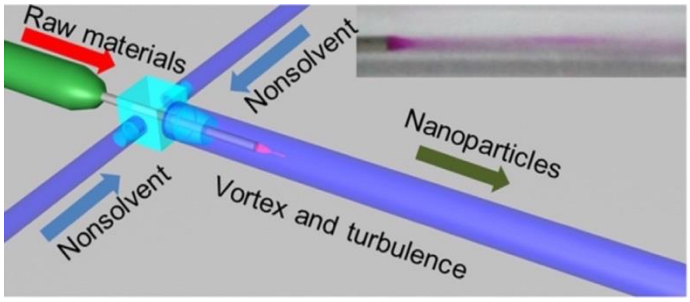

Figure 1.9: 3D flow focused chip designed to reduce the interaction between the flow and the microchannel walls (reprinted with permission from reference [72]).

1.4.6 Comparing the bulk conventional nanoprecipitation with MF platforms for polymeric NPs fabrication

Several studies in the literature suggested using the MF-assisted nanoprecipitation (MF-method) over the bulk conventional nanoprecipitation method [52,55,57,64]. This was related to the controlled mixing performed by the MF mixing devices, which produces small mono-dispersed NPs and improves the results' reproducibility. However, it is noteworthy that several studies in the field lack a consistent comparison between the MF and conventional nanoprecipitation methods. It is well known that the processing conditions with MF are different from the conventional bulk methods (i.e., polymer concentration, solvent and anti-solvent volume) due to the limitations imposed by the MF chip (design/material), as explained in **section 1.4.5**. Therefore, the processing conditions should be consistent for the two methods to be compared based on their efficiency in fabricating small, monodispersed NPs. Although this approach was applied in some studies, no study has examined the significance of the difference or provided evidence of additional therapeutic advancement.

Several studies in the literature demonstrated the efficiency of the MF systems in fabricating tuneable polymeric NPs by modifying the polymer concentration or the FRRs [52,55,57,64]. However, it is noteworthy that tuneable polymeric NPs can be fabricated by conventional bulk mixing by manipulating processing conditions such as the polymer concentration and S/AS volume ratio [13]. This emphasises that tuning the NPs properties is mainly controlled by the processing conditions.

Karnick et al. study compared the size of PLGA-PEG prepared by conventional and MF-assisted nanoprecipitation using the same processing conditions [57]. The study found that NPs prepared using MF were smaller than that of conventional NPs by 7 nm. Therefore, despite the statistically significant difference in NPs sizes in the mentioned study, the additional therapeutic advancement provided by this difference is questionable. Additionally, it was demonstrated by Reisch et al. that ultra-small NPs of 15 nm were successfully fabricated using the conventional nanoprecipitation technique by controlling the number of the charged group per polymer chain [77]. Collectively, these findings suggest that small, monodispersed NPs can also be fabricated by conventional nanoprecipitation when the processing conditions are strictly chosen and controlled.

1.5 Synthesis of PLGA NPs by double emulsion method ($W_1/O/W_2$)

The nanoprecipitation method is efficient for loading hydrophobic API; however, other methods must be used to encapsulate hydrophilic API [12]. Therefore emulsion-based approaches are adopted in several studies for polymeric NPs fabrication because of their simplicity, low cost, and adaptability to encapsulate API with different physicochemical properties [78–80]. These approaches are used to prepare single emulsions oil/water (O/W) and double emulsions water/oil/water ($W_1/O/W_2$). Generally, single emulsions are used to encapsulate hydrophobic API, whereas double emulsions are used to encapsulate hydrophilic API [80]. The double emulsion method was found efficient for loading hydrophilic drugs, proteins, pDNA, miRNAs and siRNAs [78–81]. The encapsulation of a hydrophilic candidate using this approach involves forming a water-in-oil (W/O) emulsion, where the hydrophilic candidate is dissolved in the aqueous phase and the polymer in the organic phase [82]. Subsequently, this emulsion is added to another aqueous phase containing stabilisers under high sear forces (ultra-sonication) to form the water/oil/water ($W_1/O/W_2$) emulsion [82]. Eventually, polymeric NPs are formed upon solvent removal by evaporation, diffusion or salting out. Microfluidics microchips can also be used to fabricate polymeric particles using the double emulsion method; however, the size of these particles is in the micrometre range due to the lack of the high shear energy provided by the ultra-sonication in case of the conventional synthesis [83].

The final properties of the polymeric NPs prepared using this method depend on the processing parameters, just as the case with the nanoprecipitation method. For example, using a low concentration of the surfactants increases the polydispersity and NPs aggregation; however, excessive surfactants reduce drug loading due to the strong interaction between the drugs and surfactants [79,84]. Additionally, polymer concentration and the sonication conditions (mode, time and power) significantly impact the NPs properties; therefore, it is vital to screen these conditions with each system to select the optimal conditions for preparing the desired NPs [79].

1.6 Nanoparticle's delivery systems for gene therapy: characteristics and applications

Gene therapy is an advanced field that aims to cure acquired and inherited diseases caused by genetic defects by introducing the genetic material into the cells [85]. The concept of this approach is to transfer nucleic acids into specific cells where they can enhance gene expression or inhibit the production of specific proteins associated with the disease progression. Therefore, nucleic acids and their analogues such as plasmid DNA (pDNA) and miRNAs have been used

to mediate gene knockdown via RNA interference (RNAi) mechanism to cease the progression of several diseases such as cancer, diabetes, heart diseases, bladder interstitial cystitis and osteoarthritis [3,86,87]. Therefore, gene therapy has a significant potential for curing chronic and acute diseases with genetic origins. However, the delivery of naked nucleic acids (pDNA, miRNA) suffers a group of limitations that render their delivery inefficient [3,4]. Therefore, the success of gene therapy depends on ascertaining an efficient delivery system that can circumvent a group of biological barriers, delivering intact nucleic acids to the targeted cells.

An ideal gene delivering vector should possess specific characteristics such as protecting the loaded nucleic acids from degradation by nucleases to transfer a precise amount of the nucleic acids to the cells and induce the desired therapeutic action without causing toxicity [88,89]. Additionally, an ideal vector should achieve a sufficient level and duration of transgenic expression to modify the genetic defect without inducing immunogenic reactions [88]. Accordingly, many efforts have been undertaken to identify the ideal characteristics of the delivery system, which resulted in a group of viral and non-viral vectors [88–90]. Accordingly, gene transfer using viral vectors is called transduction, while transfer via non-viral vectors is known as transfection [88,91]. Each of these vectors has a group of advantages and disadvantages. For example, viral vectors such as recombinant viruses (i.e., adenovirus, retrovirus, lentivirus) are more efficient in gene delivery than non-viral vectors; hence, a single dose is sufficient, unlike non-viral vectors where multiple doses are required to induce the desired effect [88]. The higher efficiency of viral vectors can be related to their ability to maximize gene delivery using intracellular trafficking mechanisms. However, the use of viral vectors is limited due to several drawbacks such as immunogenicity of adenovirus, induction of acute inflammatory responses, safety concerns with HIV-like viruses and the potential integration of foreign DNA into the genome [5,89,92]. Therefore, the use of viral vectors imposes significant risk factors, which was highlighted by the death of a participant in a gene therapy trial after intra-articular injection of Adeno-associated virus (AAV) [92]. In addition, besides the safety risks associated with viral vectors, these systems lack the desired tissue selectivity and are difficult to be scaled up to meet the pharmaceutical production level [93]. Therefore, non-viral gene delivering systems have been widely adopted and advanced as promising vectors with low toxicity profiles and controlled gene delivery efficiency [89].

Non-viral vectors include several systems/approaches such as electroporation, hydrodynamic gene transfer, gene gun and nanoparticles (NPs) [93]. Among these systems, NPs systems have

drawn significant attention due to several advantages offered by these systems. These advantages include the small size of NPs that allow them to transfer within the circulatory system and circumvent several biological barriers [3,94]. Additionally, NPs have lower immunogenic and oncogenic potentials and can be used to deliver genes of larger size compared to what can be delivered by viral vectors [3].

1.6.1 The journey of gene-based NPs into the cells

Understanding the underlying trafficking mechanisms of NPs is critical since the NPs success in delivering the payload (drugs/nucleic acids) to specific intracellular sites (i.e., nucleus, cytosol) is determined by their intracellular fate [95]. Additionally, understanding these mechanisms allows identifying the biological barriers that NPs must circumvent for efficient delivery. Therefore, this provides a clear idea about the appropriate design and NPs characteristics needed to achieve the highest efficiency.

1.6.1.1 Cellular uptake

Generally, the cellular uptake of NPs is mainly achieved by endocytosis after the NPs interaction with the extracellular matrix (ECM) of the cells or its components[95]. Hence, the journey of the NPs into the cell starts with NPs engulfment into membrane invaginations, followed by budding and pinching off to form endocytic vesicles [85,95,96]. Then, NPs are trafficked intracellularly to different cellular compartments. The endocytosis process can be classified into five mechanisms depending on the cell type and molecules involved in the process (i.e., proteins, lipids) [95–99]. These mechanisms are phagocytosis, clathrin-mediated endocytosis, caveolin-dependent endocytosis, clathrin/caveolae-independent endocytosis, and micropinocytosis [85,95–99] **(Figure 1.10)**.

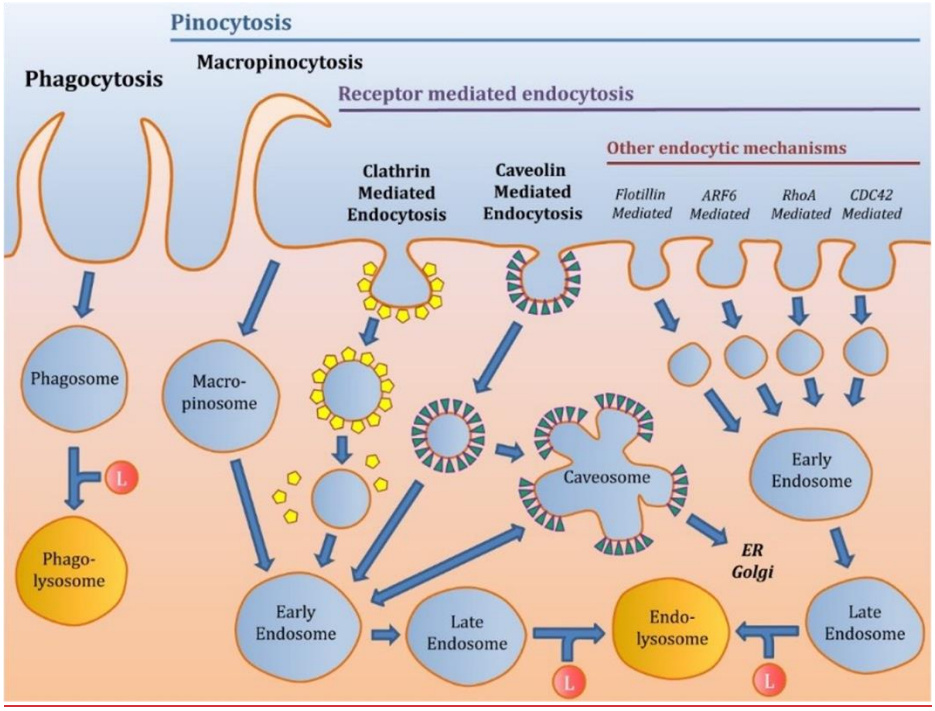

Figure 1.10: Illustration of the cell main endocytic uptake pathways and the intracellular trafficking (reprinted with permission from reference from reference [97]).

- **Phagocytosis**

Phagocytosis is the engulfment of particulate materials by the professional phagocytes (i.e., macrophages, dendritic cells, monocytes, and neutrophils) responsible for host defence and removal of dead cells. Briefly, phagocytosis of NPs is initiated by opsonins, which are extracellular proteins, such as complement proteins and immunoglobulins that induce phagocytosis by labelling the materials that must be phagocytosed [100,101]. Thereafter, the opsonised NPs get attached to the professional phagocytes, inducing a signalling cascade starting with triggering actin assembly and forming cell surface extensions followed by particles engulfment and internalisation to form what is known as a phagosome [95,102]. The uptake of NPs by the phagocytic route is governed by the NPs properties (size, material and shape) [102]. Generally, larger NPs are more efficiently uptaken by the phagocytes. For instance, a study conducted by Schäfer et al. investigated the uptake of albumin NPs in size range of 200-1500 nm and demonstrated higher phagocytic uptake for the larger NPs [103]. These findings were further confirmed by several studies [104,105].

Additionally, NPs shape significantly impacts the NPs cellular uptake [106,107]. For instance, a study conducted by Champion et al. demonstrated that worm-like particles showed negligible phagocytosis compared to spherical particles [106]. Thus, identifying the uptake pathway can

be used for drug targeting mechanisms. For instance, NPs that are highly susceptible to opsonisation preferentially accumulate in RES organs (liver and spleen), which was exploited for designing selective treatment for diseases targeting these organs, such as liver infections and hepatocarcinoma [108].

- **Clathrin-mediated endocytosis (CME)**

Clathrin-mediated endocytosis (CME) is involved in the uptake of several types of NPs [95,96,98]. Generally, CME occurs in two ways: via receptor-specific uptake or non-adsorptive uptake, also known as receptor-independent CME, where the uptake occurs via electrostatic or non-specific hydrophobic interactions [109]. In receptor-independent CME, the uptake is initiated by non-specific hydrophobic or electrostatic interactions without direct binding with membrane constituents [95]. CME occurs at the clathrin rich area of the plasma membrane, and the uptake is initiated by adaptor proteins functioning as recognition sites for the cargos (i.e., cholesterol and iron) in the docking sites on the cytoplasmic face of the plasma membrane [95]. In addition, these proteins are responsible for clathrin nucleation coordination at the internalisation sites in the membrane [95]. The nucleation triggers membrane invagination into clathrin-coated pits, stabilising the membrane deformation points. It is assumed that particles entering the cells by CME are more prone to lysosomal degradation since they frequently end up in degradative lysosomes [98,110]. Therefore, it is crucial to avoid using materials that are susceptible to lysosomal degradation for NPs synthesis. It was found that NPs made of D, L-polylactide (PLA) and polyethylene glycol co-lactide (PEG-co-PLA) get internalised via both the CME route and caveolae-dependent endocytosis explained in the paragraph below [95]. Furthermore, the NPs surface charge was found to significantly affect the uptake and trafficking mechanism; hence, anionic particles were internalised via both mechanisms in HeLa cervical cancer cells, while positively charged particles were strictly internalised by CME [111]. Additionally, PLGA NPs are generally internalised by the CME pathway mainly if positively charged, while for negatively charged NPs, the uptake is weak and achieved by CME and Caveolae independent endocytosis pathway explained below [97].

- **Caveolae-dependent endocytosis**

Caveolae-dependent endocytosis is involved in different biological processes, including cell signalling and regulation of fatty acids, membrane proteins and lipids [112]. Caveolae are 50-80 nm flask-shaped membrane invaginations present in epithelial and non-epithelial cells and

lined with caveolin, a dimeric protein responsible for the unique flask-shaped structure of the caveolae [113]. The uptake by this pathway results in forming caveolin vesicles that tend to form multicaveolar structures known as caveosomes. Afterwards, these caveosomes fuse with the early endosomes, which can be then transferred into the smooth endoplasmic reticulum or to the Golgi-trans network based on the cell type [97].

- **Clathrin/Caveolae independent endocytosis**

Clathrin/Caveolae independent endocytosis occurs in cells devoid of clathrin and caveolae. Generally, these cells can uptake cargos such as interleukin-2 and growth hormones [95,99]. Interestingly, folic acid was found to be internalised by this pathway, which was exploited for developing folate modified NPs to target cancer cell growth, which naturally has a high demand for folic acid [98]. Particles internalised via folate receptor-mediated endocytosis might circumvent the trafficking into lysosomes and often end up in endocytic compartments or get released into the cytoplasm [114].

- **Macropinocytosis**

Macropinocytosis is a unique type of pinocytosis, considering it does not involve lipid rafts or pit-forming protein. Macropinocytosis is responsible for different physiological functions, such as antigen presentation [115]. In macropinocytosis, large membrane extensions are created due to cytoskeleton rearrangement, which then fuses back onto the plasma membrane to form a large vesicle (0.2–5 μm) [116]. These large vesicles can trap a large amount of ECM fluid containing dissolved molecules and particles without the need for specific receptors. Therefore, this uptake process is a form of non-specific bulk fluid uptake that is considered essential for the uptake of larger NPs that cannot be internalised via clathrin- or caveolae-dependent endocytosis [116].

1.6.1.2 Intracellular trafficking

The NPs therapeutic efficacy depends on their intracellular trafficking mediated by a network of cellular endosomes associated with the endoplasmic reticulum (ER), Golgi apparatus and lysosomes [95,117]. Endosomes are large intracellular membrane-bound compartments produced initially by the plasma membrane and usually present in the cytoplasm of human cells [118]. Generally, endosomes can be classified into three main groups, which direct most intracellular endocytic pathways: early endosomes, recycling endosomes and late endosomes, also known as multi-vesicular bodies (MVB) **(Figure 1.11)** [95,119]. The intracellular

trafficking starts after the endocytosis process, where the cargos get entrapped into the endocytic vesicles that later pinch off the plasma membrane to fuse with early endosomes [95,119]. At this stage, the cargos become part of the early endosomes, which then mediate further trafficking of the endocytic vesicle's cargo into different cellular compartments [95]. The recycling endosomes can recycle part of this cargo to the plasma membrane at this level. However, the rest of the cargo remains in the early endosomes that eventually differentiate into late endosomes, which fuse with the plasma membrane to release its components outside the cell or fuse with the lysosomes, forming endolysosomes. The endolysosomes contents are exposed to a wide variety of degradation enzymes such as lysosomal hydrolases [95,108].

Therefore, NPs must escape the endolysosomal degradation to deliver their payload (pDNA/miRNA) intact and functional to the cytoplasm. Generally, this can be achieved in two ways: either the endocytosed NPs escape the endolysosomal degradation pathway before the late endosomes fuse with the lysosomes; hence, particles bypass the lysosomal degradation, or NPs destabilise the lysosomes by inducing lysosomal membrane lysis via the proton pump effect [120–122]. This effect is exploited and employed for delivery applications since it allows for cargo's translocation from the lysosomes to the cytoplasm. This effect can be explained by introducing the physiological conditions of the lysosomes, which require acidic pH to perform their biological functions [121,122]. Therefore, the acidic pH is maintained within the lysosomes by proton pumps. However, an increase in the pH up to the neutral pH could result in lysosomal membrane lysis [121,122].

Interestingly, it was found that cationic polymers can buffer the protons inside the lysosomes, resulting in membrane lysis, as suggested by the proton-sponge hypothesis [7,121,122]. This hypothesis was first adopted to explain the efficiency of polyethyleneimine (PEI) in escaping endolysosomal degradation [121,122]. This hypothesis proposes that the protonated PEI under acidic pH in lysosomes triggers lysosomal membrane lysis by buffering the protons in the lysosomes and inducing an influx of protons, chloride ions and water into the lysosomes. Therefore, a combination of swelling caused by osmotic pressure and PEI swelling due to the repulsion between the positively charged group result in the membrane lysis and release of lysosomes components into the cytoplasm. Similar proton buffering capacity was reported with polymethacrylates (i.e., Eudragit) with minimal toxicity compared to PEI [7]. Therefore, this explains the advantage of complexing pDNA/miRNA with positively charged polymeric NPs to ensure the highest transfection efficiency.

Generally, for miRNA-loaded NPs, the target is to ensure that NPs can escape endolysosomal degradation and deliver intact miRNA into the cytoplasm, where it can function in the RNA-induced silencing complex (RISC) [4,123]. However, pDNA delivery is more challenging since it requires the delivery of the pDNA to the nucleus [3,90,124,125]. Nevertheless, the mechanism behind the pDNA-polyplex (polymer/lipid) delivery into the nucleus is unclear. Some studies suggest that pDNA is not released in the cytoplasm from the polyplexes but trafficked with the polyplexes towards the nucleus [85,124]. However, other studies suggest that pDNA gets released from the polyplexes into the cytoplasm, where it gets associated with many cellular proteins that protect it from nucleases and mediate its trafficking to the nucleus [125]. Nevertheless, these studies agree that the cytoplasmic motion of pDNA, either free or complexed with carriers towards the nucleus, is a crucial step. However, the cytoplasm is a viscous environment packed with molecules, limiting macromolecules' mobility [125]. Therefore, the diffusion of pDNA cannot account for pDNA movement towards the nucleus. Hence, it was suggested that pDNA is directed by active transport via utilising the microtubule network and the molecular motor, dynein, for its trafficking to the nucleus [85,125]. After delivering the pDNA to the nuclear envelope, it is believed that pDNA enters the nucleus either by mitotic disassembly of the nuclear envelope in dividing cells or via nuclear pores complexes in the absence of cell division[85,125].

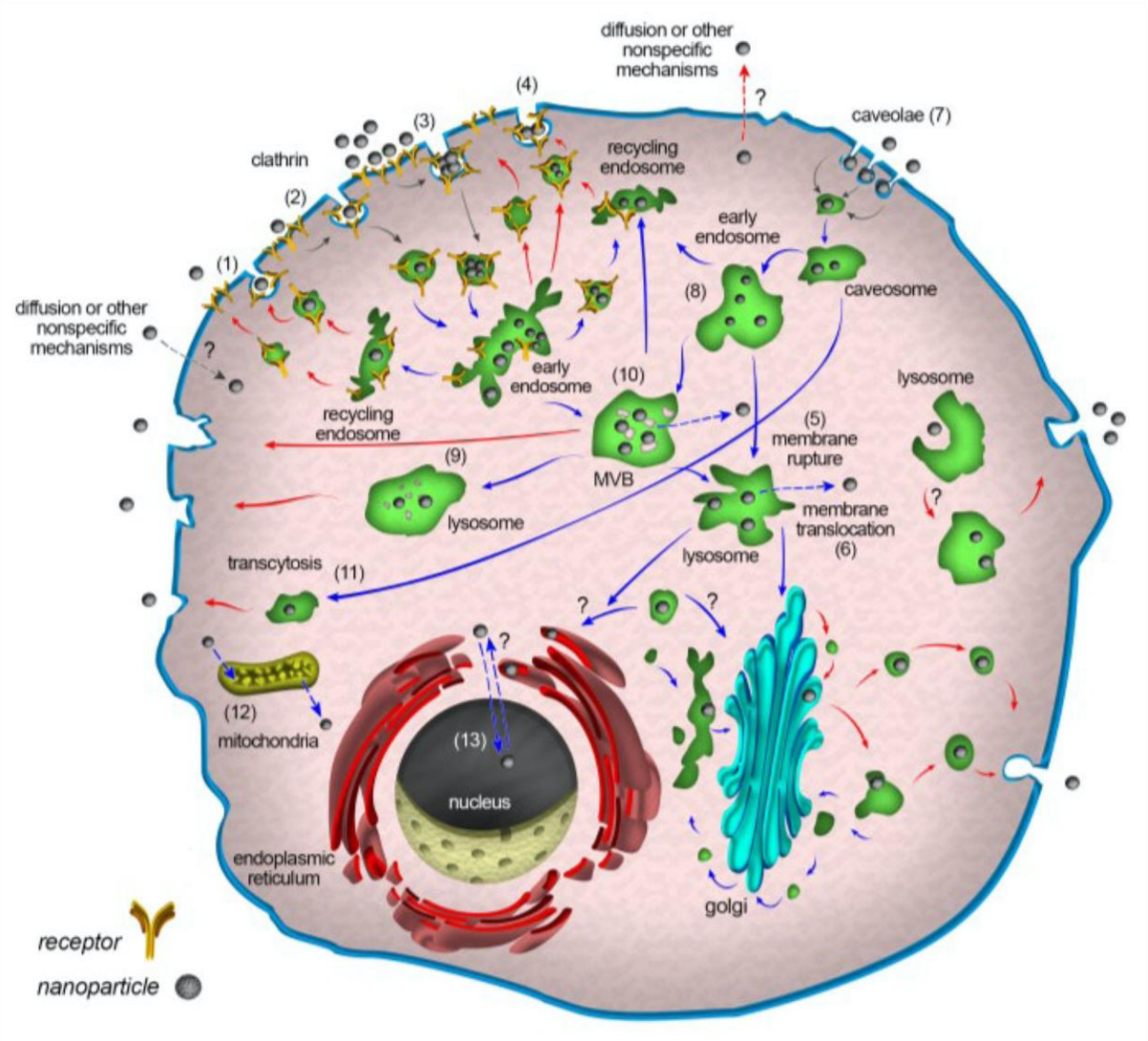

Figure 1.11: Schematic illustration of the endocytosis process represented by the grey arrows intracellular trafficking process represented by the blue arrows and cellular exocytosis represented by the red arrows of NPs. The question marks in the schematic indicate unknown mechanisms (reprinted with permission from reference [95]).

1.6.2 Factors affecting gene-based NPs uptake and transfection efficiency

Effective cellular internalisation of gene-based NPs is a bottleneck to successful gene therapy applications [126]. Therefore, several studies have investigated cellular internalisation factors since it is critical for efficient transfection. Generally, the transfection efficiency depends on the cells (type/health) and the NPs properties [85,126]. Therefore, understanding the influence of these factors can be implemented in designing an efficient delivery system.

1.6.2.1 NPs properties affecting cellular uptake and transfection efficiency

NPs systems were exploited for gene delivery applications due to their tuneable properties, including size, surface charge, shape, constituents and biological behaviour, which play a prominent role in determining the transfection efficiency [7,81,123,127,128]. Therefore, it is essential to understand the influence of each of these properties, as was demonstrated by several studies.

- **Size and shape**

The interaction between NPs and the cellular membrane (CM) is a critical step in NPs internalisation since these interactions might affect the integrity and permeability of the membrane in a size-dependent manner [97,129,130]. This hypothesis was supported by several studies that demonstrated the significant effect of NPs size on membrane permeability [131,132]. However, it is noteworthy to emphasise that the threshold NPs size required to achieve the highest uptake is highly dependent on the application, site of administration and site of action, which explains the discrepancies in the literature around the threshold NPs size. For example, some studies demonstrated that the highest cellular uptake in specific cells was achieved with 50 nm NPs, suggesting that 50 nm is the optimum NPs size [95,133]. These studies related the lower cellular uptake associated with smaller NPs (<50 nm) to their inability to bind to the receptors binding sites firmly before being engulfed by the membrane. In comparison, larger NPs (>50 nm), despite binding to these sites, were too big for efficient membrane wrapping needed for efficient endocytosis [95,133]. Additionally, a study conducted by Shan et al. investigated the influence of Au NPs size using a range of 4, 12 and 17 nm into Hela cells [134]. The study demonstrated that the larger interaction area explains the uptake increases with NPs size. However, a study conducted by Operti et al. investigated the correlation between PLGA NPs (100, 200 and >1000 nm) prepared by microfluidic-assisted nanoprecipitation and their cellular uptake by dendritic cells and mice isolated suppressor cells [64]. The study demonstrated that the uptake was most efficient for 100 nm NPs besides being cleared at a slower rate. Therefore, these studies confirm the impact of the NPs size on the cellular uptake and consequently the transfection efficiency; however, the impact is highly system-dependent, which introduces the need to fabricate different sizes of NPs to be tested for their cellular uptake on the desired cell type/model. Furthermore, besides considering the impact of the NPs size, it is vital to consider their stability at biological conditions to avoid aggregate formation that significantly mitigate the uptake. The influence of aggregation formation on cellular uptake was experimentally tested by Albanese et al. using transferrin-

coated aggregates of different citrate-capped Au NPs diameters [135]. Hence, the study compared the cellular uptake of 15 nm Au monodisperse NPs and aggregates of different sizes (26, 44 and 98 nm). The findings showed that the uptake of aggregated Au NPs was 25% lower than monodisperse Au NPs for the Hela and A549 cell lines. Additionally, the study demonstrated that the aggregate uptake could not be predicted, resulting in variable findings due to their irregular and asymmetrical shape [135].

The NPs shape is another critical factor that was investigated for its influence on cellular uptake; however, discrepant findings have been described by several studies without an apparent reason [97]. For example, it was proposed that spherical PEGylated or gold NPs have a higher cellular uptake; however other studies proposed that elongated NPs are more efficiently internalised than spherical NPs [136,137]. For instance, a study conducted by Chithrani et al. demonstrated that 74 and 14 nm spherical Au NPs were internalised into Hela cells at rates 5 and 3.75-fold higher than 74x14 nm rod-shaped NPs, respectively [133]. On the contrary, a study conducted by Banerjee et al. compared the cellular uptake of a sphere, rod, and disc-shaped polystyrene NPs conjugated with Biotin into Caco2 cells [138]. The study showed that rod-shaped NPs were internalised twice faster. Also, the study has found that biotin enhances the NPs uptake; hence, the study related the improved uptake of rod-shaped NPs to its higher surface to volume ratio, which allows for a higher biotin conjugation and better uptake.

- **Surface charge**

The NPs surface charge plays a significant role in determining the electrostatic interactions between the NPs and the cellular membrane [95,97]. Therefore, several studies probed the relation between the NPs surface charge and their cellular uptake. For example, a study conducted by Lin et al. studied the interactions of three types of Au NPs (cationic, anionic and hydrophobic) with electroneutral and electronegative bilayers [139]. The study reported that electrostatic interactions were more dominant than hydrophobic interactions between NPs and the bilayer. Also, the study addressed that cationic NPs showed a more significant disruptive influence on the bilayers. These findings were confirmed by a group of studies, demonstrating that cationic NPs are better internalised into the cells compared to neutral or anionic NPs [95,97,140]. For example, a study conducted by Cho et al. reported that cationic Au NPs had five-fold greater internalisation into SK-BR-3 cells compared to anionic NPs [95,141]. Additionally, besides the effect of the surface charge on the cellular uptake rate, it was found

that the charge can influence the uptake pathway. Hence, cationic NPs are mostly endocytosed via the CME pathway, while anionic NPs are endocytosed via the Caveolae-dependent endocytosis pathway [140,142].

- **Hydrophobicity and surface functionality**

The NPs hydrophobicity affects the interactions between the NPs and the cellular membrane; hence, several studies have studied how these interactions are affected by the NPs hydrophobicity [95,97]. For example, a study conducted by Wong-Ekkabut et al. studied the thermodynamics and penetration of fullerene aggregates, a promising hydrophobic nanomaterial, through the cellular membrane [143]. The findings showed that fullerene aggregates could penetrate easily and embed into the lipid membrane via passive diffusion.
Also, surface functionality is another critical parameter influencing NPs interactions with the cellular membrane. Therefore, engineering the NPs surface is a suggested approach to harness the NPs and control their biological behaviour. Generally, modifying the NPs surface with different ligands could affect their endocytic uptake pathway besides affecting their subsequent intracellular trafficking [95]. Therefore, the NPs can be designed with targeting ligands that can direct the NPs to the site of action.

Additionally, specific ligands could improve the internalisation via receptor-mediated endocytosis. For instance, Tao et al. developed aptamer-conjugated NPs using a novel polydopamine-based surface functionalisation approach, which resulted in enhanced therapeutic efficacy compared to unconjugated NPs [144].

Collectively, despite the availability of many studies focused on identifying the interactions between the NPs and the cellular membrane, there is still no way to predict the NP-cellular membrane interactions. Therefore, there is a considerable need to explore the effect of these parameters with each study. However, understanding the influence of these parameters on cellular uptake allows for defining critical design parameters to fabricate efficient NPs.

1.6.2.2 Cell-culture factors influencing NPs cellular uptake and transfection efficiency

Factors such as the cell type and the tissue culturing conditions play a prominent role in determining the vector therapeutic efficacy [95,126]. For example, several studies have demonstrated that cells could internalise the same material (i.e., NPs) using different endocytic

pathways. This was demonstrated by Santos et al. study that used A549 and 1321N1 cell lines to investigate the endocytic pathways of 40 nm, and 200 nm carboxylated polystyrene NPs [145]. The study demonstrated that NPs were internalised by 1321N1 cells via clathrin-mediated endocytosis (CME), while A549 utilised the caveolin-mediated pathway, suggesting that NPs might experience a different intracellular fate. Furthermore, other studies have shown that smooth muscle, endothelial cells, fibroblast and adipocytes mainly utilise the caveolae-dependent endocytosis; however, other cells such as leukocytes, neurons and HEPG2 cannot use the same pathways since they lack caveolae 1 protein [95,146–148]. Therefore, these studies provide solid evidence that the cell type plays a significant role in determining the NPs uptake and transfection efficiency. Therefore, the transfection efficiency of a particular NPs system cannot be compared with other studies that use a different cell line.

In addition to the cell type, the cell culturing conditions such as serum concentration, cell seeding density, and cell viability affect transfection efficiency. For example, adding serum to the transfection medium could improve the viability of the cells; however, it is essential to screen the effect of serum concentration on the transfection efficiency since it could interact with cationic transfection reagents. Additionally, choosing the appropriate cell seeding density is vital since actively dividing cells are required to ensure efficient plasmid uptake.

1.6.3 Probing the relation between NPs synthesis method and their gene therapeutic efficacy

Although NPs hold great potential as gene delivery systems, the clinical application is hampered by several hurdles. Encapsulation efficiency of genes (pDNA/miRNA), storage stability and NPs stability at the physiological conditions, endosomal escape, gene delivery efficiency and toxicity of NPs are the most significant challenges for clinical gene therapy using NPs [126]. Interestingly, these challenges can be tackled by modifying the NPs properties (i.e., size, shape, stability and surface charge), primarily dependent on the synthesis method and the processing parameters. Additionally, the NPs synthesis method might affect the genes encapsulation efficiency [126]. Therefore, it is essential to consider the type of gene and its characteristics (i.e., charge, structural modifications and stability under the processing conditions) when choosing the synthesis method. Hence, understanding each synthesis method's processing parameters' influence on the NPs properties is crucial to identify the critical design parameters for efficient NPs synthesis. Also, despite the availability of several

NPs synthesis methods, examining the difference between these methods in terms of efficiency and scalability is essential.

1.7 Polymeric NPs loaded with genetic materials: loading methods and applications

pDNA and miRNA can be loaded into polymeric PLGA NPs using the double emulsion method or the nanoprecipitation (solvent displacement) method [6,7,149,150]. Coupling the PLGA NPs with cationic biocompatible polymers provides higher gene loading, and transfection efficiency of PLGA NPs prepared using the two methods. pDNA/miRNA loading into PLGA NPs by nanoprecipitation relies mainly on electrostatic interactions [7,123,150–152]. Therefore, the loading occurs in a two-step process, where PLGA NPs are prepared and coated with a positively charged polymer, then pDNA or miRNA is loaded by mixing it with the NPs at different mass ratios via the electrostatic interactions. This method has been widely exploited for gene-based NPs synthesis since no external energy input is needed for NPs synthesis, which protects the pDNA/miRNA from any possible degradation. However, this method's gene encapsulation efficiency is limited by the charge of NPs and pDNA/miRNA, which might be affected by stabilisers addition or structural modifications of pDNA/miRNA. Therefore, the double emulsion method could offer better encapsulation efficiency since it relies on pDNA/miRNA physical entrapment into polymeric NPs besides the electrostatic interactions [7,123,152]. However, this method relies on external energy input (homogenisation, sonication) for NPs synthesis; hence, NPs synthesis should be carried out on the ice to prevent any possible degradation of miRNA/pDNA. Several studies have used this method to improve the pDNA/miRNAs loading into polymeric NPs [81,123,153].

1.7.1 pDNA-loaded polymeric NPs applications

pDNA loaded NPs are used in several studies to investigate their potential for treating several diseases with genetic origin [154]. For example, polymeric NPs loaded with pDNA encoding interleukin 10 (IL-10) and interleukin 4 (IL-4) have been tested for their efficiency in inhibiting the T-cell response against residual native islet cells in a prediabetic animal model [155]. The study revealed the efficiency of the formulation demonstrated by the inhibited diabetes development in 75% of the animals. In addition, other studies have investigated the potential of using pDNA loaded polymeric NPs as a therapeutic agent in pulmonary diseases. For example, a study conducted by Kumar et al. demonstrated the efficacy of chitosan interferon-

γ-pDNA NPs in reducing airway hyperresponsiveness in an allergic asthma mouse model [156].

Additionally, another study demonstrated the potential of biodegradable pDNA NPs to overcome the mucus barrier of lung airways, suggesting its use for inhaled lung gene therapy [157]. Moreover, besides the clinical applications of pDNA in several diseases, several studies have focused on using pDNA encoding green fluorescent protein (GFP) as a reporter gene to examine the transfection efficiency of the newly developed NPs system [6,149,158,159]. Generally, the product of the reporter gene is a fluorescent protein that fluoresces upon exposure to light or an enzyme that mediates a specific reaction [160]. GFP was isolated from the jellyfish *Aequorea victoria* in 1960 then became widely exploited in cell biology applications due to its appealing properties, such as its ability to form an extremely visible and efficient emitting internal fluorophore [160]. Therefore, GFP has become well established and adopted as a reporter of gene expression and protein targeting in cells, tissues and organisms. In this thesis, pDNA encoding GFP has been used as a reporter gene to investigate the transfection efficiency of the developed polymeric NPs prepared by conventional and MF-assisted nanoprecipitation.

1.7.2 miRNA-loaded polymeric NPs applications

miRNAs have been identified as biomarkers and major modulators of several pathophysiological processes contributing to several diseases such as oncogenesis and cardiovascular disease [81,123,161,162]. Moreover, miRNAs have been associated with painful disorders, including cystitis-induced chronic pain, osteoarthritis and complex regional pain syndrome [162]. These findings have paved the way for several studies to investigate the potential of using miRNAs as therapeutic agents to alleviate the symptoms and pain associated with several diseases by modifying the altered gene expression profiles and restoring homeostasis. Several studies have used polymeric NPs synthesised by the double emulsion method for encapsulating miRNA for several applications [81,123,153]. In this thesis, the application of using miRNA-140 loaded polymeric NPs as a potential therapeutic agent of osteoarthritis has been investigated.

1.8 Osteoarthritis (OA)

The joint is the point where two bones meet. A typical joint structure can be described as two bones whose articular surfaces are covered with articular cartilage, separated by the synovial cavity and connected by the joint capsule [163–166]. The extracellular matrix of the joint is made of three components: collagen, proteoglycans and water up to 80% of the cartilage weight [163]. Collagen is a fibrous protein responsible for cartilage formation and the Joint's strength, while proteoglycans are glycoproteins present between collagen fibrils responsible for the Joint's stiffness and elasticity [163,165]. Aggrecan is considered the predominant proteoglycan in articular cartilage, where it tends to form large aggregates, which provides the cartilage with its gel-like properties to resist deformations [165]. Hyaluronan, an extracellular oligosaccharide, is the central component of these aggregates [165]. This functional cartilaginous matrix is maintained and synthesised by a group of cells representing less than 1-2% of the cartilage volume known as chondrocytes [163]. Chondrocytes are embedded within the cartilage matrix and are responsible for tissue integrity. Generally, the Joint's structure and synovial microenvironment provide the joint with its physiological properties to function correctly. The normal joint function is characterised by [163]:

- Painless free movement of the opposed articular surfaces within the required range of motion.
- Stability maintenance during use
- Proper load distribution across joint tissues.
- Connective tissue matrices synthesised by intrinsic cells (i.e., osteoblasts, osteocytes and chondrocytes) are responsible for the mechanical properties.
- Ligaments, tendons and muscles, supporting the Joint's structure.

Therefore, the breakdown in the Joint's normal function associated with altered anatomy results in osteoarthritis. OA is a chronic disease of joints that disrupts joint stability and restricts the free movement of the articulating surfaces. The disease is characterised by a group of manifestations[163–165,167]:

- loss of articular cartilage
- anatomical changes in the joint shape
- inflammation of the synovial membrane
- thickening of the joint capsule and osteophytes formation at the margins of the joint

Therefore, these significant changes caused by OA result in a group of clinical manifestations, including symptoms, functional impairment, and signs [163]. Pain and stiffness are the chief complaints; however, other symptoms, including deformity and joint swelling, are associated with OA [163–165]. It is suggested that the pain arises from the stimulation of the pain fibres in the joint capsule by intra-articular hypertension caused by synovial hypertrophy and increased fluid production. Additionally, the stimulation of the periosteal nerve fibres by intra-articular hypertension and the painful enthesopathy and bursitis associated with structural alterations aggravate the OA pain [163]. In addition to the symptoms, OA can be characterised by a group of signs such as Crepitus (irregular articular surface), bony enlargement represented by osteophytes formation or remodelling, different degrees of synovitis (i.e., warmth, synovial thickening, effusion) and muscle weakness [163]. These symptoms and signs result eventually in disability, which is considered a functional impairment.

1.8.1 OA risk factors and epidemiology

OA is the most prevalent form of peripheral joint arthritis and predisposing cause of disability in the UK, affecting approximately 8.5 million people [168]. £10.2 billion is the estimated OA coasts to the NHS and wider healthcare system in 2017, and the coast is expected to reach £118.6 billion over the next decade [168]. OA is correlated with several risk factors:

- **Age**

Age is the primary risk factor of OA since the normal ageing process reduces joint proprioception, cartilage calcification, and chondrocyte's function [163,164]. For example, the Framingham study found radiographic evidence of knee osteoarthritis in 27% of those aged 63 to 70, increasing to 44% in the over 80 age group [169]. However, Other studies have found some radiographic evidence of osteoarthritis in 80% of people over the age of 65, but that incidence of symptomatic osteoarthritis decreased in men and women in their 80s [170].

- **Gender and ethnicity**

Men have a higher OA prevalence and incidence than women under the age of 50; however, women have a higher incidence and prevalence of OA once over 50. The difference becomes less obvious above the age of 80 [171]. Besides the gender effect, ethnicity was found to play a part in OA incidence and prevalence. Hence, osteoarthritis is usually commoner in Europeans than in Asians. Osteoarthritis of the hip is more common in Europeans (7%–25%) than in Chinese, Africans from Nigeria and Liberia, and Jamaicans (1%–4%) [164].

- **Obesity**

Obesity is associated with a higher prevalence of OA, as demonstrated by several studies. For example, the Chingford study demonstrated that knee OA development increased by 1.36 for every two-unit increase in body mass index (nearly 5 kg) [172]. Additionally, there is accumulated evidence that progressive OA is apparent in overweight people with localised disease. Therefore, obesity is considered the most substantial modifiable risk factor for OA [171].

- **Trauma**

Tears of collateral ligament, cruciate, meniscus or joint fracture increase the risk of osteoarthritis [163,164]. The Framingham study showed that men with a knee injury history were at a 5–6-fold increased risk of osteoarthritis development [169].

- **Other factors**

Other factors such as the occupation that relies on the repetitive use of specific joint groups and several underlying diseases, including hypertension, diabetes and hyperuricaemia, were correlated with an increased risk of OA [163].

1.8.2 Pharmacological and non-pharmacological therapies

Currently, there is no cure for osteoarthritis; however, OA management relies on managing the symptoms of the diseases pharmacologically and non-pharmacologically [163,164,173]. Several non-pharmacological options are adopted to alleviate the OA symptoms, including weight loss, exercising and physical therapy. Although these options are widely encouraged, only limited evidence of beneficial therapeutic effects was found in some cases of arthritis. Therefore, in addition to these options, other pharmacological options are recommended, including analgesics, non-steroidal anti-inflammatory drugs (NSAIDs) and Intra-articular corticosteroid injections.

- **Analgesics**

Simple analgesics such as paracetamol and aspirin can be used intermittently with mild pain [163,164,173]. Other stronger analgesics containing combinations of codeine or dextropropoxyphene and paracetamol can be used with strong pain episodes [163]. Generally,

the side effects are infrequent with moderate doses; however, some patients might experience constipation and drowsiness [163].

- **NSAIDs**

NSAIDs are widely used for pain management in OA [163,164,173]. However, their mode of action is uncertain, and no scientific evidence supports the point that NSAIDs are more effective in patients with clinical signs of joint inflammation than in patients without clinical signs. Additionally, there is no evidence that NSAIDs are more effective than paracetamol in moderate to severe chronic OA pain [164]. Nevertheless, NSAIDs are responsible for reducing OA pain by approximately 30% and 15% function improvement [174]. However, long term use imposes significant gastrointestinal and renal side effects [163,164]. Therefore, selecting the appropriate NSAID for long term OA pain management must include NSAIDs with lower-than-average side-effect profiles, such as indomethacin and naproxen [163].

- **Intra-articular corticosteroid injections**

These injections are mainly microcrystalline hydrocortisone acetate or triamcinolone hexacetonide, which remain localised to the joint or the site of administration [163]. However, these injections should be used in disease flares only since excessive use could result in severe cartilage destruction [175]. Therefore, the American College of Rheumatology guidelines suggest a maximum of 3–4 knee joint injections per year [164].

- **Surgical management of OA**

These procedures are used to replace the joint in advanced cases of OA or to alter the mechanical environment, such as the osteotomy procedure used to realign joints to relieve the pain and delay the progression of the disease [176]. However, these are invasive procedures that can result in several complications, such as bleeding, infection, fracture, blood clots and continuous pain and stiffness.

1.8.3 Genetic and molecular mechanisms of OA development

The lack of effective treatment for OA emphasises the need for a better understanding of the molecular mechanisms underlying OA pathogenesis to identify novel potential targets for OA. Generally, OA occurs in two stages, an early reversible stage and a later irreversible stage, with different pathogenesis mechanisms and manifestations of the disease at each stage. Degradation of aggrecan is a critical manifestation in early and reversible OA; hence several

studies have focused on aggrecanolysis at the molecular level to reverse the disease and prevent cartilage degradation [165]. This degradation process is mainly driven by aggrecanases, the principal proteinases in articular cartilage [87,165,177]. *ADAMTS5* is among the most efficient aggrecanases that have been identified to play a critical role in OA pathogenesis in early OA [87,165,177]. However, metalloproteinases (MMPs) were found to be active in later OA and responsible for the degradation of the collagenous ECM of cartilage as a late manifestation of irreversible OA [87,165]. Gene expression studies have reported a marked increase in collagenases, specifically *MMP-2* and *MMP-13*, in OA synovial fluid and joint tissues [87]. In addition to a significant increase in aggrecanases (*ADAMTS4* and A*DAMTS5*) in OA cartilage [87]. To understand the change in these gene expression profiles in OA, it is essential to introduce the Interleukin 1ß (IL-1ß) Pathway, a pro-inflammatory cytokine that plays a central role in OA pathogenesis by modulating the expression of the genes mentioned above[178]. Upregulation of IL-1ß possesses damaging effects on the chondrocytes function and the ECM integrity driven by proteinases activation, suppression of the anabolic pathways, and a reduction in the synthesis of the cartilage ECM [178].

Therefore, the role of IL-1ß in OA has drawn significant attention, and several studies have supported the detrimental effects of IL-1ß in OA as follows. A study conducted by Saha et al. found an upregulation of IL-1ß in human OA cartilage at the superficial and the intermediate layers [178,179]. In another study conducted by Kubota et al., levels of IL-1ß in synovial fluid of temporomandibular joints were positively correlated with OA changes [178,180]. Furthermore, IL-1ß was detected in synovial membranes from all patients with OA screened in a study conducted by Smith et al. [178,181]. These detrimental effects of IL-1ß were related to its role in elevating cartilage catabolism by upregulating *ADAMTS5* and *MMP-13* [178]. Therefore, these findings suggest that blocking the action of IL-1ß might be one way to curtail the disease progression. Besides these alterations, OA was correlated with other genetic alterations affecting the Wnt signalling pathways, such as the FZD6 gene expression. *FZD6* is one of the ten human frizzled (FZD) genes that encode integral membrane proteins, functioning in multiple signal transduction pathways [182]. These frizzled proteins act as receptors for secreted Wnt proteins, which regulate the Wnt signalling pathways [182]. These pathways include the canonical β-catenin-dependent and non-canonical β-catenin-independent signalling pathways associated with increasing evidence for their pathological role in OA [183].

Concerning the canonical Wnt signalling pathway, the outcome of several studies demonstrated the need for a moderate WNT activity to ensure chondrocytes proliferation and maintenance of their typical characteristics [183]. Hence, overexpression of WNT results in chondrocytes hypertrophy and a marked increase in the expression of metalloproteinases (MMPs) responsible for the degradation of the collagenous extracellular matrix. Conversely, excessive suppression of WNT in chondrocytes predisposes to OA phenotypes [183]. These findings emphasise the need for this balance to maintain cartilage homeostasis since over activation or suppression of WNT activity results in cartilage breakdown. Furthermore, by examining the activity of specific regulators of the Wnt/β-catenin signalling pathway in OA, several alterations in their activities were reported, suggesting them as potentially critical targets for OA [183]. For instance, the protein levels of Wnt3a and β-catenin were increased in OA induced rat models [183]. Similarly, non-canonical Wnt signal transduction, which Wnt5a predominantly activates, was correlated with cartilage degradation by increasing MMPs expression and decreasing cartilage II production [183]. Collectively, these findings address the importance of Wnt signalling pathways in maintaining cartilage homeostasis.

FZD6 has been identified as a negative regulator of the canonical Wnt signalling pathway besides its ability to promote a Wnt4 mediated β-catenin independent pathway [184]. Furthermore, several studies have demonstrated the downregulation of *FZD6* during chondrogenesis and its upregulation during osteogenic differentiation [184]. The upregulation of *FZD6* was associated with antagonised SOX9 role, which is an essential transcription factor responsible for promoting the expression of extracellular matrix (ECM) genes such as type II collagen [184,185]. Accordingly, understanding the contributing role of these genetic alterations to OA development has paved the way for several studies to explore therapeutic strategies that can reduce the proteases activity in the cartilage matrix and modify the genetic alterations to cease the progression of the disease and restore homeostasis. These studies have focused on delivering pDNA and miRNAs as potential modulators of the genetic alterations associated with OA development. For example, a study conducted by Huading et al. demonstrated that PNPs loaded with plasmid encoding transforming growth factor (*TGF-β1*) with a critical role in skeletogenesis and OA progression could increase the *TGF-β1* expression in chondrocytes and promotes proliferation [186].

Additionally, several studies demonstrated that TGF-β-loaded NPs could stimulate ECM production, form hyaline cartilage, reduce matrix degradation, and thus attenuate OA

progression [187,188]. This shows the application of pDNA-loaded NPs in the treatment of OA. miRNAs are another novel approach for targeting OA, explained in the following sections.

1.8.4 Therapeutic role of miRNA-140-5P in OA

miRNAs have been identified as critical therapeutic genes in OA since more than 30 miRNAs are expressed in the joint tissue and are responsible for maintaining cartilage homeostasis and OA development. Among these miRNAs, miRNA-140-5P has gained significant attention due to its multifactorial effects in regulating several underlying OA development mechanisms. The expression of miRNA-140 was found to be significantly reduced in OA tissue compared to normal articular cartilage. Furthermore, the treatment of chondrocytes with Interleukin 1ß (IL-1ß), a cytokine involved in OA pathogenesis, suppresses the miRNA-140 expression [165]. However, transfection of miRNA-140 into chondrocytes down-regulates *ADAMTS5* expression, one of the most efficient aggrecanases in OA pathogenesis induced by IL-1ß [165].

Additionally, a study conducted by Miyaki et al. showed that a universal knockout of miRNA-140 results in age-related OA changes; however, overexpression of miRNA-140 in chondrocytes protects from OA [189]. Collectively, these studies suggest a direct regulatory relationship between miRNA-140 and *ADAMTS5*, *MMP-13* and *FZD6*, the most likely gene candidates associated with pathological roles in OA by regulating IL-1ß. Therefore, these findings suggest that delivering miRNA-140 has vital therapeutic implications, such as restoring cartilage homeostasis and mitigating OA progression by modulating different cellular pathways involved in OA pathogenesis.

1.8.4.1 miRNAs biogenesis and mechanism of action

miRNAs are mainly transcribed by RNA polymerase II, besides some transcripts from RNA polymerase III **(Figure 1.12, step 1)** [165,190]. The structure of miRNAs can be described as a small gene located in an intergenic region and with an autonomous promoter [165]. The gene is transcribed into a transcript known as pri-miRNA, a 70 nucleotides long transcript, forming an extended stem-loop structure, described as a hairpin structure, with a partial complementary sequence in the stem region [165]. First, the pri-miRNA maturation occurs in the nucleus aided by the RNase III-type Drosha enzyme and DGCR8 (DiGeorge critical region 8) protein to cleave the hairpin structure and produce the pre-miRNA **(Figure 1.12, step 2a)** [165,190]. Then in the nucleus, pre-miRNA is recognized by Exportin5 (XPO5) and complexed with Ran-GTP to be transported to the cytosol through the nuclear pore complex (NPC) **(Figure 1.12,**

step 3) [165]. Afterwards, pre-miRNA is exposed to the RNase III Dicer that exerts its action by cutting the pre-miRNA loop and leaving the miRNA: miRNA* duplex with two nucleotides protruding at each 3' end **(Figure 1.12, steps 4 and 5)** [165]. Eventually, the miRNA action occurs within the miRNA-induced silencing complex (miRISC) after the duplex structure is unwound and loaded into the RISC compound with the aid of Argonaute 2 protein (Ago 2) **(Figure 1.12, step 6)** [165]. Therefore, after the attachment of the miRISC: miRNA complex with its target mRNA 3' UTR, miRISC: miRNA complex can act as a translational repressor by degrading the target mRNA **(Figure 1.12, step 7)**.

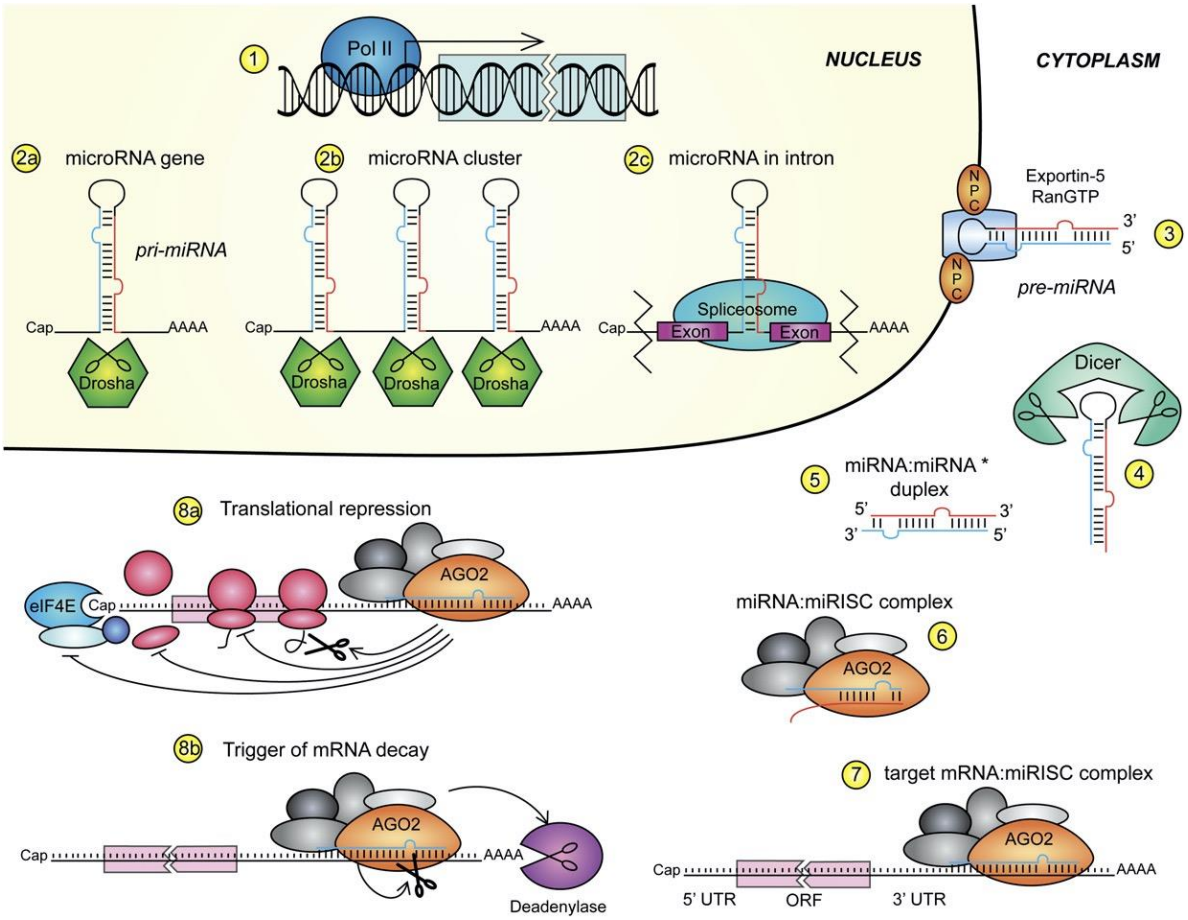

Figure 1.12: Schematic illustration of miRNAs biogenesis and mechanism of action. (Step 1) miRNAs are transcribed by RNA polymerase II. (Step 2) miRNA transcribed into pri-miRNA that gets processed by RNase III-type Drosha to produce pre-miRNA. (Step 3) pre-miRNA is recognized by Exportin5 (XPO5) and complexed with Ran-GTP to be transported to the cytosol through the nuclear pore complex (NPC). (Step 4) the loop is cleaved by Dicer leaving miRNA: miRNA* duplex (Step 5). (Step 6) the duplex structure is unwound and loaded into the RISC compound where it anneals to its target mRNA 3' UTR (Step 7). (Step 8) miRISC: miRNA complex acts as a translational repressor by degrading the target mRNA (reprinted with permission from reference [165]).

1.8.5 Design strategy of miRNA-loaded NPs for OA

Systemic administration of therapeutic molecules for targeting joint tissues suffers from poor stability and joint bioavailability and a higher risk of systemic toxicity [167]. Although direct intra-articular delivery is considered a superior alternative through bypassing the biophysical barriers correlated with systemic delivery, the rapid clearance rate from the joint remains a critical limitation for achieving the desired therapeutic efficacy [167]. Therefore, using nanomaterials systems engineered to possess particular properties increases the therapeutic molecules residence time within the joint cavity and improves the therapeutic outcome. However, designing NPs that can successfully deliver the payload to the joint tissues requires a deep understanding of the joint's structure, biophysical barriers and extracellular matrix microenvironment. Cartilage porosity influenced by the arrangement of all cartilage components, including collagen network, chondrocytes, and proteoglycans, is thought to determine the fate of NPs. The mesh size of the collagen II network is approximately 50 nm – 200 nm, which is densely filled with aggrecan molecules that are 200–350 nm long. Collectively, cartilage is commonly characterised to have a pore size between 6–11 nm [167]. Accordingly, it is widely accepted that NPs size and surface charge are critical design criteria for cartilage targeting since they are critical determinants of the NPs ability to penetrate the tissues and their residence time within the tissues. For instance, it is suggested that cationic NPs facilitate anionic joint tissue targeting, such as the synovial fluid and cartilage.

However, despite the physical characterisations provided for the cartilage structure and porosity, studies in the literature could not identify a threshold size of NPs that would ensure or prevent cartilage penetration. For example, ex-vivo studies conducted by Yan, Huimin, et al. demonstrated that NPs up to 55 nm could penetrate the entire thickness of cartilage [167,191]. However, an in-vivo study conducted by Whitmire, Rachel E., et al. demonstrated the complete cartilage penetration with 300 nm particles three days post-injection [167,192]. These discrepancies suggest other influencing factors beyond the NPs diameter, such as the NPs material properties and the change in the OA microenvironment with disease progression. Similarly, the NPs surface charge plays a pivotal role in determining the efficiency of delivery. Therefore, several studies have demonstrated that NPs engineered to possess a positive surface charge facilitated targeting anionic joint tissues such as the synovial fluid and cartilage [193].

1.9 Thesis objectives

Coupling gene therapy with polymeric NPs holds excellent potential for targeting acute and chronic diseases with genetic origins. However, the therapeutic efficacy of gene-based NPs relies on the NPs physicochemical properties that determine their intracellular fate and activity. Generally, the NPs synthesis method and the processing parameters affect the NPs properties and their gene loading efficiency. This explains the development of new mixing devices (i.e., microfluidics) that allow for stricter control over the NPs synthesis to improve their physicochemical properties. However, there is a lack of systemic studies examining the difference between conventional synthesis methods and microfluidics and assessing the difference's magnitude in the NPs therapeutic efficacy. Therefore, since NPs efficacy in gene therapy relies on their physicochemical properties, there is a need to assess the difference between the synthesis methods/platforms and their impact on the NPs cellular uptake and efficacy. After addressing the challenges of gene delivery using polymeric NPs and revealing the impact of the NPs properties on their therapeutic efficacy, the study explores the potential of miRNA-140 loaded polymeric NPs for targeting osteoarthritis (OA). Despite the lack of effective treatment of OA so far, the study aims to provide novel miRNA based polymeric NPs as a potential therapeutic agent. Therefore, the aims of the study include:

Discussed in chapter 3:

- To reveal the advantages and limitations of microfluidic technology for nanoprecipitation compared to conventional methods by investigating the effect of the processing parameters of each synthetic method (CB/MF method) on the properties of PLGA NPs.
- Provide new insights into the impact of the mixing time on the resulting NPs properties and the limitations of the available simulation models used for calculating the mixing time and predicting the NPs properties.
- Explore the potential of microfluidics in modifying the surface of PLGA NPs with Chitosan/Eudragit compared to the CB-method.

Discussed in chapter 4:

- Fabricate PLGA-Eudragit NPs in a one-step method using conventional nanoprecipitation (CB-method) and microfluidic-assisted nanoprecipitation (MF-method) that can efficiently load p-DNA encoding a green fluorescent protein (GFP).

- Evaluate the impact of the cell culture parameters on pDNA transfection efficiency using transfecting agents as positive controls. Third, examine the pDNA transfection efficiency of PLGA-Eudragit NPs prepared by the two methods using identical compositions and closely matched processing parameters.
- Explore the translational potential of microfluidic technology as a formulation manufacturing method for nanoparticle-based gene delivery platforms compared to conventional methods.

Discussed in chapter 5:

- Develop stable miRNA-140 loaded polymeric NPs and assess the formulation loading efficiency.
- Examine the efficiency of miRNA delivery in 2D and 3D C28/I2 cell culture by RT-qPCR.

Chapter 2

Materials and Methods

2.1 Introduction

This chapter provides specific information about the used materials, methodologies and characterisation methods used throughout the project. In this study, several polymers were used, comprising PLGA, Eudragit EPO and Chitosan. Additionally, a group of excipients were used, including Tween-80, polyvinyl alcohol (PVA) and D-α-tocopheryl polyethylene glycol succinate (Vitamin E TPGS). Blank polymeric NPs including PLGA, PLGA-Eudragit and PLGA-Chitosan NPs were prepared by conventional bulk (CB-method) nanoprecipitation and MF-assisted nanoprecipitation (MF-method). Plasmid DNA (pEGFP-C1 reporter gene) was loaded into PLGA-Eudragit NPs prepared by nanoprecipitation (CB/MF methods) using the concept of the electrostatic interaction; however, CY5-miRNA-140 loaded PLGA-Eudragit NPs were prepared using the double emulsion method.

Several characterisation methods were used to understand the physicochemical properties of the NPs, including differential scanning calorimetry (DSC), attenuated total reflectance Fourier transform infrared spectroscopy (ATR-FTIR), scanning electron microscope (SEM), transmission electron microscope (TEM), dynamic light scattering (DLS), zeta-sizer and rheometer. pDNA encapsulation efficiency was assayed by gel electrophoresis; however, CY5-miRNA-140 encapsulation efficiency was assayed by gel electrophoresis and spectrofluorometer based on the CY-5 fluorescence.

The transfection efficiency of pDNA-loaded PLGA-Eudragit NPs into A549 and LCC-PK1 cell lines was assayed by inverted fluorescent microscopy and flow cytometry, while the delivery of CY5-miRNA-140 by PLGA-Eudragit NPs into C28/I2 chondrocytes was assayed by confocal microscopy. MTT test was used to assay the viability of the cells. qPCR and western blotting were used to investigate the efficiency of the miRNA-140 loaded PLGA-Eudragit NPs in downregulating the targeted genes and their protein's level in C28/I2 chondrocytes.

This chapter provides the general protocols and materials sources used in the study; however, some specific protocols related to the synthesis and optimisation of NPs are given in the materials and methods section of the results chapters.

2.2 Genetic materials

2.2.1 Plasmid DNA (pEGFP-C1)

pEGFP-C1 encodes a red-shifted variant of wild-type GFP, optimized for brighter fluorescence and higher expression in mammalian cells (Excitation maximum = 488 nm; emission maximum = 507 nm) [194]. pEGFP-C1 has been widely used as a reporter gene with different types of NPs to check their transfection efficiency and study the effect of the NPs physicochemical properties (i.e., size, charge and morphology) on their transfection efficiency [6,124,156]. In this study, pEGFP-C1 was a gift from Dr Grant Wheeler (University of East Anglia).

2.2.2 miRNA-140-5P

The miRNA-140 gene is located between exons 16 and 17 of the E3 ubiquitin-protein ligase gene Wwp2 on murine chromosome 8 and the small arm of chromosome 16 in humans[165]. A study conducted by Tuddenham et al. was the first to report that miRNA-140 is highly expressed in cartilage during both flat and long bone development [195]. The role of miRNA-140 in osteoarthritis has been extensively explained in **chapter 1, section 1.8.4**. The specifications of miRNA-140 used in this study and purchased from (RIBOBIO, China) are shown in **Table 2.1**.

Table 2.1: Specifications of miRNA-140 used in this study

Product name	Product Description	miRNA sequence
micrONTM hsa-miR-140-5p mimic (5'Cy5)	5'Cy5 labelled miRNA mimic	>hsa-miR-140-5p MIMAT0000431 CAGUGGUUUUACCCUAUGGUAG

2.3 qPCR primers and probes

A complete list of qPCR primers and probes used in this study is detailed below **(Table 2.2)**.

Table 2.2: Primers and probes used in qPCR experiments

Gene of interest	Forward primer	Reverse primer	Probe #
FZD6	CGTCTATGAGCAAGTGAACAGG (Sigma Aldrich, UK)	AATTCTGGTCGAGCTTTTGC (Sigma Aldrich, UK)	14
MMP-13	TCATGATCTCTTTTGGAATTAAGGA (Sigma Aldrich, UK)	GCCCAGGAGGAAAAGAT (Sigma Aldrich, UK)	40
ADAMTS5	TCTAAGCCCTGGTCCAAATG (Sigma Aldrich, UK)	TCGTGGTAGGTCCAGCAAA (Sigma Aldrich, UK)	41

2.4 Cell lines and tissue culture

2.4.1 A549 cell line

A549 cells are adenocarcinoma human alveolar basal epithelial cells. A549 cells were purchased from (Sigma Aldrich, UK). A549 cells were cultured in RPMI media (Fisher Scientific, UK) supplemented with 10% FBS, 1% L-glutamine and 1% penicillin-streptomycin (Fisher Scientific, UK). At 70% confluency, cells were passaged 1:10 by trypsinisation.

2.4.2 LLC-PK1 cell line

LLC-PK1 is a pig derived kidney epithelial cell. LLC-PK1 cells were purchased from (Sigma Aldrich, UK). LLC-PK1 cells were cultured in RPMI media (Fisher Scientific, UK) supplemented with 10% FBS, 1% L-glutamine and 1% penicillin-streptomycin (Fisher Scientific, UK). At 70% confluency, cells were passaged 1:10 by trypsinisation.

2.4.3 C28/I2 cell line

Human chondrocyte cell line (C28/I2) is widely used as a model to study the repair mechanisms of normal and pathological cartilage related to chondrocyte physiology and biology. C28/I2 chondrocytes provided by Professor Ian Clark (University of East Anglia) were cultured in DMEM, low glucose, GlutaMAX™ Supplement, pyruvate (Thermo Fischer Scientific, UK) with 10% non-heat-inactivated FBS (Thermo Fischer Scientific, UK) and 1% penicillin-

streptomycin (Thermo Fischer Scientific, UK). At 70% confluency, C28/I2 cells were passaged 1:8 by trypsinisation. Cells were kept sub-confluent to maintain their phenotype.

2.4.4 3D micromass C28/I2 cell culture

For C28/I2 micromass cell culture, a procedure described by a literature study was employed in this study [196]. Briefly, confluent monolayer cultures of chondrocyte cell lines (C28/I2) were released by trypsin-EDTA and re-suspended in full DMEM media at a density of 25,000 (cells/µl). Micromasses were achieved by pipetting 20 µl of cell suspension into individual wells of 24-well plates. Following a 3-h attachment period without medium, full DMEM media was gently added, and cultures were left resting for a further 24 h. After then, the medium was replaced with 1x Insulin-Transferrin-Selenium medium (ITS-G) (Thermo Fischer Scientific, UK) in DMEM/F-12, HEPES, no phenol red prewarmed media. Micromasses were then ready to be treated or transfected based on the intended experiment.

2.5 Synthesis of polymeric NPs

This study used two synthesis methods to fabricate the NPs: nanoprecipitation and the double emulsion ($W_1/O/W_2$). Blank polymeric NPs, including PLGA NPs, PLGA-Eudragit NPs and PLGA-Chitosan NPs, were fabricated by the nanoprecipitation method. These NPs were fabricated either by the conventional bulk nanoprecipitation method (CB-method) or microfluidics-assisted nanoprecipitation (MF-method). The processing parameters used with each type of NPs are detailed in **chapter 3, sections 3.2.3, 3.2.4 and 3.2.5**. pDNA was loaded onto PLGA-Eudragit NPs prepared by CB or MF nanoprecipitation by electrostatic interactions.

miRNA-140 loaded PLGA-Eudragit NPs were fabricated by the double emulsion method ($W_1/O/W_2$). The synthesis parameters and the NPs optimisation are detailed in **chapter 5, sections 5.2.1 and 5.2.2**.

2.6 Solubility studies

2.6.1 PLGA Solubility

The solubility of PLGA 50:50 ester terminated (M. wt. 38000-54000 Da) (Sigma Aldrich, UK) in acetone/water binary mixtures was measured using a gravimetric method [197]. An excess amount of PLGA was placed into a vial with 1 mL of different acetone/water volume ratios ranging from 0-60% v/v. The vials were incubated in an IKA KS 3000 i-control shaking

incubator (IKA®-Werke GmbH & Co. KG, Germany) at 100 rpm and 25°C for 48hr followed by another 24hr without shaking for equilibration. Then, the supernatant was collected and filtered using a 0.45 μm syringe filter from which precise volumes (V) were transferred into pre-weighed vials (m1). The solvent was evaporated by heating in an oven at 60°C for 6 (h), and the vials were weighed again (m2). The solubility of the polymer was calculated using the following Eq. (2.1):

$$S = \frac{m_2 - m_1}{V} \qquad \text{Eq. (2.1)}$$

2.6.2 PLGA-Eudragit solubility

To understand the composition and distribution of PLGA 50:50 ester terminated (38000-54000) (Sigma Aldrich, UK) and Eudragit EPO Evonik industries (Darmstadt, Germany) in Eudragit PLGA NPs, miscibility and solubility studies were conducted. For measuring the solubility of PLGA and Eudragit in different acetone/water volume ratios binary mixtures, the gravimetric method was used [197]. Briefly, excess amounts of polymers were added into vials with 1 ml of different acetone/water volume ratios ranging from 0 to 60% v/v acetone/water. Afterwards, the vials were incubated in an IKA KS 3000 i-control shaking incubator (IKA®-Werke GmbH & Co. KG, Germany) at 100 rpm and 25°C for 48h followed by another 24h without shaking for equilibrium. Subsequently, the supernatant was collected and filtered using a 0.45μm syringe filter from which precise volumes (V) were transferred into pre-weighed vials (m_1). The solvent was evaporated in the oven at 60°C for 6h, and the vials were weighed again (m_2). The solubility of the polymers was calculated using the following Eq. (2.1).

2.7 General physicochemical characterisation methods

2.7.1 Differential scanning calorimetry (DSC)

Differential scanning calorimetry (DSC) is the most commonly used method for thermal analysis of polymers, pharmaceuticals, ceramics and inorganic materials [198]. This technique is mainly used to detect a range of thermal events, including melting, glass transitions and crystallization, by applying linear heating or cooling signals to the sample [198]. DSC offers several advantages, including the small sample size, rapidity and simplicity of the measurement and the wide temperature range (typically –120 to 600°C) [198].

This approach requires placing the sample (approximately 5-10 mg) in a metal crucible pan along with an empty reference pan in a furnace where different thermal profiles can be applied (i.e., heating or cooling at a controlled rate usually 5-10 °C/min or an isothermal setup with heating) [198]. Hence, the DSC will detect and assess the energy and temperature associated with any thermal event within the sample. Fundamentally, two types of DSC are commercially available: heat flux and power compensation. The working principle of DSC is to measure the temperature difference between the reference and the sample; however, there are slight differences between the two types of DSC [198]. For power compensation DSC, the temperature difference between the sample and reference is kept zero by locating the temperature sensors in a bridge circuit. Thus, the electrical power supplied to the sample furnace is varied to keep the temperature difference between the reference and the sample zero, explaining the term power compensation. Furthermore, the reference pan is exposed to a linear temperature program, and the sample is exposed to the same linear temperature program. Therefore, any difference in power between the reference and the sample pan must be correlated with the enthalpies and the sample's heat capacity correlated with the transitions [198].

In a heat flux DSC, the empty reference pan and the sample pan are placed symmetrically in a furnace where thermocouples are placed close to each other [198]. The cell design guarantees identical heat paths from the furnace to the reference, and the sample and thermocouples directly measure the temperature difference between the reference and the sample.

Thus, the heat flow from the furnace to each pan is given by Eq. (2.2), where Q is the heat, t is the time, ΔT is the temperature difference between the furnace and the pan, and R is thermal resistance between the furnace and the pan [198].

$$\frac{dQ}{dt} = \frac{\Delta T}{R} \qquad \text{Eq. (2.2)}$$

In addition, the heat flow can be interpreted in terms of heat capacity (Cp), defined as the energy needed to increase the material temperature by 1 degree (Kelvin), as shown in Eq. (2.3), where dQ/dt is the heat flow, and dT/dt is the heating rate [198].

$$\frac{dQ}{dt} = Cp \times \frac{dT}{dt} \qquad \text{Eq. (2.3)}$$

In this study PLGA-Eudragit miscibility was assessed using a Discovery DSC 2500 differential scanning calorimetry (TA Instruments, Delaware, United States). Both polymers were physically mixed with 10% increment increase in Eudragit content. The mixtures were placed in T-Zero pans with a sample weight of 3-5 mg. The pans were hermetically sealed and tested 20 - 90 °C (glass transition region) at a rate of 2 (°C/min). Nitrogen purge gas with 50 (mL/min) flow rate was used throughout the experiments. TA Trios software was used for the data analysis.

2.7.2 Attenuated total reflectance-Fourier transform infrared (ATR-FTIR) spectroscopy

ATR-FTIR is considered a vibrational spectroscopic technique for illustrating the chemical structure of different materials. Therefore, the technique is widely used in the pharmaceutical field to analyse small molecules or molecular complexes besides its applications in the biological field for tissue and cells analysis [199]. This technique uses the mid-infrared electromagnetic radiation (4000-400 cm^{-1}) that interacts with the vibrational modes of the molecules, resulting in a unique fingerprint for the tested sample [200]. This explains the main working principle of FTIR since each IR band is a characteristic of a specific vibrational mode.

Fundamentally, FTIR uses transmission or reflectance mode; hence, an IR spectrum is generated by determining the fraction of the incident IR that is reflected or absorbed at a particular frequency. Therefore, FTIR elucidates the molecular structure since the spectra reflect characteristic vibrations dependent on the atomic masses, intra-and intermolecular interactions and the bond strength [201]. In ATR-FTIR, the sample must be in direct contact with a crystal of high reflective index and excellent IR transmittance characteristics; thus, diamond is used mainly. The IR beam is focused onto the sample by a set of mirrors then the reflected fraction of the beam is directed to the detector to be recorded by another set of mirrors.

In this study, an FTIR spectrophotometer (Vertex 70, Bruker Optics Limited, United Kingdom) connected with an internal reflection diamond Attenuated Total Reflectance (ATR) accessory (Specac Ltd., Orpington, United Kingdom) was used to examine any chemical changes in the heterogeneity of polymers blend NPs (PLGA-Eudragit/PLGA-Chitosan) prepared by CB-method and MF method. Thirty-two scans were acquired for each sample with a resolution of

2 cm^{-1} scanning from 600 to 4000 cm^{-1}. All measurements were carried out in triplicate, and data were analysed using OPUS software.

2.7.3 Rheometer

Rheometers are widely used to examine the rheological properties of the materials, such as viscosity and viscoelasticity. Rheology science studies the flow behaviour of substances by considering three main factors: the external forces acting on the material, the internal structure, and the environmental conditions (i.e., temperature) [202]. The working principle of the rheometer relies on relating a material's property from how hard it is being forced to how far it moves by applying torque (stress) and measuring angular displacement (strain) or by commanding angular displacement (shear strain) and measuring torque (stress) [202]. Therefore, a rotational rheometer will apply or measure torque, angular displacement and angular velocity (shear rate). This leads to viscosity measurement, defined as the material resistance to deformation and interpreted as the function of shear stress or rate with temperature and time dependence.

Fluids can be classified into Newtonian and non-Newtonian fluids, in which each type has a different rheological profile [203]. Newtonian fluids follow Newton's law of viscosity; thus, viscosity is independent of the shear rate. Whereas non-Newtonian fluids do not obey Newton's law; hence, their viscosity (ratio of shear stress to shear rate) is not constant and depends on the shear rate [203]. Generally, gasses and mineral oils are considered Newtonian fluids; however, many other fluids are non-Newtonian and polymeric additives are considered the most common cause of non-Newtonian behaviour [203]. As shown in **Figure 2.1**, Newtonian and non-Newtonian fluids have different viscosity profiles:

- Pseudoplastic (shear thinning): viscosity decreases as the shear rate increases.
- Dilatant (shear thickening): viscosity increases with increasing the shear rate.
- Newtonian: viscosity is independent of the shear rate.
- Bingham: This model usually describes materials possessing yield stress followed by the Newtonian flow.

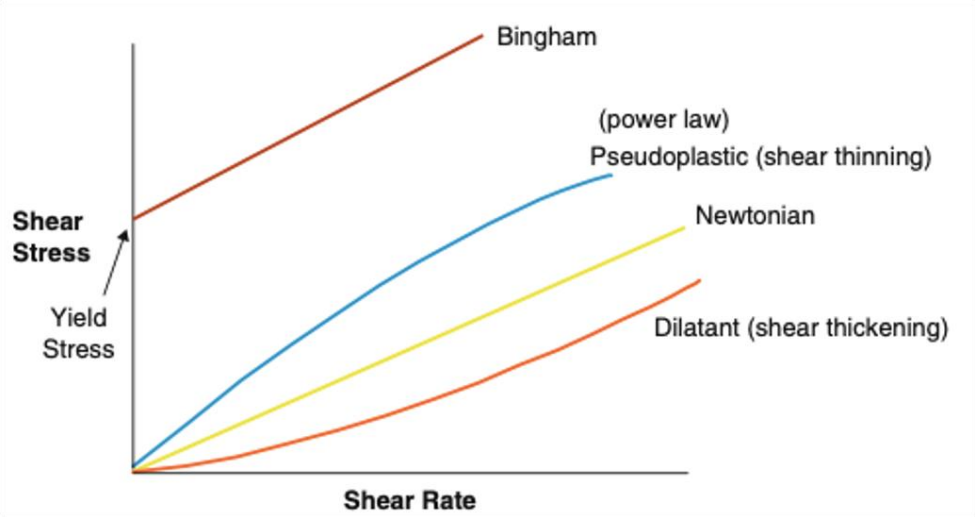

Figure 2.1: Viscosity profiles of Newtonian and non-Newtonian fluids (reprinted with permission from reference [203]).

In this study, organic phases used for NPs synthesis using CB-method and MF-method were characterised in terms of dynamic viscosity using Discovery Hybrid Rheometer (TA Instruments, Delaware, United States) equipped with a 2°, 40 mm cone-and-plate geometry. The method was set to be a flow ramp procedure from 0.1 to 100 s^{-1} at 25 ^{o}C for 60 seconds. The measurements were done in triplicate to calculate the average viscosity ± SD. Data were analysed using the Bingham model with TRIOS software (TA Instruments, Newcastle, DE, United States.

2.7.4 Dynamic light scattering (DLS)

Dynamic light scattering (DLS) is a fundamental technique in the nanomedicine field for analysing the NPs size distribution. Hence, this analysis technique provides information about the NPs size and polydispersity index. DLS measures the speed of dispersed particles undergoing Brownian motion, defined as the random movement of particles constantly colliding with the solvent molecules [204]. The speed of the particles is influenced by the temperature, viscosity and particles size. Therefore, if the temperature and viscosity are known, the hydrodynamic size of the particles can be measured from particles speed [204]. It is noteworthy to mention that the hydrodynamic size depends not only on the size of the particle core but also on the surface structure and the ions in the medium [204]. The relation between the particle size and the particle's speed is given by the Stokes-Einstein equation (Eq. (2.4)) where D is the diffusion coefficient [m^2/s], kB is Boltzmann constant [m^2kg/Ks^2], T is Temperature [K], η is the Viscosity [Pa. s] and Rh is the Hydrodynamic radius [m][204].

$$D = \frac{k\mathrm{B}\times\mathrm{T}}{6\pi\,\eta Rh} \qquad \text{Eq. (2.4)}$$

Based on the Brownian motion concept, the collision between the particles and the solvent molecules causes a certain amount of energy to be transferred, which induces particle movement. The energy transfer significantly impacts smaller particles, inducing smaller particles to move faster than larger particles.

DLS uses a single frequency laser directed to the sample where the interaction of the light with particles results in light scattering in all directions. The scattered light is detected at a certain angle over a specific time interval to monitor the movement of the particles. The intensity of the scattered light fluctuates over time, in which smaller particles that move faster than larger particles show faster fluctuation. However, larger particles show higher amplitudes between the minimum and maximum scattering intensities. Generally, the initial intensity trace is used to create a correlation function that describes the time a particle spent at the same location within the sample [205]. As shown in **Figure 2.2**, the correlation function is linear at the beginning of the measurement, indicating that the particle is still at the same location within the sample. Later, an exponential decay can be observed, indicating the particle's movement. This decay reflects the time spent by the particles to change their relative locations where small particles move quickly, so the decay is fast, unlike large particles. Hence, the size-dependent movement is included in the decay of the correlation function [205]. Therefore, the diffusion coefficient can be calculated from the correlation function using Eq. (2.5), where Γ is the decay constant, D_t is the translational diffusion coefficient, and q is the scattering vector [206].

$$\Gamma = D_t q^2 \qquad \text{Eq. (2.5)}$$

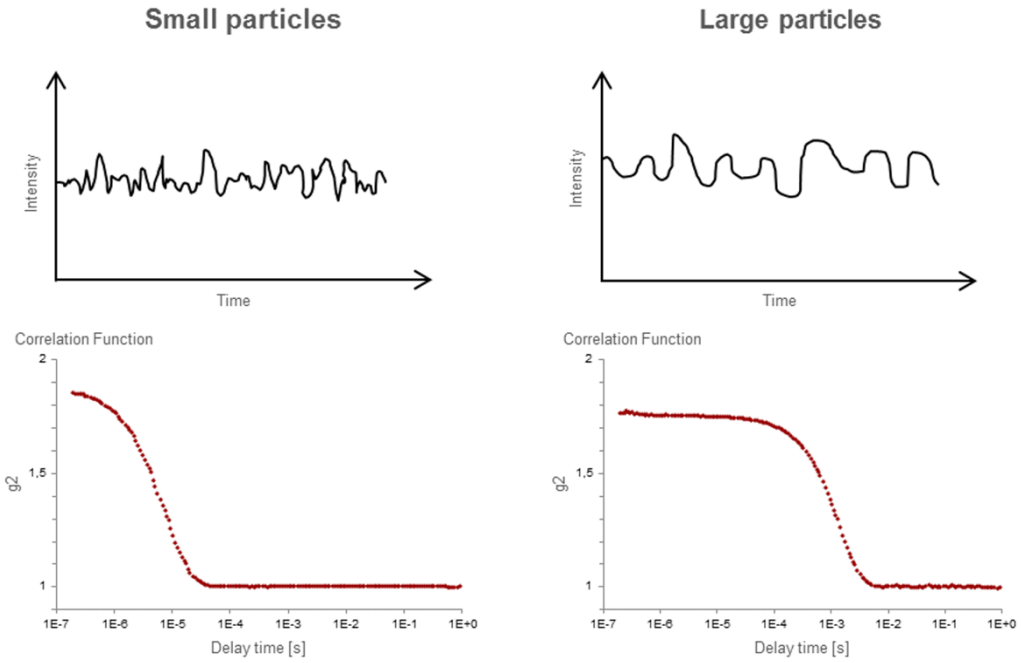

Figure 2.2: Differences in the intensity trace and correlation function of small and large particles obtained by DLS (reprinted with permission from reference [205]).

In this study, DLS was used to measure the mean particle size (Z-AVG), Number (PSD) and polydispersity index (PDI) (Zetasizer Nano, Malvern instruments Ltd, Malvern, UK). The dispersant (medium) was set to water with viscosity (cP) of 0.8872 with an equilibration temperature of 25 °C and PLGA refractive index of 1.4 [207].

2.7.5 Zeta-potential

Zeta-potential (Zeta-p) governs the degree of repulsion between the particles; hence, it offers information about the system's stability. Thus, high zeta-potential suggests that the repulsion forces exceed the attractive forces and thus, particles remain monodispersed within the system without significant aggregation. Zeta-potential is measured by electrophoresis, defined as the movement of a charged particle relative to liquid (dispersant medium) under the influence of an applied electric field [204]. This electrophoretic mobility is governed by the zeta-potential, the viscosity of the medium, dielectric constant of the medium and field strength [204]. In this study, the zeta-potential of all formulations was measured using Zetasizer (Zetasizer Nano, Malvern instruments Ltd, Malvern, UK) after diluting the samples 1:1 in 1mM NaCl.

2.7.6 Transmission electron microscopy (TEM)

Transmission electron microscopy (TEM) is the most widely used technique for nanoparticles characterisation in electron microscopy techniques. TEM provides high-resolution images that can reach down to several angstroms (almost 0.19 nm) [208]. The working principle of TEM relies on emitting electrons that transfer through a vacuum in the microscope column to pass through the specimen and impact the detector [208]. Therefore, TEM has more advantageous for NPs characterisation when compared to scanning electron microscopy (SEM) as it provides precise particle size in both bright field and dark field images besides providing detailed information regarding the NPs morphologic, crystallographic and compositional characteristics [208]. In this study, a JEOL JEM2010 200 kV transmission electron microscope (TEM) (JEOL, Japan) was used to analyse the morphologies of NPs. 10 µl of each sample was placed on the grid for 1 min, and the excess suspension was dried using a filter paper before staining the grid with phosphotungstic acid (2%, pH 6.8) to contrast the sample.

2.7.7 Scanning electron microscopy (SEM)

Scanning electron microscopy (SEM) is a versatile imaging technique for micro and nanostructures, providing information about the topography and composition of the surface[208]. The working principle of SEM relies on generating accelerated electrons using the electron gun, forming a beam that is demagnetised and focused into the sample. Therefore, SEM is considered a surface-imaging method for reflecting atomic composition and topography detail by generating signals associated with sample interaction [208]. In this study, the imaging was performed with a Gemini 300 series emission microscope (Zeiss, Germany). Images generated using 10 kV acceleration voltage. Samples were prepared by conventional Au sputter coating parameters: 30sec at 2.2 kV and 20mA. The sample is 55 mm from the gold target (Polaron SC 7640, Quorum Technologies, UK).

2.8 Preparation and purification of pDNA

pEGFP-C1 plasmid DNA was transformed into *Escherichia coli* strain DH5α. The transformed bacterial cells were propagated overnight in LB medium. The cells were pelleted, and the plasmid was extracted using NucleoBond® Xtra Midi kit plasmid purification kit (Fisher Scientific, UK) according to the manufacturer's procedure. The amount and the purity of the plasmid was assayed using gel electrophoresis and spectrophotometer Nanodrop at A260/280 and A260/230 ratios.

2.9 Encapsulation efficiency studies

2.9.1 pEGFP-C1 encapsulation efficiency

The encapsulation efficiency of pEGFP-C1 into PLGA-Eudragit NPs was assayed by agarose gel electrophoresis. This procedure was used by several studies to assay the pDNA encapsulation efficiency into the NPs since loaded pDNA will be confined to the well and will not migrate through the gel, unlike free unloaded pDNA [6,151]. In this study, the PLGA-Eudragit NPs prepared using the CB and MF nanoprecipitation methods were loaded with pDNA at different mass ratios in Nuclease-free water. Briefly, different amounts of the NPs formulations (9, 7, 5, 2.5, 1.3 µg) were mixed with a fixed amount of pDNA (0.3 µg). All the samples were made up to 10µl using Nuclease free water. Samples were mixed at room temperature and vortexed for 10 seconds, then incubated for 10 (min) before being electrophoresed on 1% agarose gel at 100 V for 60 (min). Image J was used for band intensity integration to determine the amount of the unbound DNA represented by the band intensity.

2.9.2 miRNA-140 encapsulation efficiency

The miRNA-140 encapsulation efficiency into PLGA-Eudragit NPs was assayed qualitatively by gel electrophoresis and quantitatively using a spectrofluorometer. The gel was imaged by (Image Quant LAS 4000, UK). This was performed based on a literature procedure with slight modifications [209]. Briefly, the formulation (1 mL) was centrifuged at 13,000 RCF for 20 (min), then the supernatant was removed, and the pellet was dissolved in 250 µl of an aqueous solution of SDS (1 % w/v) (Sigma Aldrich, UK). To each 20 µl sample, 3 µl of 6x gel loading dye were added. 20 µl of the complexes were then loaded onto 3% agarose gel in Tris-acetate-EDTA (TAE) buffer against a control of 5'Cy5-miRNA-140. Electrophoresis was run at 100 V for 30 (min) and imaged by (Image Quant LAS 4000, UK) using the following conditions:

- Method: fluorescence
- Option: CY5
- Light: Red (630nm Epi)
- Filter: R670
- Iris: F0.85
- Exposure time: 22 seconds

To quantify the encapsulated 5'Cy5-miRNA-140, a standard curve was prepared based on the dye fluorescence (649/670) using FS5 Spectrofluorometer (Edinburgh Instruments, UK). The conditions on the device were set as follows:

- emission scan from 654 nm to 750 nm
- step scan equals 1 nm
- Dwell time equals 0.2 min
- Bandwidth equals 3

To assay the encapsulation efficiency (EE%), 50 µl of the formulation was centrifuged at 13,000 RCF for 20 (min). Then the supernatant was removed, and the pellet was dissolved in 500 µl of acetone to be assayed on the spectrofluorometer. The encapsulation efficiency was calculated using Eq. (2.6):

$$\text{EE\%} = \frac{\text{mass of encapsulated 5'Cy5 miRN140}}{\text{mass of total 5'Cy5 miRNA140 used for encapsulation}} \times 100 \qquad \text{Eq. (2.6)}$$

2.10 Evaluating the impact of cell culture process parameters on pDNA transfection efficiency (GFP%) into A549 cells using transfection reagents and Eudragit-PLGA NPs

In this study, the transfection efficiencies of the transfection reagents and Eudragit-PLGA NPs were estimated by the assay of the transfection of the pEGFP-C1 reporter gene in A549 using fluorescent cells imaging. To ascertain the optimal conditions for achieving the highest transfection efficiency, several factors, including serum concentration in the transfection medium, cells seeding density and the choice of the optimal transfection reagent as a positive control, were screened **(Figure 2.3)**. A naked pDNA was used in these experiments as a negative control. The transfection efficiency was estimated by counting the number of green fluorescent protein (GFP) positive cells from a total of 100 cells to calculate the GFP %. Images were taken using (Zen 2.6) software and analysed using Image J (FIJI) software.

First, to examine the impact of serum on pDNA transfection efficiency, A549 cells were seeded in 1×10^5 (cells/well) density. Then, at 70% confluency, cells were transfected with pDNA using FuGENE HD (Fisher Scientific, UK): pDNA 3:1 ratio using different transfection mediums, including serum-free RPMI media, 1% serum RPMI media and Opti-MEM reduced serum medium (Thermo Fisher scientific, UK). After 6 (h) of transfection, the transfection medium was removed, and cells were washed with 7.4 PBS and incubated in Full RPMI media

(10% FBS, 1% L-glutamine, 1% penicillin-streptomycin) for 24 (h). After then, cells were washed with 7.4 PBS to be analysed by fluorescent microscope (Zeiss Axiovert 200M).

Second, to determine the optimal seeding density, a transfection study using FuGENE HD: DNA 3:1 was conducted using Opti-MEM reduced serum medium and two different seeding densities (1×10^5 and 5×10^4 (cells/well)). At 70% confluency, cells were transfected then treated in the same way mentioned above to be analysed by the fluorescent microscope.

Third, the choice of the transfection reagent and the optimisation of the transfection reagent: DNA ratio are among the essential prerequisites for achieving high transfection efficiency. Hence, FuGENE HD: DNA 3:1, FuGENE HD: DNA 4:1, Lipofectamine 2000: DNA 1:1, Lipofectamine 2000: DNA 2.5:1 and Lipofectamine 2000: DNA 5:1 were compared to ascertain the transfection reagent with the highest transfection efficiency and cells viability. Fixed cell seeding density of 1×10^5 (cells/well) and Opti-MEM reduced serum medium as transfection medium were used, and cells were treated with the same protocol mentioned above.

Finally, to test the potential of Eudragit-PLGA NPs prepared by CB and MF methods in delivering pDNA into A549 cells, a transfection study was conducted using 1×10^5 (cells/well) seeded on sterile coverslips, and Opti-MEM reduced serum medium at 70% confluency. A NP: DNA mass ratio of 2.5:0.3 was used for the transfection study due to its low toxicity and favourable stability profile. After 6 (h) of transfection, the transfection medium was removed, and cells were washed with 7.4 PBS and incubated in Full RPMI media (10% FBS, 1% L-glutamine, 1% penicillin-streptomycin) for 24 (h). After that, the cell's nucleus was stained with DAPI stain to provide a vivid contrast and visualise the morphology of the nucleus.

Staining the nucleus with 4',6-diamidino-2-phenylindole (DAPI) solution (Thermo Fischer, UK) was done as follow. After 24 (h) of transfection, cells were washed with 7.4 PBS then fixed using 4% paraformaldehyde (PFA) for 10 (min). PFA was removed after then, and cells were washed twice with 7.4 PBS. DAPI working solution was prepared with a concentration of 1 (μg/ml) in 7.4 PBS, and 50 μl was added to each coverslip. Samples were then incubated

for 10 (min) after being covered with aluminium foil to protect them from light. Samples were then washed with 7.4 PBS and mounted on slides to be imaged by the fluorescent microscope.

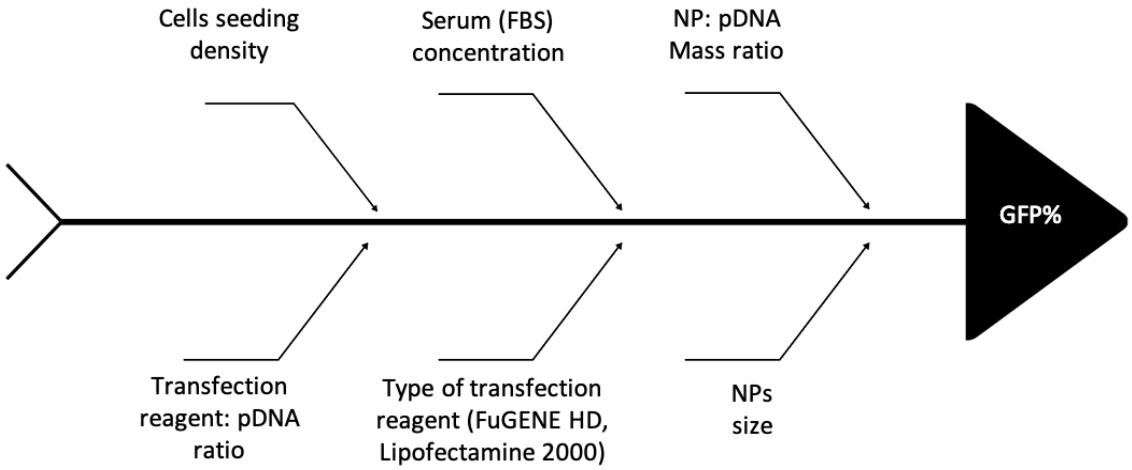

Figure 2.3: Cell culture process parameters with direct impact on pDNA transfection efficiency (GFP%).

2.11 Evaluation of pDNA-loaded PLGA-Eudragit NPs transfection efficiency in A549 and LLC-PK1 by live cell imaging and flow cytometry

Flow cytometry is a technology used for detecting, measuring and analysing various physical characteristics of a single component, usually cells [210]. These properties include relative size, internal complexity or relative granularity, and fluorescent intensity [210]. This is mainly achieved using the flow cytometer's optical-to-electronic coupling setup consisting of fluidics, optics, and electronics. The fluidics system is where the cells are injected into a stream of the sheath fluid and directed to the laser beam for interrogation. The optics system has lasers to illuminate the particles/cells in the stream and optical filters for directing the scattered light signals to the appropriate detectors. Later, the electronics system converts the light signals into electronic signals that can be processed by the computer [210].

Fundamentally, each cell within the stream is excited by the laser beam at a point known as the interrogation point, leading to light scattering and fluorescence. The light scattered in the forward direction is detected by the forward scatter channel (FSC), where the scattering intensity depends on the membrane permeability of the cell and its size and the refractive index.

However, the light scattered at 90° is detected by a side scattering channel (SSC), where the scattering intensity depends on the internal complexity of the cell. Therefore, forward and side scattering measurements allow cell differentiation based on cell size and internal complexity [210]. Additionally, the flow cytometer can be used to detect the number of fluorochrome molecules in each cell using a detector with appropriate fluorescence emission settings where the intensity is proportional to the number of fluorochrome molecules in each cell [210].

In this study, a flow cytometer was used to explore the efficiency of the NPs in delivering pDNA to different cell types and widen the comparison between PLGA-Eudragit NPs prepared by CB and MF methods. Transfection studies were conducted in A549 and LLC-PK1 cells using 1×10^5 (cells/well) seeding density and Opti-MEM reduced serum medium with Lipofectamine 2000: DNA 1:1 ratio as a positive control and naked pDNA was used as a negative control. For PLGA-Eudragit NPs, a NPs: DNA mass ratio of 2.5:0.3 was used since it was found optimal for comparing the NPs prepared by the two methods.

Generally, A549 and LLC-PK1 cells were seeded in 24 well plates at a density of 1×10^5 (cells/well) in 1 mL of RPMI 1640 culture medium 24 (h). At 70-80% confluency, cells were washed with PBS (pH 7.4) and incubated in 5% CO_2 incubator at 37° C for 6 (h) with 500 µl of Opti-MEM containing pDNA loaded PLGA-Eudragit NPs at a NP: DNA mass ratio of 2.5:0.3. After that, cells were washed with PBS and medium was replaced with 1 mL of full RPMI culture medium, then incubated for 24 (h) at the same conditions. Transfection efficiency experiments were carried out in triplicate. 24 (h) after the transfection, cells were washed with PBS to be further analyzed by flow cytometry and fluorescent microscope (Zeiss Axiovert 200M). Images were taken using (Zen 2.6) software and analyzed using Image J (FIJI) software.

To prepare the samples for flow cytometry, cells were washed with 7.4 PBS, then trypsinized for 5 (min) and resuspended in full culture medium. Cells were then centrifuged at 400 x*g* for 5 (min), and the pellets were resuspended in 1% bovine serum albumin (BSA) (Sigma Aldrich, UK) in 7.4 PBS. Cells were then analysed on a Beckman Coulter CytoFlex flow cytometer. Data were analyzed using CytExpert software (v2.3, Beckman Coulter, USA), and results are expressed as a percentage of positive cells transfected by NPs and Lipofectamine 2000

compared to cells treated with (naked DNA) negative control. An example of the gating strategy used in the study is shown in **Figure 2.4**.

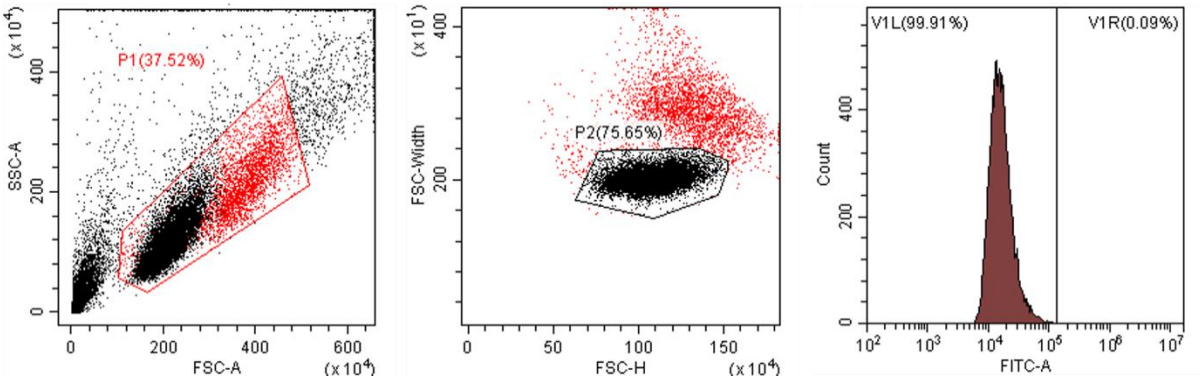

Figure 2.4: A549 gating strategy used in this study. FSC is forward scattered channel, SSC is side scattered channel and FITC-A is Fluorescein isothiocyanate channel for GFP detection.

2.12 Cytotoxicity of NPs assayed by MTT assay and propidium iodide

The MTT assay is a colorimetric assay that is widely used to measure the cells' metabolic activity. This test relies on the ability of the nicotinamide adenine dinucleotide phosphate (NADPH)-dependent cellular oxidoreductase enzymes to reduce the tetrazolium dye (MTT) into its insoluble purple formazan [211]. Generally, a solubilization solution (dimethyl sulfoxide or acidified ethanol solution) is used to dissolve the insoluble purple formazan into a coloured solution that can be quantified by measuring at a specific wavelength (usually between 500 and 600 nm) by a spectrophotometer [211].

For PLGA-Eudragit NPs prepared by the two methods, cytotoxicity of the blank NPs was tested on two cell lines: A549 and LLC-PK1 cell. Cells were seeded into 96-well plates at a density of 1×10^5 (cells/well) in 200 µl of culture medium then incubated in 5% CO_2 incubator at 37° C overnight. The culture medium was then replaced with Opti-MEM reduced serum medium containing different concentrations of PLGA-Eudragit NPs (3.125, 6.25, 12.5, 25, 50 and 100 µg/mL). Lipofectamine 2000 and 10 %v/v Triton X-100 were used in comparison. After incubating the cells for 24 (h), the media was replaced with fresh RPMI 1640 media containing 0.4 (mg/mL) of MTT reagent (Sigma Aldrich, UK). The plate was then incubated at 37° C for 90 (min) before the medium was replaced by 200 µl of Dimethyl sulfoxide (DMSO) to dissolve the formazan crystals. The plate was finally read at 570 nm by Spectramax M2 microplate reader (Molecular Devices, US). Data was collected as triplicate measurements from three biological replicates. Results are shown as the mean ± standard deviation.

The toxicity of pDNA loaded PLGA-Eudragit NPs was assessed by flow cytometry using propidium iodide (PI) (Sigma Aldrich, UK) to identify the percentage of dead cells 24 (h) after transfection. Cells were trypsinized and resuspended in 1% BSA containing 3.32 (µg/mL) PI. Cells were analyzed in triplicates using a Beckman Coulter CytoFlex flow cytometer. Results are expressed as a percentage of PI-positive cells to the total number of cells treated by NPs and Lipofectamine 2000 compared to cells treated with (naked DNA) negative control. Data were collected as triplicate measurements from three biological replicates. The data shown represent the mean ± standard deviation.

The cytotoxicity of miRNA-140 loaded PLGA-Eudragit NPs on C28/I2 chondrocytes was assayed by MTT assay using the same protocol.

2.13 Assaying the release of 5'Cy5-miRNA-140 and the stability of the formulation

To assay the release of 5'Cy5-miRNA-140 in 7.4 PBS, the total formulation (1 mL) was distributed in aliquots of 50 µl sample in each Eppendorf tube. The samples were then centrifuged at 13,000 RCF for 20 min, where the supernatant was then removed, and the pellet was resuspended in 400 µl of 7.4 PBS. Samples were incubated at 37 °C in a shaking incubator. A sample was dissolved in 500 ul of acetone to be used as the 100% release value (Reference point). At each assigned time point, the sample was centrifuged using the same conditions. The supernatant was then discarded, and the pellet was dissolved in 50 ul of acetone to be measured on the spectrofluorometer.

To check the storage stability of the formulation in terms of the 5'Cy5-miRNA-140 retention, the total formulation was distributed in 50 µl aliquots in each Eppendorf tube and kept in the fridge. At each assigned time point, the sample was centrifuged using the same conditions, where the supernatant was then removed, and the pellet was dissolved in 500 µl of acetone. Samples were then measured spectrofluorometrically to examine any change in the miRNA-140 EE% over the storage time.

2.14 Stability of 5'Cy5-miRNA-140 loaded PLGA-Eudragit NPs

To test the colloidal stability of the 5'Cy5-miRNA-140 loaded PLGA-Eudragit NPs at physiological conditions, the NPs stability was tested in 7.4 PBS, Opti-MEM serum reduced medium and bovine synovial fluid for one week. This was done by diluting the NPs down to

100 µg/mL using 7.4 PBS, Opti-MEM reduced serum medium and bovine synovial fluid provided by Dr Steven Cutts. Samples were left in the fridge for a week, and at each assigned time point, the sample was measured on DLS to check the colloidal stability.

2.15 Transfection of 5'Cy5-miRNA-140 into C28/I2 using Lipofectamine RNAiMAX

The transfection was performed using the manufacturer's protocol. Briefly, 1×10^5 cells were seeded in each well of 6 well plate. Next, 24 picomoles of 5'Cy5-miRNA-140 were diluted in 250 µl of Opti-MEM reduced serum medium, as shown in **Table 2.3**. Then, 5 µl of RNAiMAX (Thermo Fischer Scientific, UK) was diluted up to 250 µl using Opti-MEM serum reduced medium. The tubes were then combined, mixed gently and incubated at room temperature for 20 (min). Finally, the 5'Cy5-miRNA-140 lipid complex (500 µl) was added to each well, and the volume was made up to 2 mL using Opti-MEM serum reduced medium (concentration of 5'Cy5-miRNA-140=12nM). Cells were then incubated in 5% CO2 at 37° C for 6 (h). The transfection medium was then replaced with full DMEM media, and cells were incubated for 24 (h). This protocol was used to check the delivery of 5'Cy5-miRNA-140 by fluorescent imaging techniques and will be referred to as **protocol 5.1**. **Table 2.3** shows the amounts of 5'Cy5-miRNA-140 used to achieve different concentrations in the transfection medium using 48 well plate. This protocol was used to study the biological activity of the 5'Cy5-miRNA-140 delivered by Lipofectamine RNAiMAX in downregulating FZD6 using qPCR and will be referred to as **protocol 5.2**.

Table 2.3: 5'Cy5-miRNA-140 transfection protocol using Lipofectamine RNAiMAX in 48 well plate

Cells seeding density (cells/well)	**Lipofectamine RNAiMAX volume in 20 µl Opti-MEM (µl)**	**Transfection medium volume in each well (µl)**	**Picomoles of 5'Cy5-miRNA-140 in 20 µl Opti-MEM (Picomoles)**	**Concentration of 5'Cy5-miRNA-140 in the transfection medium (nM)**
15×10^3	0.4	200	10	50
			5	25
			2.4	12
			0.8	4
			0.4	2
			0.2	1

2.16 Transfection of 5'Cy5-miRNA-140 loaded PLGA-Eudragit NPs into C28/I2 cells

For 5'Cy5-miRNA-140 loaded PLGA-Eudragit NPs transfection, 1×10^5 cells were seeded in each well of 6 well plate then transfected when reaching 70% confluency. For transfection, the original NPs concentration (10 mg/mL) was diluted to different concentrations using Opti-MEM serum reduced medium to ensure the delivery of a range of 5'Cy5-miRNA-140 concentrations into the cells. **Table 2.4** shows the details of the transfection protocol employed with 5'Cy5-miRNA-140 loaded PLGA-Eudragit NPs, including formulations A and B. The concentration of 5'Cy5-miRNA-140 in the transfection medium was estimated based on the encapsulation efficiency studies.

Cells were incubated in 5% CO_2 at 37° C for 6 (h) post the transfection. The transfection medium was then replaced with full DMEM media, and cells were incubated for 24/48 (h) based on the experiment as explained in the following sections.

Table 2.4: 5'Cy5-miRNA-140 loaded PLGA-Eudragit NPs transfection protocol using 6 well plate

NPs formulation code	Transfection medium volume in each well (mL)	Concentration of NPs in the transfection medium (µg/mL)	Concentration of 5'Cy5-miRNA-140 in the transfection medium (nM)
A	2	50	4
		25	2
		12.5	1
B	2	100	24
		50	12
		25	6

2.17 Observing the delivery of 5'Cy5-miRNA-140 using inverted fluorescent and confocal microscopy

To examine the delivery of 5'Cy5-miRNA-140 by Lipofectamine RNAiMAX and NPs, cells were imaged based on the CY5 fluorescence using an inverted fluorescent and confocal microscopy. To image the cells using the confocal microscope (ZEISS LSM 980), cells were

seeded on sterilised coverslips and transfected by Lipofectamine RNAiMAX **(protocol 5.1)** and NPS as detailed in **sections 2.15 and 2.16**. After 24 (h) of incubation, the medium was removed, and cells were washed with 7.4 PBS. After that, the coverslips were removed carefully and placed in the confocal imaging chamber. Then, 7.4 PBS was added gradually into the chamber to cover the coverslip. The conditions used on the confocal microscope to image the 5'Cy5-miRNA-140 were as follows:

- Master gain: 850 V
- Digital gain: 15
- Objective lens: 40X oil

To examine the distribution of 5'Cy5-miRNA-140 delivered by NPs or Lipofectamine RNAiMAX between the lysosomes and the cytoplasm, a green lysotracker was used to label the lysosomes. To do this, cells were seeded on sterilised coverslips and transfected by Lipofectamine RNAiMAX **(protocol 5.1)** and NPS, as detailed in **sections 2.15 and 2.16**. After 24 (h) of incubation, the medium was removed, and cells were washed with 7.4 PBS. Then to each well, 0.5 µl of the LysoBrite^{TM} green, a gift from Dr Paul Thomas (University of East Anglia), was added to 500 µl of DMEM/F-12, HEPES, no phenol red (Thermo Fischer Scientific, UK) prewarmed media. Cells were then incubated for 10 (min), then the medium was removed, and cells were washed with 7.4 PBS. Finally, the coverslips were removed carefully and placed in the confocal imaging chamber. 7.4 PBS was added gradually to cover the coverslips, and imaging was done using the confocal microscope.

2.18 RNA and miRNA extraction and real-time reverse transcription PCR

These experiments were done by Paige Paddy (University of East Anglia). Briefly, total RNA was extracted from the transfected C28/I2 cells using Qiagen miRNeasy kit (Qiagen, Crawley, U.K.) in compliance with the manufacturer's instructions. For quantifying the miRNA-140 level, RNA was reverse-transcripted into cDNA using miRCURY LNA miRNA PCR kit (Qiagen, UK) according to the manufacturer's procedure. The U6 snRNA miRCURY LNA miRNA PCR Assay (Qiagen, UK) was used to detect and quantify mature miRNA-140 according to the manufacturer's instructions.

For quantifying FZD6, MMP-13 and ADAMTS5, RNA was reverse-transcripted into cDNA using SuperScriptTM II Reverse Transcriptase (Thermo Fischer Scientific, UK) according to the manufacturer's procedure. Then, TaqMan RT-PCR was performed, and gene expression

levels were calculated as described in the literature using the delta-delta Ct method [184,212]. The 18S rRNA gene was used as an endogenous control (housekeeping gene) to normalise for differences in the amount of total RNA present in each sample. All values are presented as the mean ± SD of replicates. Primer's design and probes used are shown in **Table 2.2**.

2.19 Examining the downstream effect of the delivered 5'Cy5-miRNA-140 on the FZD6 protein level using western blotting

Bicinchoninic acid (BCA) assay was done to determine the protein concentration according to the manufacturer's procedure (Thermo Fischer Scientific, UK). Western blotting was done by Dr Chris Morris (University of East Anglia). Briefly, 4-16% PAGE gel was used with 25 µg total protein load. Anti-FZD6 produced in rabbit (primary antibody) was purchased from (Merck Sigma, UK). Anti-rabbit IgG, HRP-linked Antibody (secondary antibody) was purchased from (Cell Signalling Technology, UK).

2.20 Investigating the efficiency of 5'Cy5-miRNA-140 loaded PLGA-Eudragit NPs in downregulating *FZD6, MMP-13* and *ADAMTS5* in 3D micromass cell culture treated with IL-1β using qPCR

This study aims first to examine the impact of IL-1ß (Peprotech, UK) on the expression of *FZD6, MMP-13* and *ADAMTS5*. Second, check the efficiency of 5'Cy5-miRNA-140 loaded PLGA-Eudragit in downregulating the overexpressed genes to restore homeostasis. This experiment was conducted using the following procedure:

1. Micromass were cultured as explained in **section 2.4.4** with slight modifications. Briefly, following a 3 (h) attachment period without medium, full DMEM media was gently added, and cultures were left resting for a further 24 (h). After then, the medium was replaced with 1x ITS medium in prewarmed DMEM/F-12 (+HEPES, -phenol red) media containing 20 ng/mL of (IL-1ß) and cells were incubated for another 24 (h).
2. Cells were then transfected with Lipofectamine RNAiMAX delivering 12 nM of 5'Cy5-miRNA-140 (positive control).
3. Cells were transfected with 50 µg/mL of 5'Cy5-miRNA-140 loaded PLGA-Eudragit NPs delivering 12 nM of 5'Cy5-miRNA-140 (Formulation B).
4. Six (h) post-transfection, the transfection medium was removed, and cells were washed with 7.4 PBS. Then full DMEM media was added to each well, and cells were incubated

for 48 (h). The delivery of 5'Cy5-miRNA-140 by lipofectamine RNAiMAX and PLGA-Eudragit NPs into 3D C28/I2 micromass cell culture was checked using the inverted fluorescent microscope. Images were captured using brightfield and CY5 channels (630 nm) using a 20x objective lens

5. Finally. The RNA extraction and qPCR were then performed by Paige Paddy (University of East Anglia), as explained in **section 2.18**.

2.21 Statistical analysis

Data were analysed using GraphPad software. All measurements were carried out in triplicate, and the given values represent the average ± SD. Unpaired t-test was used to evaluate the significance of the difference between the means of two variables. Statistically significant differences were attributed to ($P < 0.05$).

Chapter 3

New insights from examining the impacts of nanoparticle's synthesis method on the physicochemical properties of polymeric nanoparticles

3.1 Introduction

Polymeric nanoparticles (PNPs) have been extensively used in biomedical applications due to their favourable properties such as size tunability, biocompatibility, and ability to be modified by surface ligands [13,17,52]. Surface modification of PNPs with cationic compounds such as polysaccharides (Chitosan), polymethacrylates (Eudragit) and polyethyleneimines (PEI) has been extensively applied to improve PNPs gene transfection efficiency or mucoadhesive properties [150,213]. The application of the PNPs depends on their physicochemical properties, including size, surface charge, morphology and composition. Controlling the physicochemical properties of PNPs plays a pivotal role in determining their drug loading capacity, in vivo distribution and cellular uptake [13,133,214]. As discussed in **chapter 1**, the nanoprecipitation (solvent displacement) method is among the most used bottom-up methods for synthesising PNPs due to its simplicity and ease of scalability [12].

Nanoprecipitation (solvent displacement) method is mainly driven by homogenous nucleation [17]. However, the uniformity and rate of nucleation achieved with the solvent displacement method are controlled by the efficiency of mixing the solvent phase containing the polymer and the anti-solvent aqueous phase [15]. Due to the importance of the mixing step in nanoparticles (NPs) fabrication, microfluidics technology (MF) was employed to develop controllable and improved mixing to fabricate smaller and tuneable NPs [57]. To advance this method and expand its applications, there have been several studies in the literature focused on probing the relationship between the mixing time and the size of the resulting NPs [57,64,215]. Microfluidics technology and fluid dynamics simulation software were used simultaneously as an integrated approach to predict and control the size of the resulting NPs [215]. Most of these studies have relied on the diffusivity of the organic solvent for calculating the mixing time; however, several questions regarding the appropriate use of the mixing time to predict the size of the NPs and the accurate employment of the organic solvent diffusion coefficient remain to be addressed.

Currently, the throughput rate and costs associated with the microfluidic-assisted nanoprecipitation (MF-method) compared to the conventional bulk nanoprecipitation (CB-method) is still arguable. Therefore, it is essential to investigate and establish any additional potential therapeutic advancement that may be achieved by NPs prepared by the MF-method.

The objectives of this chapter are:

- To reveal the advantages and limitations of microfluidic technology for nanoprecipitation compared to the conventional bulk method by investigating the effect of the processing parameters of each synthetic method (CB/MF method) on the properties of PLGA NPs.
- Provide new insights into the impact of the mixing time on the resulting NPs properties and the limitations of the available simulation models used for calculating the mixing time and predicting the NPs properties.
- Explore the potential of microfluidics in modifying the surface of PLGA NPs with Chitosan/Eudragit compared to the CB-method.

3.2 Materials and methods

3.2.1 Materials

Microfluidics chips (3D Flow Focusing straight channel Chip - 100μm – Hydrophilic, Droplet Junction straight channel Chip (190μm etch depth), 100μm Micro Mixer chip were all purchased from (Dolomite Microfluidics, UK). Harvard syringe pumps (standard infuse/withdraw pump 11 Elite) were purchased from Harvard Apparatus (US).

3.2.2 Investigating the effect of the processing parameters on PLGA NPs properties

In this study, several parameters were investigated to assess their impact on the properties of NPs **(Figure 3.1a)**. For NPs prepared by CB-method these parameters include the effect of:

- Degree of supersaturation (DOS) studied by changing the polymer concentration or the solvent/antisolvent volume ratio (S/AS VR).
- Type of organic solvent (acetone/acetonitrile).
- Viscosity of the organic solvent.
- Molecular weight of PLGA.

To directly compare the impact of the synthesis method (CB/MF) on the properties of NPs, a group of processing parameters were examined for MF-method **(Figure 3.1b).** These parameters include:

- Polymer concentration.
- Flow rate ratio (FRR= flow rate of organic solvent/flow rate of aqueous solvent).
- Total flow rate (TFR= flow rate of solvent and antisolvent/minute).
- Addition of stabilisers.
- Viscosity of the organic solvent.
- Chip design/geometries.

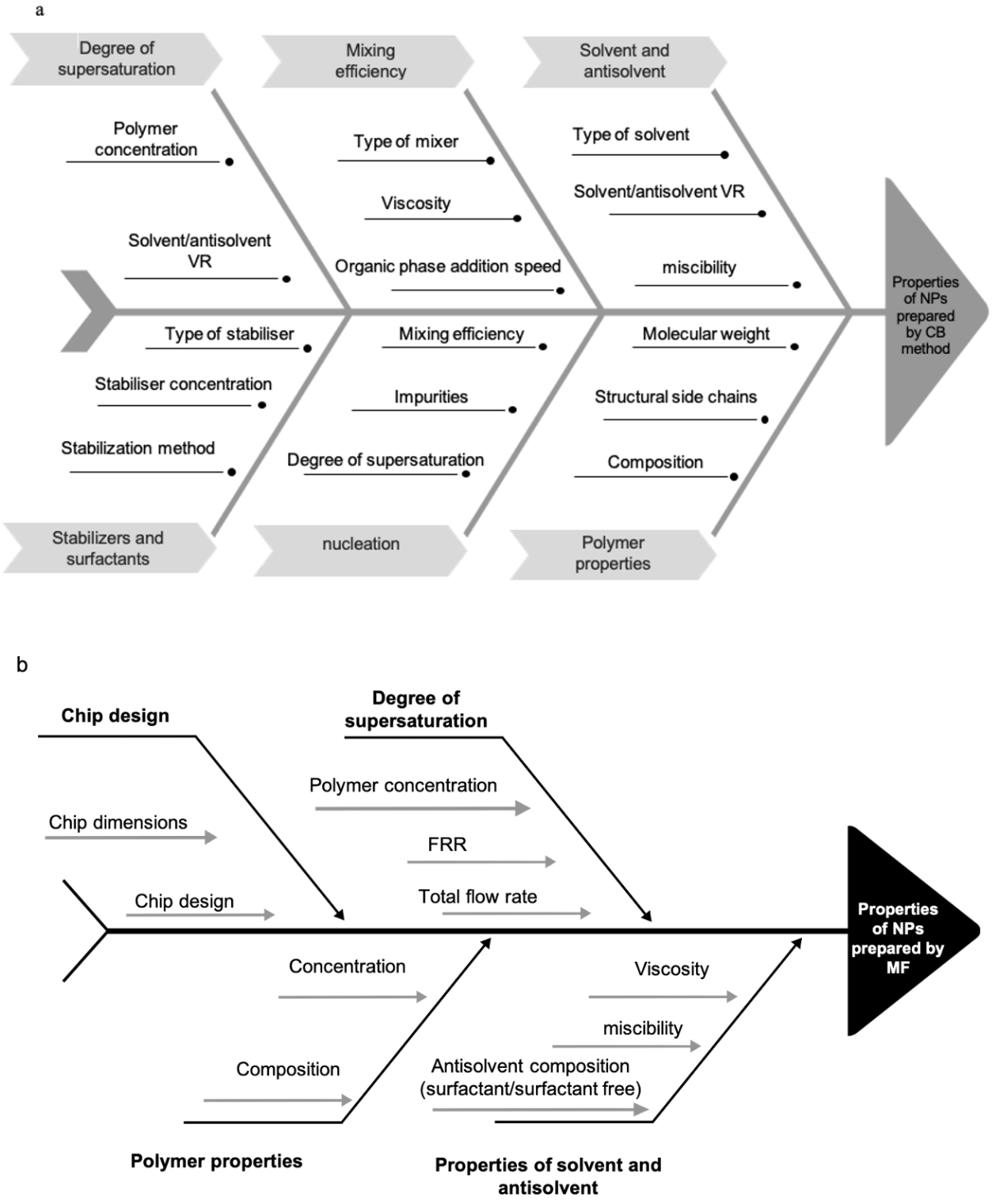

Figure 3.1: Investigating the effect of the processing parameters on the properties of the NPs prepared by (a) conventional bulk nanoprecipitation (CB-method) and (b) Microfluidics assisted nanoprecipitation (MF-method).

3.2.3 Synthesis of PLGA NPs by CB-method and MF-method

PLGA NPs were synthesised by the CB-method using the parameters shown in **Table 3.1**. All the formulations were prepared by dropwise addition of the organic solvent to the aqueous anti-solvent phase (deionized water) with magnetic stirring agitation 300 (rpm) at room temperature. All the formulations were then left on the stirrer for three hours to ensure acetone evaporation.

For PLGA NPs prepared by the MF-method, NPs were prepared using PLGA 50:50 ester terminated (M. wt 38000-54000) (Sigma Aldrich, UK) in acetone as a solvent and deionized water as an antisolvent according to processing parameters shown in **Table 3.2**. For all the formulations, NPs were left on the stirrer for three hours at room temperature to ensure acetone evaporation. The role of stabilisers in reducing the fouling issues and NPs building up inside the 190 µm droplet junction chip when using 1 (mg/mL) of PLGA in acetone as the solvent phase was assessed using 0.5 (w/v%) TPGS (Sigma-Aldrich, UK), 1 (w/v%) tween-80 (Sigma-Aldrich, UK) and 0.5 (w/v%) PVA (Sigma-Aldrich, UK) as the antisolvent phase.

Table 3.1: Processing parameters used to fabricate PLGA NPs using CB-method

Aim of the experiment	**PLGA concentration (mg/mL)**	**PLGA molecular weight (Dalton)**	**Organic solvent**	**S/AS VR**
To study the impact of the polymer concentration in organic solvent	1 5 10 20	38000-54000	Acetone	0.2
To study the impact of solvent/antisolvent volume ratio	1	38000-54000	Acetone	0.2 0.5 1
To study the impact of the M. wt	1	24000-38000 38000-54000	Acetone	0.2
To study the impact of the solvent	1	38000-54000	Acetone Acetonitrile	0.2

Table 3.2: Processing parameters used to fabricate PLGA NPs using MF-method

Aim of the experiment	Chip	PLGA concentration (mg/mL)	Solvent flow rate (µl/min)	Antisolvent flow rate (µl/min)	FRR	TFR (µl/min)
To study the impact of the polymer concentration in organic solvent and FRR	190 µm Droplet Junction straight channel	1	20	100	0.2	120
			50		0.5	150
		3	80		0.8	180
			100		1	200
To study the impact of using higher TFRs	190 µm Droplet Junction straight channel	1	283	119	0.1	402
				283	0.2	566
				354	0.5	637
				566	0.8	849
				1415	1	1698
				2830	2	3113
To study the impact of the chip dimensions	190 µm Droplet Junction straight channel	1	80	100	0.8	180
	100 µm 3D flow focusing straight channel					
To study the impact of the chip design	100 µm 3D flow focusing straight channel	1	80	100	0.8	180
	100 µm Micro Mixer					

3.2.4 Synthesis of PLGA-Eudragit NPs by CB-method and MF-method

For PLGA-Eudragit NPs prepared by CB-method (dropwise solvent addition), the impact of the Eudragit: PLGA mass ratio was initially studied in order to find the optimal mass ratio for preparing monodisperse nanoparticles. Eudragit: PLGA mass ratio ranging between (0:10 to 10:0) with a final polymer blend concentration of 2 (mg/mL) in acetone was used as the solvent phase, and deionized water was used as the antisolvent phase with a S/AS volume ratio of 0.2.

The effect of the final polymer concentration on the NPs properties was tested using concentrations of 2 (mg/mL) and 5 (mg/mL) of 1:1 Eudragit: PLGA in acetone and a S/AS volume ratio of 0.2. 2 (mg/L) of 1:1 Eudragit: PLGA in acetone was used with S/AS volume ratios of 0.2 and 0.5, to examine the effect of the volume ratio on the size of PLGA-Eudragit NPs. To assess the impact of the organic solvent addition method (Dropwise/ Quick addition using micropipette) to the antisolvent phase, 5 (mg/mL) of 1:1 Eudragit: PLGA in acetone was used at S/AS volume ratios of 0.2. All the samples were prepared while stirring at a fixed rate of 300 (rpm) and left for three hours to ensure acetone evaporation.

For PLGA-Eudragit NPs prepared by MF-method, a 190 µm droplet junction straight channel chip was used. 2 (mg/mL) and 5 (mg/mL) of 1:1 Eudragit: PLGA in acetone were used as the solvent phase, and deionized water was used as the antisolvent phase. The flow rate of the solvent phase was set to 283 (µl/min), while the flow rate of the anti-solvent was varied from 566 (µl/min) to 404 (µl/min) to achieve flow rate ratios of 0.5 and 0.7, respectively.

The impact of the chip design was further investigated by comparing the properties of the NPs prepared using 2 (mg/mL) 1:1 Eudragit: PLGA in acetone as solvent phase and deionized water as antisolvent phase using three chips (3D flow focusing chip 100 µm,190 µm droplet Junction and 100 µm Micro Mixer chip). NPs were left on the stirrer for three hours at room temperature to ensure acetone evaporation for all the formulations.

3.2.5 Synthesis of PLGA-Chitosan NPs by CB-method and MF-method

For PLGA-Chitosan (Qingdao Yunzhou Biochemistry, China), NPs prepared by CB-method (dropwise solvent addition), the following points were studied:

- First, the effect of PLGA concentration in acetone on the properties of NPs using a constant chitosan concentration was tested using 1 and 5 (mg/mL) of PLGA in acetone as the solvent phase and 0.1 (mg/mL) of water-soluble chitosan as the antisolvent phase using S/AS volume ratio of 0.2.

- Second, the influence of chitosan concentration on the properties of PLGA-Chitosan NPs at a constant PLGA concentration was examined using 0.1 and 0.5 (mg/mL) of water-soluble chitosan as the antisolvent phase and 5 (mg/mL) of PLGA in acetone as the solvent phase using S/AS volume ratio of 0.2.

For PLGA-Chitosan NPs prepared by MF-method, a 190 µm droplet junction straight channel chip was used to synthesise NPs. A group of experiments were performed to study the following points:

- The effect of the FRR on PLGA-Chitosan NPs properties was investigated by fixing the antisolvent flow rate to 370 (µl/min) and setting the solvent flow rate to 79 (µl/min) and 185 (µl/min) to achieve FRRs of 0.2 and 0.5, respectively.

- Examine the effect of PLGA concentration on the properties of PLGA-Chitosan NPs at fixed chitosan concentration. 1, 2 and 5 (mg/mL) of PLGA in acetone were used as the solvent phase, and 0.1 (mg/mL) of water-soluble chitosan was used as the antisolvent phase at FRRs of 0.2 and 0.5.

- The effect of chitosan concentration at fixed PLGA concentration was studied using 0.1 and 1 (mg/mL) of water-soluble chitosan as the antisolvent phase and 1 (mg/mL) of PLGA in acetone as the solvent phase at FRR of 0.2.

- the impact of the chip design was further investigated by comparing the properties of the NPs prepared using 1 (mg/mL) of PLGA in acetone as the solvent phase and 0.1 (mg/mL)

chitosan as the antisolvent phase using three chips (3D flow focusing straight channel chip 100 µm,190 µm droplet Junction straight channel chip and 100 µm Micro Mixer chip).

NPs were left on the stirrer for three hours at room temperature to ensure acetone evaporation for all the formulations.

3.2.6 Mixing and residence time calculations

The mixing time of the two phases within the 190 µm droplet junction straight channel chip chips was calculated using Eq. (3.1) [57]. Where D is the diffusivity of acetone (10^{-9} m^2/s)[57], w is the width of the chip (350 µm is the width of the 190 µm droplet junction straight channel chip), R is the S/AS FRR. The residence time of the phases in the 190 µm droplet junction straight channel chip was calculated based on the volume of the channel after the junction (0.74 µl) [49], and the total flow rate (TFR) used, as shown in Eq. (3.2).

$$\tau_{mix} = \frac{w^2}{9D(1+\frac{1}{R})^2} \quad \text{Eq. (3.1)}$$

$$Residence\ time\ (ms) = \frac{60000 \times 0.74}{\text{TFR}} \quad \text{Eq. (3.2)}$$

3.2.7 Freeze drying and stability of NPs

The shelf stability of NPs was tested by measuring NPs size over a week using DLS. The stability of the formulations in 7.4 PBS was tested by diluting the samples 1:50 in 7.4 PBS and incubating them for up to a week to be measured on DLS. To examine the redispersibility index (%) of the formulations, samples made by CB-method were freeze-dried using (VirTis advantage 80 freeze dryer) then resuspended in water/ 7.4 PBS. Samples were centrifuged then resuspended in 5mL of 1% (w/v) trehalose (Sigma-Aldrich, UK) before being freeze-dried. For SEM, TEM and FTIR characterisations, samples were freeze-dried without cryoprotectants. The redispersibility index (%) is given by Eq. (3.3).

$$\text{Redispersibility index} = \frac{\text{Z-AVG of reconstituted NPs}}{\text{Z-AVG size before freeze drying}} \quad \text{Eq. (3.3)}$$

3.3 Results and discussion

3.3.1 Solubility of PLGA in different acetone/water binary mixtures

Figure 3.2 shows the solubility of PLGA in acetone water mixtures over a range of volume ratios of acetone to water. Although the solubility increases with acetone to water ratios, even at 95% acetone to water, it is only about 6 (mg/mL); however, it is more than 95 (mg/mL) in pure acetone. The data was used in the following experiments to explain the impact of the PLGA degree of supersaturation (DOS) achieved with each set of parameters on the properties of PLGA NPs (size/ size distribution). The degree of supersaturation is given by Eq. (3.4).

$$\mathrm{DOS} = \frac{\text{Polymer concentration in the solvent-antisolvent binary mixture}}{\text{polymer equilibrium solubility in the solvent antisolvent binary mixture}} \qquad \text{Eq. (3.4)}$$

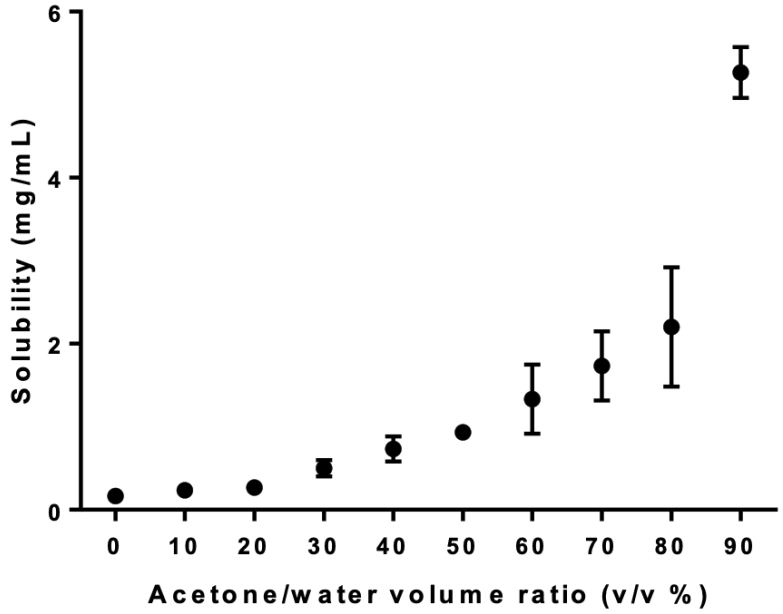

Figure 3.2: PLGA solubility in different acetone/water binary mixtures.

As discussed in chapter 1 **(section 1.3.1)**, a higher degree of supersaturation results in a higher nucleation rate with a subsequent reduction in the resulting NPs size [216]. A detailed discussion for the effect of PLGA DOS on the properties of the NPs is given in the next section **(section 3.3.2)**.

3.3.2 Comparing the physicochemical properties of unmodified PLGA NPs prepared by CB-method and MF-method

As illustrated in **Figure 3.3**, nanoprecipitation is a complex process where a group of operating parameters play a simultaneous role in controlling the size of NPs. As mentioned in the introduction, homogenous nucleation is the underpinning mechanism of NPs formation using the solvent displacement method. It is mainly driven by the polymer degree of supersaturation (DOS) achieved at the mixing stage [217].

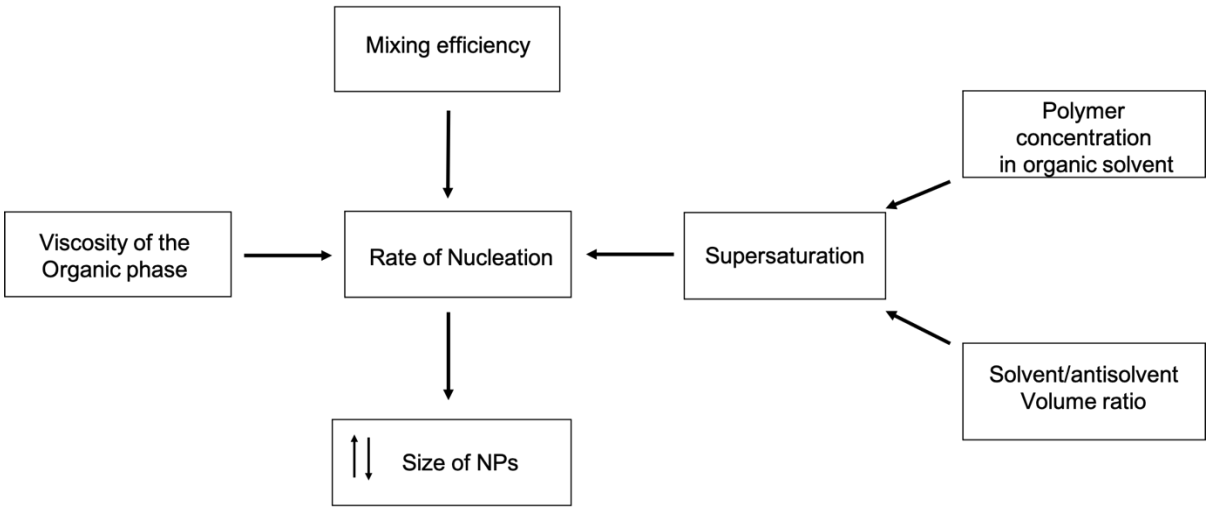

Figure 3.3: Direct and indirect factors controlling the size of PLGA NPs prepared by nanoprecipitation.

The degree of supersaturation can be increased by increasing the polymer concentration in the organic solvent. However, the role of the degree of supersaturation in reducing NPs size is limited and controlled by other parameters such as the viscosity of the binary mixture, as shown in **Figure 3.3**. As shown in **Table 3.3,** the size of NPs can be expressed by Z-AVG or number particles size distribution (PSD). The Z-AVG value is very sensitive to the presence of aggregates in the sample compared to the number PSD value, which explains the smaller size readings obtained from the number PSD value. Increasing PLGA concentration in acetone from 1 (mg/mL) to 20 (mg/mL) resulted in a significant increase ($P < 0.05$) in the size of PLGA NPs (Z-AVG and Number PSD size) as shown in **Table 3.3**. This was further confirmed by TEM as shown in **Figure 3.4 a-c**, in which the average NPs size increased from 54±27 nm when using 1 (mg/mL) PLGA in acetone to 102±35 nm and 124±45 nm with changing the PLGA concentration in acetone to 10 (mg/mL) and 20 (mg/mL), respectively. TEM data were

consistent with the number PSD size obtained from DLS. This trend agrees well with published data [13,29].

Table 3.3*:* Effect of PLGA concentration on the properties of PLGA NPs prepared by CB-method using S/AS volume ratio of 0.2, solubility of PLGA in 16% acetone-water binary mixture is 0.2 (mg/mL)

PLGA Concentration (mg/mL)	Degree of supersaturation	Z-AVG size (nm)	Number PSD (nm)	PDI	Zeta-p (mV)	TEM Size (nm)
1	0.8	88±3	46±4	0.2±0.01	-23±4	54±27
10	8	167±3	136±8	0.08±0.01	-45±1	102±35
20	17	212±3	185±3	0.07±0.01	-63±4	124±45

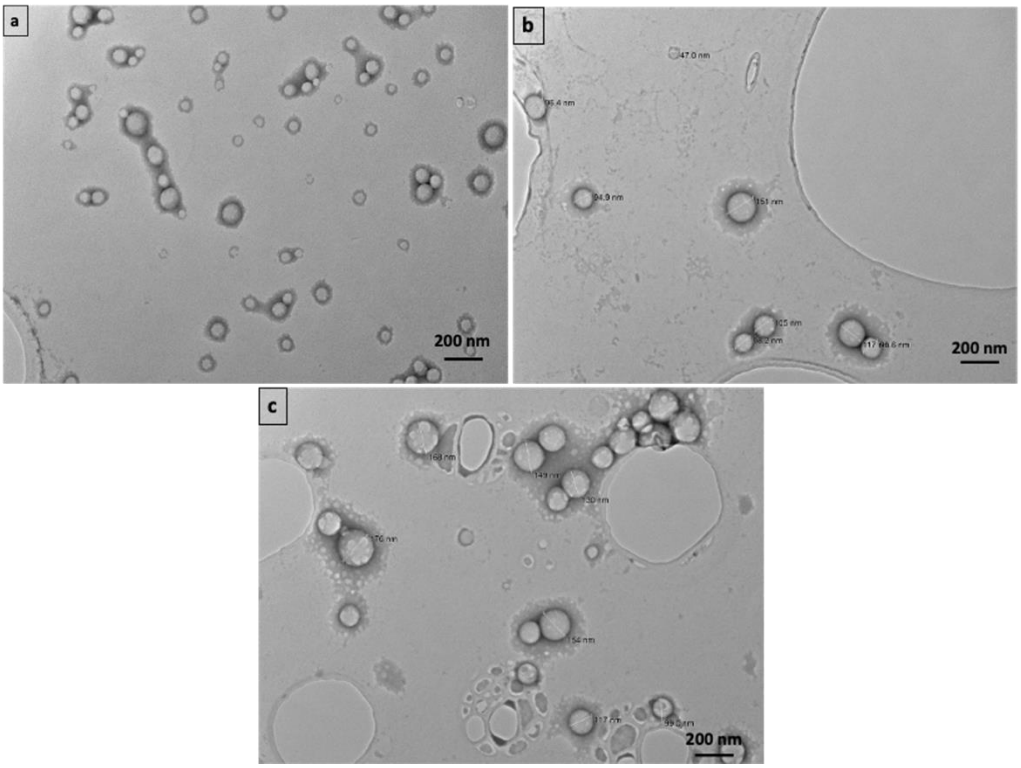

Figure 3.4: TEM of PLGA NPs prepared by CB-method using; (a) 1 (mg/mL), (b) 10 (mg/mL) and (c) 20 (mg/mL) of PLGA in acetone and 0.2 S/AS volume ratio.

The steady increase in NPs size despite the increase in the degree of supersaturation emphasises the impact of the other controlling parameters, such as the organic phase viscosity that is affected by the polymer concentration, as shown in **Figure 3.5**. As has been previously reported

in the literature, using high polymer concentration increases the number of the formed nuclei in the system, which increases the system's viscosity, reduces the diffusion rate of nuclei and increases the collision rate leading to particle's aggregation; however, there are several reasons to doubt this explanation [17,37]. First, it is expected that the increase in the number of nuclei would result in reducing the viscosity of the system, not increasing it due to the removal of the polymer from the solution. Second, if the higher collision rate and the formation of aggregations are the reasons behind the increase in size, one would expect the shape of the particles to reflect this by being irregular in shape, which does not agree with the TEM images **(Figure 3.4).**

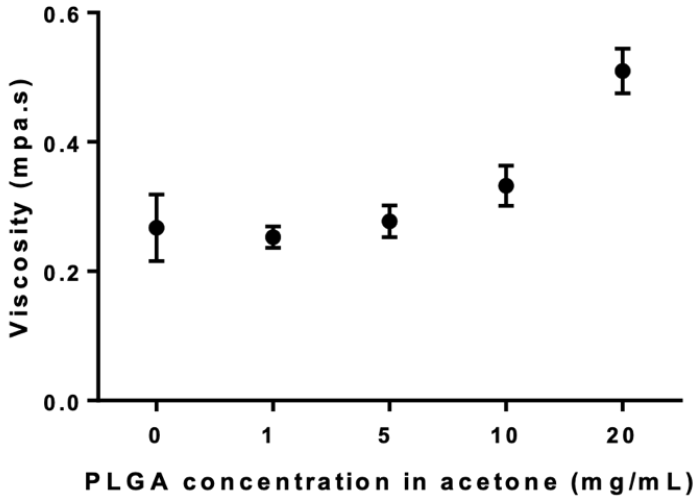

Figure 3.5: Viscosity of PLGA solutions (M. wt. 38000-54000 Da)

A suggested explanation for the relation between the polymer concentration and the size of NPs is that increasing PLGA concentration in the organic solvent increases the viscosity of the binary mixture and slows the mixing process. The polymer/polymer collision is expected to be higher at higher polymer concentration, and the polymer diffusion rate is expected to be lower. Hence, as a nucleus forms, it will grow faster and therefore larger due to the deposition of the polymer on the resulting nuclei. This explains the steady increase in NPs size with increasing PLGA concentrations despite the increase in the degree of supersaturation.

The S/AS volume ratio is another factor that significantly impacts the size of PLGA NPs. Increasing the S/AS volume ratio from 0.2 to 1 resulted in a significant increase (P-value < 0.05) in the size of PLGA NPs (Z-AVG and Number PSD), as shown in **Table 3.4**. This

increase in NPs size was correlated with a decrease in the degree of supersaturation from 0.8 to 0.5 at S/AS of 0.2 and 1, respectively, since the solubility of PLGA in 50% acetone-water binary mixture is 0.93 (mg/mL) as shown in **Figure 3.2**. A higher S/AS volume ratio increases the solubility of PLGA in the binary mixture, which results in decreasing the degree of supersaturation and increasing the size of NPs [17,28,37]. Furthermore, a higher S/AS would result in wide size distribution due to the Ostwald ripening effect induced by the dissolved polymer molecules in the residual solvent [15,17,218].

Table 3.4: Effect of S/AS volume ratio on the properties of PLGA NPs prepared by CB-method

PLGA Concentration (mg/mL)	S/AS Volume ratio	Z-AVG size (nm)	Number PSD (nm)	PDI	Zeta-p (mV)
1	0.2	88±3	46±4	0.2±0.01	-23±4
	0.5	106±8	48±5	0.2±0.02	-34±2
	1	144±17	61±7	0.3±0.05	-32±3

The nature of the organic solvent is reported to affect the size of NPs [12,13]. The choice of solvent is made according to three requirements [12,16]: (1) miscibility with water, (2) low boiling point to facilitate evaporation and (3) polymer dissolving capacity. The diffusion coefficient of the solvent is a characteristic property that was reported to affect the size of NPs. Solvents with higher diffusion coefficients into water were found to produce smaller NPs [12,13]. However, it is essential to point out that using the diffusion coefficient in predicting the mixing efficiency and size of the NPs is not clearly represented in the literature since most studies have relied on the solvent's self-diffusion coefficient. Using the self-diffusion coefficient for a system in which two different liquids are mixing by diffusion is not appropriate. In the case of a two-component system, mutual diffusion coefficients describe the mixing, and these for acetone/water can vary over a 5-fold range [219,220].

In this study, acetone was found to produce smaller NPs compared to acetonitrile **(Figure 3.6 a)**. Smaller NPs obtained using acetone might suggest that it is a better solvent for this type of PLGA. Hence, acetone was chosen for the following screening experiments.

The molecular weight of PLGA was examined in this study to assess its impact on the size of NPs. As shown in **Figure 3.6 b**, using a higher molecular weight of PLGA had no significant impact on the size of PLGA NPs (P-value > 0.05). The higher molecular weight of PLGA is expected to result in smaller NPs explained by its lower diffusion coefficient and saturated solubility in the binary mixture. However, several studies reported different results, including an increase, decrease and no impact on NPs size [221,222].

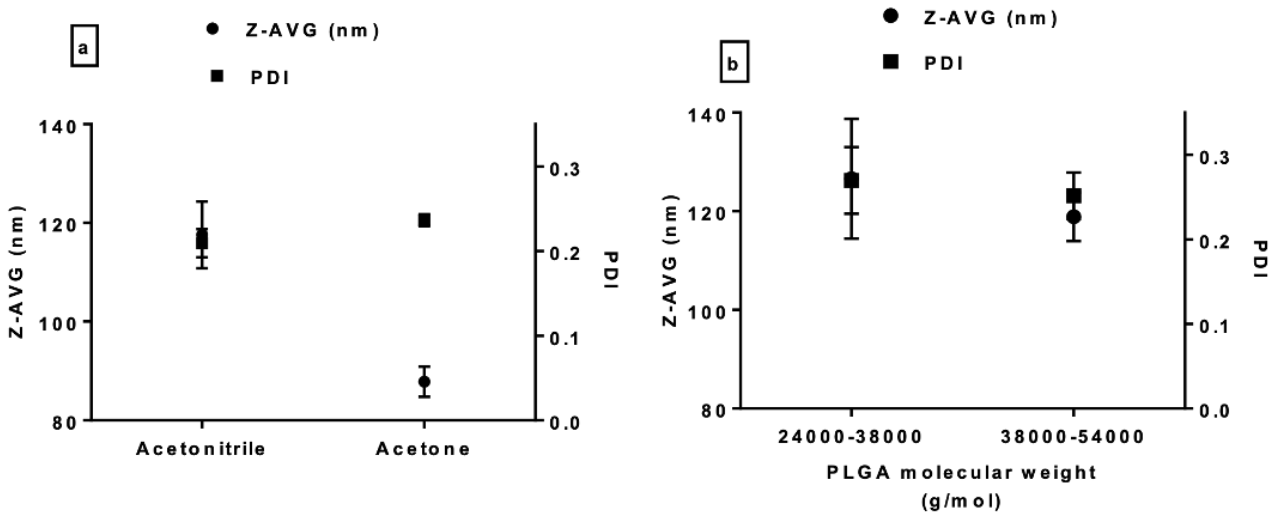

Figure 3.6: Effect of; (a) solvent type and (b) PLGA molecular weight on size of PLGA NPs prepared by CB-method.

The stirring rate was fixed for all the experiments (300 rpm) to maintain the same mixing efficiency. Efficient mixing ensures uniform supersaturation across the solvent-antisolvent mixture, which triggers uniform nucleation and results in smaller NPs with a narrow size distribution. Two-time scales are used to describe the complete precipitation process; time of mixing (t_{mix}) and precipitation time ($t_{precipitation}$). In conventional nanoprecipitation, which uses magnetic stirrers as the mixing device, the total mixing time is divided into micromixing and mesomixing. Mass transfer is driven by molecular diffusion with micromixing, whereas with mesomixing, mass transfer is driven by advection due to turbulence caused by chaotic mixing [15,17]. This explains that mixing in conventional nanoprecipitation is controlled by diffusion and advection; hence, the NPs size depends on achieving the balance between these two types of mixing. This demonstrates the need for controlling the stirring rate for all the formulations.

The zeta potential of NPs was examined to evaluate the synthesis method's effect on the colloidal system's charge stability. A steady increase in zeta potential was observed with

increasing PLGA concentration in acetone from 1 (mg/mL) up to 20 (mg/mL); however, increasing the S/AS above 0.5 had no impact on zeta potential **(Tables 3.3 and 3.4)**. Thus, there is no clear relationship between NPs concentration and Zeta potential. However, all the samples had a zeta potential value of at least 20 (mV), suggesting a stable colloidal system.

To directly compare the impact of the synthesis method (CB/MF) on the properties of PLGA NPs, a group of processing parameters were examined to understand the underpinning mechanisms responsible for the claimed size reduction with microfluidics technology [57,64]. These parameters include: PLGA concentration, FRR, TFR, stabilisers and chip design/geometries **(Figure 3.1b).** The mixing time was calculated using Eq. (3.1), which is used in the literature to predict the size of NPs [57]. These experiments were done to assess the validity of using the mixing time calculated using this equation as a prediction model for NPs properties.

Although increasing the FRR from 0.1 to 0.8 resulted in increasing the size of PLGA NPs (Z-AVG and Number PSD), size tunability was not achieved at FRRs between 0.1-0.5 when low TFRs were used **(Table 3.5)**. Significant fouling was observed at FRRs 0.1- 0.2 with low TFRs; however, fouling was less significant at the same FRRs when high TFRs were used **(Figure 3.7)**. Increasing the FRR when high TFRs were used resulted in a steady increase in NPs size (Z-AVG and Number PSD) **(Table 3.5)**.

Table 3.5: Effect of FRR and TFR on the mixing time and properties of PLGA NPs prepared using 1(mg/mL) PLGA in acetone and 190 µm droplet junction chip

	TFR (µl/min)	S/AS	FRR	Mixing time (ms)	Residence time (ms)	Z-AVG size (nm)	Number PSD (nm)	PDI	Zeta-p (mV)
	110	10/100	0.1	140	404	121±3	73±4	0.32± 0.05	-23±1
	120	20/100	0.2	470	370	126±4	76±2	0.18± 0.03	-27±3
Low TFR	150	50/100	0.5	1870	296	128±1	84±3	0.16± 0.01	-31±1
	180	80/100	0.8	3338	247	161±2	106±3	0.15±0	-32±1
	200	100/100	1	4225	222	188±5	118±21	0.18± 0.03	-50±1
	300	200/100	2	7511	148	228±7	129±36	0.23± 0.02	-58±2
	3113	283/2830	0.1	140	14	87±2	32±1	0.4± 0.02	-23±1
	1698	283/1415	0.2	470	26	121±4	72±2	0.17± 0.01	-21±1
High TFR	849	283/566	0.5	1870	52	128±6	87±6	0.13± 0.05	-18±2
	637	283/354	0.8	3338	70	171±4	117±8	0.13± 0.01	-26±1
	566	283/283	1	4225	78	185±4	122±11	0.15± 0.03	-28±3
	402	283/119	2	7511	110	191±3	144±10	0.14± 0.04	-30±2

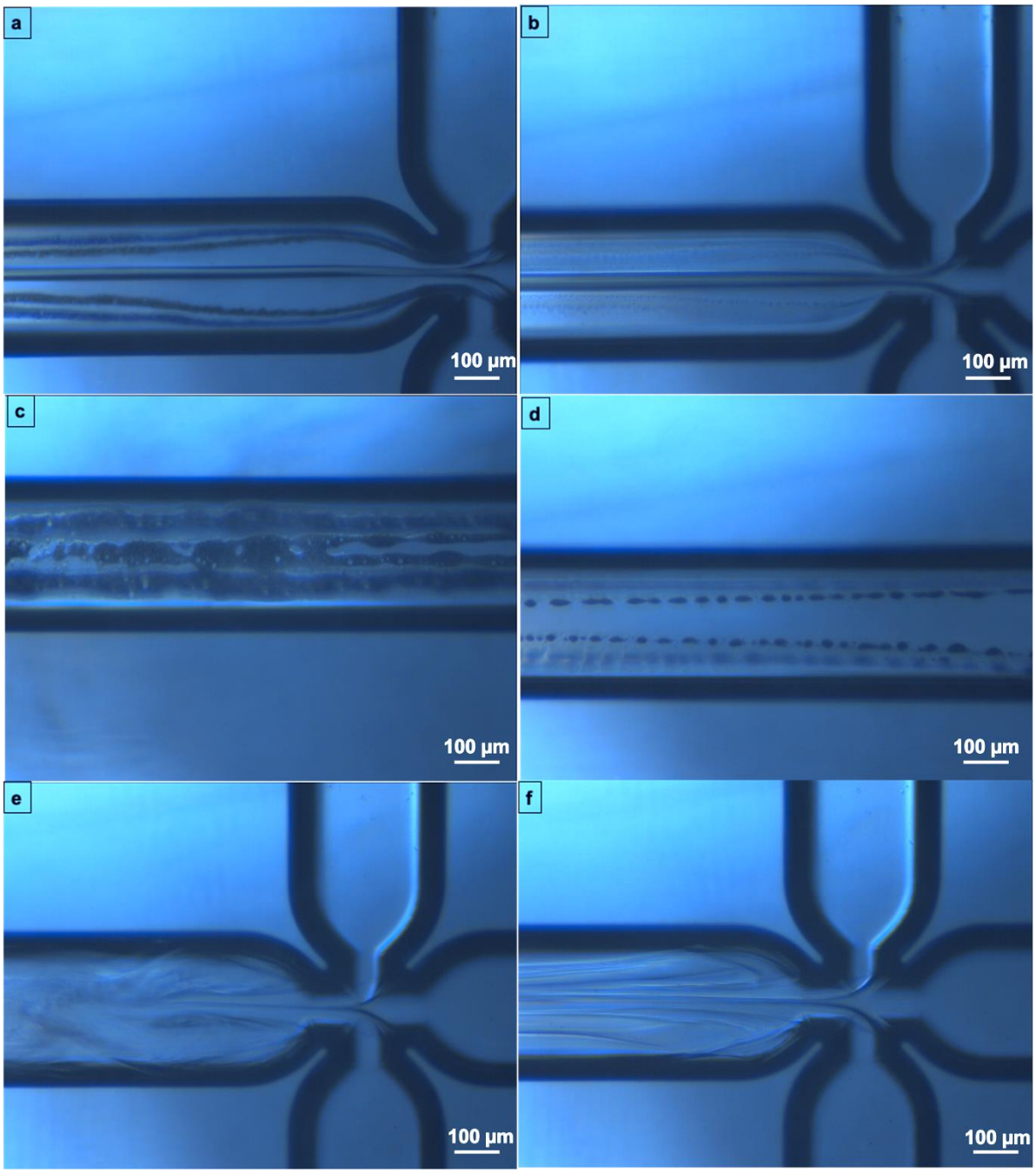

Figure 3.7: PLGA NPs synthesis using 190 µm droplet junction straight channel chip; (a) instant fouling observed in the at 0.1 FRR and 110 (µl/min) TFR, (b) effect of increasing the FRR from 0.1 to 0.2 using120 (µl/min) TFR on reducing fouling issues, (c) fouling observed after 5 (min) of collection using 0.1 FRR and 110 (µl/min) TFR, (d) fouling observed after 5 (min) of collection using 0.2 and 120 (µl/min) TFR, (e) chaotic mixing observed at 0.1 FRR and 3113 (µl/min) TFR, (f) reduction of fouling issues at 0.2 FRR and 1698 (µl/min) TFR.

Tuning the size of NPs using MF is controlled by two-time scales: mixing time (τ_{mix}) and aggregation time (τ_{agg}). The literature suggests that the formation of NPs in straight hydrodynamic flow focusing chips occurs in three stages: (1) nucleation of NPS, (2) growth of NPs through aggregation and (3) kinetically locked NPs achieved after a certain aggregation time scale [57]. The aggregation time scale represents the time scale of NPs growth, whereas the mixing time scale represents the time scale of solvent diffusion into the antisolvent phase. According to the literature, the impact of the FRR on the size of NPs is related to the width of the flow focused stream, which determines the mixing time [57,64,223]. Increasing the FRR results in increasing the mixing time due to the slower diffusion of the solvent caused by the increase in the flow-focused stream's (FFS) width, as suggested by Eq. (3.1). The growth rate of NPs in the second stage of NPs formation is limited by the formation of a brush layer on the surface of NPs when they grow sufficiently enough in size [57]. Indeed, the mixing and aggregation time scales significantly impact the size of NPs; however, few aspects can be argued in this discussion.

First, based on the data provided in **Table 3.5**, increasing the FRR from 0.2 to 2 using high or low TFRs, resulted in a significant increase in NPs size that was further proved by TEM data shown in **Figure 3.8 a and b.** However, there was no significant increase in the size of NPs (Z-AVG and Number PSD) upon increasing the FRR from 0.1 to 0.2 or 0.2 to 0.5 at low TFRs despite the increase in the width of the FFS shown in **Figure 3.9 a-c**. This would raise two possibilities; either this change in FRR was not enough to significantly alter the diffusion time scale of the solvent, or diffusion is not the only factor controlling the size of NPs. It can be argued that increasing the FRR results in decreasing the degree of supersaturation due to the significant increase in polymer solubility in the binary mixture when high FRRs are used (increased acetone content) **(Figure 3.2)**. A similar pattern of size tuning by changing the degree of supersaturation either by changing S/AS volume ratio or PLGA concentration was observed with the CB-method **(Table 3.3)**.

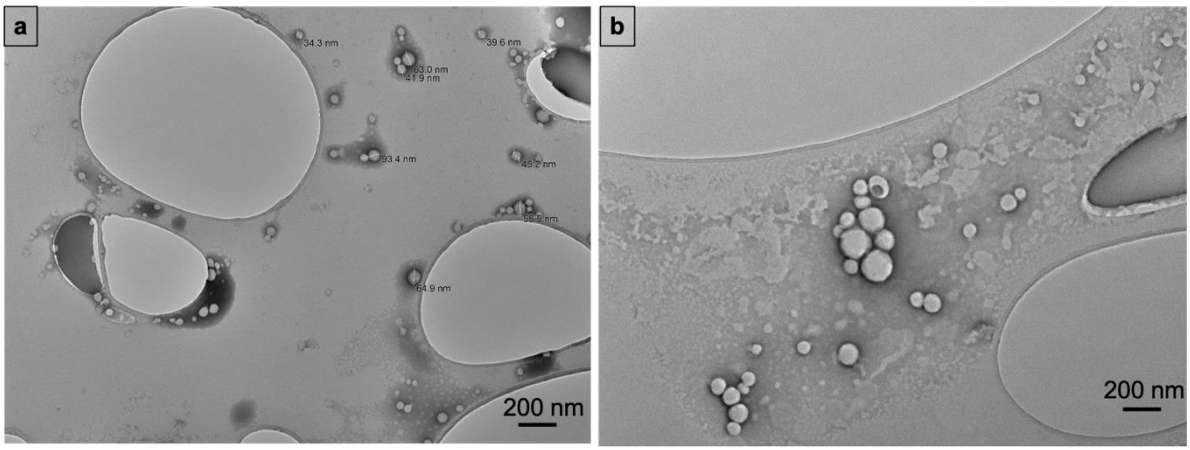

Figure 3.8: TEM of PLGA NPs prepared using MF-method using 1 (mg/mL) of PLGA in acetone at; (a) 0.2 FRR and (b) 2 FRR using 190 µm droplet junction straight channel chip.

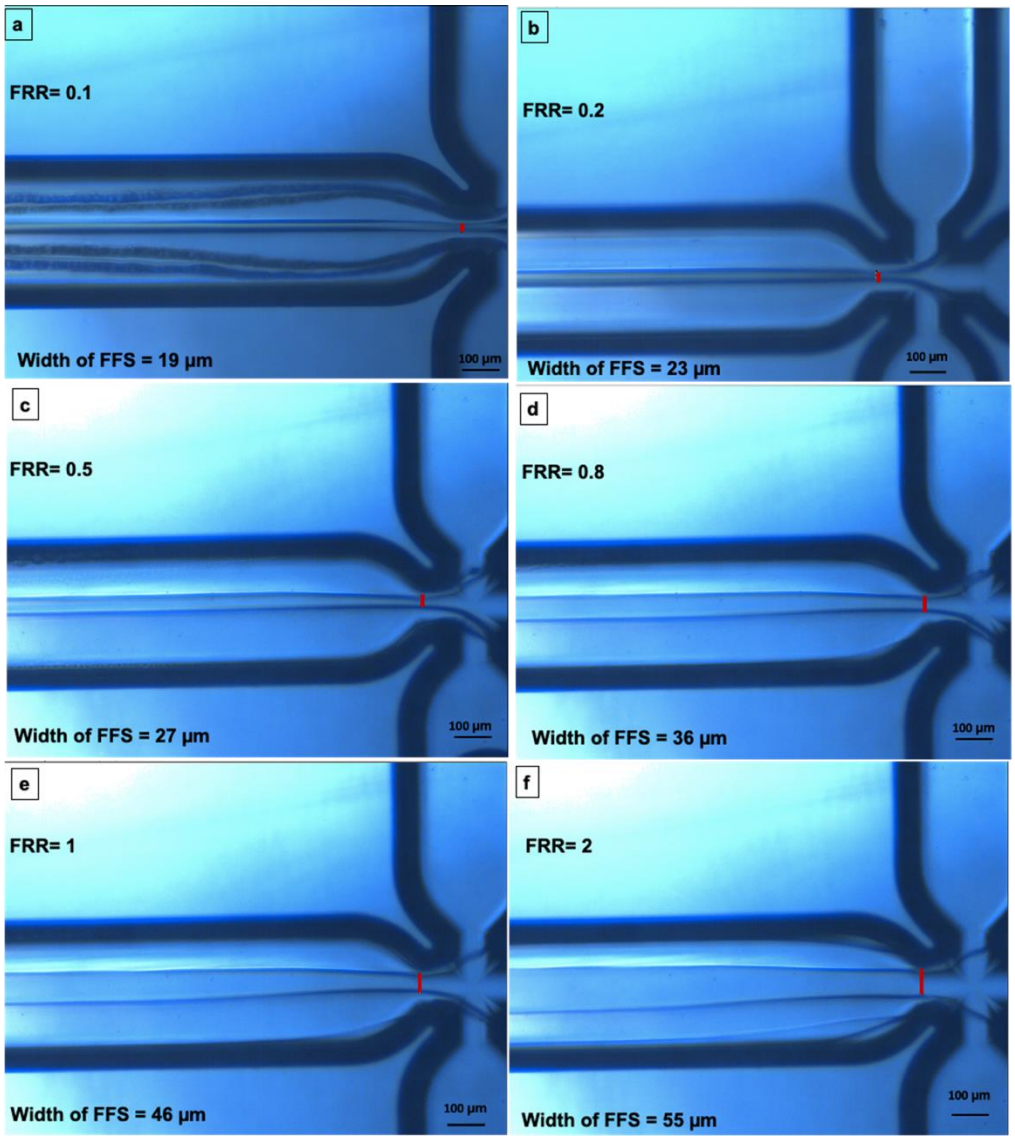

Figure 3.9: The width of the FFS at FRRs from 0.1 to 2 using low TFRs (110-300 µl/min) and 1 (mg/mL) of PLGA in acetone.

Second, the discussion in the literature around the growth of NPs suggests that the growth is limited by the formation of a brush layer on the surface of NPs after growing sufficiently in size (growth is limited by the NPs size) [57]. However, one can argue that this would presumably result in achieving the same NPs size at different FRRs, which contradicts the findings. This would suggest that the growth of NPs is not limited by the size of NPs as proposed in the literature. Hence, this introduces another explanation, which suggests that size tuning using MF can be explained based on Flory-Huggins theory and the speed of introducing the polymer to the antisolvent phase. This theory explains the polymer interaction with the solvent molecules. In solution, the polymer is expected to behave as a mobile chain that possesses different conformations based on polymer-solvent interaction. The chain is expected to expand in a good solvent due to the favoured interaction between the polymer monomers and solvent molecules [224]. On the other hand, the chain tends to contract in poor solvents to reduce the interactions with solvent molecules. This can be used to explain the different growth rates for NPs prepared at different FRRs. When the solvent phase containing the polymer interacts with the antisolvent phase at the junction, the polymer chains conformation changes from being extended in the good solvent (acetone) to being contracted in the poor solvent (binary mixture of solvent and antisolvent), (polymer-polymer interactions > polymer-solvent interactions). If this happens rapidly, which is expected at high solvent/antisolvent exchange rates, smaller NPs will be formed due to the instant limited growth.

This argument can be further demonstrated by considering the mixing and residence times in **Table 3.5** at high TFRs, where the smallest NPs size was achieved at 0.1 FRR. This cannot be attributed to the improved mixing caused by the narrower width of the flow focused stream because of the very short residence time in the chip, as shown in **Table 3.5**, which suggests that mixing and complete solvent diffusion were not achieved in the chip but in the collecting vessel. Accordingly, size tunability observed at the different FFRs at high TFRs must be due to the speed (S/AS exchange rate) of introducing the polymer to the poor solvent. The smallest NPs achieved at 0.1 FRR, and 3113 (µl/min) TFR can also be attributed to the change in the mixing type at these conditions compared to the same FRR at lower TFR 110 (µl/min). As shown in **Figure 3.7 e,** at 0.1 FRR and 3113 (µl/min) TFR, the mixing was turbulent due to the significant difference in S/AS velocities, which suggests that mass transfer was driven by both advection and diffusion, unlike the case at 0.1 FRR and 110 (µl/min) TFR, where mass transfer is driven by solvent diffusion only due to the laminar flow.

A recent study conducted by Operti et al. reported a decrease in NPs size when increasing the TFR from 4 mL/min to 8 mL/min while fixing the FRR [64]. According to this study, the decrease in NPs size was related to the faster mixing (shorter mixing time) achieved at higher TFRs; however, as suggested by the mixing time equation used in their study Eq. (3.1), mixing time is not impacted by the TFR but by FRR. Despite using a fixed FRR, it is expected that at high TFRs, the mixing time will be fixed, but the residence time will be shorter, which suggests that mixing and complete diffusion will take place in the collecting vessel instead of the chip. This reinforces our explanation of relating the size tunability to the speed of introducing the polymer to the poor solvent at the junction and suggests that relying on the mixing time only (calculated using Eq. (3.1)) to predict the NPs size can be misleading. Furthermore, the same study emphasised on the superiority of MF technology as an advanced NPs size tuning device by synthesising PLGA NPs between 100 and 400 nm in size. However, as demonstrated above, size tunability can be achieved by CB-method by changing the processing parameters. As shown in **Table 3.5,** all the samples had a zeta potential value of about 20 mV and higher, suggesting a stable colloidal system.

As shown in **Figure 3.10 a**, increasing PLGA concentration in acetone from 1 (mg/mL) to 3 (mg/mL) had no impact on NPs size at 0.2 FRR, which suggests that NPs size is independent of PLGA concentration when S/AS exchange rate is high. However, a significant increase in the size of PLGA NPs at FRRs of 0.5 or above was observed (P-value < 0.05). A similar trend was observed with conventional nanoprecipitation. Several stabilisers were used to examine their impact on reducing the fouling rate and widening the screening range of the study since significant blockages and fouling were observed using higher PLGA concentration 5 (mg/mL); however, none of the stabilisers was found efficient in mitigating the building up of the NPs in the microchip channels or the output tube **(Figures 3.10 b and 3.11 a)**. The addition of stabilisers did not impact the size of NPs except for PVA that resulted in a significant increase in PLGA NPs size, as shown in **Figure 3.10 b**.

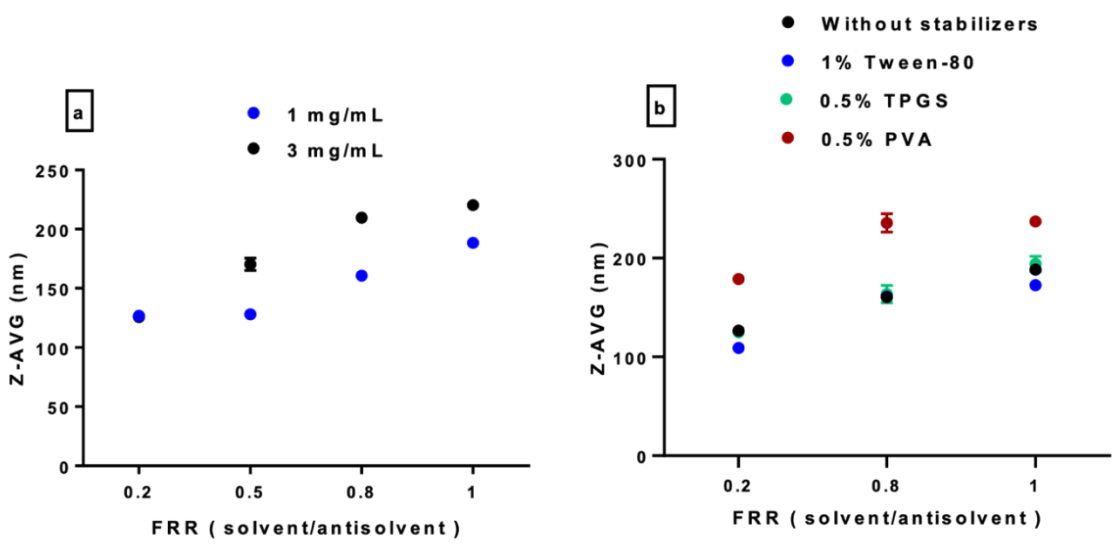

Figure 3.10: (a) effect of PLGA concentration on size of PLGA NPs prepared using 190 µm straight droplet junction chip at FRRs (0.2-1) and low TFRs (110-300 µl/min), (b) effect of stabilisers addition on size of PLGA NPs prepared using 190 µm straight droplet junction chip and 1 (mg/mL) of PLGA in acetone at FRRs (0.2-1) and low TFRs (110-300 µl/min).

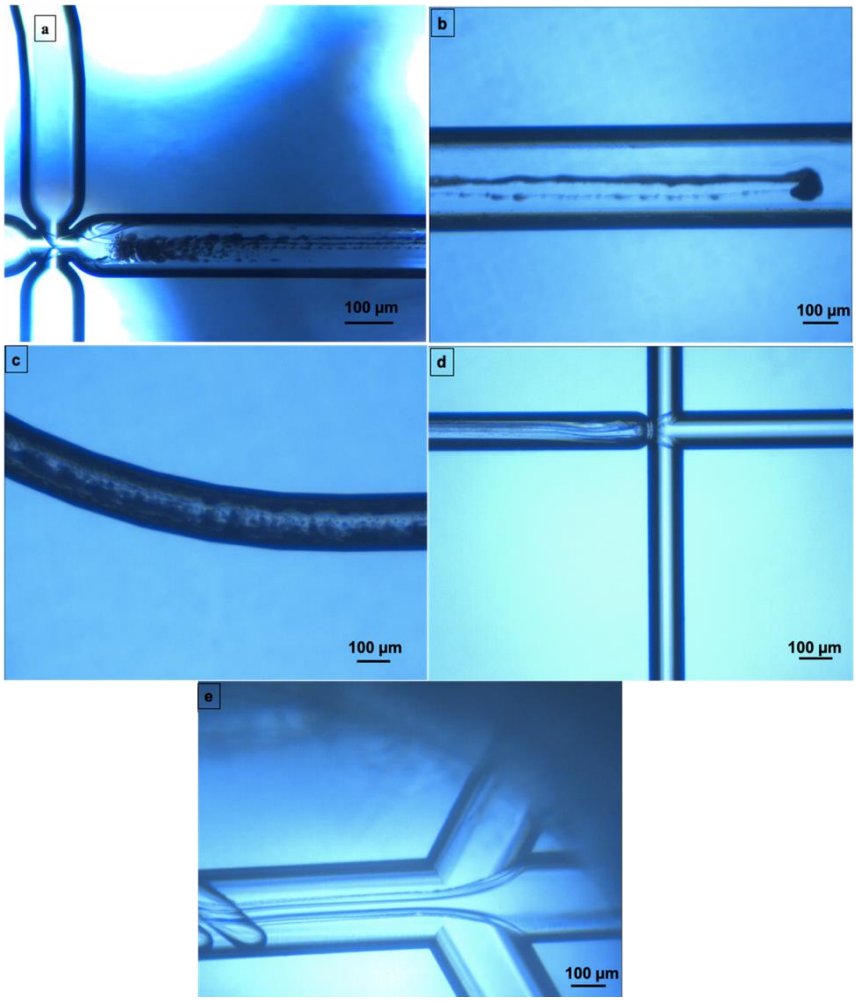

Figure 3.11: (a) instant fouling observed in the190 µm droplet junction straight channel chip when using 5 (mg/mL) PLGA at 0.2 FRR, (b) significant fouling observed in the 100 µm Micro Mixer chip outlet when using 1 (mg/mL) PLGA at FRRs below 0.8, (c) significant fouling observed in the 100 µm chip 3d-flow focusing straight channel chip when using 1 (mg/mL) PLGA at FRRs below 0.8, (d) synthesis of PLGA NPs using 1 (mg/mL) PLGA in 100 µm 3d-flow focusing straight channel chip at 0.8 FRR, (e) synthesis of PLGA NPs using 1 (mg/mL) PLGA in 100 µm Micro Mixer at 0.8 FRR.

To examine the impact of the mixing type on NPs, the size of NPs prepared at 0.8 FRR using 100 µm 3d-flow-focusing straight channel chip and 100 µm Micro Mixer chip was compared **(Figure 3.12 a)**. NPs prepared using the micromixer chip were about 50% smaller than those prepared using the 100 µm 3d-flow focusing straight channel chip. This is related to the mixing type employed in the micromixer chip since chaotic mixing is imposed by the chip design, which is expected to promote mass transfer by advection and diffusion and reduce the size of NPs. The improved mixing within the micromixer chip was confirmed by the rate of NPs building up within the chip, which was observed to be faster in the micromixer chip compared to the 100 µm 3d-flow focusing straight channel chip at similar FRR. The faster building up suggests a higher S/AS exchange rate and a better mixing efficiency. However, this has made

the synthesis of NPs at lower FRRs impossible due to the continuous blockages, which explains the use of 0.8 FRR in this study to facilitate the synthesis as much as possible **(Figure 3.11)**.

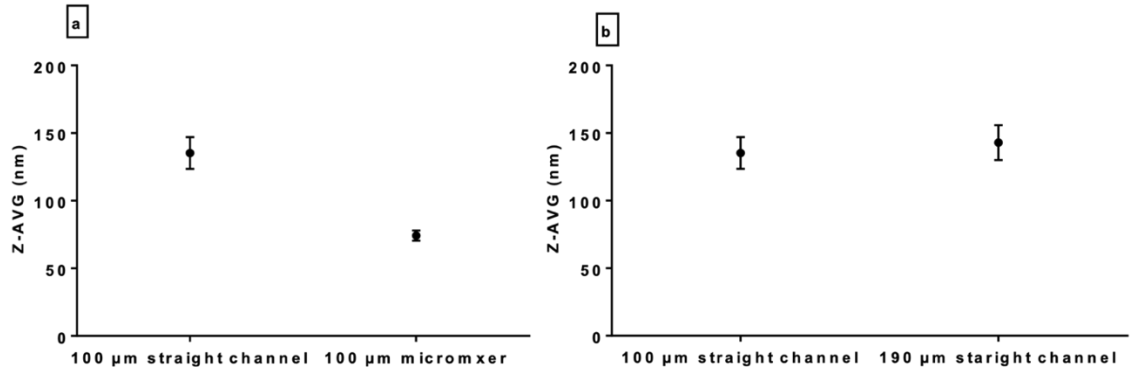

Figure 3.12: (a) effect of chip design (straight/micromixer) on size of PLGA NPs prepared using MF-method, (b) effect of chip dimensions on size of PLGA NPs prepared using MF-method.

The size of PLGA NPs prepared using a 190 µm straight droplet junction straight channel chip and 100 µm 3d-flow-focusing straight channel chip at 0.8 FRR was compared as shown in **Figure 3.12 b**. Based on Eq. (3.1), the mixing time has a direct positive relationship with the width of the chip. Hence, a narrower chip should supposedly shorten the mixing time and reduce the size of NPs. However, there was no significant difference in the size of NPs prepared using the two chips when using similar processing conditions **(Figure 3.12 b).** This would further demonstrate that size tunability is not mainly controlled by the FFS width but by the speed of introducing the polymer to the poor solvent (S/AS exchange rate).

These findings question the validity of using the mixing time to control and predict the size of the NPs, a question that has not been addressed in the literature. It is essential to point out that Eq. (3.1) considers the self-diffusion coefficient of the organic solvent, which might not be credible in this ternary system. A factor so far not considered is that the system of interest is a ternary system, and polymers will diffuse much slower than the solvent. Mutual diffusion in ternary systems is complicated, and a single mutual diffusion coefficient cannot describe diffusion. This shows one of the limitations of using the calculated mixing time to predict the efficiency of mixing and the properties of the resulting NPs.

To address any additional advancement in NPs properties prepared by MF-method compared to CB-method, several aspects related to the properties of NPs (size, PDI and Zeta-p) and ease of processing could be discussed. First, MF technology has been increasingly reported as a tool

for NPs size tuning [52,53,55,57]; however, the data revealed the feasibility of PLGA size tuning by CB-method correspondingly.

Second, MF has been proposed as a favoured method to fabricate smaller monodisperse NPs; however, the size of NPs prepared by CB-method, expressed by Z-AVG and number, was significantly smaller than MF NPs (P-value < 0.05) prepared using the 190 µm straight channel chip when similar PLGA concentration 1 (mg/mL) and S/AS volume ratio 0.2-1 were used **(Tables 3.4 and 3.5)**. Although the micromixer chip led to a significant decrease in the size of PLGA NPs prepared by MF-method to be 74±4 nm (Z-AVG) and 41±1nm (Number PSD), its use was limited to FRR of 0.8 or above due to significant blockages observed at lower FRRs. However, if the ultimate goal is to fabricate PLGA NPs within this size range, it is noteworthy that a comparable size of 88±3 nm (Z-AVG) and 46±4 nm (Number PSD) was achieved with CB-method **(Table 3.3)**. Also, it is noteworthy to mention that conventional nanoprecipitation could be efficiently used to prepare ultra-small polymeric NPs of 15 nm by optimizing the experimental conditions [77].

In a study conducted by Karnick et al., the size of NPs prepared using MF was found to be smaller than that of conventional NPs by 7 nm [57]. Therefore, despite the statistically significant difference in NPs sizes in the mentioned study, it is highly doubted that this slight difference (7nm) would result in additional therapeutic advancement. Finally, the controlled mixing achieved by MF is known to improve the robustness of the nanoprecipitation method by improving the reproducibility of the results; however, the data showed that CB-method is just as robust as MF-method as indicated by the minor standard deviations for a set of triplicates **(Tables 3.3, 3.4 and 3.5)**.

3.3.3 Comparing the physicochemical properties of PLGA-Eudragit NPs prepared by CB-method and MF-method

Most reported studies on using MF for nanoprecipitation are focused on using a single polymer such as PLGA but not a blend of polymers. Therefore, there is a significant lack of understanding of MF capabilities in synthesising polymer blend NPs. Eudragit was chosen in this study to modify the surface charge of PLGA NPs by adding it to the organic solvent. Several parameters were studied to investigate their impact on the nanoprecipitation process and the subsequent resulting PLGA-Eudragit NPs prepared by CB/MF-methods. For CB-

method, these parameters include, Eudragit: PLGA mass ratio, polymer blend concentration, S/AS volume ratio and the speed of adding the organic phase to the aqueous antisolvent phase (dropwise/quick addition). As shown in **Figure 3.13a**, NPs size increased significantly when Eudragit: PLGA mass ratio exceeded 1:1. The surface charge modification was confirmed by the change in the zeta potential of NPs from negative for unmodified PLGA to positive for PLGA-Eudragit NPs **(Figure 3.13b)**.

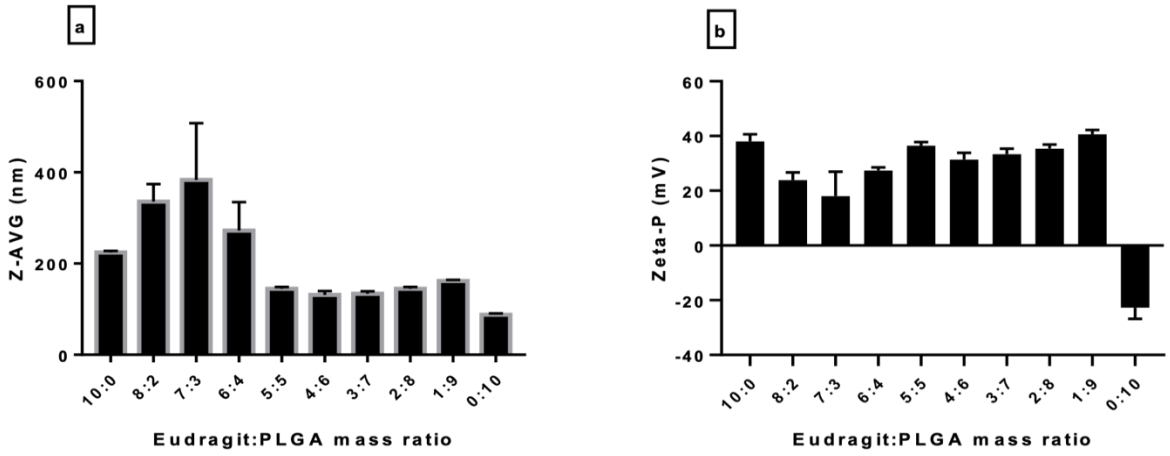

Figure 3.13: Effect of Eudragit: PLGA mass ratio on PLGA-Eudragit prepared by CB-method; (a) Z-AVG and (b) Zeta potential. The error bars represent the standard deviation and n=3.

Eudragit: PLGA mass ratio was fixed to 1:1 for the following screening experiments. Increasing the polymer blend concentration from 2 (mg/mL) to 10 (mg/mL) resulted in a significant increase in the size of PLGA-Eudragit NPs (P-value < 0.05) **(Table 3.6).** This can be related to the increase in polymer/polymer collision and the reduction of the polymer diffusion rate upon increasing the polymer concentration, as explained in **section 3.3.2 (Figure 3.14 a).** Increasing the S/AS volume ratio from 0.2 to 0.5 resulted in a significant increase in NPs size (P-value < 0.05), as shown in **Table 3.6**. These findings tie well with the unmodified PLGA NPs results discussed in the previous section and highlight the efficiency of the CB-method in tuning the size of polymeric NPs by adjusting the processing parameters.

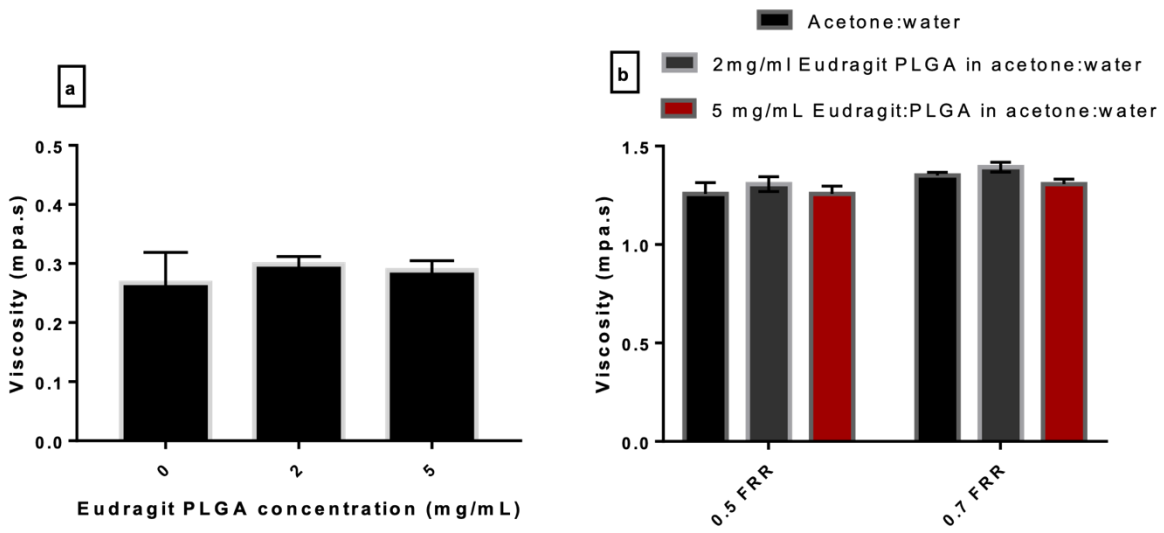

Figure 3.14: (a) effect of PLGA-Eudragit concentration on the viscosity of the solution, (b) comparing the viscosity of acetone:water binary mixture containing different amounts of PLGA-Eudragit to polymer free acetone water binary mixture processed using MF at FRRs of 0.5 and 0.7. The error bars represent the standard deviation and n=3.

Table 3.6: Effect of PLGA Eudragit concentration and S/AS volume ratio on the size of PLGA-Eudragit NPs prepared by CB-method

S/AS VR	PLGA-Eudragit concentration (mg/mL)	Z-AVG (nm)	Number PSD (nm)	PDI	Zeta-p (mV)
0.2	2	149±10	112±11	0.08±0.03	38±1
	5	241±18	147±11	0.31±0.01	37±1
	10	257±4	193±29	0.19±0.11	55±5
0.5	2	215±34	172±41	0.09±0.06	41±10

As explained in **section 3.3.2,** the complete precipitation process can be explained by two-time scales; time of mixing (t_{mix}) and precipitation time ($t_{precipitation}$). Hence, changing the mixing device or the mixing speed affects these time scales and the properties of the resulting NPs. The speed of phases addition (solvent to antisolvent) and mixing were considered in this study by comparing dropwise solvent addition to quick solvent addition using a micropipette. NPs prepared using quick solvent addition had a significantly smaller size and PDI value compared to those prepared by dropwise addition (P-value < 0.05) **(Table 3.7)**. However, it is noteworthy that the size of NPs was not tuneable by changing the polymer concentration using the quick addition method **(Table 3.7)**. This suggests that the size is independent of the polymer

concentration when the S/AS exchange rate is high. This was previously discussed in **section 3.3.2,** where PLGA concentration had no impact on the size of PLGA NPs prepared using MF-method at FRR of 0.2, which is expected to be due to the high S/AS exchange rate at this FRR.

Table 3.7: The impact of the solvent addition method on the properties of PLGA-Eudragit NPs prepared by CB-method

S/AS VR	PLGA-Eudragit concentration (mg/mL)	Addition method of solvent	Z-AVG size (nm)	Number PSD (nm)	PDI	Zeta-p (mV)
0.2	5	Dropwise	241±18	147±11	0.31±0.01	37±1
		Quick using micropipette	108±12	60±8	0.18±0.02	37±2
	1	Quick using micropipette	114 ±14	24±2	0.32±0.03	36±1

The difference in NPs sizes between the two conventional methods (dropwise/quick addition) can also be attributed to the size of the droplet. The size of the droplet is another factor that can play a prominent role in controlling the size of the resulting NPs. When two solvents (labelled A and B) mix by diffusion, the movement of a molecule of A into solvent B displaces 1 or more molecules of B. These necessarily have to move to solvent A since if they did not the density of B would increase and continue to increase indefinitely. This means that for a net flow of A into B, there must be a corresponding flow of B into A. The rate of molecules arrival of A into B and vice versa by diffusion is given by the flux, J, mol m^{-2}/s^{-1}, as follows [225]:

$$J_{A,B} = -D_{A,B}\frac{\partial C_A}{\partial x} \quad \text{Eq. (3.5)}$$

$$J_{B,A} = -D_{B,A}\frac{\partial C_B}{\partial x} \quad \text{Eq. (3.6)}$$

J is the flux of A into B or B into A and has units of $mol/m^2/s$, *D* is the mutual diffusion coefficient of A or B, *C* is concentration, and *x* is the distance. So, if we considered a spherical droplet, as might be formed in CB mixing, it has a volume of $4/3\pi r^3$ and surface area of $4\pi r^2$, so the flux per unit volume is 3J/r. This implies that small droplets will get more antisolvent quicker than large droplets. It may be that one could control particle size by controlling droplet

size in the CB experiment. One way to control this is to use a syringe pump to precisely control the volume of the organic phase droplet. This aspect has not been investigated in this study but would improve the CB-method and its scalability.

To explore the capabilities and limitations of MF in preparing polymer blend NPs, the processing parameters were matched with those used with the CB-method. The screening experiments were done using the 190 µm droplet junction straight channel chip to reduce the continuous fouling, which was inevitable with the 100 µm 3d-flow-focusing straight channel chip or the 100 µm Micro Mixer chip. The fouling issues limited the choice of FRRs; hence high TFRs were used, and FRRs below 0.5 were excluded due to the continuous blockages **(Figure 3.15 a).** As shown in **Table 3.8**, increasing the FRR from 0.5 to 0.7 resulted in a significant increase in the size of NPs (P-value < 0.05). Although increasing the PLGA-Eudragit (polymer blend) concentration had no significant impact on the size of NPs, it increased the fouling rate inside the chip and the outlet tube **(Figure 3.15 a)**.

Table 3.8: Effect of FRR and TFR on the mixing time and properties of PLGA-Eudragit NPs prepared 190 µm droplet junction chip

PLGA-Eudragit concentration (mg/mL)	TFR (µl/min)	FRR	Mixing time (ms)	Residence time (ms)	Z-AVG size (nm)	Number PSD (nm)	PDI	Zeta-p (mV)
2	849	0.5	1870	52	166±11	97±26	0.17±0.01	27±2
	687	0.7	2865	65	188±6	126±6	0.19±0.01	29±0.1
5	849	0.5	1870	52	167±3	113±6	0.13±0	26±2
	687	0.7	2865	65	186±11	127±25	0.15±0.04	25±2

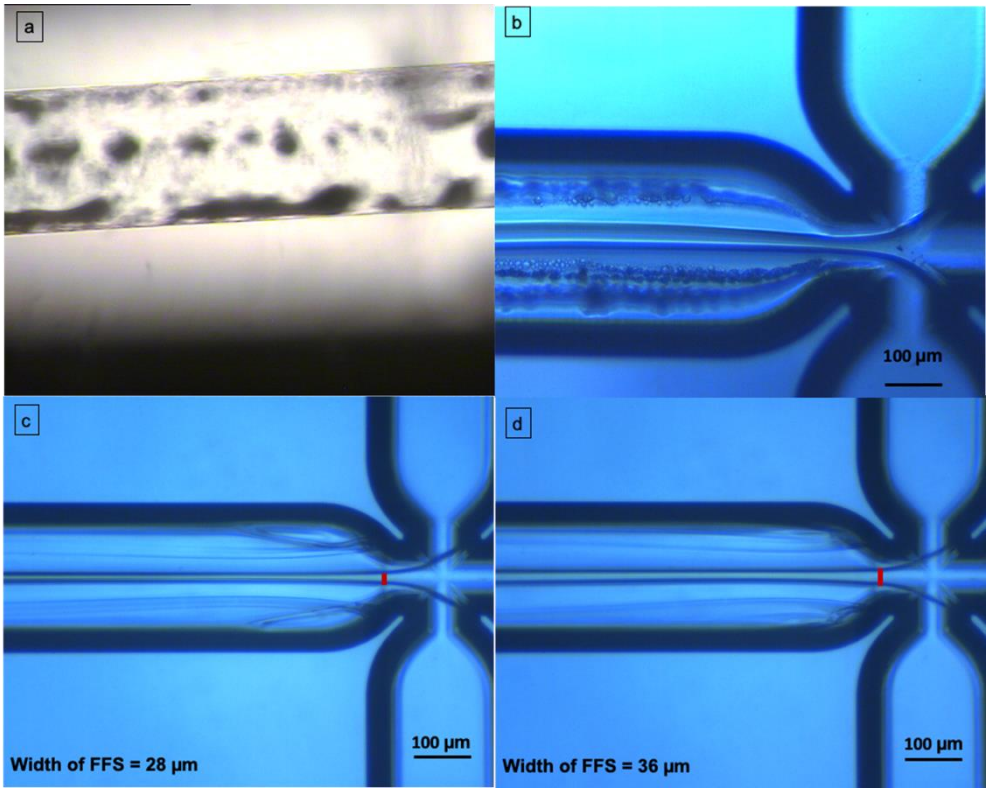

Figure 3.15: (a) fouling observed in the output tube when PLGA-Eudragit concentration exceeds 2 (mg/mL), Images of 190 µm droplet junction straight chip showing: (b) fouling observed at 0.5 FRR when low TFR was used (150 µl/min), (c) PLGA-Eudragit NPs synthesis using 0.5 FRR at higher TFR (849 µl/min), (d) PLGA-Eudragit NPs synthesis using 0.7 FRR at higher TFR (687 µl/min).

The increase in fouling rate and blockages with this type of polymer blend NPs can be related to the significant electrostatic interaction that can arise between the positively charged PLGA-Eudragit NPs and negatively charged silicate glass surfaces of the chip when exposed to water [226]. Although increasing the TFRs was reported to reduce fouling issues, this was not found efficient when strong deposits tend to form in the chip [227].

The viscosity of the fluids is believed to be a significant contributor to fouling issues; however, there was no significant difference in solvent/antisolvent binary mixture viscosity with and without polymers when processed at the same FRR and TFR **(Figure 3.14 b)**. Fouling observed with this type of NPs was significant enough to block the 100 µm Micro Mixer chip within one minute of processing, and the Z-AVG size of NPs prepared using this chip at 0.8 FRR and 180 (µl/min) TFR was found to be 328±33 nm and PDI of 0.5±0.01 due to the large aggregates in the sample. Increasing the TFR was not found efficient in reducing the building up in the 100 µm Micro Mixer chip. Although using PDMS chips might reduce this type of fouling, the use of these chips is limited by their poor resistance to a range of organic solvents, including

acetone. This reveals the limitations of MF-method for synthesising surface-modified PLGA NPs by positively charged polymers.

By comparing the properties of PLGA-Eudragit NPs prepared by CB-method and MF-method, it can be seen that smaller NPs were fabricated by CB-method using quick solvent addition method, whereas MF-method resulted in larger NPs and significant processing issues due to continuous fouling. The difference in NPs size between the two methods (CB-method with quick solvent addition/MF-method) can be attributed to the mixing time scale (S/AS exchange rate) and aggregation time (growth rate).

Two processes control the growth of NPs size: growth controlled by diffusion and growth controlled by surface properties [20]. When the growth process is controlled by the diffusion of the growth species from the bulk solution to the particle surface, the growth rate (dR/dt) is given by Eq. (3.7) [228]. Where D is the diffusion coefficient of the growth species, Cb is the bulk concentration, Ceq represents the equilibrium concentration of monomers in the solution at the surface of the nanoparticle, Ω is the volume of monomer, and R is the radius of the spherical nucleus.

$$dR/dt = \frac{D\Omega\,(Cb\text{-}Ceq)}{R} \qquad \text{Eq. (3.7)}$$

The effect of the FRR on the size of NPs can be further explained using Eq. (3.7) [58]. At lower FRRs, the polymer concentration in the flow focused stream is diluted, which results in reducing the concentration on the surface of NPs. This consequently reduces the $(Cb - Ceq)$ term and the growth rate of the NPs. Although this might explain the size tunability achieved at the different FRRs, it points out that nucleation in microfluidic chips occurs at the flow focused stream interface. Therefore, if the mixing is slow, which is the case when using the straight chips, the nucleation rate will be lower. This results in forming fewer nuclei across the interface and promoting the growth by polymer deposition on the surface of the formed nuclei. However, with CB-method using quick solvent addition, the mixing is believed to be faster and not localized (homogenous through the solvent-antisolvent mixture), which results in a higher nucleation rate and limited growth, leading to smaller NPs fabrication. This can be considered as another possible explanation for the size tunability observed with microfluidics besides the speed of introducing the polymer to the poor solvent proposed before.

CB-method and MF-method produced spherical NPs, as shown by the TEM and SEM images in **Figures 3.16 and 3.17**. Overall, the data suggest that the CB-method was more efficient in fabricating PLGA-Eudragit NPs in terms of NPs properties and ease of processing.

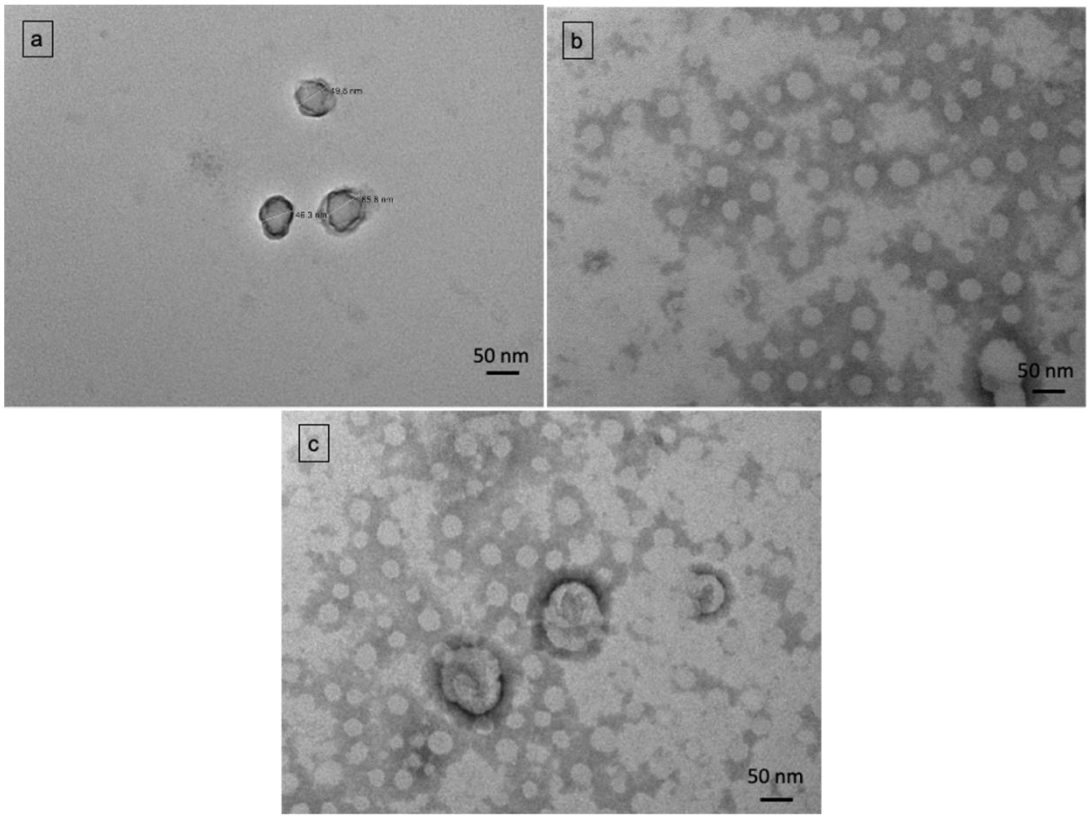

Figure 3.16: TEM images of ; (a) PLGA-Eudragit NPs prepared by CB-method using quick solvent addition (2 mg/mL PLGA-Eudragit, 0.2 S/AS VR), (b) PLGA-Eudragit NPs prepared using MF-method (2 mg/mL PLGA-Eudragit, 0.5 FRR, 849 µl/min TFR), (c) PLGA-Eudragit NPs prepared using MF-mehod (2 mg/mL PLGA-Eudragit ,0.7 FRR, 687 µl/min TFR).

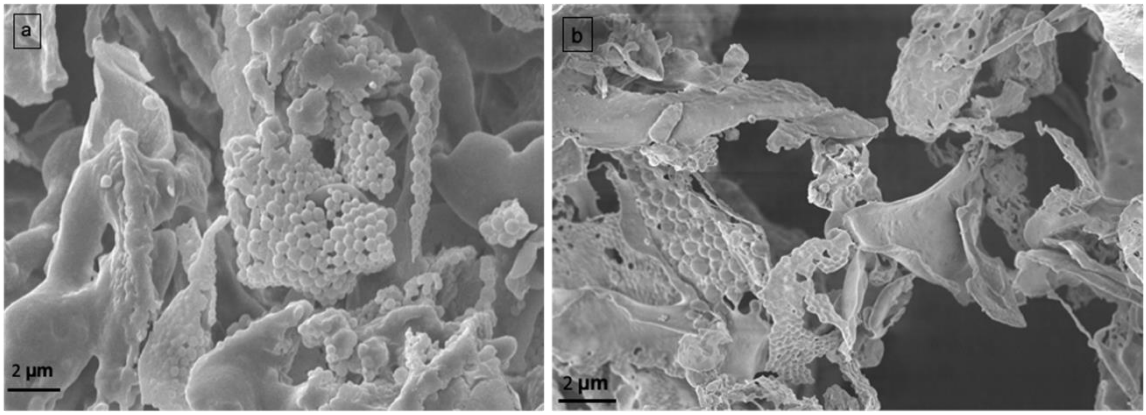

Figure 3.17: SEM images of ; (a) Freeze dried PLGA-Eudragit NPs prepared by CB-method using quick solvent addition (2 mg/mL PLGA-Eudragit, 0.2 S/AS VR), (b) Freeze dried PLGA-Eudragit NPs prepared using MF-method (2 mg/mL PLGA-Eudragit , 0.5 FRR, 849 µl/min TFR).

3.3.4 Comparing the physicochemical properties of PLGA-Chitosan NPs prepared by CB-method and MF-method

Chitosan is extensively studied as a promising material for drug and gene delivery due to its favoured properties, including its safety, biocompatibility, and biodegradability. In **section 3.3.3**, the efficiency of MF-method compared to CB-method for surface-modified PLGA NPs synthesis was studied by modifying the organic phase; however, this part of the study is focused on modifying the NPs surface by modifying the aqueous phase using water-soluble chitosan. This method relies on coating the surface of PLGA NPs with low molecular weight chitosan using CB-method and MF-methods. For PLGA-Chitosan NPs prepared by CB-method (dropwise solvent addition), parameters including PLGA concentration in acetone and chitosan concentration in water were screened for their impact on the properties of PLGA-Chitosan NPs.

As shown in **Table 3.9**, increasing PLGA concentration in acetone resulted in a significant increase in PLGA-Chitosan NPs size (P-value < 0.05). However, increasing the chitosan concentration from 0.1 (mg/mL) to 0.5 (mg/mL) when using 5 (mg/mL) of PLGA resulted in a slight decrease in NPs size. It is noteworthy to mention here that the relation between chitosan concentration and NPs size is not direct and varies according to the relative amount of chitosan available for adsorption on PLGA NPs. This can be seen in **Table 3.10**, where increasing chitosan concentration when using 1 (mg/mL) of PLGA resulted in larger NPs fabrication using MF-method. The successful coating of PLGA NPs surface was confirmed by the flip in zeta potential values from negative to positive, as shown in **Table 3.9**. The speed of adding the solvent to the antisolvent was also considered in this study; however, quick solvent addition by micropipette resulted in unstable formulations.

Table 3.9: Effect of PLGA and Chitosan concentrations on the properties of PLGA-Chitosan NPs prepared by CB-method

S/AS VR	Chitosan concentration (mg/mL)	PLGA concentration (mg/mL)	Z-AVG size (nm)	Number PSD (nm)	PDI	Zeta-p (mV)
0.2	0.1	1	201±9	175±8	0.07±0.02	26±5
		5	356±3	335±12	0.12±0.04	25±3
	0.5	5	323±1	310±23	0.24±0.02	38±1

Parameters including PLGA concentration, chitosan concentration, FRR and chip design and geometries were screened to examine any potential advancement in NPs properties prepared by the MF-method. The 190 µm droplet junction straight chip was used for the screening experiments. As shown in **Table 3.10**, a steady increase in NPs size was observed with increasing the FRRs. To mitigate the fouling issues, the collection time had to be shortened to one minute to prevent significant blockages while collecting the sample. Increasing PLGA concentration resulted in a larger size of NPs; however, the change in size was not statistically significant for the different concentrations at 0.2 FRR. This finding was observed and explained with the previous two systems **(unmodified PLGA NPs in section 3.3.2 and PLGA-Eudragit NPs in section 3.3.3)**. The use of the 100 µm micromixer chip was limited by the significant fouling in the chip; hence, the synthesis process was not continuous, and several washing steps had to be done for a single sample collection. The Z-AVG size of NPs prepared using the micromixer chip using 0.8 FFR and TFR of 180 (µL/min) was 1164±482 nm with a PDI of 0.5±0.04. This can be explained by the large aggregates pushed from the chip to the sample while processing due to the significant fouling in this chip.

Table 3.10: Effect of PLGA concentration, chitosan concentration and FRRs on the properties of PLGA-Chitosan NPs prepared using 190 µm droplet junction straight channel chip

Chitosan concentration (mg/mL)	PLGA concentration (mg/mL)	TFR (µl/min)	FRR	Mixing time (ms)	Residence time (ms)	Z-AVG size (nm)	Number PSD (nm)	PDI	Zeta-p (mV)
0.1	1	449	0.2	470	99	205±2	161±7	0.11±0.03	14±2
		555	0.5	2865	80	221±4	184±7	0.11±0.01	19±1
	2	449	0.2	470	99	200±3	151±10	0.18±0.01	28±2
		555	0.5	1870	80	244±4	188±14	0.21±0.02	37±1
	5	449	0.2	470	99	216±6	172±5	0.13±0.02	28±1
1	1	449	0.2	470	99	312±4	328±4	0.19±0.02	41±2

No significant difference in the size of PLGA-Chitosan NPs fabricated from 1 (mg/mL) PLGA in acetone and 0.1 (mg/mL) of chitosan using CB-method (0.2 S/AS VR) or MF-method (190 µm droplet junction straight channel chip at 0.2 FRR) (P-value > 0.05). However, as shown in **Tables 3.9 and 3.10**, PLGA-Chitosan NPs prepared by the MF-method (FRR=0.2) were significantly smaller than the CB-method NPs (S/AS VR= 0.2) when using 5 (mg/mL) of PLGA and 0.1 (mg/mL) of chitosan (P-value < 0.05). Furthermore, it is noteworthy that samples prepared by the CB-method had a poor polymer wettability observed as a thin layer of the polymer on the surface of the nanosuspensions, which was not observed with MF samples.

It is expected that MF-method possesses a better control over chitosan deposition on the surface of PLGA NPs explained by the controlled laminar flow of the phases. Uncontrolled mixing can lead to random deposition of chitosan on the surface of NPs, which can be translated into larger NPs size and inter-variabilities. This is more expected to happen with the CB-method using quick solvent addition or with turbulent MF mixing such as that in 100 µm Micro Mixer chips, which might explain samples instabilities observed with quick solvent addition. Furthermore, this emphasises that Micro Mixer chips are not always the chip of choice for fabricating smaller NPs since this depends on the nature of the materials and NPs. CB-method (Dropwise solvent addition) and MF-method produced spherical NPs as shown by the TEM and SEM images in **Figure 3.18.**

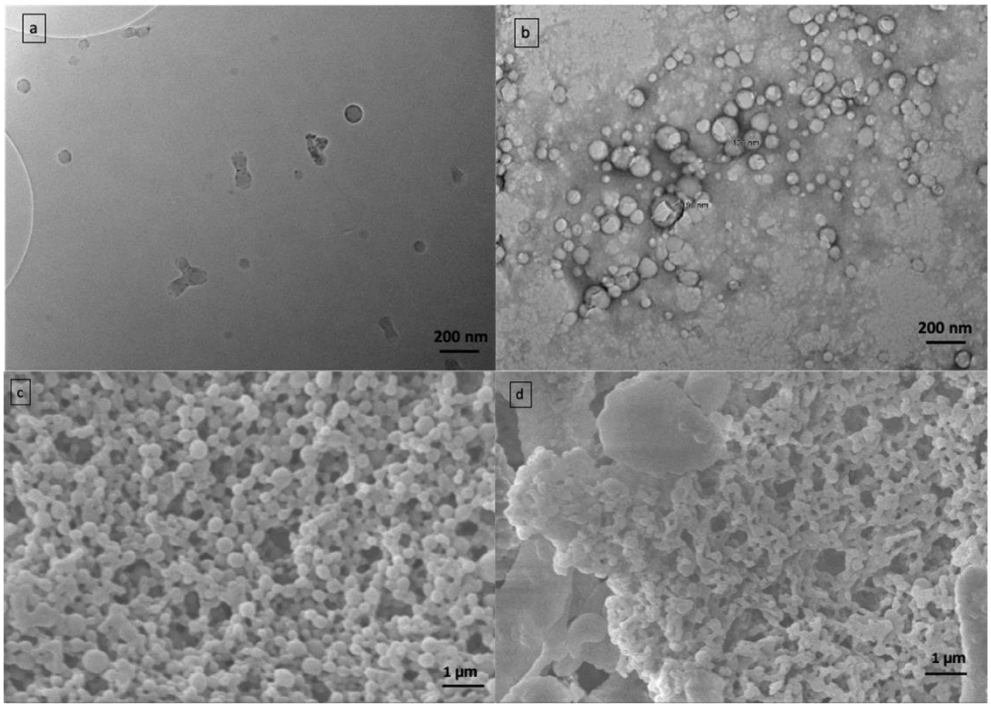

Figure 3.18: TEM of PLGA-Chitosan NPs prepared using (a) MF-method using 190 µm droplet junction straight chip at 0.5 FRR, (b) CB-dropwise method at 0.2 S/AS VR, SEM of PLGA-Chitosan NPs prepared using (c) CB-dropwise method at 0.2 S/AS VR and (d) MF-method using 190 µm droplet junction straight chip at 0.5 FRR. All samples were prepared using 5 (mg/mL) PLGA and 0.1 (mg/mL) chitosan.

3.3.5 Comparing the physicochemical properties of NPs prepared by CB-method and MF-method using ATR-FTIR spectroscopy

To examine any chemical changes between NPs prepared by CB-method and MF-method, samples were freeze-dried and tested by FTIR. **Table 3.11** shows a complete characterisation of Eudragit EPO and PLGA polymers peaks observed in the spectra. As shown in **Figure 3.19 a**, there is no difference in the structure of PLGA-Eudragit NPs prepared by CB or MF-method; however, peaks observed in Eudragit EPO and PLGA spectra were observed in CB and MF spectra. The formulations were compared to a physical mix of 1:1 Eudragit NP: PLGA NP. No significant difference was found in the ATR-FTIR spectra of the NPs prepared by the two methods, which suggests that the type of mixing (chaotic mixing in CB-method and controlled mixing in MF-method) did not ultimately change the chemical interactions between the polymers. Within the fingerprint region of the spectra, Eudragit EPO shows a band at 1147 cm-1, which represents the C-C stretching. At 1168 cm-1, a C-O stretching band is observed in the PLGA ATR-FTIR spectra. Although both peaks were observed in the physical mix, they were shifted to lower wavenumber in the spectra. This can be attributed to hydrophobic interactions. The C=O stretching bands of Eudragit and PLGA are at 1724 cm^{-1} and 1750 cm^{-1}, respectively

(Figure 3.19 b). The C=O band of Eudragit EPO was shifted from 1724 cm^{-1} to 1728 cm^{-1} in the PLGA-Eudragit NPs, indicating the likelihood of hydrogen bonding, whereas, as expected, this is not observed in the spectra of the physical mixes. This suggests that there is no observable difference between the two methods in terms of the NPs structure.

Table 3.11: ATR-FTIR characterisation of Eudragit EPO and PLGA polymers

Compound	**Chemical group**	**Peak wavenumber cm^{-1}**
Eudragit EPO	CH stretching for CH3	2951
	CH stretching for CH2	2822
	CH stretching for CH	2771
	C=O stretching	1724
	CH bending	1454
	C-O stretching	1387
	C-O-C stretching	1269, 1238
	C-C stretching	1147
PLGA	CH stretching for CH3	2998, 2950
	C=O stretching	1750
	CH bending	1452
	Carboxylic acid OH bending	1423
	C-O stretching	1384
	C-O-C stretching	1270
	C-O stretching	1168, 1131, 1086

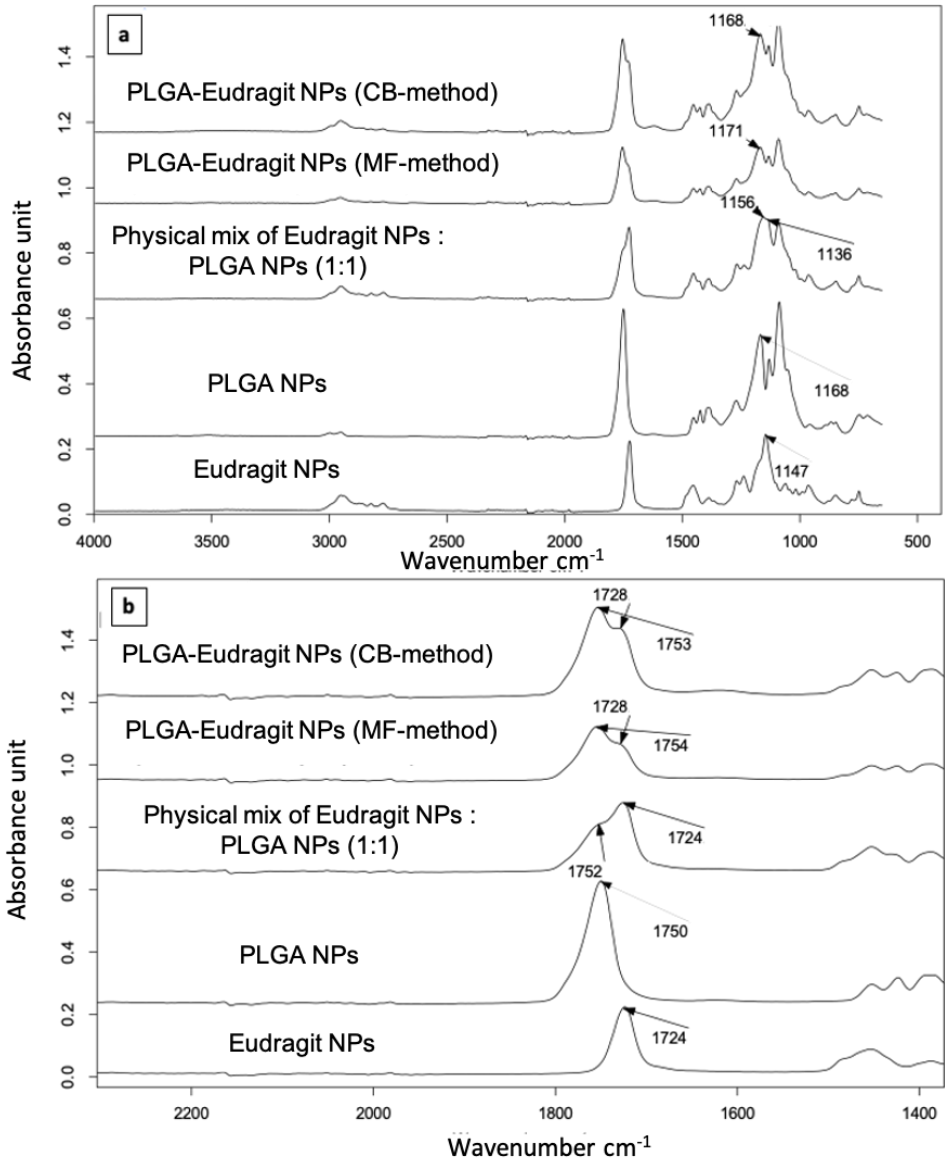

Figure 3.19: FTIR characterisation of PLGA, Eudragit EPO, PLGA-Eudragit NPs prepared CB-method (quick solvent addition), PLGA-Eudragit NPs prepared by MF-method at wavenumber; (a) 500-4000 cm^{-1} and (b) 1400-2200 cm^{-1}.

For PLGA-Chitosan NPs, there was no difference in the chemical structures of the NPs prepared by the two methods, as shown in **Figure 3.20**. Although a peak was observed in the chitosan spectrogram at 3346 cm^{-1}, which can be related to N-H stretching, this peak was not observed in the physical mix or the PLGA-Chitosan NPs prepared by CB-method or MF-method. Considering the Zeta-p data provided before, which confirm the surface modification of PLGA NPs, the absence of the peak can be related to the low Chitosan: PLGA mass ratio (1:100), which might be below the sensitivity level of the ATR-FTIR machine.

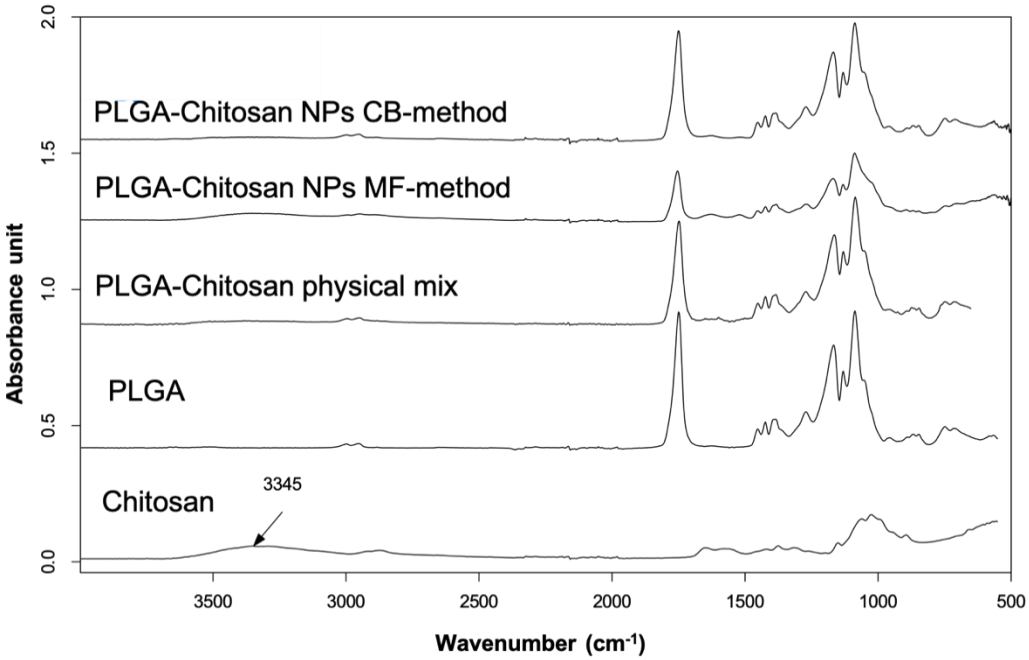

Figure 3.20: FTIR characterisation of PLGA, Chitosan, 1:100 Chitosan: PLGA physical mix, PLGA-Chitosan NPs prepared by MF-method and PLGA-Chitosan prepared by CB-method.

3.3.6 Freeze drying and stability studies

To evaluate the influence of the preparation method on the shelf colloidal stability of NPs, the particle size was monitored over a week at room temperature. As shown in **Figure 3.21 a and b**, PLGA NPs prepared by CB/MF method were found to be stable for a week. PLGA-Eudragit NPs and PLGA-Chitosan NPs prepared by CB/MF method had a good stability profile over a week, as shown in **Figure 3.21 c-f**. This suggests no actual difference between CB and MF method in terms of fabricating stable NPs. To provide an insight into the stability of these NPs in physiological conditions, samples were incubated in 7.4 PBS and size was monitored by DLS. Unmodified PLGA NPs were unstable in 7.4 PBS with instant precipitation of NPs after diluting the sample in 7.4 PBS. However, PLGA-Eudragit NPs were found to be stable in 7.4 PBS for a week, as shown in **Figure 3.22.**

On the contrary, the size of PLGA-Chitosan NPs suspended in 7.4 PBS increased from 216±6 nm for fresh sample to 342±11 nm after 4 hours, followed by a significant increase after 24 hours (Z-AVG size after 24 hours= 811±314 nm). This can be related to the PKa values since the amine group of the chitosan has a PKa of around 6 [35]. Therefore, it is expected that an increase in pH from around 5 to 7.4 would result in neutralising the amine groups. Alternatively, Eudragit EPO has a tertiary amine group PKa of around 10, suggesting a high

positive charge on the surface of PLGA-Eudragit NPs in 7.4 PBS medium, which can minimise the aggregations and improve the colloidal stability of the NPs at this pH. This suggests that Eudragit is a potential candidate for modifying the surface of PLGA NPs while maintaining NPs stability in 7.4 PBS.

After freeze-drying, the formulations using 1% Trehalose as a cryoprotectant, PLGA NPs and PLGA-Chitosan NPs were non-redispersible, unlike PLGA-Eudragit NPs that were redispersible into the nanometre range after freeze-drying. Freeze-dried PLGA-Eudragit NPs were resuspended in 7.4 PBS, and the Z-AVG size before and after freeze-drying was compared. Z-AVG was found to be 115±2 nm and 172±3 nm before and after freeze-drying, respectively (re-dispersibility index ~ 1.5). This emphasises the appealing properties of Eudragit in improving the redispersibility of PLGA NPs after freeze-drying compared to chitosan or unmodified PLGA NPs.

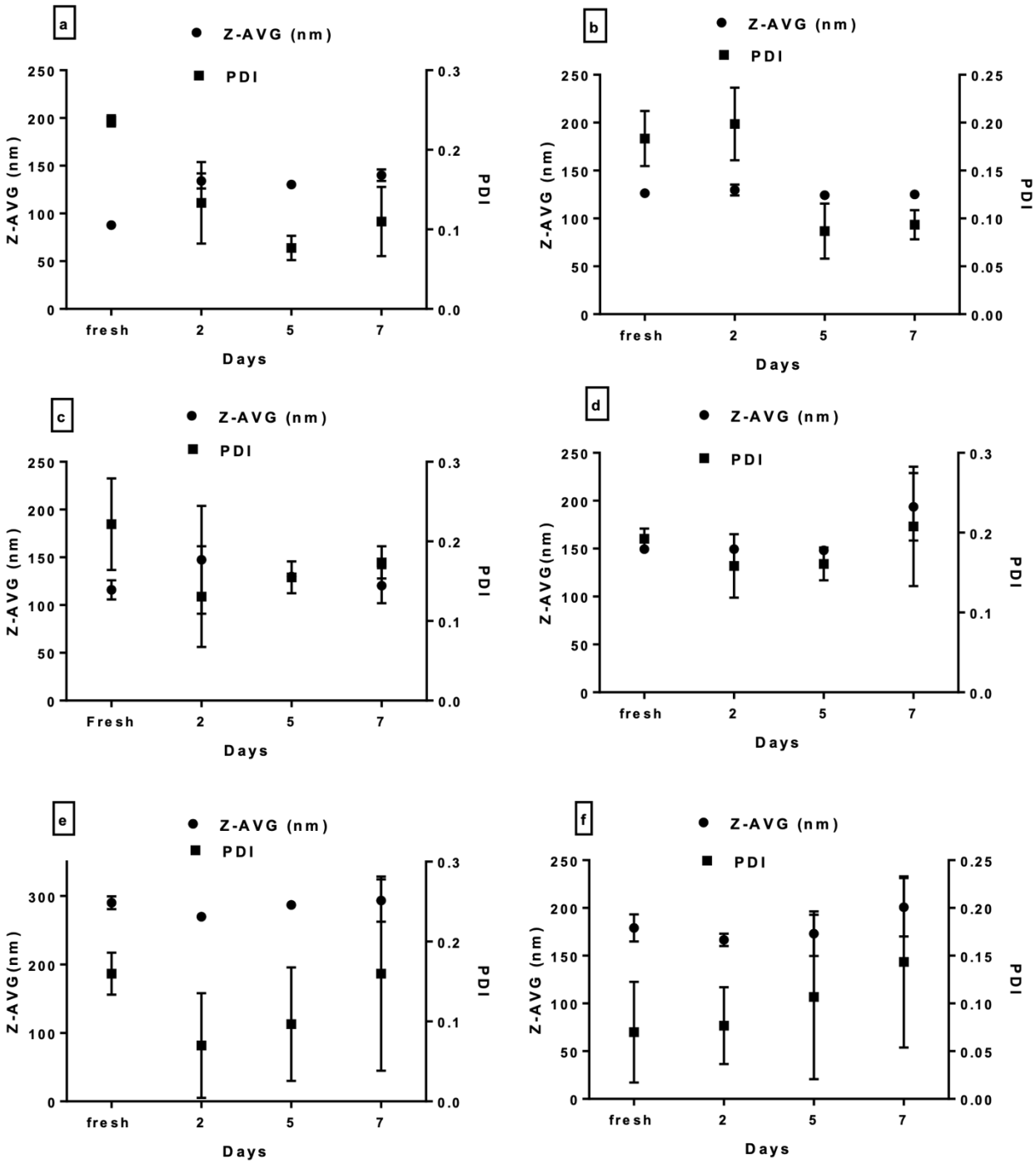

Figure 3.21: Shelf stability of : (a) PLGA NPs prepared by CB-method (1 mg/mL PLGA in acetone using 0.2 S/AS VR), (b) PLGA NPs prepared by MF-method (1 mg/mL PLGA in acetone at 0.2 FRR, 120 µl/min), (c) PLGA-Eudragit NPs prepared by CB-method (quick solvent addition) (5 mg/mL PLGA-Eudragit in acetone using 0.2 S/AS VR) , (d) PLGA-Eudragit NPs prepared by MF-method (2 mg/mL of PLGA-Eudragit in acetone using 0.5 FRR, 849 µl/min TFR), (e) PLGA-Chitosan NPs prepared by CB-method (5 mg/mL of PLGA in acetone with 0.1 mg/mL of chitosan using 0.2 S/AS VR) , (f) PLGA-Chitosan NPs prepared by MF-method (5 mg/mL of PLGA in acetone with 0.1 mg/mL of chitosan using 0.2 FRR and 449 µl/min TFR). The error bars represent the standard deviation and n=3.

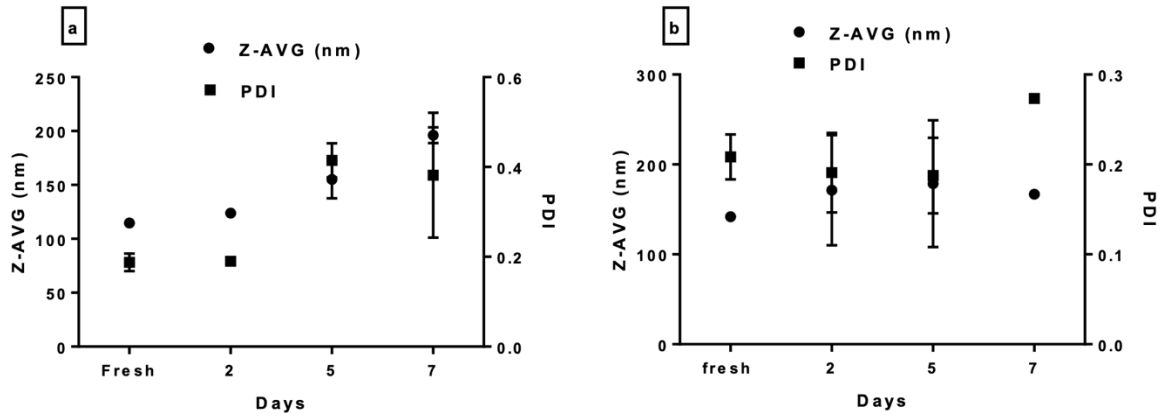

Figure 3.22: Stability of PLGA-Eudragit in 7.4 PBS prepared by: (a) CB-method (quick solvent addition) (5 mg/mL PLGA-Eudragit in acetone using 0.2 S/AS VR, (b) MF-method (2 mg/mL of PLGA-Eudragit in acetone using 0.5 FRR, 849 µl/min TFR). The error bars represent the standard deviation and n=3.

3.4 Conclusion

Microfluidic technology has been proposed as an advanced superior method for controlled nanoprecipitation compared to conventional bulk nanoprecipitation. Several appealing advantages have been related to microfluidics assisted nanoprecipitation, including NPs size reduction, size tunability, better reproducibility and controlled mixing within the chip compared to a larger size, higher polydispersity and batch to batch variations obtained with conventional bulk nanoprecipitation. However, this study revealed that this depends on the processing parameters, nature of the materials used, and the chip's design.

For unmodified PLGA NPs, it was found that CB-method and MF-method are both feasible for size tuning within the same size range. PLGA NPs prepared by the CB-method were found to be smaller than those prepared by the MF-method using a 190 µm droplet junction straight channel chip and 100 µm 3d-flow-focusing straight channel chip However, using the 100 µm Micro Mixer chip resulted in a significant decrease in the size of PLGA NPs to be 14±1 nm smaller than the NPs prepared by the CB-method. However, its use was limited by significant fouling observed with higher PLGA concentrations. Size tunability and small NPs size were achievable even when mixing time was much longer than the residence time, as the data at high TFRs showed. This suggests no optimum mixing time range where size tunability or smaller NPs can be obtained. Furthermore, this proposes that MF-method can be used at high TFRs to prepare NPs that possess similar characteristics as NPs prepared at conditions where mixing

time is shorter than residence time, which promotes its use as a quick screening tool for NPs formulations and mitigates fouling issues.

For PLGA-Eudragit NPs, the CB-method can be used to tune the size of NPs when the solvent phase is added dropwise to the antisolvent phase but not with quick solvent addition. However, significantly smaller PLGA-Eudragit NPs were fabricated using CB-method with quick solvent addition compared to those prepared by dropwise addition or MF-method. For PLGA-Chitosan NPs, smaller NPs were prepared by the MF-method (FRR=0.2) compared to the CB-method (S/AS VR= 0.2) when using 5 (mg/mL) of PLGA and 0.1 (mg/mL) of chitosan; however, the difference in size between the two methods was not significant at lower PLGA concentrations.

On the contrary, using the 100 µm Micro Mixer chip resulted in significantly larger PLGA-Chitosan NPs with a wide size distribution due to the significant fouling. Both methods resulted in the formation of spherical NPs. Although the MF-method is proposed as a superior method for controlled nanoprecipitation to reduce batch to batch variations, the CB-method was found to be as robust as the MF-method. Formulations prepared using CB-method and MF-method had a good shelf stability profile for up to one week. Also, no difference in the chemical structure of the NPS prepared by the two methods was observed.

Chapter 4

Assessment of Microfluidic-Assisted Synthesis of Polymeric Nanoparticles for Plasmid DNA Delivery

4.1 Introduction

Gene therapy is a biomedical field that uses a potential gene delivery strategy for targeted treatment of autoimmune and gene associated diseases [3,126,229]. The targeting relies on delivering the introduced genes to the pathological cells where they can instigate a change in the genes expression to cease the progression of a disease. Since Naked DNA delivery is reported inefficient due to their negative charge and susceptibility to degradation by serum nucleases, polymeric NPs (PNPs) have drawn significant attention as potential pDNA carriers [213,222].

PLGA NPs have been reported as a potential pDNA carrier when their surface is modified by a cationic polymer such as polymethacrylates (Eudragit) or chitosan [7,150,213,222]. Although there are numerous biomedical applications of this strategy, many barriers mitigate the delivery and the clinical outcome of this therapy. Most of these challenges lie in ascertaining an ideal pharmaceutical formulation that can circumvent biological barriers and effectively deliver genetic molecules. This mainly depends on the NPs fabrication method due to its significant impacts on NPs size, size distribution and surface charge, which can be translated into variable results in cellular uptake, gene encapsulation efficiency and gene transfection efficiency[12,17,95].

The objectives of this chapter are:

- To fabricate PLGA-Eudragit NPs in a one-step method using conventional nanoprecipitation (CB-method) and microfluidic-assisted nanoprecipitation (MF-method) that can efficiently load p-DNA encoding a green fluorescent protein (GFP).
- To evaluate the impact of the cell culture parameters on pDNA transfection efficiency using transfecting agents as positive controls. Third, examine the pDNA transfection efficiency of PLGA-Eudragit NPs prepared by the two methods using identical compositions and closely matched processing parameters.
- To explore the translational potential of microfluidic technology as a formulation manufacturing method for nanoparticle-based gene delivery platforms compared to conventional methods.

4.2 Materials and methods

4.2.1 Materials

Microfluidics Droplet Junction straight channel Chip (190µm etch depth) was purchased from (Dolomite Microfluidics, UK). Harvard syringe pumps (standard infuse/withdraw pump 11 Elite) were purchased from Harvard Apparatus (US).

4.2.2 Preparation of PLGA-Eudragit by CB and MF nanoprecipitation method

For CB-nanoprecipitation, PLGA-Eudragit NPs were prepared using 5 (mg/mL) 1:1 Eudragit: PLGA in acetone and a 0.2 (1:5) overall solvent/anti-solvent (S/AS) volume ratio. NPs were prepared by quick addition of 1 mL of the organic solvent phase into 5 mL of the anti-solvent phase using micropipette under constant stirring at room temperature to ensure solvent evaporation. For MF-nanoprecipitation, 2 (mg/mL) of 1:1 Eudragit: PLGA in acetone was used as the solvent phase and NPs were fabricated using a 190 µm droplet junction straight channel chip with deionized water as the antisolvent phase. The flow rate of the solvent phase was set to 283 (µl/min), while the flow rate of the anti-solvent was set to 566 (µl/min) to achieve flow rate ratios (FRR) of 0.5 and TFR of 849 (µl/min). The final concentration of NPs prepared by the two methods is 1 (mg/mL). All NPs formulations were stored in solution for characterisation and stability testing.

4.3 Results and discussion

4.3.1 PLGA-Eudragit solubility and miscibility studies

The structure of PLGA-Eudragit NPs prepared by nanoprecipitation can be predicted based on the miscibility of the two polymers and their solubilities in the solvent/anti-solvent (S/AS) binary mixture. As illustrated in **Figure 4.1 a**, upon mixing the organic phase composed of 1:1 Eudragit: PLGA in acetone with the aqueous antisolvent phase (water), it is expected that homogenous nucleation will be induced by the increase in the solute concentration above the critical nucleation concentration (Cn) needed to induce nucleation. The point where the supersaturation of each polymer is achieved depends on their solubilities in the S/AS binary mixture. To ensure simultaneous precipitation of both species, both should have close supersaturation degrees and very low solubilities in the binary mixture leading to simultaneous precipitation. Therefore, the solubilities of the PLGA and Eudragit in acetone/water mixtures with a range of S/AS ratios were measured. As shown in **Figure 4.1 b**, both polymers have similarly low solubility in the acetone/water mixtures up to the S/AS ratio of 1:1(v/v). However, Eudragit becomes significantly more soluble in the mixture than PLGA when the solvent content exceeds 50% by volume. in this study, PLGA-Eudragit NPs were prepared using 1:5 (0.2 S/AS) volume ratio using CB-nanoprecipitation method and 0.5 flow rate ratio (FRR) using MF-method. At these low S/AS volume ratios, assuming completely homogeneous mixing, it can be expected that Eudragit and PLGA molecules will be randomly distributed throughout the solvent and will reach the supersaturation (C_n) upon mixing with the antisolvent phase simultaneously. De-mixing of separate Eudragit and PLGA is not expected if precipitation is sufficiently rapid, suggesting by this the formation of NPs containing a random distribution of both species.

Miscibility studies evaluated using DSC-based thermal methods, particularly the glass transition temperature (T_g) was used in the literature to examine polymer-polymer miscibility and detect any phase separation [218,230–232]. A single (T_g) (at a temperature between the T_gs of the pure polymers) should be detected from the solid dispersion mixture formed by either thermal or solvent evaporation methods if the two polymers were completely miscible at the used ratio. However, two separate T_gs should be detected from a physical mixture of the two polymers if mixed without forming a solid dispersion. As seen in **Figure 4.1 c,** a single T_g at a higher temperature than the T_g of pure PLGA (lower than the T_g of pure Eudragit) was seen for physical mixes containing 10 and 20% of Eudragit. Based on this data, it can be assumed that

there is a level of dissolution for Eudragit in PLGA. At 30-50% Eudragit, a separation of Eudragit and PLGA T_gs can be seen, suggesting the saturation of PLGA with Eudragit where excess Eudragit transition can be observed. When 60% PLGA: Eudragit was used, a low T_g appears at the same temperature as seen for pure PLGA, implying a phase separation with a pure or PLGA-rich phase and a second phase. Considering that the second T_g is slightly lower than the T_g of the pure Eudragit, it can be assumed that the second phase is a mixture of Eudragit-PLGA. This lower temperature peak shifts to a higher temperature by increasing the Eudragit content, demonstrating a higher content of Eudragit in the PLGA-rich phase. An apparent T_g at a reduced temperature compared to pure Eudragit can be observed when using 90% Eudragit, suggesting some dissolution of PLGA; however, the asymmetry in the peak can still be related to the presence of PLGA-rich phase. The results of the miscibility study of the physical mixtures demonstrate that at a solid-state, Eudragit and PLGA are partially miscible when the mixing process is slow (mixing achieved by heating within the DSC). From these results, it can be assumed that with nanoprecipitation, one would expect at a 1:1 polymer ratio that two transitions would be observed (as the physical mixture data shown in **Figure 4.1 d**) if the co-precipitation was slow compared to the de-mixing. The fact that a single Tg (between the T_gs of pure PLGA and Eudragit) can be seen for Eudragit-PLGA NPs prepared by both CB and MF methods suggests that the system is mixed at the molecular level.

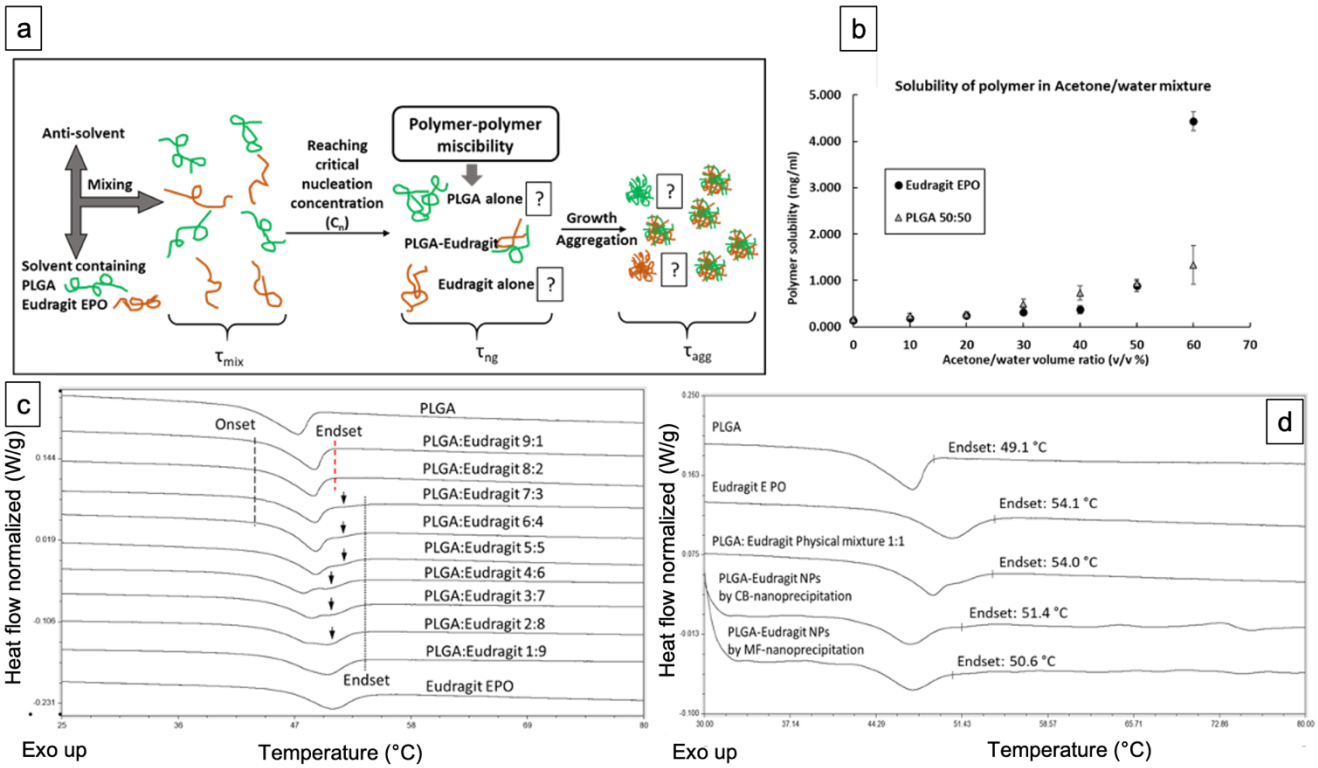

Figure 4.1: (a) Schematic illustration of the formation of NPs via nanoprecipitation; (b) Solubilities of the polymer in action/water mixtures; (c) DSC results of the T_g regions of the physical mixtures of PLGA and Eudragit; (d) DSC results of the NPs in comparison to the raw materials and physical mixture of PLGA and Eudragit with 1:1 ratio.

4.3.2 Physicochemical characterization of blank Eudragit-PLGA NPs prepared by CB and MF assisted nanoprecipitation

As discussed in **chapter 3**, PLGA-Eudragit NPs prepared by CB-nanoprecipitation using a polymer concentration of 5 (mg/mL) and S/AS volume ratio of 0.2 (1:5) were smaller compared to those prepared by MF-nanoprecipitation with an average size of 98±13 nm ($P < 0.05$**)**. The average size of PLGA-Eudragit NPs prepared by MF-nanoprecipitation using a 190-µm droplet junction chip and 2 (mg/mL) of 1:1 Eudragit: PLGA at 0.5 FRR was 170±3 nm. PLGA-Eudragit NPs prepared by both methods were spherical, as shown by TEM data in **chapter 3**. Also, FTIR data shown in **chapter 3** suggested no observable difference between the two methods in terms of NPs structure. The polydispersity index (PDI) values of PLGA-Eudragit NPs prepared by both methods were below 0.3, suggesting the formation of monodisperse NPs. The zeta-potential of PLGA-Eudragit NPs prepared by CB-method was 29±4 (mV) compared to 37±6 (mV) for NPs prepared by MF-method.

4.3.3 Preparation and purification of pDNA

pEGFP-C1 was efficiently transformed into DH5α competent E. coli. The purity of the extracted pDNA from the bacterial cell pellets can greatly influence the outcome of the transfection efficiency study. For an efficient and successful pDNA transfection, the pDNA should be free from proteins, chemical and biological contaminations, which can affect cells viability and transfection efficiency. The (A260/280) and (A260/230) for the purified pEGFP-C1 was found to be 1.88 and 2, respectively, suggesting by this a pure pDNA [233]. As shown in **Figure 4.2,** the integrity of the purified pEGFP-C1 was confirmed by running it on 1% agarose gel against a control of pEGFP-C1.

Figure 4.2: Gel electrophoresis for L-1kb ladder; C- pEGFP-C1 control and P-purified pEGFP-C1.

4.3.4 Optimisation and characterization of pDNA loaded PLGA-Eudragit NPs

As the particle size and zeta potentials are considered the key parameters for systemic administration and transfection efficiency of NPs, several NP: DNA mass ratios were investigated to optimise the DNA loading, the size and the surface charge of the particles. In general, the pDNA-loaded NPs prepared by MF-nanoprecipitation were larger in size in comparison to those prepared by CB-nanoprecipitation (**Figure 4.3**). No significant change in size was observed after DNA loading, and the size of the pDNA-loaded NPs was not affected by the NP: DNA mass ratio (**Figure 4.3 a, b, and c**). The NPs obtained using lower NP: DNA mass ratios were not stable. The loading of the pDNA reduced the surface charge of the NPs prepared by CB-nanoprecipitation, but no such impact was seen on the NPs prepared by MF-nanoprecipitation. Varying the NP: DNA ratio shows no effect on the surface charge of the pDNA-loaded NPs prepared by both methods (**Figure 4.3 b**).

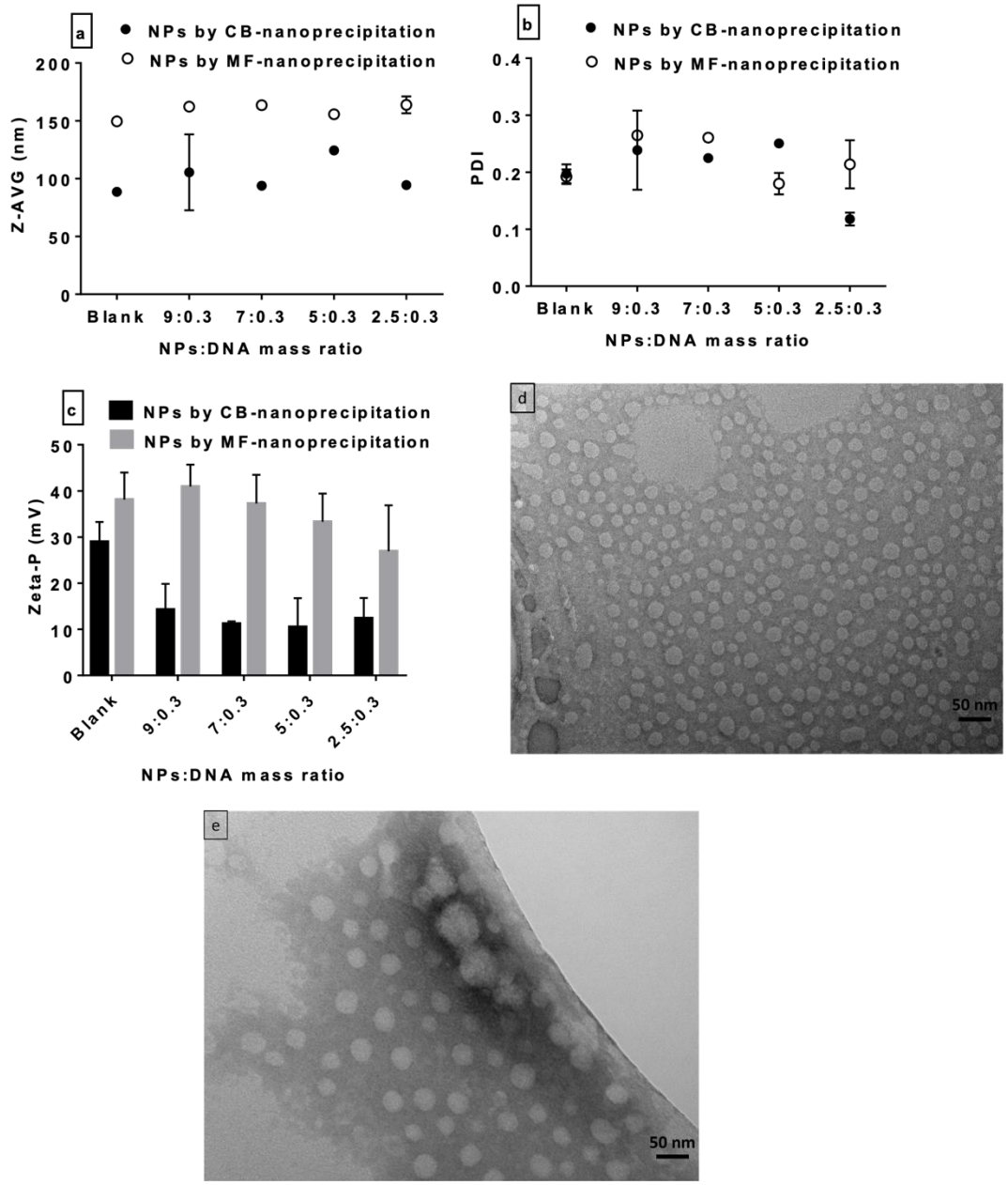

Figure 4.3: Characterisation of pDNA-loaded PLGA-Eudragit NPs: (a) the effect of NP: DNA mass ratio on the size of NPs prepared by CB-nanoprecipitation method and MF-nanoprecipitation method (b) the effect of NP: DNA mass ratio on PDI of NPs prepared by CB-nanoprecipitation and MF-nanoprecipitation method, (c) the effect of NP: DNA mass ratio on surface charge of NPs prepared by CB-nanoprecipitation and MF-nanoprecipitation method; the TEM images of the pDNA-loaded PLGA-Eudragit NPs prepared at NP:DNA mass ratio of 2.5:0.3 by (d) MF-nanoprecipitation and (e) CB-nanoprecipitation methods. The Error bars represent the standard deviation and n=3.

4.3.5 pDNA loading efficiency of PLGA-Eudragit NPs estimated by gel electrophoresis

The electrophoretic mobility of the DNA within agarose gel was used to prove the plasmid loading and assess the difference in the extent of plasmid entrapment for the two formulations [6,150,151]. As shown in **Figure 4.4 a**, PLGA-Eudragit NPs prepared CB-nanoprecipitation had a 100% plasmid entrapment efficiency at all the NPs: DNA mass ratios tested (from 9:0.3 down to 1.3:0.3). In contrast, those prepared by MF-nanoprecipitation only show a 100% entrapment efficiency for the two highest NPs: DNA mass ratios (9:0.3 and 7:0.3), with 9 %, 61% and 59 % unloaded plasmid in the formulations with 5:0.3, 2.3:0.3 and 1.3:0.3 NPs: DNA mass ratios, respectively **(Figure 4.4 b)**. These findings suggest that NPs prepared by CB-nanoprecipitation are more efficient for loading DNA than the ones prepared by MF-nanoprecipitation. We speculate that this is mainly due to the smaller particle size, thus larger surface area per unit mass of the CB-NPs. In the DNA binding experiments, a constant weight of particles was used. Because of the size, difference this implies that different numbers of NPs would be present. The mass of the particle is given by $\frac{4}{3}\pi r^3\rho$. Where r is the radius of the particle and ρ is its density. A fixed weight of particles will contain N particles, so for a radius of r_1, there will be N_1 particles, as shown by Eq. (4.1).

$$w = N_1 \frac{4}{3}\pi r_1^3 \rho \qquad \text{Eq. (4.1)}$$

According to this, if there are two sets of particles of the same weight, w, then the relation can be given by Eq. (4.2).

$$w = N_1 \frac{4}{3}\pi r_1^3 \rho = N_2 \frac{4}{3}\pi r_2^3 \rho. \text{ So } N_1/N_2 = (r_2/r_1)^3 \qquad \text{Eq. (4.2)}$$

Since the hydrodynamic particle sizes of the CB- and MF-NPs are averagely 98 and 170 nm, this leads to the ratio of particles numbers of CB-NPs to MF-NPs of about 5.2:1 as calculated from Eq. (4.2). The total surface area (SA) of the particles in weight is given by Eq. (4.3):

$$SA_i = N_i 4\pi r_i^2 \qquad \text{Eq. (4.3)}$$

Based on Eq. (4.3), the ratio of the total surface area of the CB- and MF-NPs available for DNA loading is given by Eq. (4.4).

$$\frac{SA_1}{SA_2} = \frac{N_1 4\pi r_1^2}{N_2 4\pi r_2^2} = 5.2 \times \frac{r1^2}{r2^2} \qquad \text{Eq. (4.4)}$$

By solving Eq. (4.4) using r_1= 98 nm (CB-NPs) and r_2= 170 nm (MF-NPs), $\frac{SA_1}{SA_2} = 1.72$ so the total surface area of a unit weight of MF-NPs (SA_2) that is available for pDNA loading is about 57% of that of the same weight of CB-NPs. This correlates well to the pDNA loading seen in **(Figure 4.4).**

However, when the ratio of NPs: DNA is 1.3:0.3, there is sufficient surface area available of the CB-NPs to take up all the pDNA. The total surface area available for the MF-NPs (1.3:0.3 ratio) is about half of that of the CB-NPs, and correspondingly takes about half the amount of the pDNA. When the ratio of NPs to pDNA is 2.5:0.3, the total surface area available of the MF-NPs is equal to the surface area of the CB-NPs when the ratio of the NPs: DNA is 1.3:0.3. Therefore, it would be expected that there would be sufficient surface area for the MF-NPs to take up all the pDNA. However, this is not the case, as seen in **Figure 4.4**. This implies either that the hydrodynamic radii obtained by DLS do not represent the effective radii of the particles or that there are significant differences in the surfaces of the two types of particles. Such a difference is consistent with differences in zeta potential behaviour seen when the particles are loaded with pDNA.

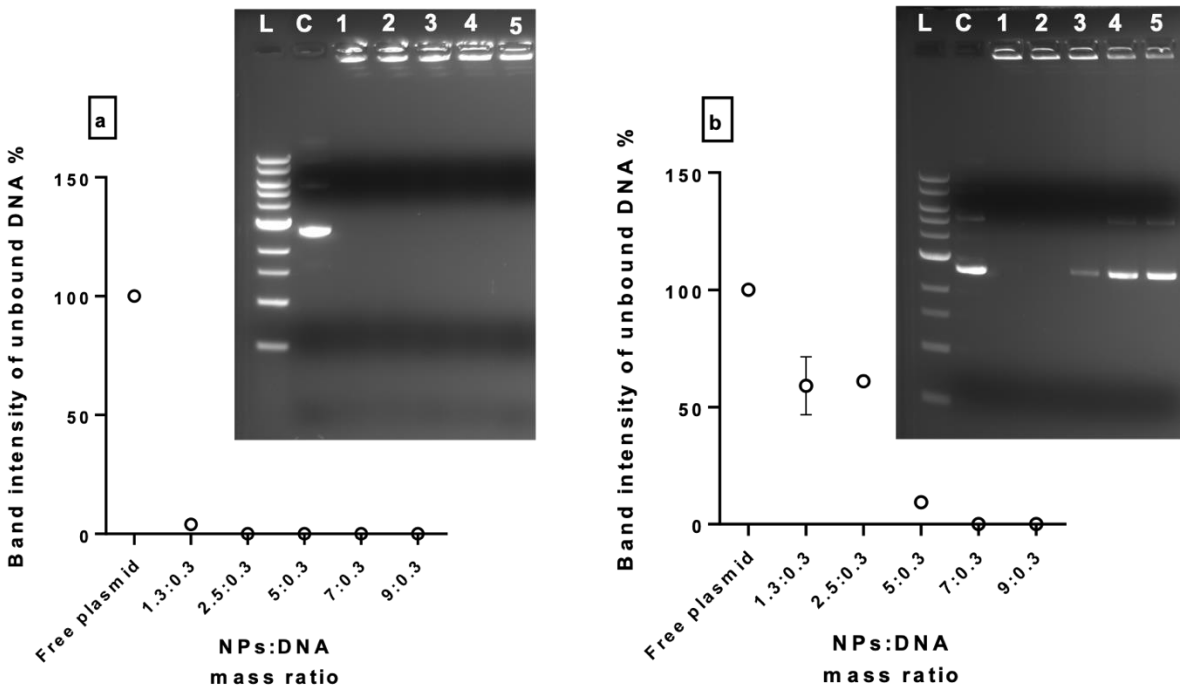

Figure 4.4: Gel retardation assay of the DNA band intensity (with insert image) for PLGA-Eudragit NPs prepared (a) by CB-nanoprecipitation and (b) by MF-nanoprecipitation. The abbreviations used in the inserted images stand for: L-1kb ladder; C-pDNA control; 1-9:0.3 NPs: DNA mass ratio; 2-7:0.3 NP: DNA mass ratio; 3-5:0.3 NP: DNA mass ratio; 4-2.5:0.3 NP: DNA mass ratio; 5-1.3:0.3 NP: DNA mass ratio. The Error bars represent the standard deviation and n=3.

4.3.6 Evaluating the impact of cell culture parameters on pDNA transfection efficiency (GFP%) into A549 cells using transfection reagents and Eudragit-PLGA NPs

As shown in **Figures 4.5, 4.6 and 4.7**, the lowest pDNA transfection efficiency (2%) using FuGENE HD: DNA 3:1 was observed when serum-free RPMI medium was used as the transfection medium. Although the addition of 1% serum has improved the viability of A549 cells and increased the transfection efficiency to (37%), the highest transfection efficiency of (42%) was achieved with Opti-MEM reduced serum medium. The improvement in transfection efficiency with serum addition can be related to its positive influence in improving cells viability. Although the presence of serum in the transfection medium can improve the pDNA transfection efficiency, this can be limited when using cationic lipid transfection reagents due to their interaction with some serum proteins. Opti-MEM reduced serum medium was found optimal for maintaining good cells viability and transfection efficiency according to these results. Hence, Opti-MEM reduced serum medium was used as the transfection medium in the following experiments.

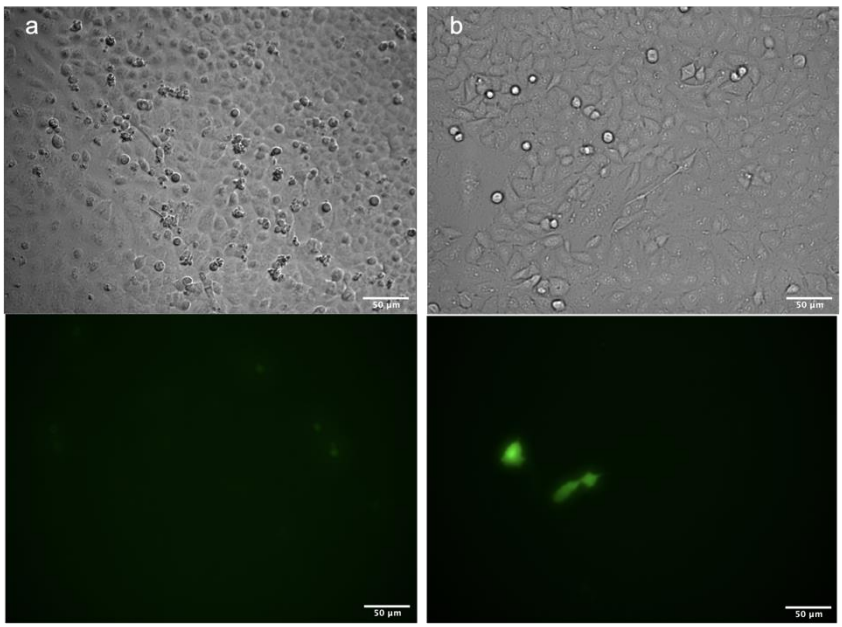

Figure 4.5: Transfection efficiency in A549 using 0% serum and 1×10^5 cells/well seeding density transfection analysed by fluorescent microscope (bright field image at the top and fluorescent image at the bottom of each panel) for: a) plasmid DNA as negative control; b) 3:1 FuGENE HD: DNA as positive control (GFP%= 2%). Scale bars represent 50 µm.

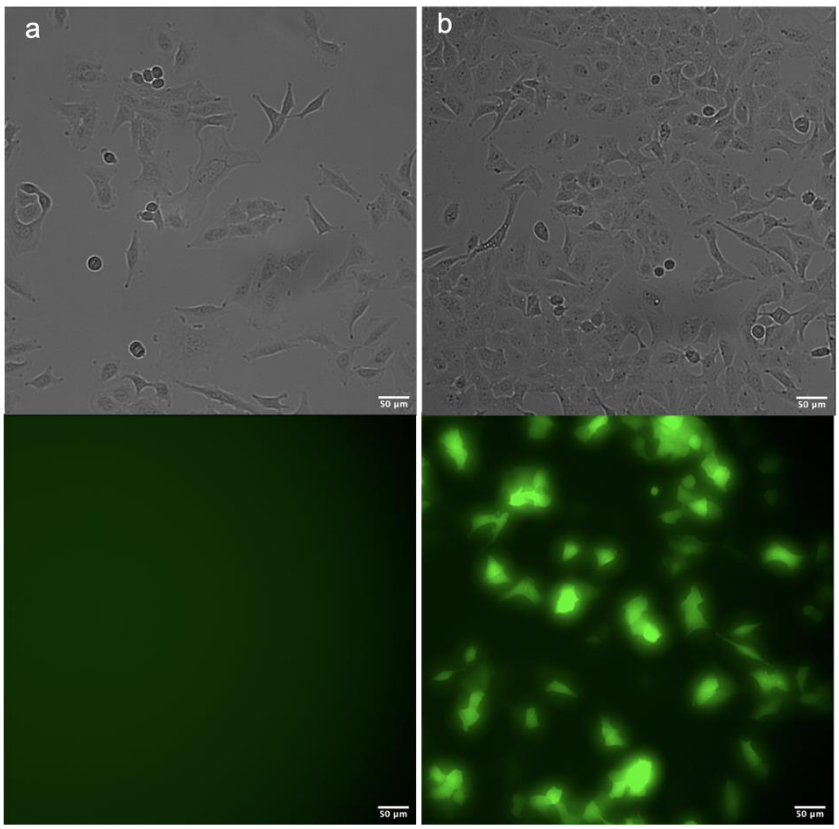

Figure 4.6: Transfection efficiency in A549 using 1% serum transfection and 1×10^5 cells/well seeding density analysed by fluorescent microscope (bright field image at the top and fluorescent image at the bottom of each panel) for: a) plasmid DNA as negative control; b) 3:1FuGENE HD: DNA as positive control (GFP%= 37%). Scale bars represent 50 µm.

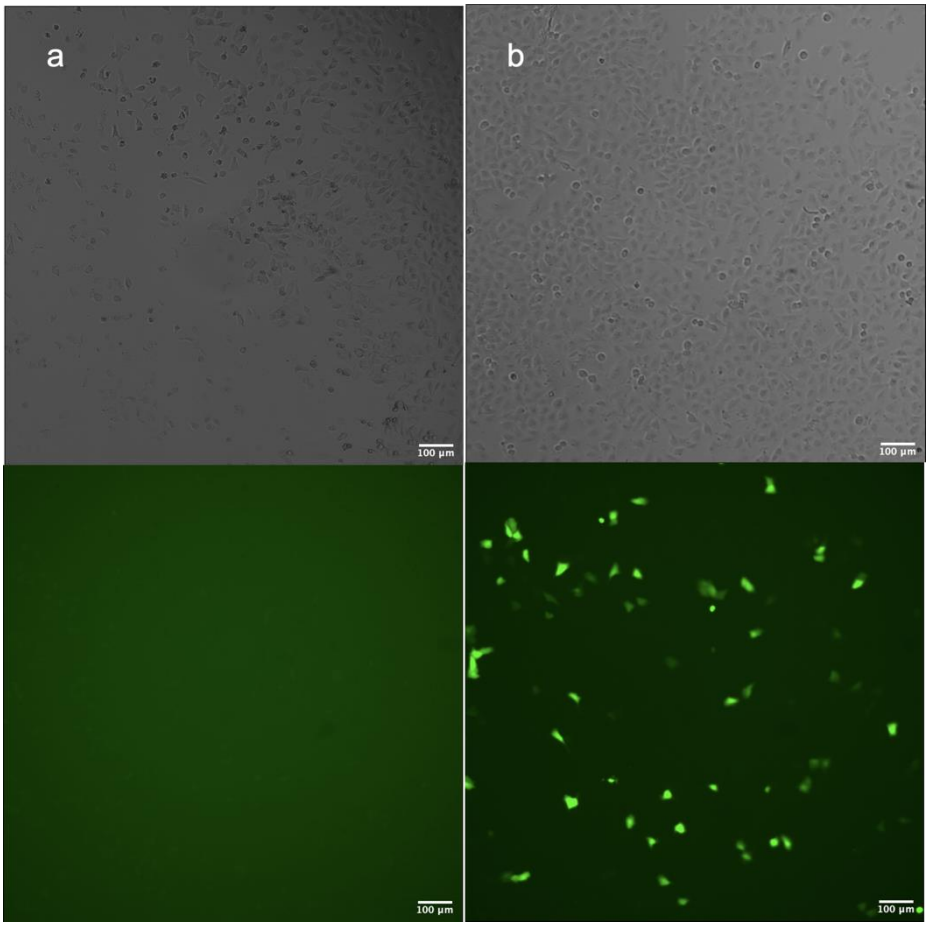

Figure 4.7: Transfection efficiency in A549 using Opti-MEM reduced serum transfection medium and 1×10^5 (cells/well) seeding density analysed by fluorescent microscope (bright field image at the top and fluorescent image at the bottom of each panel) for: a) plasmid DNA as negative control; b) 3:1FuGENE HD: DNA as positive control (GFP%= 42%). Scale bars represent 100 µm.

Cells seeding density is another factor that significantly influences gene transfection efficiency. Actively dividing cells are needed to ensure efficient uptake of the introduced plasmid. Hence optimizing the cells density is critical since high cells density results in diminished contact and hindered pDNA uptake resulting in lower transfection efficiency. Similarly, using low cells density would result in low transfection efficiency due to poor cellular contact and growth. However, as shown in **Figures 4.7 and 4.8**, there is no significant difference in transfection efficiency (GFP%) for A549 cells transfected with FuGENE HD: DNA 3:1 using two different seeding densities 1×10^5 and 5×10^4 cells/well), suggesting that both densities can be optimal for gene transfection.

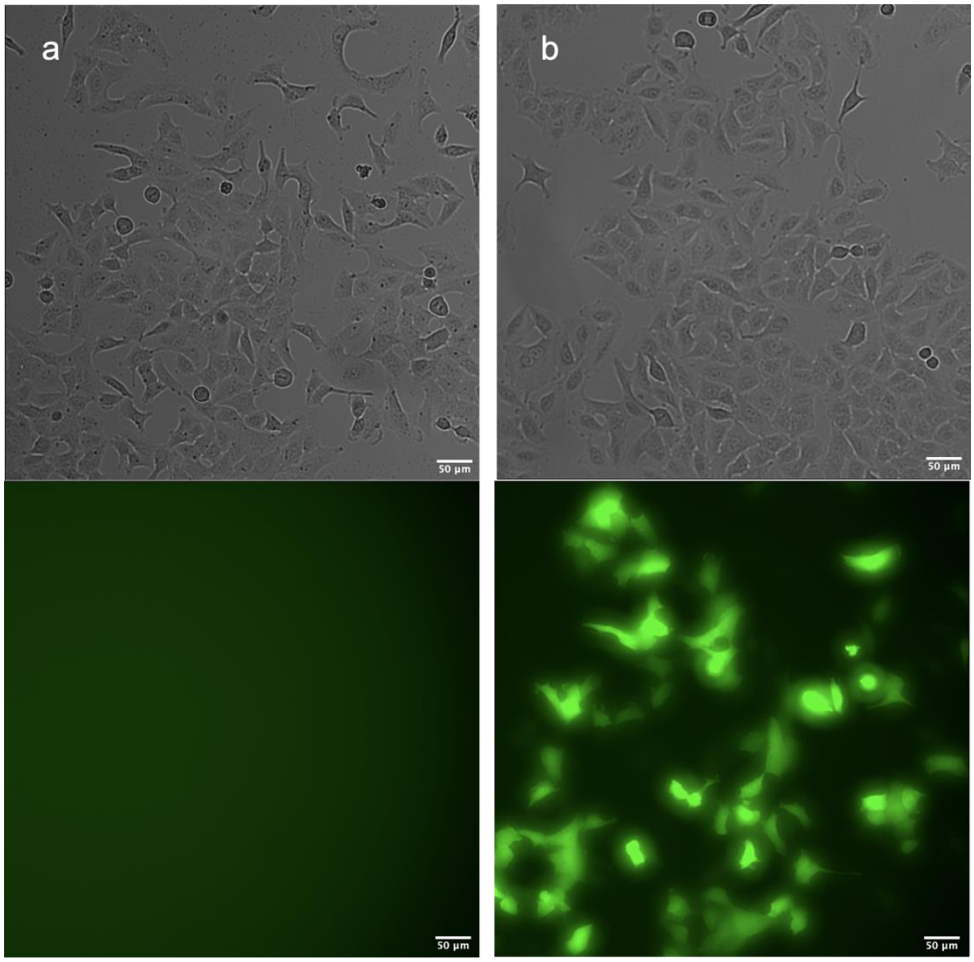

Figure 4.8: Transfection efficiency in A549 using Opti-MEM reduced serum transfection medium and 5×10^4 (cells/well) seeding density analysed by fluorescent microscope (bright field image at the top and fluorescent image at the bottom of each panel) for: a) plasmid DNA as negative control; b) 3:1FuGENE HD: DNA as positive control. Scale bars represent 50 µm.

The choice of the transfection reagent (positive control) and the optimisation of the transfection reagent: DNA ratio are among the essential prerequisites for achieving high transfection efficiency. As shown in **Figure 4.9**, FuGENE HD: DNA 3:1 had the lowest transfection efficiency of about (37%) compared to (52%) with increasing the FuGENE HD: DNA ratio to 4:1. However, the transfection efficiency was significantly higher with 1:1 Lipofectamine 2000: DNA (GFP%= 92%), as shown in **Figure 4.10**. Increasing Lipofectamine: DNA ratio had no significant impact on the transfection efficiency; hence using the lowest Lipofectamine: DNA ratio would be the most convenient choice to reduce any undesirable cytotoxic effects. Overall, these findings indicate that the highest GFP% can be achieved using Lipofectamine 2000: DNA 1:1 ratio with (1×10^5 cells/well) seeding density in Opti-MEM reduced serum medium.

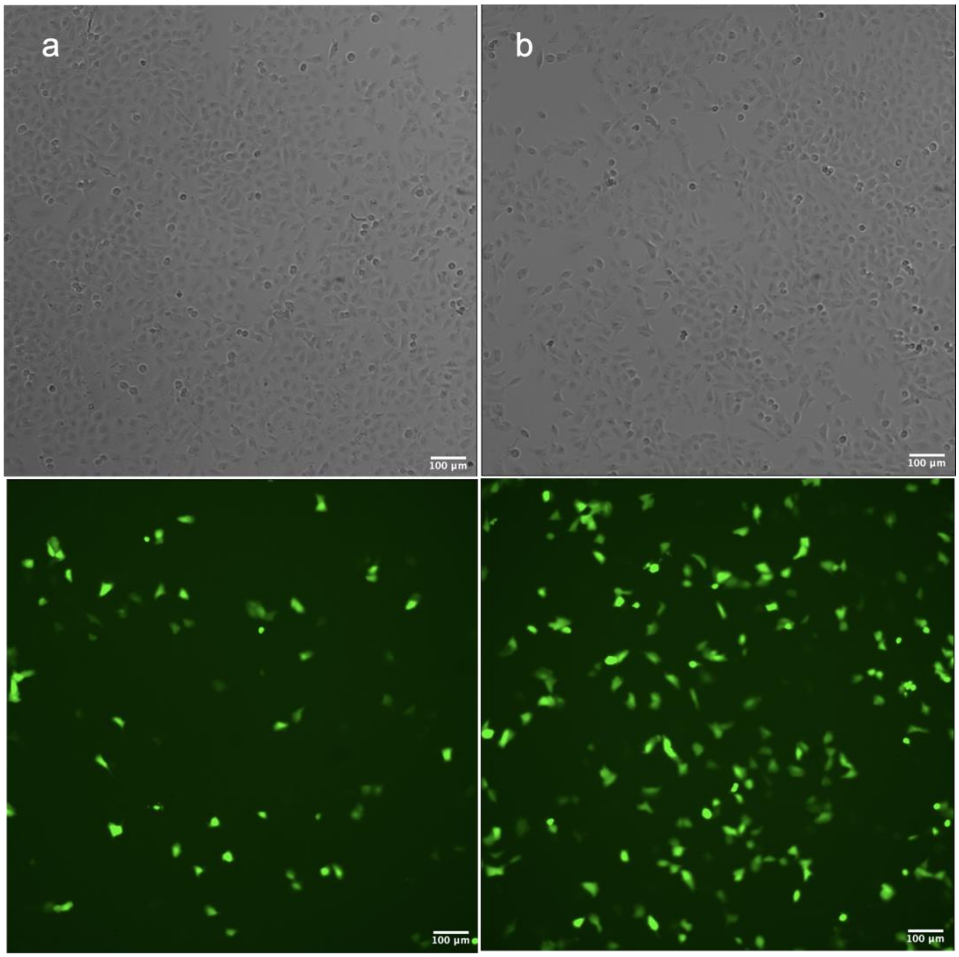

Figure 4.9: Transfection efficiency in A549 using Opti-MEM reduced serum transfection medium and 1×10^5cells/well seeding density analysed by fluorescent microscope (bright field image at the top and fluorescent image at the bottom of each panel) for: a) 3:1FuGENE HD: DNA (GFP%= 37%); (b) 4:1FuGENE HD: DNA (GFP%= 52%). Scale bars represent 100 µm.

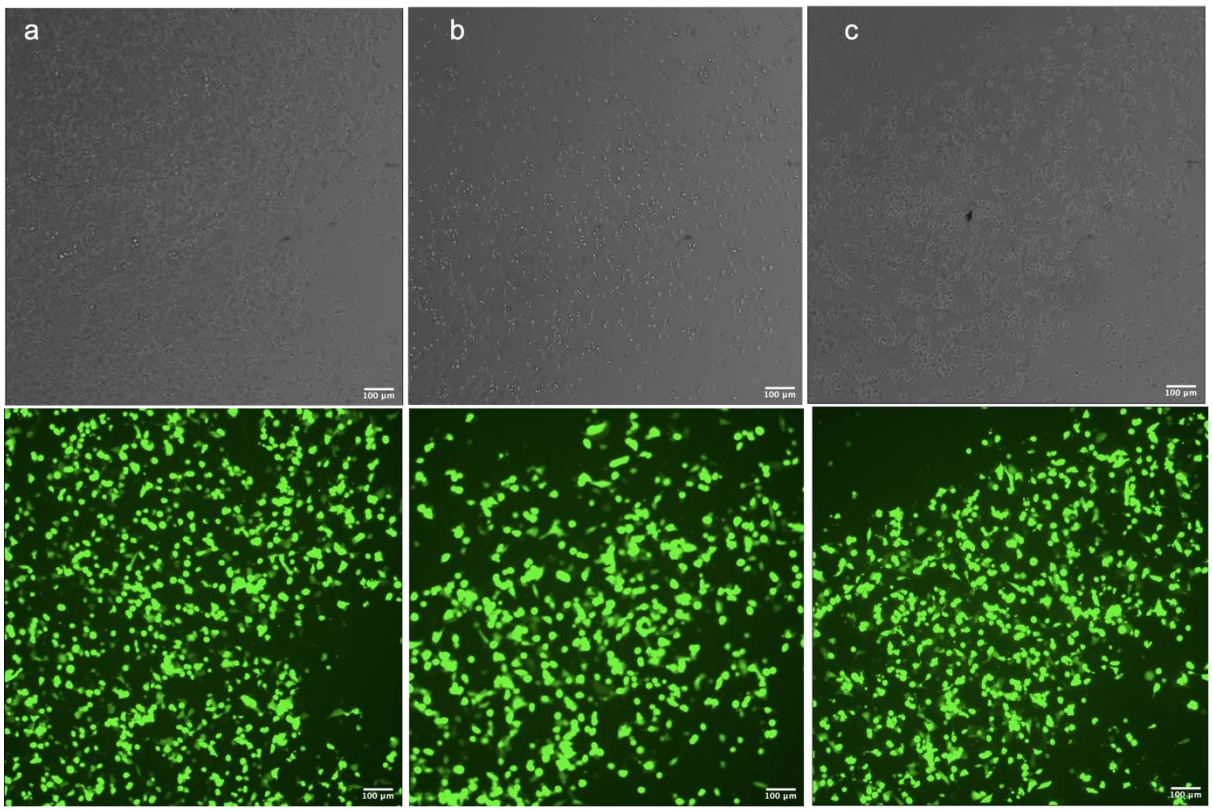

Figure 4.10: Transfection efficiency in A549 using Opti-MEM reduced serum transfection medium and 1×10^5 cells/well seeding density analysed by fluorescent microscope (bright field image at the top and fluorescent image at the bottom of each panel) for: a) 1:1 Lipofectamine 2000: DNA (GFP%= 92%); (b) 2.5:1 Lipofectamine 2000: DNA; (c) 5:1 Lipofectamine 2000: DNA. Scale bars represent 100 µm.

For delivering pDNA using NPs, the transfection efficiency of pDNA-loaded NPs is highly dependent on the targeted cell line and the cellular uptake of the NPs [95,126,229]. The cellular internalization relies on the physicochemical properties of the NPs, including surface chemistry, size and morphology of NPs [214,234]. After internalization, the loaded NPs must evade a series of biological barriers to deliver DNA into the nucleus. The success of the formulation depends on its ability to protect the DNA from degradation before reaching the nucleus [85,124,235,236]. As shown in **Figures 4.11 and 4.12**, successful pDNA delivery demonstrated by gene expression expressed by the green fluorescent protein was observed in cells treated with PLGA-Eudragit NPs prepared by CB and MF methods with a NP: DNA mass ratio of 2.5:0.3; however, further experiments were conducted in the following sections to quantify and assay the efficiency of these NPs in delivering pDNA.

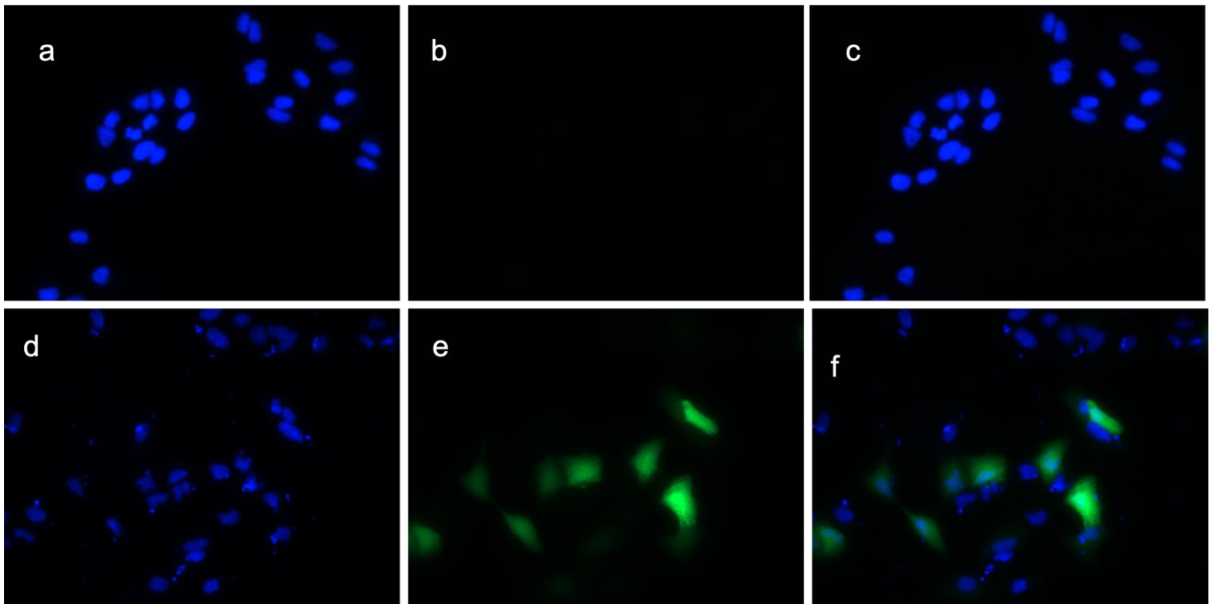

Figure 4.11: Transfection efficiency in A549 using Opti-MEM reduced serum transfection medium and 1×10^5 cells/well seeding density analysed by fluorescent microscope for plasmid DNA as negative control where: a) DAPI channel, b) green fluorescent protein channel, c) DAPI and green fluorescent protein overlay and for 3:1FuGENE HD: DNA where: d) DAPI channel, e) green fluorescent protein channel, f) DAPI and green fluorescent protein overlay

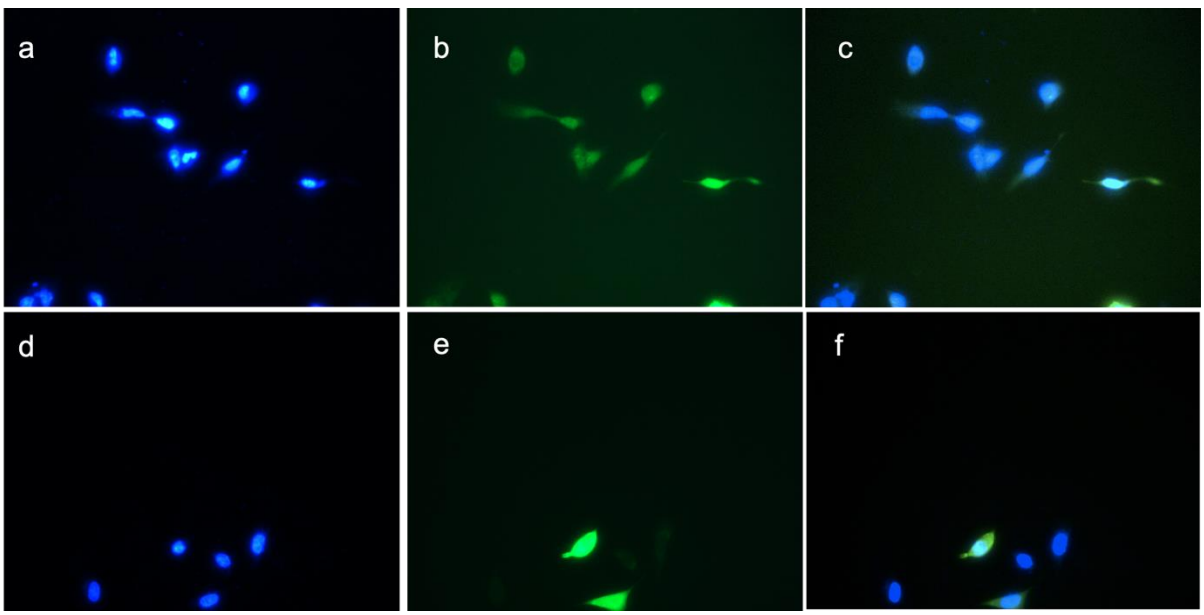

Figure 4.12: Transfection efficiency in A549 using Opti-MEM reduced serum transfection medium and 1×10^5 cells/well seeding density analysed by fluorescent microscope for Eudragit PLGA prepared by CB-nanoprecipitation using 2.5:0.3 NP:DNA where: a) DAPI channel, b) green fluorescent protein channel, c) DAPI and green fluorescent protein overlay and MF-nanoprecipitation using 2.5:0.3 NP:DNA where: d) DAPI channel, e) green fluorescent protein channel, f) DAPI and green fluorescent protein overlay.

4.3.7 Evaluation of pDNA-loaded PLGA-Eudragit NPs transfection efficiency in A549 and LLC-PK1 by live cell imaging and flow cytometry

Microscopic examination of A549 and LLC-PK1 cells **(Figures 4.13 and 4.14)** demonstrated that the transfection efficiency of the NPs prepared by CB-nanoprecipitation is higher than the ones prepared by MF-nanoprecipitation. Consistent with the fluorescent microscope data, a significant difference in the GFP %, for both A549 and LLC-PK1 cell lines measured using the green fluorescence channel on a flow cytometer, can be seen between the NPs prepared by both methods ($P < 0.05$), with the NPs prepared by the CB-nanoprecipitation method showing 2 folds higher transfection efficiency the NPs prepared by MF-nanoprecipitation **(Figure 4.15 c)**. This agrees well with the 2 folds higher pDNA loading of the NPs prepared by CB-nanoprecipitation than the ones prepared by MF-nanoprecipitation. Lipofectamine 2000 shows a higher transfection efficiency than the NPs in both cell lines **(Figure 4.15 c)**.

When comparing with the transfection efficiency reported in the literature, the highest transfection efficiency of the NPs made from the derivatives of Eudragit, Eudragit RS and RL, using double emulsion method was 7% in MDA-MB 231 cells and 4% in MCF-7 cell line [6]. Another study has reported using Eudragit E100 to improve the transfection efficiency of PEI, but with high toxicity [150]. In this study, the transfection efficiency achieved with PLGA-Eudragit NPs was improved to be 12% ± 1.7% for the NPs prepared by CB-nanoprecipitation and 4% ± 1.6% for the NPs prepared by MF-nanoprecipitation in A549 cell lines. For the LLC-PK1 cell line, the transfection efficiency was 11% ± 0.4% and 5% ± 0.5% for the NPs prepared by CB- and MF-nanoprecipitation, respectively. These results indicate the potential of PLGA-Eudragit NPs with particle size prepared by CB-nanoprecipitation being a promising nano-carrier for DNA delivery.

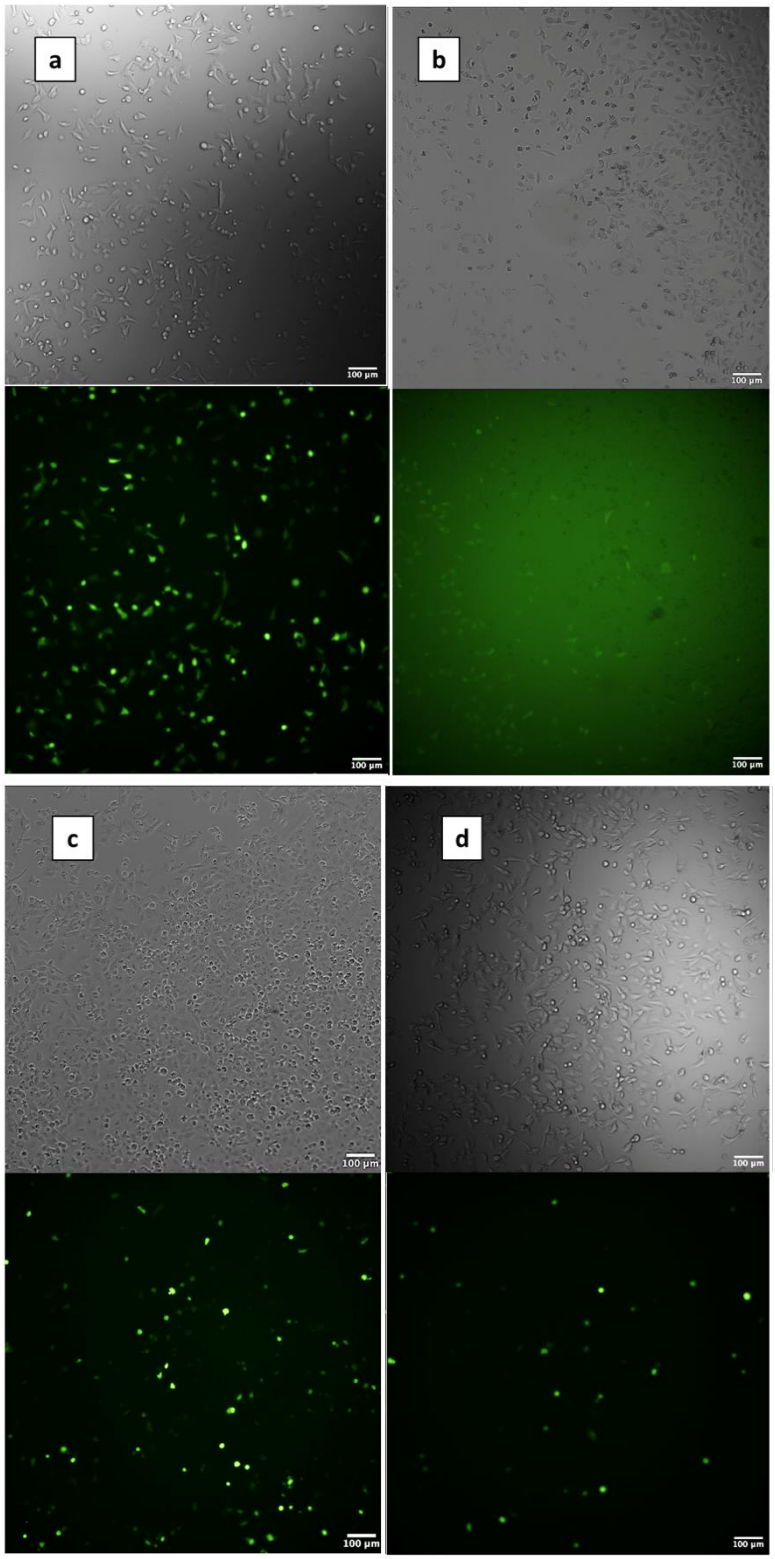

Figure 4.13: Transfection efficiency in A549 analysed by fluorescent microscope (bright field image at the top and fluorescent image at the bottom of each panel) for: a) Lipofectamine 2000; b) plasmid DNA as negative control; c) pDNA-loaded PLGA-Eudragit NPs prepared by CB-nanoprecipitation; d) pDNA-loaded PLGA-Eudragit NPs prepared by MF-nanoprecipitation. The scale bar represents 100 µm.

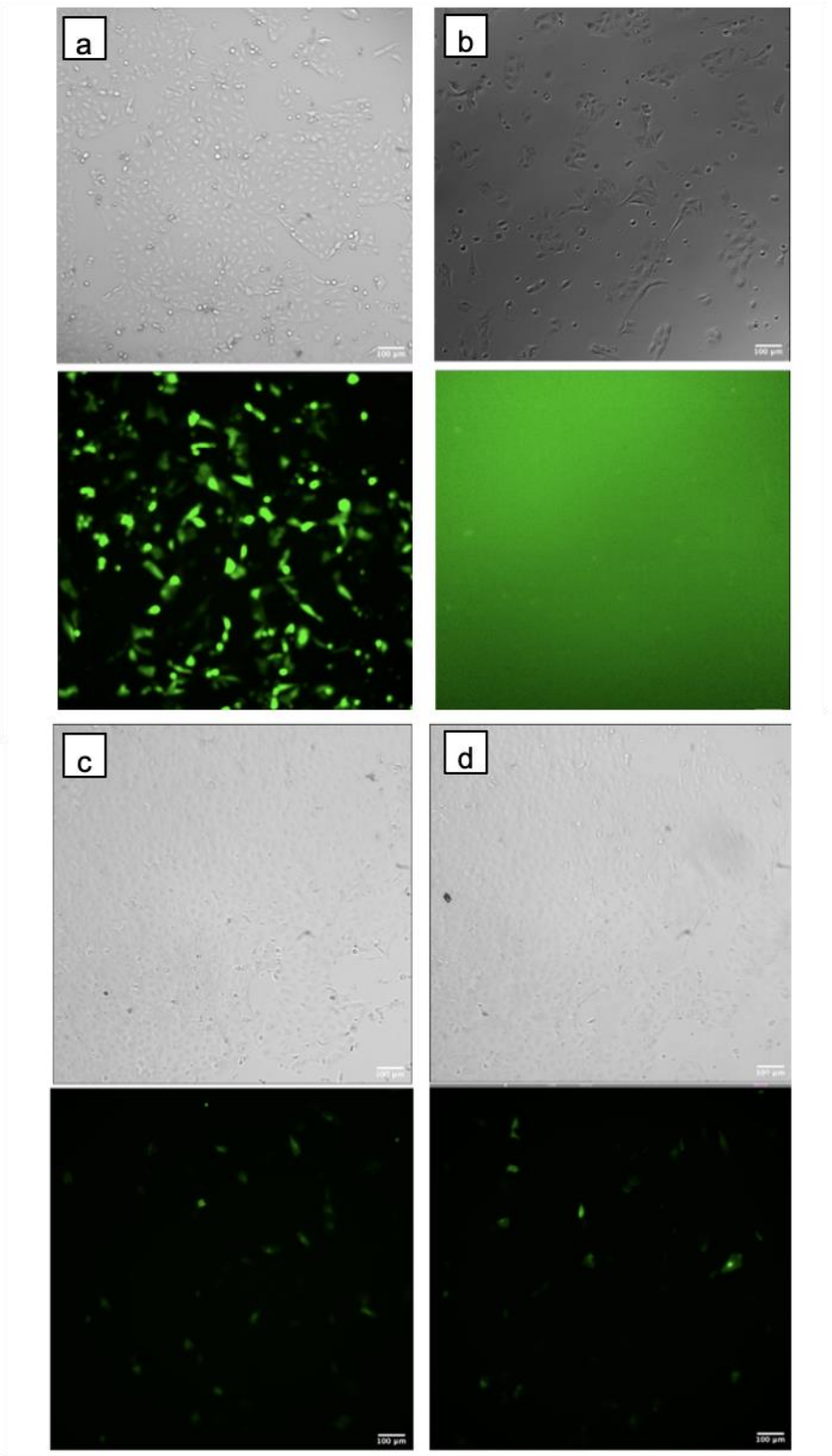

Figure 4.14: Transfection efficiency in LLC-PK1 cells analysed by fluorescent microscope for (a) Lipofectamine 2000 (10x), (b) plasmid DNA as negative control (10x), (c) Eudragit-PLGA nanoparticles prepared by conventional nanoprecipitation (10x) and (d) PLGA-Eudragit nanoparticles prepared by microfluidics (10x). The scale bar represents 100 µm.

4.3.8 Cytotoxicity of blank and pDNA loaded Eudragit-PLGA NPs

Assaying the cytotoxicity of the plasmid nanocarriers is an essential requirement to establish a therapeutic window where NPs concentration would not affect the viability of the cells during gene transfection studies. For PLGA-Eudragit NPs, MTT assays were used to examine the A549 and LLC-PK1 cells viability after being incubated with different concentrations of blank PLGA-Eudragit NPs for 24 (h). As shown in **Figure 4.15 a**, there was no significant reduction in A549 or LLC-PK1 cells viability when using PLGA-Eudragit NPs at a 100-3.125 (µg/mL) concentration range. However, Lipofectamine 2000 showed reduced cell viability by 25-30% in both cell types. The data are in line with previous studies findings wherein Eudragit E was found safe to be used without inducing significant toxicity [7,150].

The cytotoxicity of the pDNA-loaded formulations and Lipofectamine 2000 control were further assessed by flow cytometry. The assay was based on the proportions of a cell population that were propidium iodide positive, indicating the presence of a compromised plasma membrane compared to untreated cells[158]. The proportion of PI positive cells in the control (untreated group) was 0.77% in the A549 and 0.9% in LLC-PK1. The pDNA-loaded formulations prepared by both methods exhibit no significant toxicity on the A549 cells. The PI% positive cells seen after treatment with NPs prepared by MF-nanoprecipitation was 2.8-folds lower than the PI% of the NPs prepared by CB- nanoprecipitation **(Figure 4.15 b)** and 5-folds lower than the gold-standard transfection agent, Lipofectamine 2000 in A549 cell line. The higher PI% reported for A549 cell viability treated with Lipofectamine 2000 can be attributed to the higher transfection efficiency achieved with this cell line. A negative correlation between cell viability and transfection efficiency was reported by a study that was conducted on ten different cell lines [124]. This can be related to the lysosomal rupture that induces necrosis and cytotoxicity, besides the effect of the cationic transfection agents affecting the integrity of the cell [159,237–239]. The PI% values of all tests on the LLC-PK1 cells were significantly lower than the ones on A549 cells, which reinforces the fact that transfection efficiency and cytotoxicity are dependent on the cell type [237]. pDNA-loaded NPs prepared by MF-nanoprecipitation were less toxic ($P<0.05$) to both cell lines than the particles prepared by the conventional method **(Figure 4.15 d)**. However, this may be attributed to their low transfection efficiency. Taken together, the MTT and PI uptake assays support the conclusion that PLGA-Eudragit NP formulations display favourable biocompatibility across a therapeutically relevant concentration range appropriate for gene delivery.

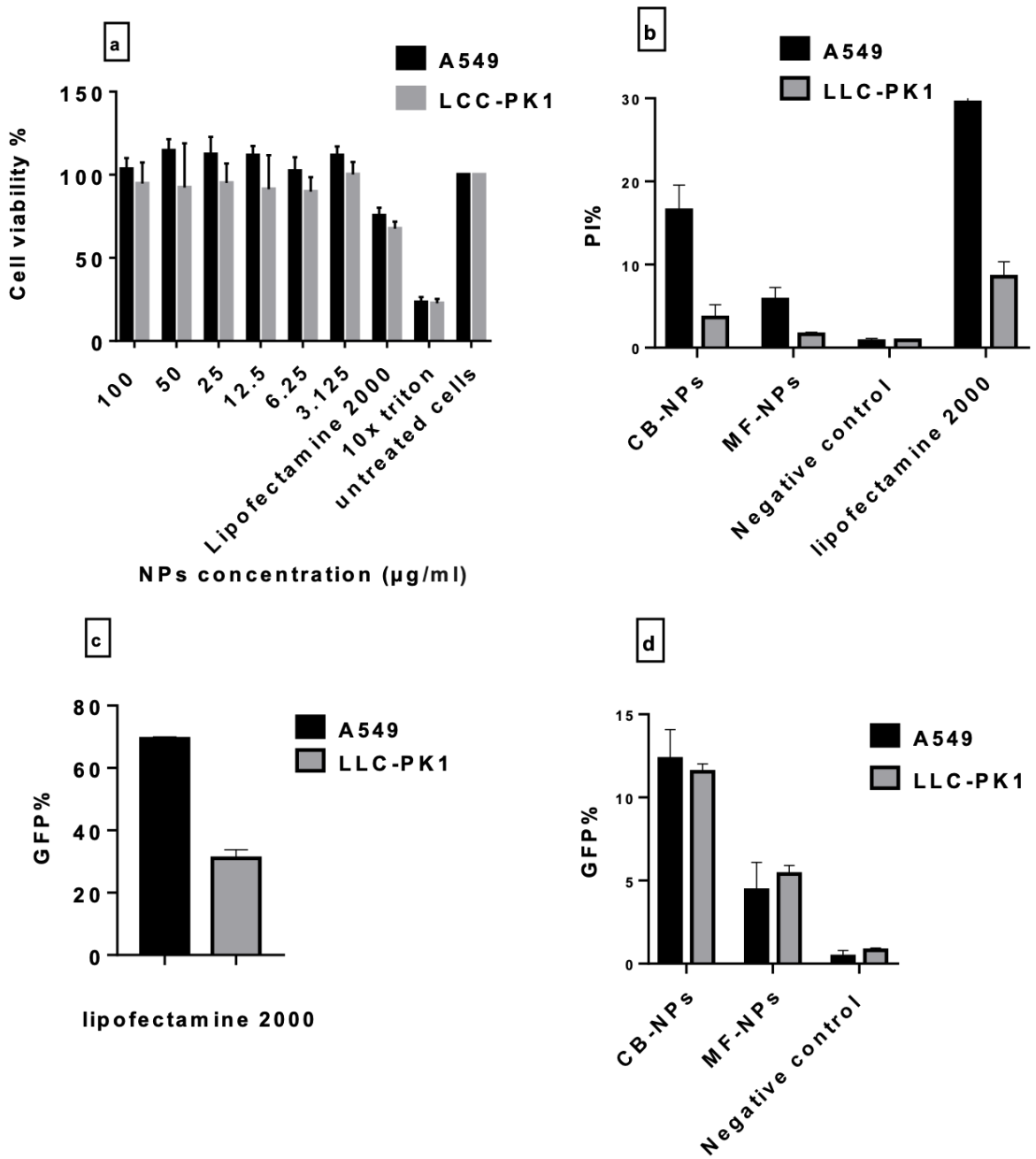

Figure 4.15: a) Cell viability data obtained from MTT assay of PLGA-Eudragit NPs on A549 and LLC-PK1 cell lines for 24 (h); (b) cell death percentage (PI positive cells) after 24 (h) post transfections with Lipofectamine 2000, negative control (naked pDNA) and pDNA-loaded PLGA-Eudragit NPs prepared by CB-nanoprecipitation and MF-nanoprecipitation; (c) the transfection efficiency (GFP%) of Lipofectamine 2000 (positive control); (d) the transfection efficiency (GFP%) of PLGA-Eudragit NPs prepared by CB- and MF-nanoprecipitation. The Error bars represent the standard deviation and n=3.

4.4 Conclusion

There have been general claims in the literature of microfluidics being superior in producing NPs with tuneable size and physicochemical properties. This study provides new insights from examining the effect of the synthesis method (CB- vs MF-nanoprecipitation) on the physicochemical properties and the subsequent gene delivery efficiency of the polymer blend NPs. The solubility and miscibility screening results confirmed the high likelihood of the formation of coprecipitated PLGA-Eudragit nanoparticles, which was further confirmed by the NPs characterisation. The differences in the mixing conditions of the CB- and MF-nanoprecipitation methods led to the significant differences in the particle sizes. Although CB-nanoprecipitation was unable to tune the particle size, the use of PLGA with Eudragit resulted in significant fouling issues within the microfluidics chips that affected the continuity of the synthesis process.

The difference in particle size of the NPs prepared by the two methods was translated into differences in their plasmid DNA loading efficiency, transfection efficiency and cytotoxicity. PLGA-Eudragit NPs prepared by CB-nanoprecipitation were found to have smaller size, higher pDNA loading efficiency and transfection efficiency than those prepared by MF-nanoprecipitation. These results suggest that PLGA-Eudragit NPs can be considered a promising gene vector, and the CB-nanoprecipitation method can be used to manufacture them with a high throughput rate. The difference in the gene transfection efficiency between the two methods can be explained by the larger particle size and the lower plasmid loading efficiency exhibited by the MF-NPs. These variations were translated into lower transfection efficiency in both cell lines.

Chapter 5

Delivery of miRNA-140-5P by polymeric nanoparticles to functionally alter osteoarthritis gene targets

5.1 Introduction

Osteoarthritis (OA) is a debilitating disease of joints characterised by deterioration of the articular cartilage surface and inflammation of the synovial membrane [165]. OA is associated with increased gene expression of aggrecanases (ADAMTS5/ADAMTS4), metalloproteinases (MMPs) and FZD6, which results in the loss of the protective aggrecan layer from the cartilage [165,184]. Molecular mechanisms underpinning OA development have revealed the key role of miRNAs: single-stranded non-coding RNA molecules that mediate gene silencing by binding to the target mRNA [165,184,189,240].

miRNA-140 has been identified to play a pivotal role in OA pathogenesis emphasised by age-related OA changes after miRNA-140 knockout [165]. Furthermore, a significant reduction in miRNA-140 expression was associated with an overexpression of aggrecanases, MMPs and FZD6 genes in OA [165,184,189]. Therefore, the delivery of miRNA-140 was correlated with repressed osteogenesis and improved chondrogenesis by controlling the expression of aggrecanases, MMPs and FZD6 [184]. These findings provided a novel insight into novel therapeutic implications to control the molecular mechanisms underlying OA development.

miRNA delivery remains challenging due to their hindered uptake by cells caused by the strong negative charge of RNA and their short half-life under physiological conditions due to the nucleases. Hence, this study aims to investigate the therapeutic potential of novel polymeric nanoparticles (PNPs) for miRNA-140 encapsulation and delivery into C28/I2 human chondrocytes.

The objectives of this chapter are as follows:

- Develop stable miRNA-140 loaded polymeric NPs and assess the formulation loading efficiency.
- Examine the efficiency of miRNA delivery in 2D and 3D C28/I2 cell culture by RT-qPCR.

5.2 Materials and methods

5.2.1 Synthesis of blank PLGA-Eudragit NPs

To screen the impact of the processing parameters on the NPs properties, different formulations were prepared according to the processing parameters shown in **Table 5.1**. These formulation parameters include:

- Eudragit: PLGA mass ratio
- PVA concentration (w/v%)
- Sonication time (min)

PLGA-Eudragit NPs were synthesised by the droplet double emulsion method ($W_1/O/W_2$) using the probe sonicator (Sonic Dismembrator, Thermo Fisher Scientific, UK). 100 µl of nuclease-free water was used as the first aqueous phase (W_1), dichloromethane (DCM) containing the polymers was used as the organic phase (O), and water containing different concentrations of PVA was used as the second aqueous phase (W_2), as shown in **Table 5.1**. The first aqueous phase (W_1) was added dropwise to 1 mL of the organic phase (O) containing 10 (mg/mL) of PLGA-Eudragit using different mass ratios then sonicated for 1 (min) to form the first emulsion (W_1/O), as shown in **Table 5.1**. Then the first emulsion was added dropwise to 10 mL of 1% or 1.5% PVA aqueous solution followed by sonication for 2 or 3 (min) to form the final emulsion ($W_1/O/W_2$), as shown in **Table 5.1**. The formulations were then left on the stirrer (300 rpm) for three (h) at room temperature to ensure DCM evaporation. The sonication process was done using 40% amplitude. Finally, the formulations were centrifuged at 13,000 RCF for 20 min using (Megafuge™ 16 Centrifuge, Thermo Fisher Scientific, UK) and resuspended in 1 mL of Nuclease-free water. Accordingly, the final concentration of the NPs is 10 (mg/mL).

Table 5.1: The experimental design employed to study the effect of the processing parameters on the properties of blank PLGA-Eudragit NPs

Aim of the experiment	Eudragit %	PLGA %	Final polymer blend concentration (mg/mL)	PVA concentration (w/v%)	Sonication time for W_1/O (min)	Sonication time for $W_1/O/W_2$ (min)
To study the impact of Eudragit: PLGA mass ratio	10	90	10	1	1	3
	50	50				
To study the impact of PVA concentration	10	90	10	1	1	3
				1.5		
To study the impact of the sonication time	10	90	10	1.5	1	3
						2

5.2.2 Synthesis of 5'Cy5-miRNA-140 loaded PLGA-Eudragit NPs

A stock solution of 5'Cy5-miRNA-140 was prepared according to the manufacturer's procedure. Hence, freeze-dried 5'Cy5-miRNA-140 (50 nmol) with a molecular weight of 14309.7 (g/mol) was reconstituted by adding 40 µl of nuclease-free water to make a final concentration of 17.88 (µg/ µl), which equals 1.2 (nmol/ µl). The stock solution was then frozen in 5 µl aliquots until used to minimize degradation by freeze/thaw cycles.

The choice of the processing parameters for 5'Cy5-miRNA-140 loaded PLGA-Eudragit NPs was decided based on the results of the blank PLGA-Eudragit NPs. Hence, 1 mL of 10 (mg/mL) polymer blend concentration constituting 10% of Eudragit and 90% of PLGA in DCM was used as the organic phase (O), and 10 mL of 1.5 (w/v%) PVA aqueous solution was used as the second aqueous phase (W_2). Furthermore, regarding the first aqueous phase (W_1), two formulations (A and B) were developed containing different amounts of the 5'Cy5-miRNA-140 in 100 µl of nuclease-free water to deliver different doses of miRNA-140 into C28/I2 cells, as shown in **Table 5.2**.

To synthesise the 5'Cy5-miRNA-140 loaded PLGA-Eudragit NPs, the first aqueous phase (W_1) was added dropwise to the organic phase (O) then sonicated on ice for 1 min (4 watts) using 40% amplitude to form the first emulsion (W_1/O). Then the first emulsion was added dropwise to 10 mL of 1.5% PVA aqueous solution followed by sonication on ice for 3 min (15 watts) using 40% amplitude to form the final emulsion ($W_1/O/W_2$). After then, the formulations were left on the stirrer (300 rpm) for three (h) at room temperature to ensure DCM evaporation. Finally, the formulations were centrifuged and resuspended following the same procedure in **section 5.2.2**.

Table 5.2: Experimental design for 5'Cy5-miRNA-140 loaded PLGA-Eudragit NPs

Formulation code	**5'Cy5-miRNA-140 (nmol)**	**Volume of W_1 (µl)**	**Volume of organic phase (O) mL**	**Volume of W_2 (mL)**
A	1	100	1	10
B	3			

5.3 Results and discussion

5.3.1 Characterisation of blank PLGA-Eudragit NPs

Designing NPs that can successfully deliver a payload to the chondrocytes after intra-articular injection requires a deep understanding of the OA joint microenvironment. Generally, the efficiency of the formulation is determined by its ability to penetrate the extracellular matrix of cartilage (ECM), acting as a physical barrier. Accordingly, NPs should be synthesised with a controlled size and surface charge that allow for their ECM penetration. Hence, it is crucial to investigate the effect of the processing parameters on the NPs physiochemical properties, including size and charge.

As shown in **Table 5.3**, size and charge tunability can be achieved by changing the processing conditions. Increasing the Eudragit mass ratio up to 50%, using 1% PVA, resulted in smaller NPs with higher zeta potential (P-value < 0.05). However, the study was designed to use the Eudragit just as a dopant to modify the charge of the negatively charged PLGA NPs, allowing for better miRNA-140 loading by electrostatic interactions. Hence, only 10% of Eudragit was used, and the formulation was further improved by changing the PVA concentration. Although

increasing the PVA concentration up to 1.5% using 10% of Eudragit resulted in smaller NPs, it was associated with a significant reduction in zeta potential (P-value < 0.05). The reduction in NPs size with 1.5% PVA can be related to its ability to reduce the aggregations by steric stabilization; however, PVA deposition on the NPs surface is expected to reduce the surface charge. The total sonication time was another critical parameter that significantly affected the size demonstrated by the significant increase in NPs size with 3 (min) compared to 4 (min) of total sonication (P-value < 0.05).

NPs formulation possessing the smallest Z-AVG size when using 10% of Eudragit was selected for the following experiments to maximise penetration into cartilage. Hence, 10% of Eudragit with 1.5% of PVA and 4 (min) of total sonication time were used as the optimal conditions to fabricate NPs possessing Z-AVG size of 190±2 nm, PDI of 0.14±0.03 and zeta-potential of 10±0.5 mV. However, according to the literature studies, it is still difficult to draw a structure-function relationship regarding the influence of the particle's properties on cartilage penetration and therapeutic outcome [167]. The design strategy of miRNA-loaded NPs and the optimal characteristics of these NPs (i.e., size and charge) for OA targeting was summarised in the introduction chapter **(section 1.8.5)**. Overall, the design of NPs developed in this study, including size and charge, is broadly in line with several studies that demonstrated successful penetration of the cartilage network [167,192,241].

Table 5.3: Synthesis of blank PLGA-Eudragit NPs using different parameters

Eudragit %	PLGA %	Final polymer blend concentration (mg/mL)	PVA concentration (w/v%)	Total Sonication Time (min)	Z-AVG size (nm)	PDI	Zeta-p (mV)
10	90	10	1	4	311±11	0.16±0.08	11±1
50	50		1	4	287±2	0.19±0.01	35±1
10	90		1	4	311±11	0.16±0.08	11±1
10	90		1.5	4	190±2	0.14±0.03	10±1
10	90		1.5	4	190±2	0.14±0.03	10±1
10	90		1.5	3	237±3	0.19±0.01	11±1

5.3.2 Characterisation of 5'Cy5-miRNA-140 loaded PLGA-Eudragit NPs

As shown in **Table 5.4**, dynamic light scattering of 5'Cy5-miRNA-140 loaded PLGA-Eudragit NPs showed a Z-AVG size range between 183±5 and 197±4 nm, for formulation A and B, respectively. The Zeta potential was 8±1 (mV) and 10±1 (mV) for formulation A and B, respectively. Hence, there is no significant change in the properties of loaded NPs compared to the blank NPs, which can be related to the small amount used of 5'Cy5-miRNA-140 relative to the weight of polymers. The morphology of the NPs was examined using TEM showing spherical monodisperse NPs as shown in **Figure 5.2**.

The encapsulation efficiency (EE%) of 5'Cy5-miRNA-140 was assayed using the spectrofluorometer based on the dye fluorescence (649/670). Therefore, a calibration curve of 5'Cy5-miRNA-140 was prepared to be used for the EE% measurements **(Figure 5.1)**. As shown in **Table 5.4**, the EE% were found to be 84±2% and 87±3% for formulation A and B, respectively. EE% was further examined by optical CCD camera imaging-based quantification for the coloaded 5'Cy5-miRNA-140 after resolving the NPs by agarose gel electrophoresis. As shown in **Figure 5.3 a**, the bands of different amounts of 5'Cy5-miRNA-140 were clearly detected on the gel. Furthermore, a clear band of 5'Cy5-miRNA-140 extracted from the loaded NPs **(Formulation B)** was observed on the gel; however, it was not detected from the supernatant, which suggests that 5'Cy5-miRNA-140 is mostly loaded into the NPs (**Figure 5.3 a and c**). Additionally, a sample of 5'Cy5-miRNA-140 loaded NPs have shown a complete entrapment of 5'Cy5-miRNA-140 as shown in **Figure 5.3 b** in well number 2 (indicated by the arrow on the figure). Collectively, these findings demonstrate efficient loading of 5'Cy5-miRNA-140 into PLGA-Eudragit NPs.

Table 5.4: Characterisation of 5'Cy5-miRNA-140 loaded PLGA-Eudragit NPs

Formulation code	5'Cy5-miRNA-140 (nmol)	Z-AVG size (nm)	PDI	Zeta-p (mV)	EE%
A	1	183±5	0.06±0.02	8±1	84±2
B	3	197±4	0.06±0.01	10±1	87±3

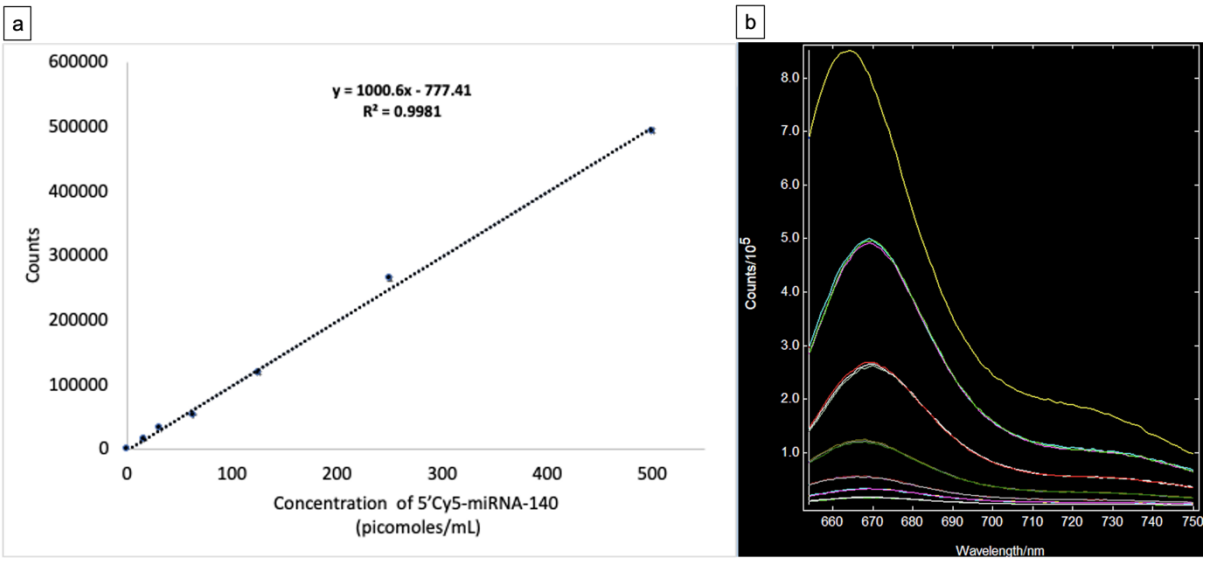

Figure 5. 1: (a) Calibration curve of 5'Cy5-miRNA-140 assayed using the spectrofluorometer based on the dye fluorescence (649/670), (b) fluorescence spectrum of 5'Cy5-miRNA-140 (from 1000 picomoles/mL down to 15.6 picomoles/mL).

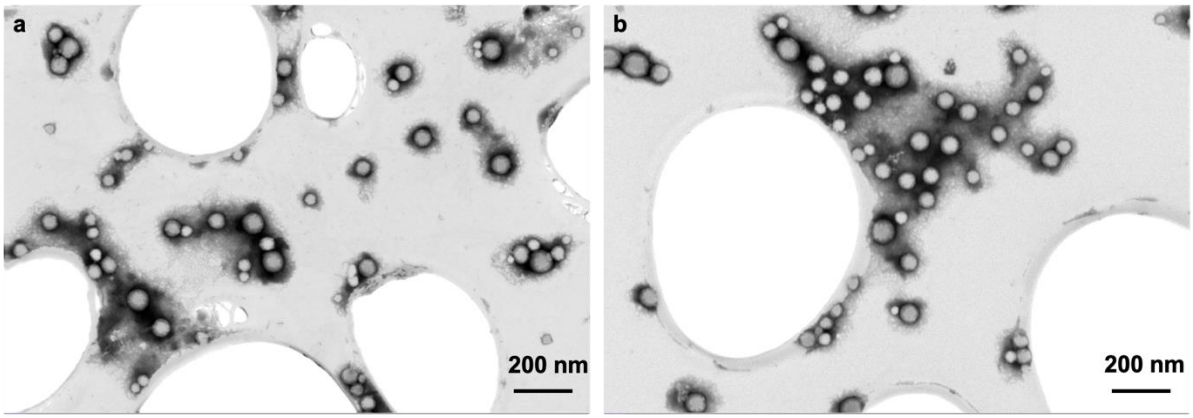

Figure 5.2: TEM characterisation of 5'Cy5-miRNA-140 loaded PLGA-Eudragit NPs for (a) formulation A and (b) formulation B.

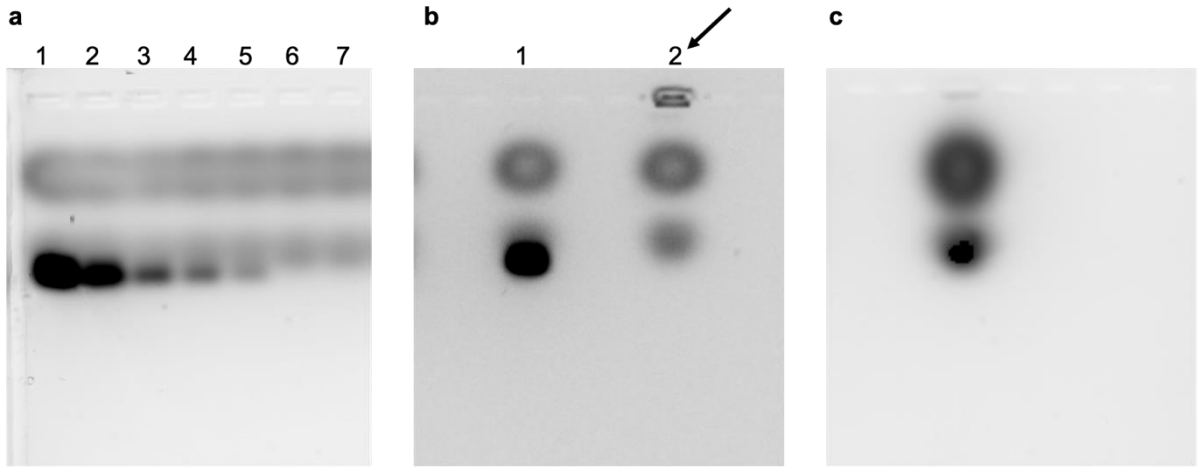

Figure 5.3: Evaluation of coloaded 5'Cy5-miRNA-140 (Formulation B) after being resolved in 3% agarose gel electrophoresis by optical CCD-camera imaging for (a) 1-125 picomoles,2-62.5 picomole, 3-31.25 picomoles ,4-15.6 picomoles, 5-7.8 picomoles, 6 and 7 are samples from the supernatant of the loaded NPs, (b)1-62.5 picomoles of 5'Cy5-miRNA-140 and 2-5'Cy5-miRNA-140 loaded NPs (formulation B), (c) 5'Cy5-miRNA-140 extracted from loaded NPs (formulation B) using 1% SDS.

5.3.3 Assaying the release of 5'Cy5-miRNA-140 and the stability of the formulation

The release kinetics of 5'Cy5-miRNA-140 from the NPs **(Formulation B)** was measured to investigate the miRNA delivery characteristics of the PLGA-Eudragit NPs. 5'Cy5-miRNA-140 showed an initial burst release into 7.4 PBS with 40% 5'Cy5-miRNA-140 released during the first 6 (h), followed by a slow-release up to 96 (h) **(Figure 5.4 a)**. A similar release pattern has been observed with siRNA and miRNA mimics from positively charged nanoparticles in several studies [123,152].

A stored formulation was tested for its 5'Cy5-miRNA-140 retention for up to 72 (h) to examine the impact of the storage conditions on the 5'Cy5-miRNA-140 EE%. EE% was not impacted

for up to 24 (h); however, a slight reduction in the EE% was observed after 48 (h) **(Figure 5.4 b)**. This suggests that the formulation should be used for transfection studies within the first 24 (h) to ensure the delivery of the total loaded 5'Cy5-miRNA-140. These tests were done using formulation B since it was loaded with a higher amount of 5'Cy5-miRNA-140; hence the assay was more accurate and within the sensitivity level of the used quantification method.

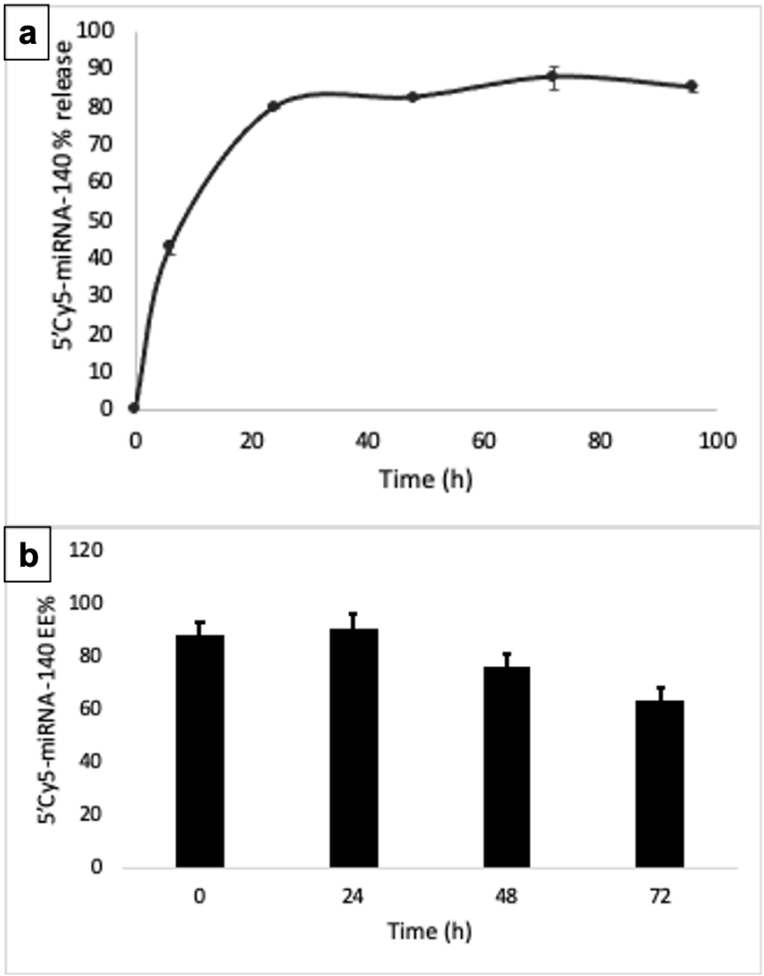

Figure 5.4: (a) Release kinetics of 5'Cy5-miRNA-140 at 37° C from PLGA-Eudragit NPs (Formulation B), (b) impact of storage condition on 5'Cy5-miRNA-140 EE% (formulation B). Error bars represent the standard deviation and n=3.

5.3.4 Stability of 5'Cy5-miRNA-140 loaded PLGA-Eudragit NPs

The stability of NPs at physiological conditions is an essential prerequisite for their application as a gene delivery system. As shown in **Figure 5.5**, there was no significant difference in the size of miRNA-140 loaded PLGA-Eudragit NPs between various physiological media (7.4 PBS, Opti-MEM serum reduced medium and bovine synovial fluid). Thus, the data demonstrate that the stability profile of these NPs is sufficient to ensure suitable therapeutic application. In comparison with other developed formulations for gene delivery, such as

chitosan NPs, PLGA-Eudragit NPs shows longer colloidal stability; however, a significant change in size was observed with siRNA loaded chitosan NPs after 24 (h) of incubation in the presence of serum [152].

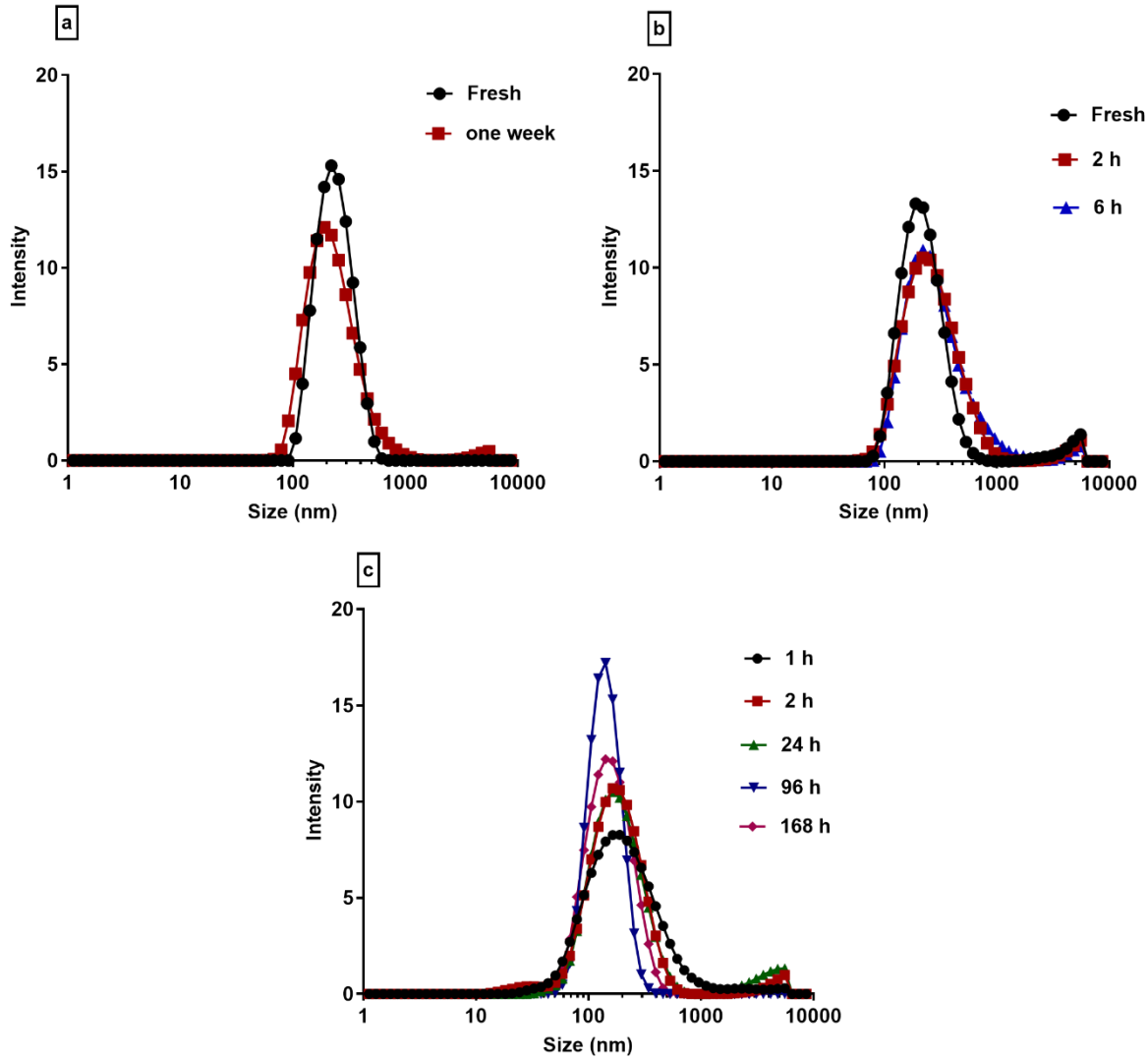

Figure 5.5: Colloidal stability of 5'Cy5-miRNA-140 loaded PLGA-Eudragit NPs in (a) 7.4 phosphate-buffer-saline (PBS), (b) Opti-MEM serum reduced medium and (c) Bovine synovial fluid.

5.3.5 Cytotoxicity of PLGA-Eudragit NPs assayed by MTT assay

Blank PLGA-Eudragit and 5'Cy5-miRNA-140 loaded PLGA-Eudragit NPs were evaluated for biocompatibility in C28/I2 cells by MTT assay. Blank PLGA-Eudragit NPs and Lipofectamine RNAiMAX did not cause any severe toxicity in C28/I2 cells across the particle concentration range (100-3.125 µg/mL) as shown in **Figure 5.6 a**. Hence, further investigation was done to evaluate the biocompatibility of the 5'Cy5-miRNA-140 loaded PLGA-Eudragit NPs compared to lipofectamine RNAiMAX. As shown in **Figure 5.6 b**, 5'Cy5-miRNA-140 loaded PLGA-Eudragit NPs did not induce any severe toxicity compared to cells treated with blank PLGA-

Eudragit NPs. Therefore, polymer equivalent of up to 100 (µg/mL) of PLGA-Eudragit NPs containing 24 nM 5'Cy5-miRNA-140 in media could be used without significant toxic effect. However, marked cell proliferation was observed with lipofectamine RNAiMAX loaded with 12 nM of 5'Cy5-miRNA-140 in media. There are various discrepancies in the studies around the impact of lipofectamine on cell viability; however, this can be related to the cells type, transfection procedure, and the delivered miRNA type [123,242]. Together, these results suggest that 5'Cy5-miRNA-140 loaded PLGA-Eudragit NPs are nontoxic and can maintain cell viability in vitro.

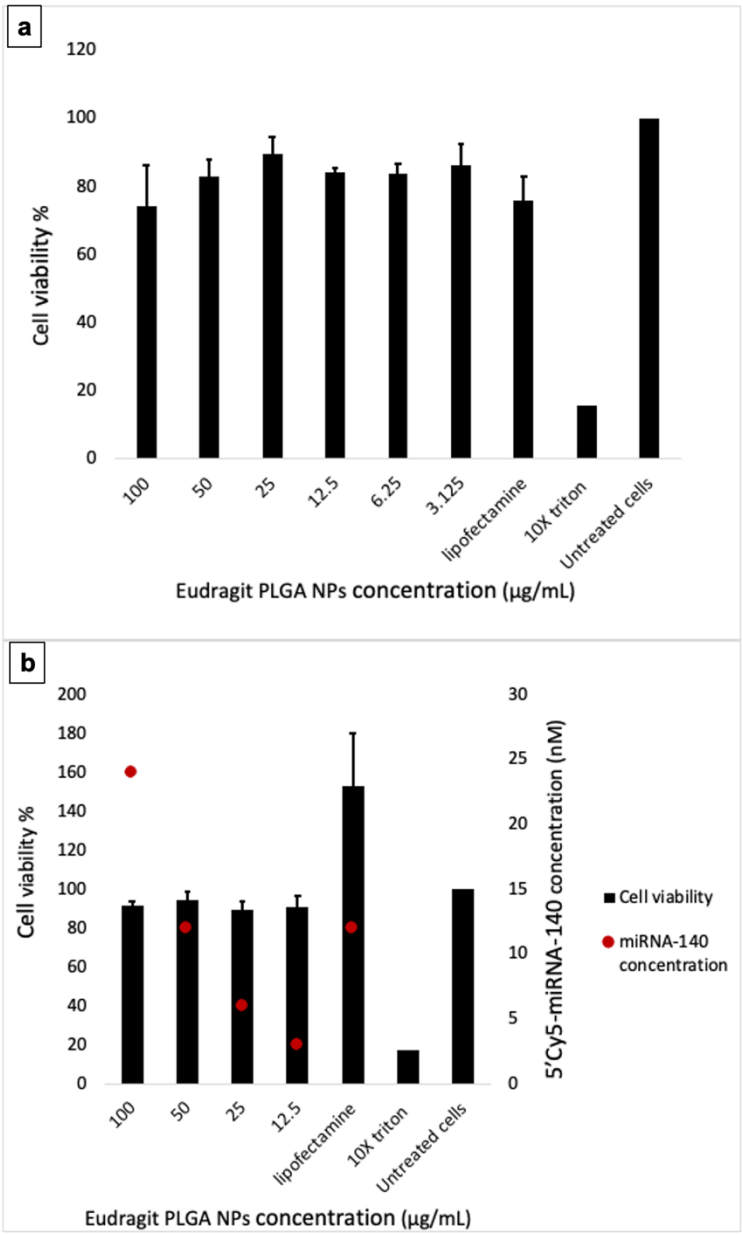

Figure 5.6: MTT assay for viability of C28/I2 cells incubated for 24 (h) with (a) lipofectamine RNAiMAX and blank PLGA-Eudragit concentration and (b) lipofectamine RNAiMAX and PLGA-Eudragit NPs loaded with different 5'Cy5-miRNA-140 ranging between 3-24 nM in media. Error bars represent the standard deviation and n=3.

5.3.6 Delivery of 5'Cy5-miRNA-140 loaded NPs examined using confocal microscopy

Several genes regulated by miRNAs have been proposed as potential targets in OA. miRNAs which control gene expression post-transcriptionally are essential for normal skeletal development [184]. miRNA-140, in particular, has been identified to play a critical role in chondrogenesis and OA pathogenesis, as explained in detail in the introduction chapter **(section 1.8.4)**. However, the delivery of miRNA mimics faces a group of hurdles that mitigate their clinical application. These challenges can be mostly related to the molecular structure of miRNA mimics. For instance, the negative charge of the miRNA mimics limits their cellular uptake, besides other challenges linked to their limited stability due to their rapid degradation or inactivation by nucleases [4]. These challenges highlight the need for implementing a criterion design of efficient miRNAs delivery vectors that can circumvent the biological barriers. Hence, several studies have screened the efficacy of NPs in delivering miRNA mimics in vitro and in vivo [4,81,123,153]. The main conclusion that can be drawn from these studies is that the efficacy of the formulation is mainly determined by its ability to load the miRNA mimics then successfully deliver them to the cytoplasm by evading the endolysosomal degradation. Generally, the type of materials used for NPs synthesis determines the NPs intracellular trafficking, cellular fate and therapeutic efficacy. In this study, Eudragit was used as a dopant to provide a cationic charge on the surface of the PLGA NPs to maximize the miRNA-140 loading and to enhance the endolysosomal escape by its proton buffering capacity, as explained in the introduction chapter **(section 1.6.1.2)**.

As shown in **Figure 5.7**, successful delivery of 5'Cy5-miRNA-140 was observed with Lipofectamine RNAiMAX compared to control of naked 5'Cy5-miRNA-140 without a transfection agent. Similar observations were ascertained with 5'Cy5-miRNA-140 loaded PLGA-Eudragit NPs, and the uptake was confirmed with different NPs concentrations **(Figure 5.8).** Therefore, further analysis was done to determine the location of the 5'Cy5-miRNA-140 loaded PLGA-Eudragit NPs in the cell. As shown in **Figure 5.9**, part of the 5'Cy5-miRNA-140 ended up in the lysosomes; however, a significant amount was also observed in the cytoplasm, demonstrating the formulation's efficacy in escaping the endolysosomal degradation. As discussed in the following sections, the 5'Cy5-miRNA-140 amount delivered to the cytoplasm was enough to alter the target genes expression. Together these data suggest that PLGA-Eudragit NPs can be used effectively to deliver the 5'Cy5-miRNA-140 into C28/I2 cells.

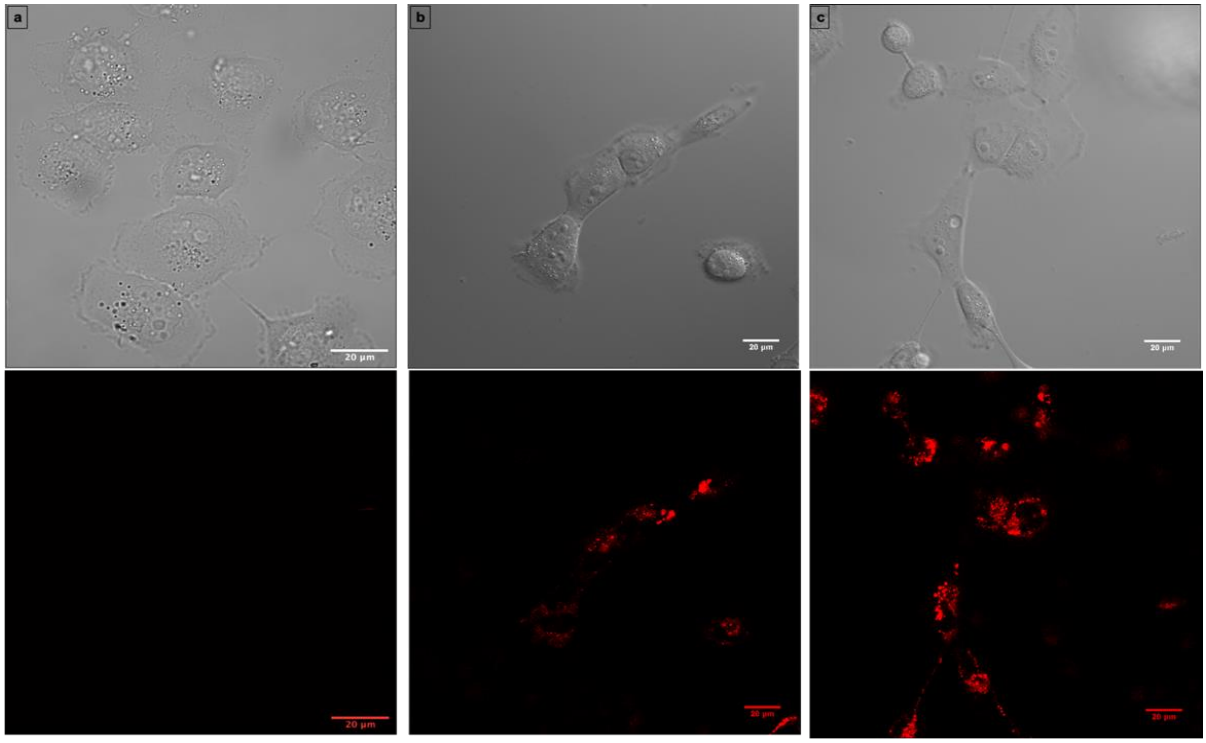

Figure 5.7: Examining the uptake of (a) 12 nM of naked 5'Cy5-miRNA-140, (b) 4 nM of 5'Cy5-miRNA-140 delivered by lipofectamine RNAiMAX and (c) 12 nM of 5'Cy5-miRNA-140 delivered by lipofectamine RNAiMAX visualised using confocal microscopy. Scale bar represents 20 µm.

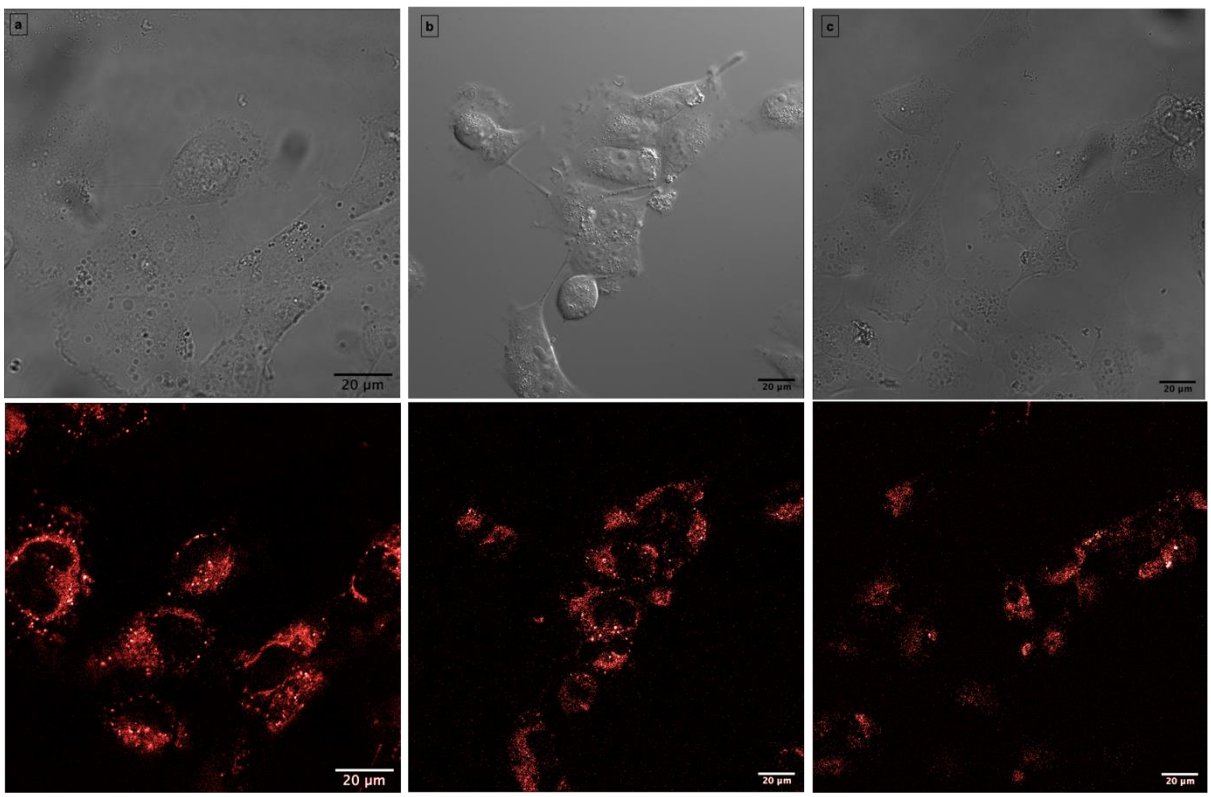

Figure 5.8: Examining the uptake of 5'Cy5-miRNA-140 loaded PLGA-Eudragit NPs by confocal microscopy where (a) 100 µg/ mL of NPs formulation B (24 nM 5'Cy5-miRNA-140),

(b) 50 µg/ mL of NPs formulation B (12 nM 5'Cy5-miRNA-140) and (c) 50 µg/ mL of NPs formulation A (4 nM 5'Cy5-miRNA-140). Scale bar represents 20 µm.

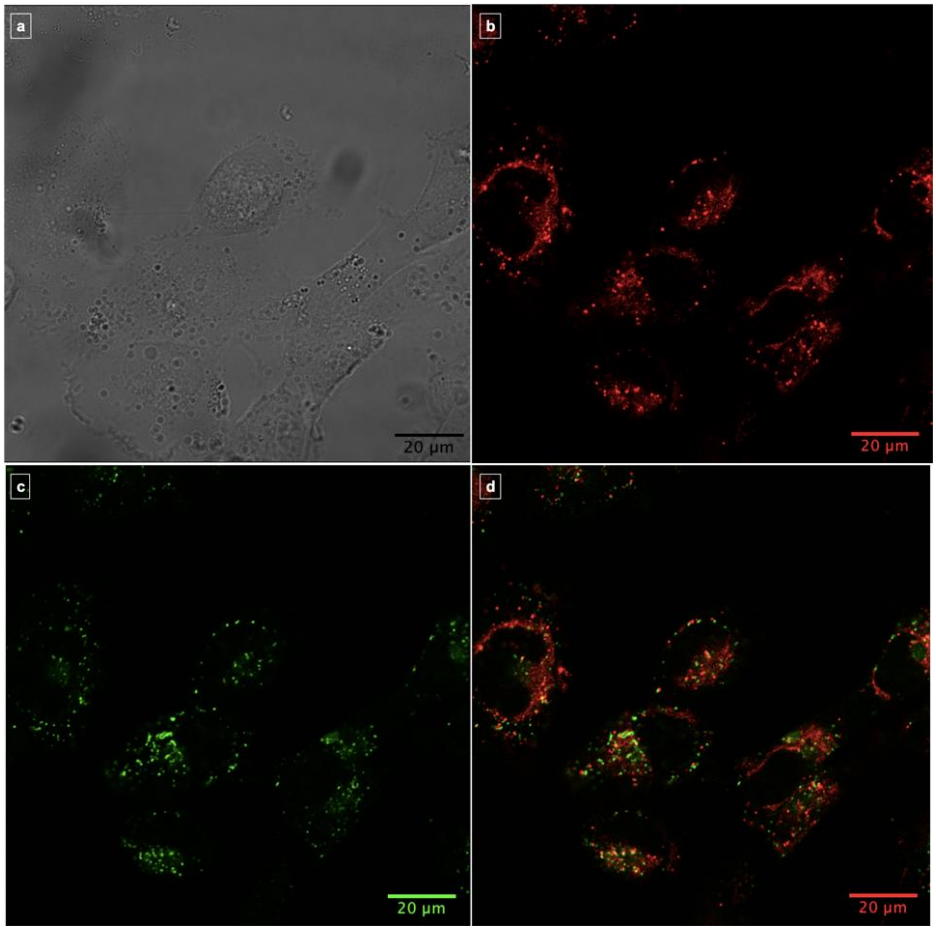

Figure 5.9: Examining the accumulation of the 5'Cy5-miRNA-140 loaded PLGA-Eudragit NPs in the C28/I2 lysosomes and cytoplasm by confocal microscopy: (a) C28/I2 bright-filed channel, CY5 red channel, lysotracker green channel and (d) merged image of CY5 red and lysotracker green. Scale bar represents 20 µm.

5.3.7 Measuring 5'Cy5-miRNA-140 delivery into C28/I2 cells by qPCR

As explained in **section 5.3.6**, endosomal escape is a bottleneck in successfully delivering miRNA mimics. Therefore, the miRNA vector should escape the endosomes to ensure the delivery of intact miRNAs to the cytoplasm. For transfection reagents such as lipofectamine RNAiMAX, the mechanism of miRNA delivery relies on forming complexes of miRNA-liposomes that get internalised by the cells via fluid endocytosis [243]. The miRNAs must then escape from the endosome to remain intact and functional. However, this delivery method is described as a random, stochastic process since a fraction of the miRNA sticks in a nonspecific manner to the cell surface, and an unknown fraction fails to escape the endosomes, which impact the final quantity of intact miRNA that successfully end up in the cytoplasm [123,243].

Hence, to confirm that lipofectamine RNAiMAX and PLGA-Eudragit NPs can protect and deliver intact miRNAs to C28/I2 cells, the miRNA-140 level was measured by qPCR 48 (h) post-transfection. For C28/I2 cells transfected with miRNA-140 using lipofectamine RNAiMAX, a concentration-dependent increase in miRNA-140 level was detected with transfections up to 12 nM miRNA-140. However, there was no significant increase (P-value > 0.05) in miRNA-140 level for cells transfected with higher miRNA-140 concentrations using lipofectamine RNAiMAX **(Figure 5.10 a)**. Furthermore, for C28/I2 cells transfected with miRNA-140 using PLGA-Eudragit NPs, a concentration-dependent increase in miRNA-140 expression was detected with transfections up to 6 nM miRNA-140. However, there was no significant increase (P-value > 0.05) in miRNA-140 level for cells transfected with higher miRNA-140 concentrations using PLGA-Eudragit NPs **(Figure 5.10 b)**. As shown in **Figure 5.10 d**, PLGA-Eudragit NPs show similar efficacy compared to lipofectamine RNAiMAX in their ability to transfect intact miRNA-140 to C28/I2 using 4 and 12 nM of miRNA-140. However, as shown in **Figure 5.10 c**, there is no significant difference in miR-140 level in C28/I2 cells transfected with PLGA-Eudragit NPs delivering 6 nM and lipofectamine RNAiMAX delivering 12 nM. This suggests that PLGA-Eudragit NPs loaded with a lower amount of miRNA-140 compared to lipofectamine RNAiMAX results in a comparable increase in miRNA-140 level. These findings demonstrate the efficacy of PLGA-Eudragit NPs in delivering intact miRNA-140 to the C28/I2 cells.

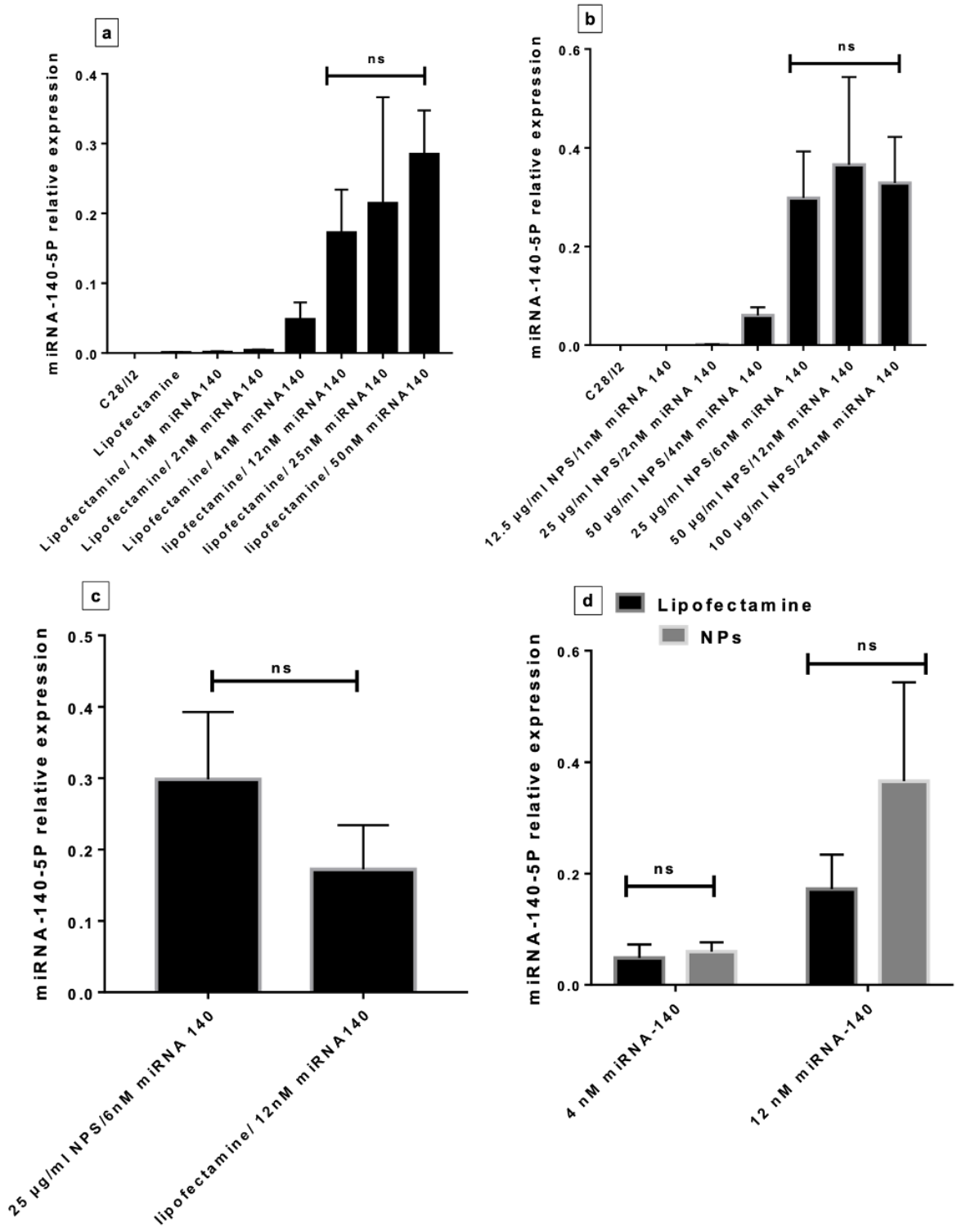

Figure 5.10: miRNA-140-5p relative expression in C28/I2 human chondrocytes transfected with miRNA-140 using: (a) Lipofectamine RNAiMAX, (b) PLGA-Eudragit NPs, (c) PLGA-Eudragit delivering 6 nM of miRNA-140 compared to 12 nM miRNA-140 delivered by lipofectamine RNAiMAX and (d) 4 nM and 12 nM of miRNA-140 delivered by NPs and lipofectamine RNAiMAX. miRNA-140 expression was measured by qPCR 48 (h) post-transfection. Error bars represent the standard deviation and n=3.

5.3.8 Regulation of FZD6 gene expression by 5'Cy5-miRNA-140 assayed by qPCR

The activity of miRNAs as regulators for gene expression takes place within the miRNA-induced silencing complex (miRISC). Therefore, to determine if PLGA-Eudragit NPs deliver miRNA-140 that can function in the RISC, changes in the target gene expression was measured by qPCR. In this study, *FZD6* expression was measured in response to NPs treatment as a potential target for miRNA-140-5p and OA, as explained in the introduction chapter **(section 1.8.3)**. This suggests that successful delivery of miRNA-140-5p should supposedly downregulate *FZD6* and restore homeostasis.

To confirm this and determine the required dose of miRNA-140 needed to alter FZD6 gene expression, a dose-response curve of miRNA-140 transfected into C28/I2 chondrocytes using lipofectamine RNAiMAX was created. As shown in **Figure 5.11 a**, the increase in miRNA-140 expression was consistent with a downregulation of FZD6 expression at the mRNA level. Furthermore, as shown in **Figure 5.11 b**, a knockdown efficiency of 35%±18% was detected with 4 nM of miRNA-140 transfected using lipofectamine RNAiMAX. Moreover, the knockdown efficiency increased significantly to 97%±0.3% with 12 nM of miRNA-140 compared to 4 nM (P-value < 0.01). Additionally, the knockdown efficiency increased to 99%±0.4% with 25 nM of miRNA compared to 12 nM (P-value < 0.001), demonstrating a dose-response effect. However, there was no significant difference in the knockdown efficiency between 25 and 50 nM of miRNA-140. Collectively, the data indicated that the delivered miRNA-140 was functional, and 12 nM or higher doses can effectively alter the FZD6 gene expression with a knockdown efficiency higher than 95%.

A similar pattern of *FZD6* downregulation with miRNA-140 increased level was observed in C28/I2 cells treated with 5'Cy5-miRNA-140 loaded PLGA-Eudragit NPs **(Figure 5.12 a)**. The knockdown efficiency was found to be 68%±16%, 94%±4%, 97%±1% and 98%±1% with 4 nM, 6 nM, 12 nM and 24 nM of miRNA-140 delivered by PLGA-Eudragit NPS, respectively **(Figure 5.12 b)**. As shown in **Figure 5.12 c**, PLGA-Eudragit NPs are more efficient than lipofectamine RNAiMAX in downregulating FZD6 mRNA expression when delivering a fixed dose of miRNA-140 (12 nM) (P-value < 0.05). Additionally, there was no significant difference in *FZD6* expression ascertained with 6 nM of miRNA-140 delivered by NPs compared to 12 nM delivered by lipofectamine RNAiMAX. Hence, the data show that PLGA-Eudragit NPs are more efficient than lipofectamine RNAiMAX in downregulating *FZD6* expression when providing similar dose of miRNA-140. Additionally, equivalent knockdown efficiency can be

achieved with lower dose of miRNA-140 loaded PLGA-Eudragit NPs loaded compared to Lipofectamine, suggesting a more potent effect compared to lipofectamine RNAiMAX. By this, it can be assumed that PLGA-Eudragit NPs can escape the endosomal compartment and deliver intact miRNA-140 to the cytoplasm that can efficiently alter the *FZD6* gene expression. The IC50 of miRNA-140 delivered by Lipofectamine RNAiMAX was found to be 0.59±0.05 (miRNA-140 dose = 3.9 nM) compared to 0.42±0.021 for miRNA-140 delivered by PLGA-Eudragit NPs (miRNA-140 dose = 2.6 nM), suggesting that NPs are more potent than lipofectamine RNAiMAX **(Figures 5.11 c and 15.12 d)**.

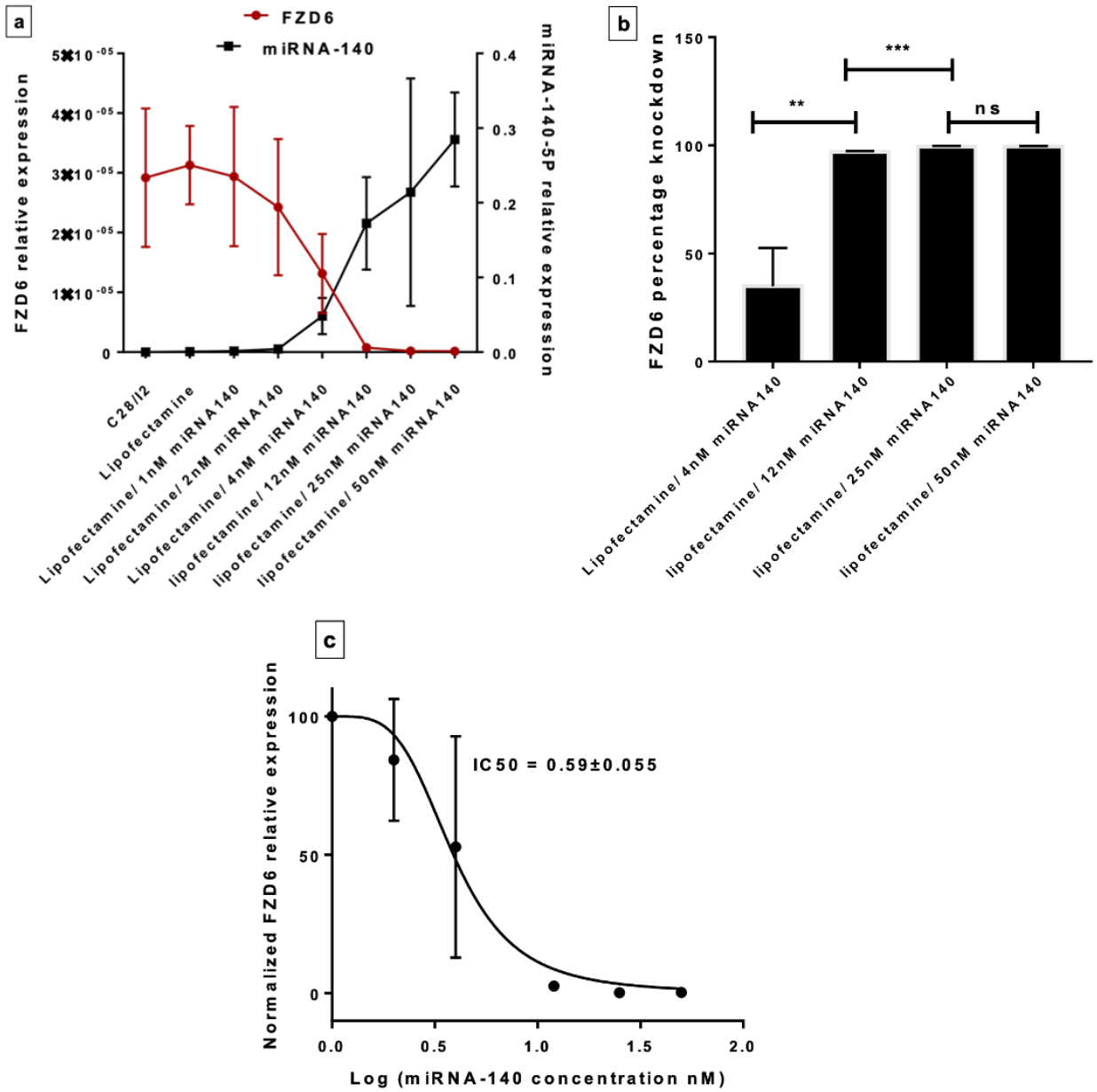

Figure 5.11: miRNA-140-5p can be delivered to C28/I2 chondrocytes using Lipofectamine RNAiMAX where it downregulates *FZD6* expression represented as (a) miRNA-140/*FZD6* dose-response relationship, (b) *FZD6* percentage knockdown (knockdown efficiency) using different concentrations of miRNA-140 delivered by Lipofectamine RNAiMAX and (c) dose-response curve of miRNA-140 delivered by Lipofectamine RNAiMAX effect on *FZD6* expression. *FZD6* gene expression was measured by qPCR 48 (h) post-transfection. ** (P-value < 0.01), *** (P-value < 0.001) and ns (P-value ≥ 0.05). Error bars represent the standard deviation and n=3.

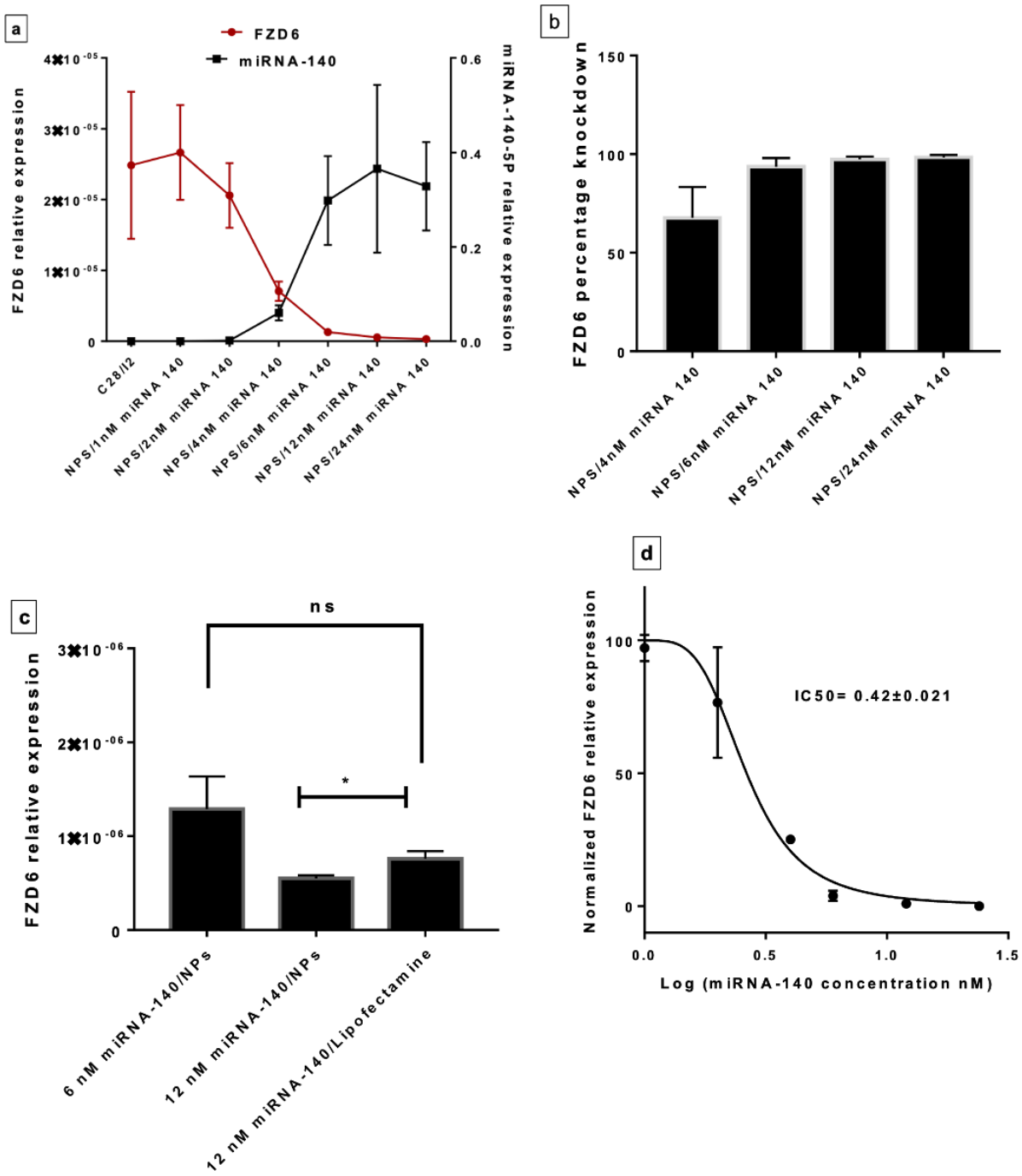

Figure 5.12: miRNA-140-5P can be delivered to C28/I2 chondrocytes using PLGA-Eudragit NPs where it can function to downregulate *FZD6* expression represented as (a) miRNA-140/*FZD6* dose-response relationship, (b) *FZD6* percentage knockdown (knockdown efficiency) using different concentrations of miRNA-140 delivered by NPs, (c) comparing the downregulation level of *FZD6* gene expression by PLGA-Eudragit NPs and Lipofectamine RNAiMAX and (d) dose-response curve of miRNA-140 delivered by PLGA-Eudragit NPs effect on *FZD6* expression. *FZD6* gene expression was measured by qPCR 48 (h) post-transfection. * (P-value < 0.05) and ns (P-value ≥ 0.05). Error bars represent the standard deviation and n=3.

5.3.9 Examining the downstream effect of the delivered 5'Cy5-miRNA-140 on FZD6 protein expression

It is assumed that changes in specific mRNA levels are accompanied by commensurate changes in the encoded proteins; however, various steps between transcription and translation may provide many diverse regulatory opportunities. Therefore, it is essential to check if the changes in the *FZD6* expression on mRNA level will be manifested as changes on the protein level.

As shown in **Figure 5.13**, cells transfected with miRNA-140 delivered using Lipofectamine RNAiMAX and PLGA-Eudragit NPs reduced the expression of FZD6 at the protein level by 75% and 20% for miRNA-140 delivered by RNAiMAX, and PLGA-Eudragit NPs, respectively. Although PLGA-Eudragit NPs showed a higher knockdown efficiency on FZD6 mRNA level than lipofectamine RNAiMAX when delivering 12 nM of miRNA-140 as demonstrated by the qPCR, lipofectamine RNAiMAX shows a higher knockdown efficiency on the FZD6 protein level when delivering 12 nM of miRNA-140 as shown by the Western blot data.

Although several studies in the literature have investigated the role of miRNA-140 delivery in OA, to our knowledge, no study has yielded a polymeric NPs delivery platform for miRNA-140 into human chondrocytes [165,184,185,189]. However, a recent study has explored the role of the miR-141/200c cluster in OA pathogenesis and developed an aptamer (tgg2)-PEG2000-PAMAM6.0-cy5.5 (TPPC) nanoplatform for delivering it to the chondrocytes [244]. The developed nanoplatform was found efficient in targeting the miR-141/200c cluster; however, since the NPs properties and the miRNA used in this study are different from our study, no direct comparison can be drawn.

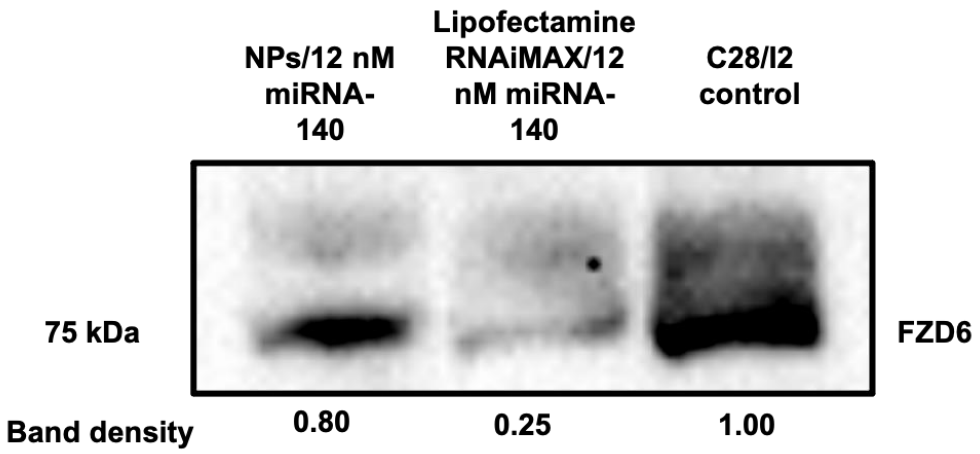

Figure 5.13: FZD6 protein level in C28/I2 cells transfected with miRNA-140 using PLGA-Eudragit NPs/12 nM of miRNA-140 and lipofectamine RNAiMAX/12 nM of miRNA-140 compared to untreated C28/I2 chondrocytes control. Protein level was measured 48 (h) post-transfection.

5.3.10 Investigating the efficiency of 5'Cy5-miRNA-140 loaded PLGA-Eudragit NPs in downregulating *FZD6, MMP-13* and *ADAMTS5* in 3D micromass cell culture treated with IL-1ß using qPCR

2D cell culturing is the most widely used type of cell culture by virtue of its easiness and low-cost maintenance of the cell culture [245]. However, numerous disadvantages are associated with adherent 2D cell cultures. The concept of 2D cell culturing relies on growing the cells as a monolayer in a culture flask where cells attach to the plastic surface [245]. Hence, using this culturing method diminishes the cell-cell and cell-extracellular matrix interactions, which are responsible for cells proliferation, differentiation and, more importantly, expression of genes and proteins [245]. Additionally, it was found that 2D cell culture affects the morphology of the cells and the mode of division, which affect the organization of the intracellular structures and cell signalling [245]. Collectively, several studies have reported that 2D cell culturing results in changes in the gene expression and biochemistry of the cell that predisposes to the loss of diverse phenotypes [245–247].

Therefore, owing to the disadvantages of the 2D cell culturing that might affect the accuracy of the gene expression studies results, 3D cell cultures have gained attention as a more accurate model of tissues. The concept of 3D cell culturing relies on growing the cells as multilayer spheroid structures where cell-cell and cell-extracellular matrix interactions are maximized [245]. Thus, 3D cell culture provides conditions similar to cells growing *in vivo* in terms of signalling and gene expression [245]. Hence, this experiment examines the effect of miRNA-

140 delivery in chondrocyte phenotype regulation in 3D micromass C28/I2 chondrocytes cell culture, which has been shown to have a more representative gene expression profile that better models OA [196].

In this experiment, the effect of miRNA-140 in regulating *FZD6*, *ADAMTS5* and *MMP13*, three of the most identified potential targets for OA, was studied. The regulatory effect of miRNA-140 on these genes was explained in detail in the introduction chapter (**sections 1.8.3 and 1.8.4)**. **Figure 5.14** shows the morphology of the C28/I2 micromass cell cultures. As shown in **Figure 5.14 d and e**, 5'Cy5-miRNA-140 was successfully delivered to the cells using lipofectamine RNAiMAX and PLGA-Eudragit NPs compared to a negative control of naked 5'Cy5-miRNA-140 **(Figure 5.14 c)**. Unlike 2D cell cultures, where the cells growing as a monolayer have unlimited access to the medium ingredients, cells have limited access to these ingredients in 3D cell cultures, making them more challenging to be transfected. Hence, the delivery data shows that lipofectamine RNAiMAX and PLGA-Eudragit NPs efficiently overcome this burden and deliver the 5'Cy5-miRNA-140 to the cells.

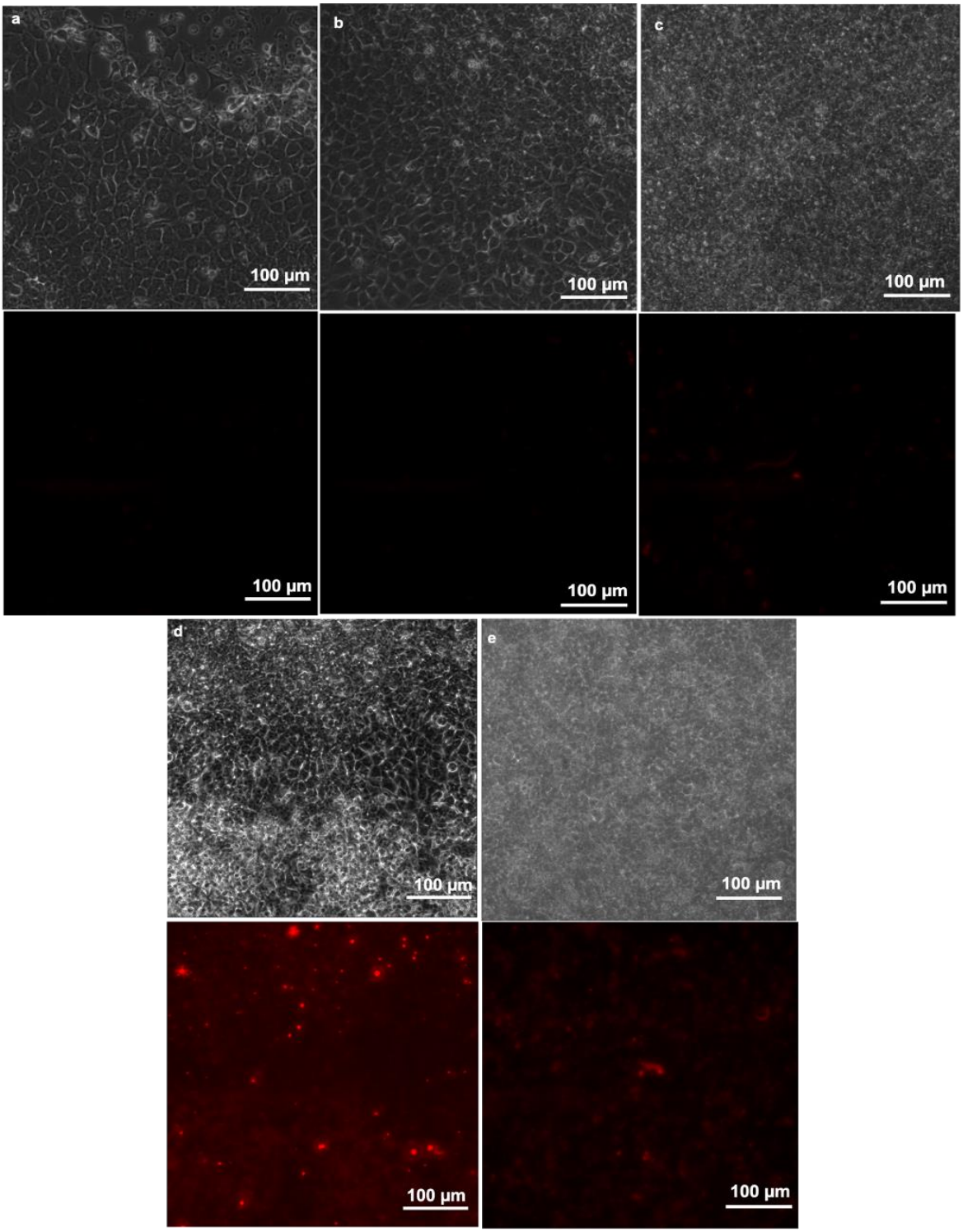

Figure 5.14: Brightfield (upper) and fluorescence (lower)images of C28/I2 micromass cell culture where (a) C28/I2 chondrocytes control in ITS media, (b) C28/I2 chondrocytes control treated with 20 ng/mL of IL-1ß, (c) C28/I2 chondrocytes transfected with 12 nM of naked miRNA-140 after being treated with 20 ng/mL of IL-1ß, (d) C28/I2 chondrocytes transfected with 12 nM of miRNA-140 using lipofectamine RNAiMAX after being treated with 20 ng/mL of IL-1ß and (e) C28/I2 chondrocytes transfected with 12 nM of miRNA-140 delivered by NPs after being treated with 20 ng/mL of IL-1ß. Images were taken 48 (h) post-transfection using an inverted fluorescent microscope.

In this study, IL-1ß was used to induce the mRNA level of OA-relevant proteases such *ADAMTS5* and *MMP-13*, besides exploring its effect on FZD6. Therefore, this experiment's data showed no significant increase in FZD6 expression in C28/I2 micromass culture after being treated with 20 ng/mL of IL-1B (P-value ≥ 0.05) **(Figure 5.15)**. Hence, this suggests no direct regulatory relationship between IL-1ß and FZD6 gene expression in C28/I2 chondrocytes. To our knowledge, no study examined the impact of IL-1ß on the FZD6 mRNA level. Furthermore, 12 nM of miRNA-140 delivered by lipofectamine RNAiMAX caused no significant downregulation of *FZD6* expression (P-value ≥ 0.05). In contrast, PLGA-Eudragit NPs delivering the same miRNA-140 dose caused significant FZD6 downregulation of 87% ± 16%, (P-value < 0.05) (**Figure 5.15)**. From the results, it is clear that miRNA-140 loaded PLGA-Eudragit NPs are more efficient than lipofectamine RNAiMAX in delivering functional miRNA-140 to C28/I2 micromass cell culture.

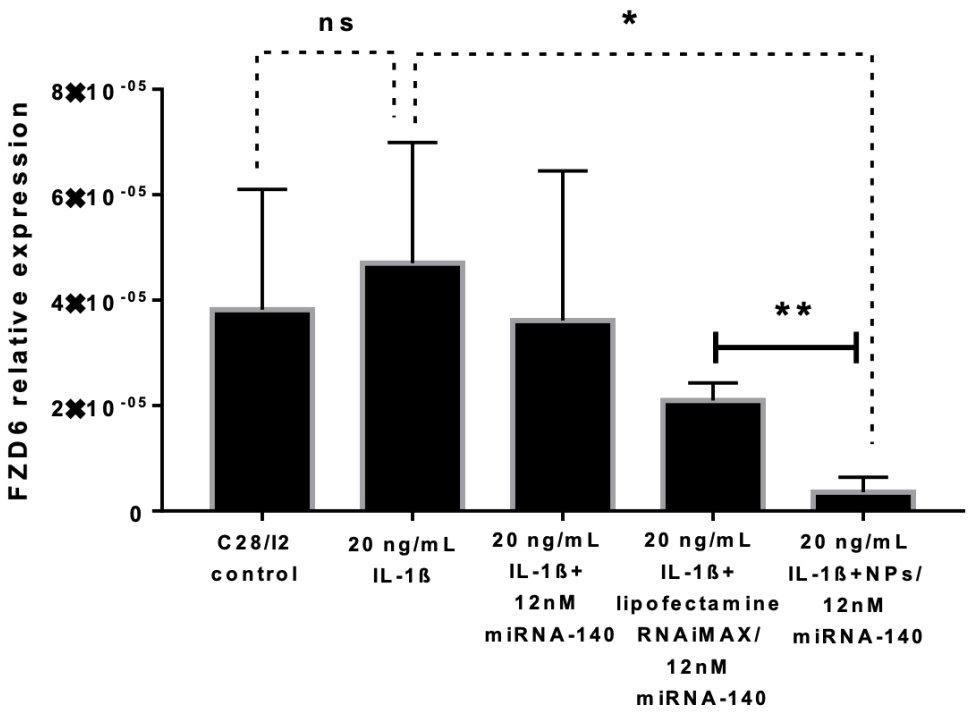

Figure 5.15: Effect of miRNA-140-5P delivered to C28/I2 chondrocytes micromass cell culture using PLGA-Eudragit NPs and lipofectamine RNAiMAX on *FZD6* gene expression after treating the cells with 20 ng/mL IL-1ß. *FZD6* gene expression was measured by qPCR 48 (h) post-transfection. * (P-value < 0.05), ** (P-value < 0.01) and ns (P-value ≥ 0.05). Error bars represent the standard deviation and n=3.

As shown in **Figure 5.16**, a significant increase in *MMP-13* expression (5-fold) was observed after treating the cells with 20 (ng/mL) of IL-1ß (P-value < 0.05). This finding is in line with several studies that suggested the role of IL-1ß in inducing the mRNA level of OA-relevant proteases, *MMP-13* in particular, as mentioned in the introduction chapter **(section 1.8.4)**. Similar findings to those observed with the *FZD6* expression were observed with the *MMP-13* expression **(Figure 5.16)**. Although 12 nM of miRNA-140 delivered by lipofectamine RNAiMAX showed no significant effect in downregulating *MMP-13* expression (P-value ≥ 0.05), PLGA-Eudragit NPs delivering a similar concentration of miRNA-140 showed significant MMP-13 downregulation of 76% ± 13%, (P-value < 0.05). These findings confirm the efficacy of PLGA-Eudragit NPs in delivering functional miRNA-140 compared to the traditional transfection agent (lipofectamine RNAiMAX).

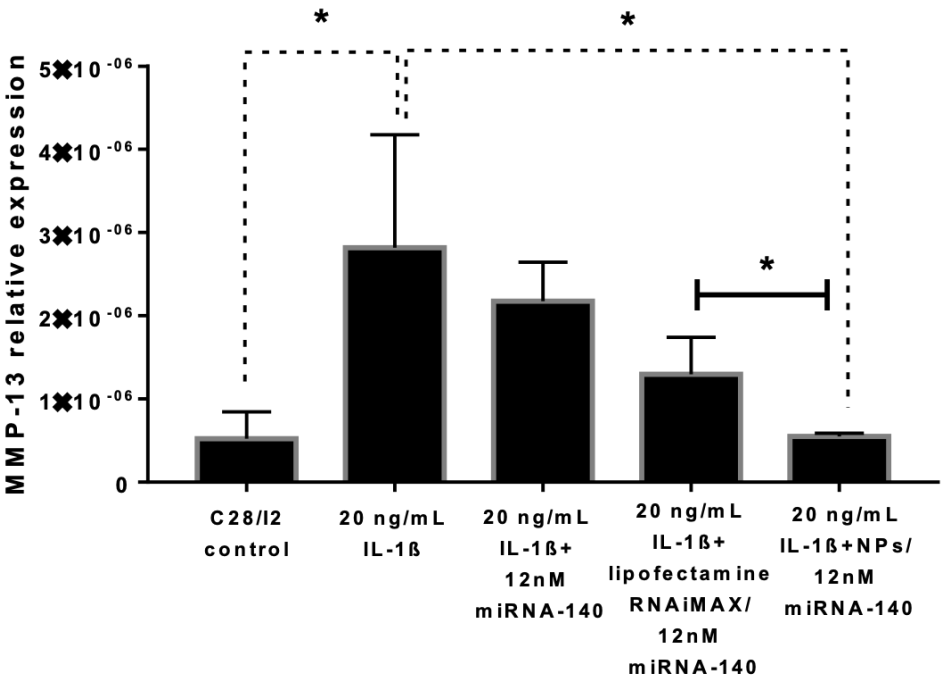

Figure 5.16: Effect of miRNA-140-5P delivered to C28/I2 chondrocytes micromass cell culture using PLGA-Eudragit NPs and lipofectamine RNAiMAX on *MMP13* gene expression after treating the cells with 20 ng/mL IL-1ß. *MMP13* gene expression was measured by qPCR 48 (h) post-transfection. * (P-value < 0.05). Error bars represent the standard deviation and n=3.

The increase in *ADAMTS5* expression following the treatment with IL-1ß was not found significant in this study (P-value ≥ 0.05) **(Figure 5.17)**. However, the efficacy of miRNA-140 delivered by PLGA-Eudragit NPs compared to lipofectamine RNAiMAX was confirmed in this experiment. Hence, a significant downregulation of ADAMTS5 gene expression (77% ± 14%) was detected with 12 nM of miRNA-140 delivered by Eudragit NPs (P-value < 0.05); however, no significant change was observed with the same concentration of miRNA-140 delivered by lipofectamine RNAiMAX (P-value ≥ 0.05) **(Figure 5.17)**.

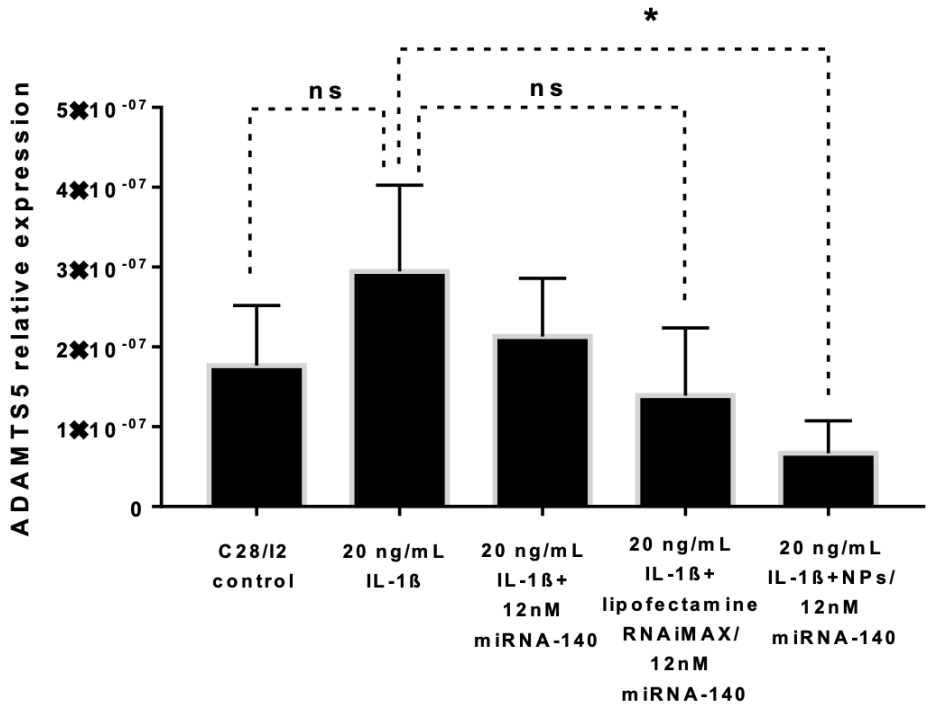

Figure 5.17: Effect of miRNA-140-5P delivered to C28/I2 chondrocytes micromass cell culture using PLGA-Eudragit NPs and lipofectamine RNAiMAX on *ADAMTS5* gene expression after treating the cells with 20 ng/mL IL-1ß. *ADAMTS5* gene expression was measured by qPCR 48 (h) post-transfection. * (P-value < 0.05) and ns (P-value ≥ 0.05). Error bars represent the standard deviation and n=3.

Collectively, the qPCR micromass data indicate that PLGA-Eudragit NPs could deliver miRNA-140 that maintained its functional capability to downregulate target genes expression in C28/I2 3D micromass cell culture. This suggests that PLGA-Eudragit NPs can be used as a novel therapeutic platform for efficient miRNA-140 delivery to reverse the progression of the disease and restore joint homeostasis. Compared to 2D cell culture, 3D micromass cell culture is a challenging model explained by the diffusional barriers imposed by this model. However, this suggests that 3D micromass cell culture is a small step towards modelling the diffusional

barrier of the cartilage that is commonly characterised to have a pore size between 6 –11 nm, as mentioned in the introduction chapter **(section 1.8.5)**. Although the 3D micromass cell culture is challenging, the NPs formulation has shown positive effects in this model, suggesting that the next step would be to test the formulation's efficacy in miRNA-140 knockout mouse model or human cartilage explants.

5.4 Conclusion

In summary, 5'Cy5-miRNA-140 loaded PLGA-Eudragit NPs were successfully developed in this study using the droplet double emulsion method. miRNA-140 was efficiently loaded into PLGA-Eudragit NPs by physical entrapment and electrostatic interaction with an EE% higher than 80%. In addition, the NPs showed a stable profile in synovial fluid, 7.4 PBS and transfection medium with miRNA-140 release profile for up to 96 (h).

Interestingly, 5'Cy5-miRNA-140 loaded PLGA-Eudragit NPs have efficiently escaped the endolysosomal degradation confirmed by the significant increase in intracellular miRNA-140 levels, commensurate with a significant reduction in *FZD6* gene expression in C28/I2 chondrocytes. Additionally, PLGA-Eudragit NPs were found more efficient in downregulating the *FZD6* gene expression compared to lipofectamine RNAiMAX when delivering similar concentrations of miRNA-140. The downregulation of *FZD6* expression by PLGA-Eudragit NPs was translated into the FZD6 protein level; however, lipofectamine RNAiMAX was more efficient than the NPs in this aspect.

The positive effect of miRNA-140-loaded PLGA-Eudragit NPs was confirmed in 3D micromass C28/I2 cell culture. This was manifested as a significant reduction in *FZD6*, *MMP-13*, and *ADAMTS5* genes expression in C28/I2 cells transfected with 5'Cy5-miRNA-140 loaded PLGA-Eudragit NPs. However, miRNA-140 delivered by lipofectamine RNAiMAX resulted in no significant change in *FZD6*, *MMP-13* and A*DAMTS5*, demonstrating that NPs were more efficient than lipofectamine RNAiMAX.

On this basis, the study provides a novel polymeric NPs platform that can efficiently deliver miRNA-140 to the chondrocytes to restore homeostasis by regulating three of the well-identified potential gene targets in OA.

Chapter 6

Conclusions and future outlook

6.1 General conclusions

The presented work provides an overview of the different preparation methods of polymeric NPs. In addition, it investigates the impact of the critical processing parameters of each synthesis method on the properties of NPs, including size, shape and surface charge, as a leading approach to develop efficient gene delivery platforms. NPs provides a promising strategy for curing complex diseases by delivering nucleic acids (pDNA/miRNAs) that can restore homeostasis by targeting the molecular mechanisms behind the development of specific diseases [7,123,151]. Therefore, this study was interested in investigating the potential of gene loaded PNPs to target the molecular mechanisms behind OA development despite the lack of effective treatments.

6.1.1 Impact of the critical processing parameters on the properties of PNPs

As discussed in the introduction chapter, PNPs can be prepared by several methods, including nanoprecipitation and double emulsion methods. Each synthesis method has a group of advantages and limitations that affect the final properties of NPs and their intended application. In addition to this, each of these methods has a group of critical processing parameters that were observed to have complex interactions, affecting the final properties of NPs. The study in **chapter 3** has provided a comprehensive comparison between conventional nanoprecipitation (CB-method) and microfluidic-assisted nanoprecipitation (MF-method) for PNPs preparation. This was achieved by studying and comparing the impact of the processing parameters of each method on the NPs properties. Furthermore, the study in **chapter 3** addressed the limitations and challenges of each method.

As discussed in **chapter 3**, nanoprecipitation is a complex process where a group of parameters play a simultaneous role in controlling the properties of the fabricated NPs, including the degree of supersaturation, solvent type and mixing efficiency. Furthermore, the data presented in **chapter 3** demonstrated that CB-method and MF-method are both feasible for size tuning if the processing parameters are well controlled. The study revealed the impact of the chip design and geometries on the size of PLGA NPs, with the smallest NPs being prepared using the 100 µm Micro Mixer chip. However, the study addressed the significant limitations of using the Micro Mixer chip when a blend of polymers was used (PLGA and Eudragit/ PLGA and chitosan) displayed as continuous fouling and blockages within the chip. Additionally, it is well known that microfluidics is proposed as a superior method for controlled

nanoprecipitation and lower batch to batch variations; however, as was discussed in **chapter 3**, the CB-method was found to be as robust as the MF-method.

In addition to these points, the study in **chapter 3** addresses several questions on the validity of using the solvent self-diffusion coefficient and the mixing time within the MF chips to predict the mixing efficiency and the size of the resulting NPs. As was demonstrated by the data at high TFRs in **chapter 3**, size tunability and small NPs size were achievable even when mixing time was much longer than the residence time, suggesting no optimum mixing time range for fabricating smaller NPs or achieving size tunability. Overall, the study in **chapter 3** provides an insight into the effect of the nanoprecipitation parameters for CB and MF methods on the NPs properties, offering a better understanding of each method advantages, expectations and limitations.

The study in **chapter 5** has explored the development of PNPs using the double emulsion method. Several parameters were found to impact the size and the surface charge of the fabricated NPs, including polymer concentration, stabiliser concentration and the sonication time. This emphasises the need to experimentally study the processing parameters' effect on the NPs properties to achieve the desired NPs properties.

6.1.2 Synthesis of polymeric NPs for plasmid DNA delivery

As discussed in the introduction chapter, an ideal pDNA delivering NPs should possess specific characteristics such as protecting the loaded nucleic acid from degradation by nucleases and delivering the pDNA to the nucleus to induce its therapeutic action without causing significant toxicity[88,89]. Furthermore, the transfection efficiency primarily relies on the NPs properties (material, size, shape and charge), which explains the need to screen the impact of the used NPs synthesis methods on the properties of the NPs and their transfection efficiency. Therefore, the study in **chapter 4** explored the translational potential of microfluidic technology as a formulation manufacturing method for nanoparticle-based pDNA delivery platforms compared to conventional methods.

In **chapter 3**, it was found that PLGA-Eudragit NPs prepared by CB-method were significantly smaller in size compared to those prepared by MF-method. Therefore, the impact of this difference on the pDNA loading and transfection efficiencies was tested in **chapter 4**. Hence,

it was found that the difference in particle size of the NPs prepared by the two methods was translated into differences in their plasmid DNA loading efficiency, transfection efficiency and cytotoxicity. The data demonstrated a higher loading and transfection efficiency for PLGA-Eudragit NPs prepared by CB-method than those prepared by MF-method. Overall, it can be concluded from the results in **chapter 4** that PLGA-Eudragit NPs can be considered as a promising gene vector, and the CB-method can be used to manufacture them with a high throughput rate. Although the study was focused on using pDNA encoding a green fluorescent protein as a reporter gene to compare the transfection efficiency of the NPs developed by the two methods, pDNA loaded NPs has several clinical applications, including the delivery of plasmid encoding *TGF-β1* for OA treatment, as mentioned in the introduction chapter **(section 1.7.1)**.

6.1.3 Synthesis of miRNA-140 loaded polymeric NPs to functionally alter OA gene targets

Chapter 5 was focused on developing a formulation of stable miRNA-140 loaded PNPs to examine its efficiency in regulating the potential gene targets in OA. As already discussed in the introduction chapter **(section 1.8.4)**, miRNA-140 plays a pivotal role in regulating several underlying OA development mechanisms; however, efficient loading and delivery of miRNAs are challenging and requires a reliable experimental design for NPs development and transfection [4,87]. miRNA-140 loaded PLGA-Eudragit NPs were successfully developed in **chapter 5**. The developed NPs showed a high miRNA-140 EE% exceeding 80% with an excellent colloidal stability profile at physiological conditions. Furthermore, as demonstrated by the qPCR data **(chapter 5)**, the NPs formulation efficiently delivered intact and functional miRNA-140 to the C28/I2 human chondrocytes. Interestingly, the formulation was more efficient than Lipofectamine RNAiMAX control in downregulating the *FZD6* expression on the mRNA level in the 2D C28/I2 cell culture model. This downregulatory effect was translated into the FZD6 protein level; however, Lipofectamine RNAiMAX was more efficient than the formulation on this level.

The formulation's efficacy was challenged by testing it on a 3D micromass C28/I2 cell culture model, and interestingly, the formulation was more efficient than the Lipofectamine RNAiMAX in downregulating the *FZD6*, *MMP13* and *ADAMTS5* expression. Furthermore, considering the diffusional barriers imposed by the cartilage structure, as explained in the introduction chapter **(section 1.8.5)**, the 3D micromass cell culture could better model the OA

joint besides having a more representative gene expression profile as suggested by several studies. Overall, the study **(chapter 5)** provides a novel polymeric NPs platform that can efficiently deliver miRNA-140 to the chondrocytes to restore homeostasis by regulating potential gene targets in OA, as shown in **Figure 6.1**.

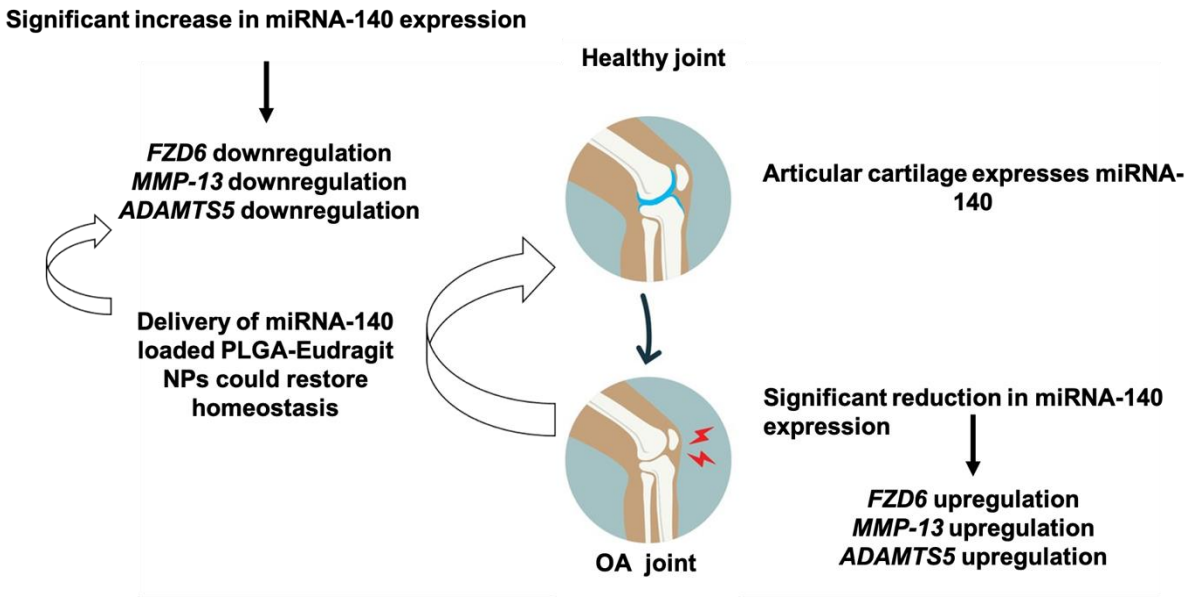

Figure 6.1: Summary of the role of miRNA-140 loaded PLGA-Eudragit NPs in reversing the molecular mechanisms underlying OA development by regulating OA potential gene targets.

6.2 Future outlook

The conducted studies in this project provided information about the critical parameters and processing conditions that should be considered to fabricate PNPs possessing the desired characteristics for gene delivery applications. However, further studies could be done to study the effect of the synthesis method (CB/MF method) on the stability of the NPs. Hence, a stability study of the polymeric NPs prepared by the two methods could be designed for a few months to examine the effect of the synthesis method on the NPs stability profile.

Moreover, miRNA-140 loaded PLGA-Eudragit NPs is among the promising formulations developed in this study; however, further studies are needed to outline the full potential of the formulation. As discussed in **chapter 5**, the NPs formulation was found efficient in downregulating the *FZD6*, *MMP13* and *ADAMTS5* expression in the 3D micromass cell culture

model; however, further Western blotting experiments are needed to confirm if the changes in the mRNA levels will be translated to changes in the protein levels in the 3D C28/I2 model.

In addition, despite the positive effects of the miRNA-140-loaded PLGA-Eudragit NPs formulation observed in 2D and 3D cell culture models, further investigation is needed to examine if these findings could be translated into positive effects in a mouse model or human cartilage explants. Accordingly, the following experiments could be conducted to gain more information about the formulation's efficacy in these models.

6.2.1 NPs penetration into bovine cartilage explants

This experiment could provide information about the penetration and distribution profile of the formulation compared to naked miRNA-140 throughout a section of cartilage explant [248]. Generally, these cartilage explants are biopsied from young bovine knee joints then trimmed to 1 mm thickness to be cultured [248]. Since the NPs are loaded with CY5-labelled miRNA-140, the distribution of the NPs could be tracked over a specific time interval by confocal microscopy. Therefore, the results of this experiment could offer an indication of the transport performance of the formulation in animal models.

6.2.2 Intra-articular injection of the formulation into a miRNA-140 null mouse

After confirming the formulation's efficacy in 2D and 3D cell culture models and observing the NPs distribution profile in bovine cartilage explants, checking the formulation's efficacy in a miRNA-140 null mouse would be a reasonable step. The formulation could be injected into the intra-articular space under anaesthesia, and then the following experiments could be conducted after a specific time interval to examine the efficacy of the injected formulation.

6.2.2.1 miRNA-140 level and potential OA gene targets expression assayed by qPCR

qPCR experiments could be conducted to measure the miRNA-140 level and the expression of its potential gene targets in the tissues.

6.2.2.2 Histology analysis

This experiment is mainly conducted to examine the structural and morphological changes in the cartilage following the therapy [248]. Generally, this experiment is conducted after

euthanasia as the joints are excised, fixed and stained with immunohistochemical to detect the collagen and the aggrecan layer.

6.2.2.3 Motor and gait assessment

Generally, motor dysfunction, pain, gait assessment and radiographic changes are used for the clinical evaluation and diagnosis of OA in patients [249,250]. Therefore, these tests are considered one way to check the efficacy of the delivered formulation in animal models

References

[1] J.K. Patra, G. Das, L.F. Fraceto, E.V.R. Campos, M.D.P. Rodriguez-Torres, L.S. Acosta-Torres, L.A. Diaz-Torres, R. Grillo, M.K. Swamy, S. Sharma, S. Habtemariam, H.S. Shin, Nano based drug delivery systems: Recent developments and future prospects. Journal of Nanobiotechnology. 16 (2018) 1–33.

[2] M.J. Mitchell, M.M. Billingsley, R.M. Haley, M.E. Wechsler, N.A. Peppas, R. Langer, Engineering precision nanoparticles for drug delivery, Nat. Rev. Drug Discov. 20 (2021) 101–124.

[3] Y.S. Choi, M.Y. Lee, A.E. David, Y.S. Park, Nanoparticles for gene delivery: Therapeutic and toxic effects, Mol. Cell. Toxicol. 10 (2014) 1–8.

[4] S.W.L. Lee, C. Paoletti, M. Campisi, T. Osaki, G. Adriani, R.D. Kamm, C. Mattu, V. Chiono, MicroRNA delivery through nanoparticles, J. Control. Release. 313 (2019) 80–95.

[5] J. Luten, C.F. van Nostrum, S.C. De Smedt, W.E. Hennink, Biodegradable polymers as non-viral carriers for plasmid DNA delivery, J. Control. Release. 126 (2008) 97–110.

[6] M. Gargouri, A. Sapin, S. Bouali, P. Becuwe, J.L. Merlin, P. Maincent, Optimization of a new non-viral vector for transfection: Eudragit nanoparticles for the delivery of a DnA Plasmid, Technol. Cancer Res. Treat. 8 (2009) 433–444.

[7] A. Basarkar, J. Singh, Poly (lactide-co-glycolide)-polymethacrylate nanoparticles for intramuscular delivery of plasmid encoding interleukin-10 to prevent autoimmune diabetes in mice, Pharm. Res. 26 (2009) 72–81.

[8] J.A. Loureiro, M.C. Pereira, PLGA based drug carrier and pharmaceutical applications: The most recent advances, Pharmaceutics. 12 (2020) 1–5.

[9] C.C. Jian-Ming Lü, Xinwen Wang, Christian Marin-Muller, Hao Wang, Peter H Lin, Qizhi Yao, Current advances in research and clinical applications of PLGA- based nanotechnology, 23 (2011) 1–7.

[10] W.T. Godbey, K.K. Wu, A.G. Mikos, Poly(ethylenimine)-mediated gene delivery affects endothelial cell function and viability, Biomaterials. 22 (2001) 471–480.

[11] J. Ghitman, E.I. Biru, R. Stan, H. Iovu, Review of hybrid PLGA nanoparticles: Future of smart drug delivery and theranostics medicine, Mater. Des. 193 (2020).

[12] K. Miladi, S. Sfar, H. Fessi, A. Elaissari, Nanoprecipitation Process: From Particle Preparation to In Vivo Applications, in: Polym. Nanoparticles Nanomedicines, Springer International Publishing, 2016: pp. 17–53.

[13] W. Huang, C. Zhang, Tuning the Size of Poly(lactic-co-glycolic Acid) (PLGA) Nanoparticles Fabricated by Nanoprecipitation, Biotechnol. J. 13 (2018).

[14] M. Pande, A.N. Bhaskarwar, Nanoparticles : Preparation and Characterization, in: Momentum Press, New York [New York] [222 East 46th Street, New York, NY 10017], 2016.

[15] B. Sinha, R.H. Müller, J.P. Möschwitzer, Bottom-up approaches for preparing drug nanocrystals: Formulations and factors affecting particle size, Int. J. Pharm. 453 (2013) 126–141.

[16] D. Quintanar-Guerrero, E. Allémann, H. Fessi, E. Doelker, Preparation techniques and mechanisms of formation of biodegradable nanoparticles from preformed polymers, Drug Dev. Ind. Pharm. 24 (1998) 1113–1128.

[17] S.I. Hamdallah, R. Zoqlam, P. Erfle, M. Blyth, A.M. Alkilany, A. Dietzel, S. Qi, Microfluidics for pharmaceutical nanoparticle fabrication: The truth and the myth, Int. J. Pharm. 584 (2020).

[18] N.T.K. Thanh, N. Maclean, S. Mahiddine, Mechanisms of nucleation and growth of nanoparticles in solution, Chem. Rev. 114 (2014) 7610–7630.

[19] D. KASHCHIEV, nucleation basic theory with applications, OXFORD, 2003.

[20] C. Guozhong, Nanostructures & Nanomaterials: Synthesis, Properties & Applications, Imperial college press, 2004.

[21] N.T.K. Thanh, N. Maclean, S. Mahiddine, Mechanisms of nucleation and growth of nanoparticles in solution, Chem. Rev. 114 (2014) 7610–7630.

[22] J. Tao, S.F. Chow, Y. Zheng, Application of flash nanoprecipitation to fabricate poorly water-soluble drug nanoparticles, Acta Pharm. Sin. B. 9 (2019) 4–18.

[23] B. Sinha, R.H. Müller, J.P. Möschwitzer, Bottom-up approaches for preparing drug nanocrystals: Formulations and factors affecting particle size, Int. J. Pharm. 453 (2013) 126–141.

[24] P.G. Vekilov, Nucleation, Cryst. Growth Des. 10 (2010) 5007–5019.

[25] S.G. Kwon, T. Hyeon, Formation mechanisms of uniform nanocrystals via hot-injection and heat-up methods, Small. 7 (2011) 2685–2702.

[26] S.A. Guhagarkar, V.C. Malshe, P. V. Devarajan, Nanoparticles of polyethylene sebacate: A new biodegradable polymer, AAPS PharmSciTech. 10 (2009) 935–942.

[27] J. Cheng, B.A. Teply, I. Sherifi, J. Sung, G. Luther, F.X. Gu, E. Levy-Nissenbaum, A.F. Radovic-Moreno, R. Langer, O.C. Farokhzad, Formulation of functionalized PLGA-PEG nanoparticles for in vivo targeted drug delivery, Biomaterials. 28 (2007) 869–876.

[28] M. Kakran, N.G. Sahoo, L. Li, Z. Judeh, Fabrication of quercetin nanoparticles by anti-solvent precipitation method for enhanced dissolution, Powder Technol. 223 (2012) 59–

64.

[29] S. V. Dalvi, R.N. Dave, Controlling particle size of a poorly water-soluble drug using ultrasound and stabilizers in antisolvent precipitation, Ind. Eng. Chem. Res. 48 (2009) 7581–7593.

[30] B.Y. Gajera, D.A. Shah, R.H. Dave, Development of an amorphous nanosuspension by sonoprecipitation-formulation and process optimization using design of experiment methodology, Int. J. Pharm. 559 (2019) 348–359.

[31] S. Verma, S. Kumar, R. Gokhale, D.J. Burgess, Physical stability of nanosuspensions: Investigation of the role of stabilizers on Ostwald ripening, Int. J. Pharm. 406 (2011) 145–152.

[32] A.A. Thorat, S. V. Dalvi, Liquid antisolvent precipitation and stabilization of nanoparticles of poorly water soluble drugs in aqueous suspensions: Recent developments and future perspective, Chem. Eng. J. 181–182 (2012) 1–34.

[33] Y. Dong, S.S. Feng, Methoxy poly(ethylene glycol)-poly(lactide) (MPEG-PLA) nanoparticles for controlled delivery of anticancer drugs, Biomaterials. 25 (2004) 2843–2849.

[34] M.L.T. Zweers, D.W. Grijpma, G.H.M. Engbers, J. Feijen, The Preparation of Monodisperse Biodegradable Polyester Nanoparticles with a Controlled Size, J. Biomed. Mater. Res. - Part B Appl. Biomater. 66 (2003) 559–566.

[35] A.A.O. Kubo, Preparation of aqueous polymeric nanodispersions by a reversible salting-out process : influence of process parameters on particle size." International journal of pharmaceutics 87.1-3 (1992): 247-253.

[36] C.J. Martínez Rivas, M. Tarhini, W. Badri, K. Miladi, H. Greige-Gerges, Q.A. Nazari, S.A. Galindo Rodríguez, R.Á. Román, H. Fessi, A. Elaissari, Nanoprecipitation process: From encapsulation to drug delivery, Int. J. Pharm. 532 (2017) 66–81.

[37] J. Tao, S.F. Chow, Y. Zheng, Application of flash nanoprecipitation to fabricate poorly water-soluble drug nanoparticles, Acta Pharm. Sin. B. 9 (2019) 4–18.

[38] G.M. Whitesides, The origins and the future of microfluidics, Nature. 442 (2006) 368–373.

[39] N.T. Nguyen, S.A.M. Shaegh, N. Kashaninejad, D.T. Phan, Design, fabrication and characterization of drug delivery systems based on lab-on-a-chip technology, Adv. Drug Deliv. Rev. 65 (2013) 1403–1419.

[40] Y.F. Soon-Eng Ong , Sam Zhang , Hejun Du, Fundamental principles and applications of microfluidic systems, Transport. (2008) 2757–2773.

[41] Patrick tabeling, introduction to microfluidics, OXFORD, 2005.

[42] M. Ferreira, A. Correia, H.A. Santos, Microfluidics as a Cutting-Edge Technique for Drug Delivery Applications, (2016).

[43] S.D. Cho, An integrated droplet based microfluidic platform for high throughput , multi-parameter screening of photosensitiser activity, (2013).

[44] A. Dietzel, Microsystems for Pharmatechnology, Braunschweig, Germany, n.d.

[45] Y. Zhang, H.F. Chan, K.W. Leong, Advanced materials and processing for drug delivery: The past and the future, Adv. Drug Deliv. Rev. 65 (2013) 104–120.

[46] R. Mukhopadhyay, When PDMS isn't the best, Anal. Chem. 79 (2007) 3249–3253.

[47] Zhou, Jinwen, Dmitriy A. Khodakov, Amanda V. Ellis, Nicolas H. Voelcker, Surface modification for PDMS-based microfluidic devices, Electrophoresis. 33 (2012) 89–104.

[48] T. Panagiotou, S. V. Mesite, R.J. Fisher, Production of norfloxacin nanosuspensions using microfluidics reaction technology through solvent/antisolvent crystallization, Ind. Eng. Chem. Res. 48 (2009) 1761–1771.

[49] The Dolomite Centre, Droplet junction chips product data sheet, MAR-000063 v1.4, (n.d.) 1–10.

[50] N.T. Nguyen, X. Huang, Modelling, fabrication and characterization of a polymeric micromixer based on sequential segmentation, Biomed. Microdevices. 8 (2006) 133–139.

[51] W.S. Saad, R.K. Prud'Homme, Principles of nanoparticle formation by flash nanoprecipitation, Nano Today. 11 (2016) 212–227.

[52] J. Xu, S. Zhang, A. MacHado, S. Lecommandoux, O. Sandre, F. Gu, A. Colin, Controllable Microfluidic Production of Drug-Loaded PLGA Nanoparticles Using Partially Water-Miscible Mixed Solvent Microdroplets as a Precursor, Sci. Rep. 7 (2017) 1–12.

[53] S. Rezvantalab, M. Keshavarz Moraveji, Microfluidic assisted synthesis of PLGA drug delivery systems, RSC Adv. 9 (2019) 2055–2072.

[54] P.M. Valencia, P.A. Basto, L. Zhang, M. Rhee, R. Langer, O.C. Farokhzad, R. Karnik, Single-step assembly of homogenous lipid-polymeric and lipid-quantum dot nanoparticles enabled by microfluidic rapid mixing, ACS Nano. 4 (2010) 1671–1679.

[55] N. Lababidi, V. Sigal, A. Koenneke, K. Schwarzkopf, A. Manz, M. Schneider, Microfluidics as tool to prepare size-tunable PLGA nanoparticles with high curcumin encapsulation for efficient mucus penetration, Beilstein J. Nanotechnol. 10 (2019) 2280–2293.

[56] B.K. Johnson, R.K. Prud'homme, Mechanism for rapid self-assembly of block copolymer nanoparticles, Phys. Rev. Lett. 91 (2003): 118302.

[57] F. Gu, O.C. Farokhzad, W. Kyei-Manu, C. Cannizzaro, R. Karnik, L. Dean, P. Basto, R. Langer, Microfluidic Platform for Controlled Synthesis of Polymeric Nanoparticles, Nano Lett. 8 (2008) 2906–2912.

[58] A.S. Lari, A. Khatibi, P. Zahedi, H. Ghourchian, Microfluidic-assisted production of poly(caprolactone) and cellulose acetate nanoparticles: effects of polymers, surfactants, and flow rate ratios, Polymer Bulletin 78 (2021) 5449–5466.

[59] R. Donno, A. Gennari, E. Lallana, J.M.R. De La Rosa, R. d'Arcy, K. Treacher, K. Hill, M. Ashford, N. Tirelli, Nanomanufacturing through microfluidic-assisted nanoprecipitation: Advanced analytics and structure-activity relationships, Int. J. Pharm. 534 (2017) 97–107.

[60] T. Baby, Y. Liu, A.P.J. Middelberg, C.X. Zhao, Fundamental studies on throughput capacities of hydrodynamic flow-focusing microfluidics for producing monodisperse polymer nanoparticles, Chem. Eng. Sci. 169 (2017) 128–139.

[61] B. Amoyav, O. Benny, Controlled and tunable polymer particles' production using a single microfluidic device, Appl. Nanosci. 8 (2018) 905–914.

[62] Y. Morikawa, T. Tagami, A. Hoshikawa, T. Ozeki, The use of an efficient microfluidic mixing system for generating stabilized polymeric nanoparticles for controlled drug release, Biol. Pharm. Bull. 41 (2018) 899–907. https://doi.org/10.1248/bpb.b17-01036.

[63] E. Chiesa, R. Dorati, T. Modena, B. Conti, I. Genta, Multivariate analysis for the optimization of microfluidics-assisted nanoprecipitation method intended for the loading of small hydrophilic drugs into PLGA nanoparticles, Int. J. Pharm. 536 (2018) 165–177.

[64] M.C. Operti, Y. Dölen, J. Keulen, E.A.W. van Dinther, C.G. Figdor, O. Tagit, Microfluidics-assisted size tuning and biological evaluation of PLGA particles, Pharmaceutics. 11 (2019) 1–17.

[65] R. Othman, G.T. Vladisavljević, Z.K. Nagy, Preparation of biodegradable polymeric nanoparticles for pharmaceutical applications using glass capillary microfluidics, Chem. Eng. Sci. 137 (2015) 119–130.

[66] P. Erfle, J. Riewe, H. Bunjes, A. Dietzel, Goodbye fouling: a unique coaxial lamination mixer (CLM) enabled by two-photon polymerization for the stable production of monodisperse drug carrier nanoparticles, Lab Chip. 21 (2021) 2178–2193.

[67] M. Rhee, P. Valencia, M. Rodriguez, R. Langer, O.C. Farokhzad, R. Karnick, Synthesis

of Size-tunable Polymeric Nanoparticles Enabled by 3D Hydrodynamic Flow Focusing in Single-Layer Microchannels, Advanced Materials 23.12 (2011): H79-H83.

[68] H. Bolze, P. Erfle, J. Riewe, H. Bunjes, A. Dietzel, T.P. Burg, A microfluidic split-flow technology for product characterization in continuous low-volume nanoparticle synthesis, Micromachines. 10 (2019).

[69] M. Schoenitz, L. Grundemann, W. Augustin, S. Scholl, Fouling in microstructured devices: A review, Chem. Commun. 51 (2015) 8213–8228.

[70] J. Riewe, P. Erfle, S. Melzig, A. Kwade, A. Dietzel, H. Bunjes, Antisolvent precipitation of lipid nanoparticles in microfluidic systems – A comparative study, Int. J. Pharm. 579 (2020).

[71] J.L. Perry, S.G. Kandlikar, Fouling and its mitigation in silicon microchannels used for IC chip cooling, Microfluid. Nanofluidics. 5 (2008) 357–371.

[72] J.M. Lim, A. Swami, L.M. Gilson, S. Chopra, S. Choi, J. Wu, R. Langer, R. Karnik, O.C. Farokhzad, Ultra-high throughput synthesis of nanoparticles with homogeneous size distribution using a coaxial turbulent jet mixer, ACS Nano. 8 (2014) 6056–6065.

[73] J.M. Lim, N. Bertrand, P.M. Valencia, M. Rhee, R. Langer, S. Jon, O.C. Farokhzad, R. Karnik, Parallel microfluidic synthesis of size-tunable polymeric nanoparticles using 3D flow focusing towards in vivo study, Nanomedicine Nanotechnology, Biol. Med. 10 (2014) 401–409.

[74] D. Liu, H. Zhang, S. Cito, J. Fan, E. Mäkilä, J. Salonen, J. Hirvonen, T.M. Sikanen, D.A. Weitz, H.A. Santos, Core/Shell Nanocomposites Produced by Superfast Sequential Microfluidic Nanoprecipitation, Nano Lett. 17 (2017) 606–614.

[75] T. Lorenz, S. Bojko, H. Bunjes, A. Dietzel, An inert 3D emulsification device for individual precipitation and concentration of amorphous drug nanoparticles, Lab Chip. 18 (2018) 627–638.

[76] X. Kang, C. Luo, Q. Wei, C. Xiong, Q. Chen, Y. Chen, Q. Ouyang, Mass production of highly monodisperse polymeric nanoparticles by parallel flow focusing system, Microfluid. Nanofluidics. 15 (2013) 337–345.

[77] A. Reisch, A. Runser, Y. Arntz, Y. Mély, A.S. Klymchenko, Charge-controlled nanoprecipitation as a modular approach to ultrasmall polymer nanocarriers: Making bright and stable nanoparticles, ACS Nano. 9 (2015) 5104–5116.

[78] R.L. McCall, R.W. Sirianni, PLGA nanoparticles formed by single- or double-emulsion with vitamin E-TPGS., J. Vis. Exp. (2013) 51015.

[79] Y. Wang, P. Li, T.T.D. Tran, J. Zhang, L. Kong, Manufacturing techniques and surface

engineering of polymer based nanoparticles for targeted drug delivery to cancer, Nanomaterials. 6 (2016) 1–18.

[80] M.C. Operti, A. Bernhardt, S. Grimm, A. Engel, C.G. Figdor, O. Tagit, PLGA-based nanomedicines manufacturing: Technologies overview and challenges in industrial scale-up, Int. J. Pharm. 605 (2021).

[81] R. Devulapally, N.M. Sekar, T. V. Sekar, K. Foygel, T.F. Massoud, J.K. Willmann, R. Paulmurugan, Polymer nanoparticles mediated codelivery of AntimiR-10b and AntimiR-21 for achieving triple negative breast cancer therapy, ACS Nano. 9 (2015) 2290–2302.

[82] R. Dinarvand, N. Sepehri, S. Manoochehri, H. Rouhani, F. Atyabi, Polylactide-co-glycolide nanoparticles for controlled delivery of anticancer agents., Int. J. Nanomedicine. 6 (2011) 877–895.

[83] Dolomite Microfluidics, Microfluidic Production of 20 to 50 µm Core-Shell PLGA Beads, (2019) 1–14.

[84] S.Y. Xie, S.L. Wang, B.K. Zhao, C. Han, M. Wang, W.Z. Zhou, Effect of PLGA as a polymeric emulsifier on preparation of hydrophilic protein-loaded solid lipid nanoparticles, Colloids Surfaces B Biointerfaces. 67 (2008) 199–204.

[85] C. Pichon, L. Billiet, P. Midoux, Chemical vectors for gene delivery: Uptake and intracellular trafficking, Curr. Opin. Biotechnol. 21 (2010) 640–645..

[86] Y. Hou, H. Li, W. Huo, MicroRNA-495 alleviates ulcerative interstitial cystitis via inactivating the JAK–STAT signaling pathway by inhibiting JAK3, Int. Urogynecol. J. 32 (2021) 1253–1263.

[87] L. Duan, Y. Liang, X. Xu, Y. Xiao, D. Wang, Recent progress on the role of miR-140 in cartilage matrix remodelling and its implications for osteoarthritis treatment, Arthritis Res. Ther. 22 (2020) 1–9.

[88] S. Mali, Delivery systems for gene therapy, Indian J. Hum. Genet. 19 (2013) 3–8.

[89] Y. Seow, M.J. Wood, Biological gene delivery vehicles: Beyond viral vectors, Mol. Ther. 17 (2009) 767–777.

[90] J. Panyam, V. Labhasetwar, Biodegradable nanoparticles for drug and gene delivery to cells and tissue, Adv. Drug Deliv. Rev. 55 (2003) 329–347.

[91] S.Biçeroğlu, A. Memiş, Gene therapy: applications in interventional radiology, Interv. Radiol. 11 (2005) 2005.

[92] D. Psimadas, P. Georgoulias, V. Valotassiou, G. Loudos, Formulating Poly(Lactide-co-Glycolide) Particles for Plasmid DNA Delivery, J. Pharm. Sci. 101 (2012) 2271–2280.

[93] D. Psimadas, P. Georgoulias, V. Valotassiou, G. Loudos, Nonviral Approaches for Targeted Delivery of Plasmid DNA and Oligonucleotide, J. Pharm. Sci. 101 (2012) 2271–2280.

[94] V.J. Mohanraj, Y. Chen, Nanoparticles – A Review, 5 (2006) 561–573.

[95] S. Behzadi, V. Serpooshan, W. Tao, M.A. Hamaly, M.Y. Alkawareek, E.C. Dreaden, D. Brown, A.M. Alkilany, O.C. Farokhzad, M. Mahmoudi, Cellular uptake of nanoparticles: Journey inside the cell, Chem. Soc. Rev. 46 (2017) 4218–4244.

[96] B. Yameena, W.l. Choia, C. Vilosa, A. Swamia, J. Shia, Insight into nanoparticle cellular uptake and intracellular targeting, Journal of controlled release 190 (2014): 485-499.

[97] D. Manzanares, V. Ceña, Endocytosis: The nanoparticle and submicron nanocompounds gateway into the cell, Pharmaceutics. 12 (2020).

[98] G.J. Doherty, H.T. McMahon, Mechanisms of endocytosis, Annu. Rev. Biochem. 78 (2009) 857–902.

[99] S. Kumari, S. Mg, S. Mayor, Endocytosis unplugged: Multiple ways to enter the cell, Cell Res. 20 (2010) 256–275.

[100] J.A. Swanson, Shaping cups into phagosomes and macropinosomes, Bone. 23 (2008) 1–7.

[101] A. Aderem, D.M. Underhill, Mechanisms of phagocytosis in macrophages, Annu. Rev. Immunol. 17 (1999) 593–623.

[102] H. Hillaireau, P. Couvreur, Nanocarriers' entry into the cell: Relevance to drug delivery, Cell. Mol. Life Sci. 66 (2009) 2873–2896.

[103] V. Schäfer, H. von Briesen, R. Andreesen, A.M. Steffan, C. Royer, S. Tröster, J. Kreuter, H. Rübsamen-Waigmann, Phagocytosis of Nanoparticles by Human Immunodeficiency Virus (HlV)-Infected Macrophages: A Possibility for Antiviral Drug Targeting, Pharm. Res. An Off. J. Am. Assoc. Pharm. Sci. 9 (1992) 541–546.

[104] Y.Tabata, Y.lkada, Effect of the size and surface charge of polymer microspheres on their phagocytosis by macrophage, (1987).

[105] Y. Liu, A.Ibricevic, J.A. Cohen, J.L. Cohen, S.P. Gunsten, J.M. J. Fréchet, M.J. Walter, M.J. Welch, S.L.Brody, Impact of hydrogel nanoparticle size and functionalization on in vivo behavior for lung imaging and therapeutics, Bone. 23 (2008) 1–7.

[106] J.A. Champion, S. Mitragotri, Shape induced inhibition of phagocytosis of polymer particles, Pharm. Res. 26 (2009) 244–249.

[107] A.E. Nel, L. Mädler, D. Velegol, T. Xia, E.M.V. Hoek, P. Somasundaran, F. Klaessig, V. Castranova, M. Thompson, Understanding biophysicochemical interactions at the

nano-bio interface, Nat. Mater. 8 (2009) 543–557.

[108] G.Sahay, D.Y Alakhova, and A.V Kabanov, Endocytosis of Nanomedicines, J Control Release. 145 (2010) 182–195.

[109] S.D. Conner, S.L. Schmid, Regulated portals of entry into the cell, Nature. 422 (2003) 37–44.

[110] M. Ehrlich, W. Boll, A. Van Oijen, R. Hariharan, K. Chandran, M.L. Nibert, T. Kirchhausen, Endocytosis by random initiation and stabilization of clathrin-coated pits, Cell. 118 (2004) 591–605.

[111] O. Harush-Frenkel, N. Debotton, S. Benita, Y. Altschuler, Targeting of nanoparticles to the clathrin-mediated endocytic pathway, Biochem. Biophys. Res. Commun. 353 (2007) 26–32.

[112] L.Pelkmans and A. Helenius, Endocytosis Via Caveolae, Traffic 3.5 (2002) 311–320.

[113] I. Fernandez, Y. Ying, J. Albanesi, R.G.W. Anderson, Mechanism of caveolin filament assembly, Proc. Natl. Acad. Sci. U. S. A. 99 (2002) 11193–11198.

[114] L.E. Kelemen, The role of folate receptor α in cancer development, progression and treatment: Cause, consequence or innocent bystander?, Int. J. Cancer. 119 (2006) 243–250.

[115] C.C. Norbury, L.J. Hewlett, A.R. Prescott, N. Shastri, C. Watts, Class I MHC presentation of exogenous soluble antigen via macropinocytosis in bone marrow macrophages, Immunity. 3 (1995) 783–791.

[116] J.P. Lim, P.A. Gleeson, Macropinocytosis: An endocytic pathway for internalising large gulps, Immunol. Cell Biol. 89 (2011) 836–843.

[117] F. Zhao, Y. Zhao, Y. Liu, X. Chang, C. Chen, Y. Zhao, Cellular uptake, intracellular trafficking, and cytotoxicity of nanomaterials, Small. 7 (2011) 1322–1337.

[118] J. Huotari, A. Helenius, Endosome maturation, EMBO J. 30 (2011) 3481–3500.

[119] M. Jovic, M. Sharma, J. Rahajeng, S. Caplan, The early endosome: A busy sorting station for proteins at the crossroads, Histol. Histopathol. 25 (2010) 99–112.

[120] M. Dominska, D.M. Dykxhoorn, Breaking down the barriers: siRNA delivery and endosome escape, J. Cell Sci. 123 (2010) 1183–1189.

[121] R. V. Benjaminsen, M.A. Mattebjerg, J.R. Henriksen, S.M. Moghimi, T.L. Andresen, The possible "proton sponge " effect of polyethylenimine (PEI) does not include change in lysosomal pH, Mol. Ther. 21 (2013) 149–157.

[122] S. Roy, D. Zhu, W.J. Parak, N. Feliu, Lysosomal Proton Buffering of Poly(ethylenimine) Measured in Situ by Fluorescent pH-Sensor Microcapsules, ACS

Nano. 14 (2020) 8012–8023.

[123] M.A. Nguyen, H. Wyatt, L. Susser, M. Geoffrion, A. Rasheed, A.C. Duchez, M.L. Cottee, E. Afolayan, E. Farah, Z. Kahiel, M. Cote, S. Gadde, K.J. Rayner, Delivery of MicroRNAs by Chitosan Nanoparticles to Functionally Alter Macrophage Cholesterol Efflux in Vitro and in Vivo, ACS Nano. 13 (2019) 6491–6505.

[124] B. Neuhaus, B. Tosun, O. Rotan, A. Frede, A.M. Westendorf, M. Epple, Nanoparticles as transfection agents: A comprehensive study with ten different cell lines, RSC Adv. 6 (2016) 18102–18112.

[125] H. Bai, G.M.S. Lester, L.C. Petishnok, D.A. Dean, Cytoplasmic transport and nuclear import of plasmid DNA, Biosci. Rep. 37 (2017) 1–17.

[126] J. Chen, Z. Guo, H. Tian, X. Chen, Production and clinical development of nanoparticles for gene delivery, Mol. Ther. - Methods Clin. Dev. 3 (2016) 16023.

[127] S. Gao, H. Tian, Y. Guo, Y. Li, Z. Guo, X. Zhu, X. Chen, MiRNA oligonucleotide and sponge for miRNA-21 inhibition mediated by PEI-PLL in breast cancer therapy, Acta Biomater. 25 (2015) 184–193.

[128] B. Neuhaus, B. Tosun, O. Rotan, A. Frede, A.M. Westendorf, M. Epple, Nanoparticles as transfection agents: A comprehensive study with ten different cell lines, RSC Adv. 6 (2016) 18102–18112.

[129] M.S. Bradley, E.E. Burke, C. Grenier, C.L. Amundsen, S.K. Murphy, and N.Y. Siddiqui, A genome-scale DNA methylation study in women with interstitial cystitis/bladder pain syndrome. Neurourology and urodynamics 37.4 (2018): 1485-1493.

[130] L. Johannes, S. Mayor, Induced domain formation in endocytic invagination, lipid sorting, and scission, Cell. 142 (2010) 507–510.

[131] M.R.R. De Planque, S. Aghdaei, T. Roose, H. Morgan, Electrophysiological characterization of membrane disruption by nanoparticles, ACS Nano. 5 (2011) 3599–3609.

[132] S. Zhang, A. Nelson, P.A. Beales, Freezing or wrapping: The role of particle size in the mechanism of nanoparticle biomembrane interaction, Langmuir. 28 (2012) 12831–12837.

[133] B.D. Chithrani, A.A. Ghazani, W.C.W. Chan, Determining the size and shape dependence of gold nanoparticle uptake into mammalian cells, Nano Lett. 6 (2006) 662–668.

[134] Y. Shan, S. Ma, L. Nie, X. Shang, X. Hao, Z. Tang, H. Wang, Size-dependent endocytosis of single gold nanoparticles, Chem. Commun. 47 (2011) 8091–8093.

[135] A. Albanese, W.C.W. Chan, Effect of gold nanoparticle aggregation on cell uptake and toxicity, ACS Nano. 5 (2011) 5478–5489.

[136] F. Paquin, J. Rivnay, A. Salleo, N. Stingelin, C. Silva, Multi-phase semicrystalline microstructures drive exciton dissociation in neat plastic semiconductors, J. Mater. Chem. C. 3 (2015) 10715–10722.

[137] B. Parakhonskiy, M. V. Zyuzin, A. Yashchenok, S. Carregal-Romero, J. Rejman, H. Möhwald, W.J. Parak, A.G. Skirtach, The influence of the size and aspect ratio of anisotropic, porous CaCO3 particles on their uptake by cells, J. Nanobiotechnology. 13 (2015) 1–13.

[138] A. Banerjee, J. Qi, R. Gogoi, J. Wong, S. Mitragotri, Role of nanoparticle size, shape and surface chemistry in oral drug delivery, Journal of Controlled Release, 238 (2016): 176-185.

[139] J. Lin, H. Zhang, Z. Chen, Y. Zheng, Penetration of lipid membranes by gold nanoparticles: Insights into cellular uptake, cytotoxicity, and their relationship, ACS Nano. 4 (2010) 5421–5429.

[140] A. Asati, S. Santra, C. Kaittanis, J.M. Perez, Localization, Surface-charge-dependent Cell Nanoparticles, Cerium Oxide, ACS Nano. 4 (2011) 5321–5331.

[141] E.C. Cho, J. Xie, P.A. Wurm, Y. Xia, Understanding the role of surface charges in cellular adsorption versus internalization by selectively removing gold nanoparticles on the cell surface with a I 2/KI etchant, Nano Lett. 9 (2009) 1080–1084.

[142] L. Billiet, J.P. Gomez, M. Berchel, P.A. Jaffrès, T. Le Gall, T. Montier, E. Bertrand, H. Cheradame, P. Guégan, M. Mével, B. Pitard, T. Benvegnu, P. Lehn, C. Pichon, P. Midoux, Gene transfer by chemical vectors, and endocytosis routes of polyplexes, lipoplexes and lipopolyplexes in a myoblast cell line, Biomaterials. 33 (2012) 2980–2990.

[143] J. Wong-Ekkabut, S. Baoukina, W. Triampo, I.M. Tang, D.P. Tieleman, L. Monticelli, Computer simulation study of fullerene translocation through lipid membranes, Nat. Nanotechnol. 3 (2008) 363–368.

[144] W. Tao, X. Zeng, J. Wu, X. Zhu, X. Yu, X. Zhang, J. Zhang, G. Liu, L. Mei, Polydopamine-based surface modification of novel nanoparticle-aptamer bioconjugates for in vivo breast cancer targeting and enhanced therapeutic effects, Theranostics. 6 (2016) 470–484.

[145] T. dos Santos, J. Varela, I. Lynch, A. Salvati, K.A. Dawson, Effects of transport inhibitors on the cellular uptake of carboxylated polystyrene nanoparticles in different

cell lines, PLoS One. 6 (2011).

[146] R.G. Parton, M.A. Del Pozo, Caveolae as plasma membrane sensors, protectors and organizers, Nat. Rev. Mol. Cell Biol. 14 (2013) 98–112.

[147] R.G. Parton, K. Simons, The multiple faces of caveolae, Nat. Rev. Mol. Cell Biol. 8 (2007) 185–194.

[148] J. Sottile, J. Chandler, Fibronectin matrix turnover occurs through a caveolin-1-dependent process, Mol. Biol. Cell. 16 (2005) 757–768.

[149] X. Yuan, B.A. Shah, N.K. Kotadia, J. Li, H. Gu, Z. Wu, The development and mechanism studies of cationic chitosan-modified biodegradable PLGA nanoparticles for efficient siRNA drug delivery, Pharm. Res. 27 (2010) 1285–1295.

[150] N. Kanthamneni, B. Yung, R.J. Lee, Effect of Eudragit on in vitro transfection efficiency of PEI-DNA complexes, Anticancer Res. 36 (2016) 81–86.

[151] M.N.V. Ravi Kumar, U. Bakowsky, C.M. Lehr, Preparation and characterization of cationic PLGA nanospheres as DNA carriers, Biomaterials. 25 (2004) 1771–1777.

[152] M.A.G. Raja, H. Katas, T.J. Wen, Stability, intracellular delivery, and release of siRNA from chitosan nanoparticles using different cross-linkers, PLoS One. 10 (2015) 1–19.

[153] M. Martínez-Fernández, C. Rubio, C. Segovia, F.F. López-Calderón, M. Dueñas, J.M. Paramio, EZH2 in bladder cancer, a promising therapeutic target, Int. J. Mol. Sci. 16 (2015) 27107–27132.

[154] A.P. Singh, A. Biswas, A. Shukla, P. Maiti, Targeted therapy in chronic diseases using nanomaterial-based drug delivery vehicles, Signal Transduct. Target. Ther. 4 (2019) 1–21.

[155] K.S. Ko, M. Lee, J.J. Koh, S.W. Kim, Combined administration of plasmids encoding IL-4 and IL-10 prevents the development of autoimmune diabetes in nonobese diabetic mice, Mol. Ther. 4 (2001) 313–316.

[156] M. Kumar, X. Kong, A.K. Behera, G.R. Hellermann, R.F. Lockey, S.S. Mohapatra, Chitosan IFN-γ-pDNA nanoparticle (CIN) therapy for allergic asthma, Genet. Vaccines Ther. 1 (2003) 1–10.

[157] P. Mastorakos, A.L.D. Silva, J. Chisholm, E. Song, W.K. Choi, M.P. Boyle, M.M. Morales, J. Hanes, J.S. Suk, Highly compacted biodegradable DNA nanoparticles capable of overcoming the mucus barrier for inhaled lung gene therapy, Proc. Natl. Acad. Sci. U. S. A. 112 (2015) 8720–8725.

[158] M.C. Durán, S. Willenbrock, A. Barchanski, J.M.V. Müller, A. Maiolini, J.T. Soller, S. Barcikowski, I. Nolte, K. Feige, H. Murua Escobar, Comparison of nanoparticle-

mediated transfection methods for DNA expression plasmids: Efficiency and cytotoxicity, J. Nanobiotechnology. 9 (2011) 47.

[159] X. Wang, L. Zhou, Y. Ma, X. Li, H. Gu, Control of aggregate size of polyethyleneimine-coated magnetic nanoparticles for magnetofection, Nano Res. 2 (2009) 365–372.

[160] I. Serganova, R.G. Blasberg, Molecular imaging with reporter genes: Has its promise been delivered?, J. Nucl. Med. 60 (2019) 1665–1681.

[161] G. Yu, W. Yao, W. Xiao, H. Li, H. Xu, B. Lang, MicroRNA-34a functions as an anti-metastatic microRNA and suppresses angiogenesis in bladder cancer by directly targeting CD44, J. Exp. Clin. Cancer Res. 33 (2014) 1–13.

[162] H.H. Andersen, M. Duroux, P. Gazerani, MicroRNAs as modulators and biomarkers of inflammatory and neuropathic pain conditions, Neurobiol. Dis. 71 (2014) 159–168.

[163] M. Doherty, Color Atlas and text of osteoarthritis, Saunders, 1994.

[164] I. Haq, E. Murphy, J. Dacre, Osteoarthritis, Postgrad. Med. J. 79 (2003) 377–383.

[165] E. Araldi, E. Schipani, MicroRNA-140 and the silencing of osteoarthritis, Genes Dev. 24 (2010) 1075–1080.

[166] K. Onishi, A. Utturkar, E. Chang, R. Panush, J. Hata, D.Perret-Karimi, Osteoarthritis: A Critical Review, in Physical and Rehabilitation Medicine 24.3-4 (2012).

[167] S. Brown, S. Kumar, S. Sharma, Intra-articular targeting of nanomaterials for the treatment of osteoarthritis. Acta biomaterialia 93 (2019): 239-257.

[168] NICE National Institute for Health and Care Excellence, Introduction | Osteoarthritis: care and management, Www.Nice.Org.Uk. (2014) 1.

[169] D.T. Felson, Incidence and natural history of knee OA in the elderly Arthritis & Rheumatism: Official Journal of the American College of Rheumatology 38.8 (1995): 1134-1141.

[170] S.A. Oliveria, D.T. Felson, J.I. Reed, P.A. Cirillo, A.M. Walker, Incidence of symptomatic hand, hip, and knee osteoarthritis among patients in a health maintenance organization, Arthritis Rheum. 38 (1995) 1134–1141.

[171] D.T. Felson, Y. Zhang, An update on the epidemiology of knee and hip osteoarthritis with a view to prevention, Arthritis Rheum. 41 (1998) 1343–1355.

[172] D.J.Hart, T.D. Spector, The relationship of obesity, fat distribution and osteoarthritis in women in the general population: the Chingford Study, J. Rheumatol. 20 (1993) 331–335.

[173] E. Yusuf, Pharmacologic and Non-Pharmacologic Treatment of Osteoarthritis, Curr. Treat. Options Rheumatol. 2 (2016) 111–125.

[174] K.D. Brandt, P. Courtney, M. Doherty, Key questions concerning paracetamol and NSAIDs for OA [13] (multiple letters), Ann. Rheum. Dis. 62 (2003) 287.

[175] X. Ayral, Injections in the treatment of osteoarthritis, Best Pract. Res. Clin. Rheumatol. 15 (2001) 609–626.

[176] J.N. Katz, B.E. Earp, A.H. Gomoll, Surgical management of osteoarthritis, Arthritis Care Res. 62 (2010) 1220–1228.

[177] J. Bondeson, S. Wainwright, C. Hughes, B. Caterson, The regulation of the ADAMTS4 and ADAMTS5 aggrecanases in osteoarthritis: A review, Clin. Exp. Rheumatol. 26 (2008) 139–145.

[178] M. Daheshia, J.Q. Yao, The interleukin 1β pathway in the pathogenesis of osteoarthritis, J. Rheumatol. 35 (2008) 2306–2312.

[179] N. Saha, F.Moldovan, G.Tardif, J.P.Pelletier, J.M. Cloutier, J.M.Pelletier, Interleukin-1beta-converting enzyme/caspase-1 in human osteoarthritic tissues: localization and role in the maturation of interleukin-1beta and interleukin-18, Arthritis & Rheumatism: Official Journal of the American College of Rheumatology 42.8 (1999): 1577-1587.

[180] K.M. E Kubota 1 , H Imamura, T Kubota, T Shibata, Interleukin 1 beta and stromelysin (MMP3) activity of synovial fluid as possible markers of osteoarthritis in the temporomandibular joint, J Oral Maxillofac Surg. 55(1):20–7 (1997) discussion 27-8.

[181] M.D. Smith, S. Triantafillou, A. Parker, P.P. Youssef, M. Coleman, Synovial membrane inflammation and cytokine production in patients with early osteoarthritis, J. Rheumatol. 24 (1997) 365–371.

[182] H.C. Huang, P.S. Klein, The frizzled family: Receptor for multiple signal transduction pathways, Genome Biol. 5 (2004) 1–7.

[183] Y. Wang, X. Fan, L. Xing, F. Tian, Wnt signaling: A promising target for osteoarthritis therapy, Cell Commun. Signal. 17 (2019) 1–14.

[184] M.J. Barter, M. Tselepi, R. Gõmez, S. Woods, W. Hui, G.R. Smith, D.P. Shanley, I.M. Clark, D.A. Young, Genome-wide microRNA and gene analysis of mesenchymal stem cell chondrogenesis identifies an essential role and multiple targets for miR-140-5p, Stem Cells. 33 (2015) 3266–3280.

[185] R.N. Al-Modawi, J.E. Brinchmann, T.A. Karlsen, Extensive downregulation of immune gene expression by microRNA-140-3p 5′ isomiR in an in vitro model of osteoarthritis, Osteoarthr. Cartil. Open. 3 (2021) 100189.

[186] H. Lu, L. Lv, Y. Dai, G. Wu, H. Zhao, F. Zhang, Porous Chitosan Scaffolds with Embedded Hyaluronic Acid/Chitosan/Plasmid-DNA Nanoparticles Encoding TGF-β1

Induce DNA Controlled Release, Transfected Chondrocytes, and Promoted Cell Proliferation, PLoS One. 8 (2013) 1–13.

[187] M. Fathi-Achachelouei, D. Keskin, E. Bat, N.E. Vrana, A. Tezcaner, Dual growth factor delivery using PLGA nanoparticles in silk fibroin/PEGDMA hydrogels for articular cartilage tissue engineering, J. Biomed. Mater. Res. - Part B Appl. Biomater. 108 (2020) 2041–2062.

[188] X. Li, B. Dai, J. Guo, L. Zheng, Q. Guo, J. Peng, J. Xu, L. Qin, Nanoparticle–Cartilage Interaction: Pathology-Based Intra-articular Drug Delivery for Osteoarthritis Therapy, Nano-Micro Letters 13.1 (2021): 1-48.

[189] S.Miyaki, T.Nakasa, S.Otsuki, S.Grogan, R.Higashiyama, A.Inoue, Y.Kato, T.Sato, M.K.Lotz, H.Asahara, MicroRNA-140 is expressed in differentiated human articular chondrocytes and modulates IL-1 responses, Arthritis & Rheumatism 60.9 (2009): 2723-2730.

[190] J. Winter, S. Jung, S. Keller, R.I. Gregory, S. Diederichs, Many roads to maturity: MicroRNA biogenesis pathways and their regulation, Nat. Cell Biol. 11 (2009) 228–234.

[191] H. Yan, X. Duan, H. Pan, N. Holguin, M.F. Rai, A. Akk, L.E. Springer, S.A. Wickline, L.J. Sandell, C.T.N. Pham, Suppression of NF-κB activity via nanoparticle-based siRNA delivery alters early cartilage responses to injury, Proc. Natl. Acad. Sci. U. S. A. 113 (2016) E6199–E6208.

[192] R.E. Whitmire, D. Scott Wilson, A. Singh, M.E. Levenston, N. Murthy, A.J. García, Self-assembling nanoparticles for intra-articular delivery of anti-inflammatory proteins, Biomaterials. 33 (2012) 7665–7675.

[193] S.R. Kim, M.J. Ho, E. Lee, J.W. Lee, Y.W. Choi, M.J. Kang, Cationic PLGA/eudragit RL nanoparticles for increasing retention time in synovial cavity after intra-articular injection in knee joint, Int. J. Nanomedicine. 10 (2015) 5263–5271.

[194] Addgene, pEGFP-C1 Vector Information, (2003) 3. papers://10e8b09b-2029-4a89-baf0-b90acb9a6c30/Paper/p6124.

[195] L. Tuddenham, G. Wheeler, S. Ntounia-Fousara, J. Waters, M.K. Hajihosseini, I. Clark, T. Dalmay, The cartilage specific microRNA-140 targets histone deacetylase 4 in mouse cells, FEBS Lett. 580 (2006) 4214–4217.

[196] K.V.Greco, A.J.Iqbal, L.Rattazzi, G.Nalesso, N.Moradi-Bidhendi, A.R.Moore, M.B.Goldring, F.Dell'Accio, M.Perretti, High density micromass cultures of a human chondrocyte cell line: A reliable assay system to reveal the modulatory functions of

pharmacological agents, Biochemical pharmacology 82.12 (2011): 1919-1929.

[197] B.A. Miller-Chou, J.L. Koenig, A review of polymer dissolution, Prog. Polym. Sci. 28 (2003) 1223–1270.

[198] D.Q.M. Craig, M. Reading, Thermal analysis of pharamaceuticals, CRC press, 2006.

[199] C. Berthomieu, R. Hienerwadel, Fourier transform infrared (FTIR) spectroscopy, Photosynth. Res. 101 (2009) 157–170.

[200] J.C.Rochet, Pharmaceutical Analysis: A Textbook for Pharmacy Students and Pharmaceutical Chemists, *American Journal of Pharmaceutical Education* 70.2 (2006):3.

[201] A.A. Bunaciu, H.Y. Aboul-Enein, S. Fleschin, Application of fourier transform infrared spectrophotometry in pharmaceutical drugs analysis, Appl. Spectrosc. Rev. 45 (2010) 206–219.

[202] T.A. Instruments, Rheology theory and applications, 2010.

[203] F.Qureshi, H.F.George, Newton's Law of Viscosity, Newtonian and Non-Newtonian Fluids, Encyclopedia of tribology, 2013.

[204] R. Shaw, Dynamic Light Scattering Training Achieving reliable nano particle sizing (Available from: http://www.chem.uci.edu/%7Edmitryf/manuals/Fundamentals/DLS%20concept.pdf), ATA Sci. Malvern. (2014). http://www.chem.uci.edu/~dmitryf/manuals/Fundamentals/DLS concept.pdf.

[205] Anton paar, The principles of dynamic light scattering, (2017).

[206] C. Dessy, D. Seeman, T. Analytical, Optimising DLS Measurements for Protein Characterisation, 5–6.

[207] R. Ismail, T. Sovány, A. Gácsi, R. Ambrus, G. Katona, N. Imre, I. Csóka, Synthesis and Statistical Optimization of Poly (Lactic-Co-Glycolic Acid) Nanoparticles Encapsulating GLP1 Analog Designed for Oral Delivery, Pharm. Res. 36 (2019).

[208] P. Senthil Kumar, K. Grace Pavithra, M. Naushad, Characterization techniques for nanomaterials, Nanomater. Sol. Cell Appl. (2019) 97–124.

[209] D. Cosco, F. Cilurzo, J. Maiuolo, C. Federico, M.T. Di Martino, M.C. Cristiano, P. Tassone, M. Fresta, D. Paolino, Delivery of miR-34a by chitosan/PLGA nanoplexes for the anticancer treatment of multiple myeloma, Sci. Rep. 5 (2015) 1–11.

[210] G.E. Marti, M. Stetler-Stevenson, J.J.H. Bleesing, T.A. Fleisher, Introduction to flow cytometry, 2001.

[211] V. Kuete, O. Karaosmanoğlu, H. Sivas, Anticancer Activities of African Medicinal

Spices and Vegetables, Med. Spices Veg. from Africa Ther. Potential Against Metab. Inflammatory, Infect. Syst. Dis. (2017) 271–297.

[212] K.J. Livak, D. S, Analysis of Relative Gene Expression Data Using Real-Time Quantitative PCR and the 2−ΔΔCT Method, 408 (2001) 402–408.

[213] D. Cosco, C. Federico, J. Maiuolo, S. Bulotta, R. Molinaro, D. Paolino, P. Tassone, M. Fresta, Physicochemical features and transfection properties of chitosan/poloxamer 188/poly(D,L-lactide-co-glycolide) nanoplexes, Int. J. Nanomedicine. 9 (2014) 2359–2372.

[214] S.E.A. Gratton, P.A. Ropp, P.D. Pohlhaus, J.C. Luft, V.J. Madden, M.E. Napier, J.M. DeSimone, The effect of particle design on cellular internalization pathways, Proc. Natl. Acad. Sci. U. S. A. 105 (2008) 11613–11618.

[215] W. Li, Q. Chen, T. Baby, S. Jin, Y. Liu, G. Yang, C.X. Zhao, Insight into drug encapsulation in polymeric nanoparticles using microfluidic nanoprecipitation, Chem. Eng. Sci. 235 (2021).

[216] X. Zhang, Q. Xia, N. Gu, Preparation of all-trans retinoic acid nanosuspensions using a modified precipitation method, Drug Dev. Ind. Pharm. 32 (2006) 857–863.

[217] H. Haberkorn, D. Franke, T. Frechen, W. Goesele, J. Rieger, Early stages of particle formation in precipitation reactions - Quinacridone and boehmite as generic examples, J. Colloid Interface Sci. 259 (2003) 112–126.

[218] B.Y. Gajera, D.A. Shah, R.H. Dave, Development of an amorphous nanosuspension by sonoprecipitation-formulation and process optimization using design of experiment methodology, Int. J. Pharm. 559 (2019) 348–359.

[219] V. Vitagliano, A. Zagari, R. Sartorio, Diffusion and Viscosity in CHCl3-CH3COOH System at 25°C, J. Chem. Eng. Data. 18 (1973) 370–372.

[220] R. Krishna, Uphill diffusion in multicomponent mixtures, Chem. Soc. Rev. 44 (2015) 2812–2836.

[221] K.P. Seremeta, D.A. Chiappetta, A. Sosnik, Poly(e{open}-caprolactone), Eudragit® RS 100 and poly(e{open}-caprolactone)/Eudragit® RS 100 blend submicron particles for the sustained release of the antiretroviral efavirenz, Colloids Surfaces B Biointerfaces. 102 (2013) 441–449.

[222] I.L.Blouza, C. Charcosset, S. Sfar, H. Fessi, Preparation and characterization of spironolactone-loaded nanocapsules for paediatric use, Int. J. Pharm. 325 (2006) 124–131.

[223] Y. Dong, W.K. Ng, J. Hu, S. Shen, R.B.H. Tan, A continuous and highly effective static

mixing process for antisolvent precipitation of nanoparticles of poorly water-soluble drugs, Int. J. Pharm. 386 (2010) 256–261.

[224] J. Goodwin, Colloids and interfaces with surfactants and polymers, John Wiley & Sons, 2009.

[225] J.W. Westwater, H.G. Drickamer, The Mathematics of Diffusion, J. Am. Chem. Soc. 79 (1957) 1267–1268.

[226] S.H. Behrens, D.G. Grier, The charge of glass and silica surfaces, The Journal of Chemical Physics 115.14 (2001): 6716-6721.

[227] S.N.Kazi, Fouling and Fouling Mitigation on Heat Exchanger Surfaces S. N. Kazi Department of Mechanical and Materials Engineering, Intechopen,2012.

[228] T. Wen, L.N. Brush, K.M. Krishnan, A generalized diffusion model for growth of nanoparticles synthesized by colloidal methods, J. Colloid Interface Sci. 419 (2014) 79–85.

[229] S.M. Dizaj, S. Jafari, A.Y. Khosroushahi, A sight on the current nanoparticle-based gene delivery vectors, Nanoscale Res. Lett. 9 (2014) 1–9.

[230] S. Qi, P. Belton, K. Nollenberger, A. Gryczke, D.Q.M. Craig, Compositional analysis of low quantities of phase separation in hot-melt-extruded solid dispersions: A combined atomic force microscopy, photothermal fourier-transform infrared microspectroscopy, and localised thermal analysis approach, Pharm. Res. 28 (2011) 2311–2326.

[231] M. Alhijjaj, P. Belton, L. Fábián, N. Wellner, M. Reading, S. Qi, Novel Thermal Imaging Method for Rapid Screening of Drug-Polymer Miscibility for Solid Dispersion Based Formulation Development, Mol. Pharm. 15 (2018) 5625–5636.

[232] P.J. Marsac, T. Li, L.S. Taylor, Estimation of drug-polymer miscibility and solubility in amorphous solid dispersions using experimentally determined interaction parameters, Pharm. Res. 26 (2009) 139–151.

[233] B. Matlock, Assessment of Nucleic Acid Purity, Tech. Bull. NanoDrop Spectrophotometers. (2015) 1–2.

[234] W. Zauner, N.A. Farrow, A.M.R. Haines, In vitro uptake of polystyrene microspheres: Effect of particle size, cell line and cell density, J. Control. Release. 71 (2001) 39–51.

[235] F.C. Pérez-Martínez, J. Guerra, I. Posadas, V. Ceña, Barriers to non-viral vector-mediated gene delivery in the nervous system, Pharm. Res. 28 (2011) 1843–1858.

[236] I.S. Zuhorn, J.B.F.N. Engberts, D. Hoekstra, Gene delivery by cationic lipid vectors: Overcoming cellular barriers, Eur. Biophys. J. 36 (2007) 349–362.

[237] M. Breunig, U. Lungwitz, R. Liebl, A. Goepferich, Breaking up the correlation between

efficacy and toxicity for nonviral gene delivery, Proc. Natl. Acad. Sci. U. S. A. 104 (2007) 14454–14459.

[238] T.G. Park, J.H. Jeong, S.W. Kim, Current status of polymeric gene delivery systems, Adv. Drug Deliv. Rev. 58 (2006) 467–486.

[239] H. Lv, S. Zhang, B. Wang, S. Cui, J. Yan, Toxicity of cationic lipids and cationic polymers in gene delivery, J. Control. Release. 114 (2006) 100–109.

[240] J. O'Brien, H. Hayder, Y. Zayed, C. Peng, Overview of microRNA biogenesis, mechanisms of actions, and circulation, Front. Endocrinol. (Lausanne). 9 (2018) 1–12.

[241] X. Chen, S. Gu, B.F. Chen, W.L. Shen, Z. Yin, G.W. Xu, J.J. Hu, T. Zhu, G. Li, C. Wan, H.W. Ouyang, T.L. Lee, W.Y. Chan, Nanoparticle delivery of stable miR-199a-5p agomir improves the osteogenesis of human mesenchymal stem cells via the HIF1a pathway, Biomaterials. 53 (2015) 239–250.

[242] B. Li, D. Xie, H. Zhang, MicroRNA-101-3p advances cisplatin sensitivity in bladder urothelial carcinoma through targeted silencing EZH2, J. Cancer. 10 (2019) 2628–2634.

[243] M.A. Pop, B.D. Almquist, Controlled Delivery of MicroRNAs into Primary Cells Using Nanostraw Technology, Adv. NanoBiomed Res. 1 (2021) 2170063.

[244] M.L. Ji, H. Jiang, F. Wu, R. Geng, L.K. Ya, Y.C. Lin, J.H. Xu, X.T. Wu, J. Lu, Precise targeting of miR-141/200c cluster in chondrocytes attenuates osteoarthritis development, Ann. Rheum. Dis. 80 (2021) 356–366.

[245] M. Kapałczyńska, T. Kolenda, W. Przybyła, M. Zajączkowska, A. Teresiak, V. Filas, M. Ibbs, R. Bliźniak, Ł. Łuczewski, K. Lamperska, 2D and 3D cell cultures – a comparison of different types of cancer cell cultures, Arch. Med. Sci. 14 (2018) 910–919.

[246] C. Li, M. Kato, L. Shiue, J.E. Shively, M. Ares, R.J. Lin, Cell type and culture condition-dependent alternative splicing in human breast cancer cells revealed by splicing-sensitive microarrays, Cancer Res. 66 (2006) 1990–1999.

[247] A. Birgersdotter, R. Sandberg, I. Ernberg, Gene expression perturbation in vitro - A growing case for three-dimensional (3D) culture systems, Semin. Cancer Biol. 15 (2005) 405–412.

[248] N.J. Shah, B.C. Geiger, M.A. Quadir, N. Hyder, Y. Krishnan, A.J. Grodzinsky, P.T. Hammond, Synthetic nanoscale electrostatic particles as growth factor carriers for cartilage repair, Bioeng. Transl. Med. 1 (2016) 347–356.

[249] J. Favre, B.M. Jolles, Gait analysis of patients with knee osteoarthritis highlights a pathological mechanical pathway and provides a basis for therapeutic interventions,

EFORT Open Rev. 1 (2016) 368–374.

[250] M.Z.C Ruan, R.M.Patel, B.C.Dawson, M.M.Jiang, B.H.L.Lee. Pain, motor and gait assessment of murine osteoarthritis in a cruciate ligament transection model, Osteoarthritis and cartilage. 21.9 (2013): 1355-1364.